Numerical Studies on Folds and related Deformation Structures in Anisotropic Viscous Materials undergoing Ductile Deformation

Dissertation
der Mathematisch-Naturwissenschaftlichen Fakultät
der Eberhard Karls Universität Tübingen
zur Erlangung des Grades eines
Doktors der Naturwissenschaften
(Dr. rer. nat.)

vorgelegt von
Yuanbang Hu
aus Chengdu / Volksrepublik China

Tübingen
2023

Gedruckt mit Genehmigung der Mathematisch-Naturwissenschaftlichen Fakultät der Eberhard Karls Universität Tübingen.

Tag der mündlichen Qualifikation:	23.06.2023
Dekan:	Prof. Dr. Thilo Stehle
1. Berichterstatter/-in:	Prof. Dr. Paul D. Bons
2. Berichterstatter/-in:	Prof. Dr. Reinhard Drews

Erklärung

Ich erkläre hiermit, dass ich die zur Promotion eingereichte Arbeit selbständig verfasst, nur die angegebenen Quellen und Hilfsmittel benutzt und wörtlich oder inhaltlich übernommene Stellen als solche gekennzeichnet habe. Ich erkläre, dass die Richtlinien zur Sicherung guter wissenschaftlicher Praxis der Universität Tübingen (Beschluss des Senats vom 25.5.2000) beachtet wurden. Ich versichere an Eides statt, dass diese Angaben wahr sind und dass ich nichts verschwiegen habe. Mir ist bekannt, dass die falsche Abgabe einer Versicherung an Eides statt mit Freiheitsstrafe bis zu drei Jahren oder mit Geldstrafe bestraft wird.

Tübingen, 5. Mai 2023

PhD Project Supervisors:

Prof. Dr. Paul D. Bons

Prof. Dr. Shu-gen Liu

Abstract

Folds are common structures in deformed rocks and ice sheets from the microscale to lithospheric scale. This thesis present numerical studies on folds and related deformation structures in anisotropic viscous materials undergoing ductile deformation with various boundary conditions. Mechanical anisotropy considered her is due to a crystallographic preferred orientation (CPO), for example by of alignment of micas or the basal planes of ice crystals. The modelling aims to numerically better understand the various fold geometries that are observed in natural rocks or ice drill cores. This thesis covers two main topics: (i) the influence of an initial CPO and intensity of anisotropy on resulting crenulation geometries in a single-phase material that deforms in moderate strain in dextral simple shear deformation, and (ii) the influence of an initial CPO, intensity of anisotropy and viscosities on evolving fold geometries of single-phase or poly-phase materials that deform in layer-parallel pure shear. The modelling is performed with the Viscoplastic Full-Field Transform (VPFFT) crystal plasticity code coupled with the two-dimensional platform modelling platform Elle.

Mechanical anisotropy can enhance shear localisation and redistribute the strain, resulting in localised shear domains with strain concentration and low-strain domains in between. This strain localisation dominates the formation of structures in anisotropic materials and is visualised by foliated layers or foliations. The fold and crenulation geometries displayed in this thesis are made by systematically varying (i) the initial orientation of the anisotropy (CPO), (ii) the intensity of anisotropy, and (iii) the viscous property differences of materials.

In simple shear with a CPO in the stretching field from the beginning, three types of localisation behaviour are synthetic shear localisation, antithetic shear localisation and distributed localisation. However, the resulting visible crenulation geometries are very varied and include ‘S-C’ structure (C & C’ bands), ‘anti S-C’ structure (C’’ bands), or mixes of both, or even in some cases no crenulation at all. This highlights that crenulation geometries are primarily due to the strong mechanical anisotropy of rocks.

Mechanical anisotropy also affects layer-parallel pure shear shortening simulations. Here we observe two end-member geometries: The first is buckle folding and thickening of a competent layer similar to classical Biot-type buckle folds. An axial planar crenulation cleavage forms in the anisotropic matrix. In the absence of a competent layer, folds in the anisotropic matrix are self-similar with no characteristic length scale. This is observed in polar ice sheets.

In this case it was also observed that fold amplification ceased after some strain, due to the rotation of the CPO. This confirms the hypothesis proposed for the shear margins of the Northeast Greenland Ice Stream (NEGIS), where fold amplification ceased about 2000 a BP. The second end member is layer-extension folding with strong amplification of fold amplitudes due to the formation of conjugate, localised bands in the matrix. Other geometries are in between.

Zusammenfassung

Falten sind häufige Strukturen in deformierten Gesteinen und Eisschilden von der Mikro- bis zur Lithosphärenskala. In dieser Dissertation werden numerische Studien über Falten und verwandte Verformungsstrukturen in anisotropen viskosen Materialien vorgestellt, die sich unter verschiedenen Randbedingungen duktil verformen. Die hier betrachtete mechanische Anisotropie ist auf eine kristallographische Vorzugsorientierung zurückzuführen (CPO), zum Beispiel durch die Ausrichtung von Glimmern oder die Basalebenen von Eiskristallen. Ziel der Modellierung ist es, die verschiedenen Faltengeometrien, die in natürlichen Gesteinen oder Eisbohrkernen beobachtet werden, numerisch besser zu verstehen. Diese Dissertation behandelt zwei Hauptthemen: (i) der Einfluss eines anfänglichen CPO und der Intensität der Anisotropie auf die resultierenden Krenulierungsgeometrien in einem einphasigen Material, das sich unter mäßiger Dehnung bei dextraler einfacher Scherverformung verformt, und (ii) der Einfluss eines anfänglichen CPO, der Intensität der Anisotropie und der Viskositäten auf sich entwickelnde Faltengeometrien von ein- oder mehrphasigen Materialien, die sich bei schichtparalleler reiner Scherung verformen. Die Modellierung erfolgt mit dem Kristallplastizitätscode Viskoplastische Vollfeldtransformation (VPFFT, Viscoplastic Full-Field Transform), Die Modellierung erfolgt mit dem Kristallplastizitätscode VPFFT (Viscoplastic Full-Field Transform), der mit der zweidimensionalen Modellierungsplattform Elle.

Mechanische Anisotropie kann die Scherlokalisierung verbessern und die Dehnung umverteilen, was zu lokalisierten Scherdomänen mit Dehnungskonzentration und Domänen mit geringer Dehnung führt, die arm an Dehnung sind. Diese Dehnungslokalisierung dominiert die Bildung von Strukturen in anisotropen Materialien und wird durch schichtförmige Schichten oder Folierungen sichtbar gemacht Die in dieser Dissertation gezeigten Falten- und Rillengeometrien werden durch systematisches Variieren (i) der anfänglichen Orientierung der Anisotropie (CPO), (ii) der Intensität der Anisotropie und (iii) der viskosen Eigenschaftsunterschiede von Materialien hergestellt.

Bei einfacher Scherung mit einem CPO, das sich von Anfang an im Streckfeld befindet, gibt es drei Arten von Lokalisierungsverhalten: synthetische Scherlokalisierung, antithetische Scherlokalisierung und verteilte Lokalisierung. Die daraus resultierenden sichtbaren Zackengeometrien sind jedoch sehr unterschiedlich, und umfassen eine "S-C"-Struktur (C- und C-Bänder), eine "Anti-S-C"-Struktur (C''-Bänder), Mischungen aus beiden, oder in einigen Fällen sogar überhaupt keine Krenulierung. Dies macht deutlich, dass die

Krenulierungsgeometrien in erster Linie auf die starke mechanische Anisotropie des Gesteins zurückzuführen sind.

Mechanische Anisotropie wirkt sich auch auf schichtparallele reine Scherverkürzungssimulationen aus. Hier beobachten wir zwei Endgliedgeometrien: Bei der ersten handelt es sich um eine Knickfaltung und Verdickung einer kompetenten Schicht, die der klassischen Biot-Knickfaltung ähnelt. In der anisotropen Matrix bildet sich eine axiale planare Krenulierungsspaltung. In Abwesenheit einer kompetenten Schicht sind die Falten in der anisotropen Matrix selbstähnlich und haben keine charakteristische Längenskala. Dies wird bei polaren Eisschilden beobachtet. In diesem Fall wurde auch beobachtet, dass die Faltamplifikation aufgrund der Rotation des CPO nach einer gewissen Belastung aufhörte. Dies bestätigt die Hypothese, die für die Scherränder des Nordostgrönland-Eisstroms (NEGIS) vorgeschlagen wurde, wo die Faltamplifikation um 2000 a BP aufhörte. Das zweite Endelement ist eine Schichterweiterungsfaltung mit starker Verstärkung der Faltungsamplituden aufgrund der Bildung von konjugierten, lokalisierten Bändern in der Matrix. Andere Geometrien liegen dazwischen.

Acknowledgements

Finishing this thesis is strongly supporting and supervising of Prof. Paul Bons. Paul has guiding me into the numerical world for scientific research, helping in ideas, lectures, discussions, and field work through almost whole process along this thesis. Also, a friendly, pleasure, and scientific environment in Tübingen ‘arbeitsgruppe-strukturgeologie’.

Another strongly supporting from Prof. Shugen Liu. I appreciate that unconditional support from Prof. Liu on both the financial supports of field work in LongMen mountain structural belt, and the deep, advanced, scientific thinking in Structural Geology that has influence me quite a lot.

Special thanks to Prof. Xuelin Cai, vice-Prof. Zhongjian Hou and vice-Prof. Jianghong Deng, all who have long been an inspiring to me and encouraging the beginning of my PhD career.

A warm thanks to all my warm colleagues in Tübingen: Rainer Babiel, Dr. Till Sachau, Tamara de Riese, Prof. Zuochen Li, Prof. Pengfei Li, Isaac Naaman, Yu Zhang, Dr. He Tian, Dongsheng Cao, Dr. Yuzhen Fu, vice-Prof. Dian Li and Dr. Catherine Bauer, who share and discuss the ideas and help each other unreservedly. Also, thanks to colleagues from AWI and Barcelona: Prof. Ilka Weikusat, Dr. Steven Franke, Dr. Maria-Gema Llorens, Dr. Enrique Gomez-Rivas, Dr. Albert Griera, Eloi González-Esvertit, etc. Then, thanks to colleagues in Chengdu: Dr. Kui Tong, Dr. Zijian Wang, Tian Hua, Ke Li, Dr. Yuyue Han, Shengwu Liu, Xun Jiang, Dr. Bin Xiao, Dr. Han Wang, Yu He, Prof. Bin Deng, vice-Prof. Jinxi Li, Prof. Bo Ran, Prof. Wei Sun, Prof. Zhiwu Li, etc.

I would also like to give special thanks to my friends Zheng, Shouhai, Zhaoliang, Jinting, Jun, Xuexue, Junru, Yunfeng, Pietro, Kuo, Chen, Yu, Ju, Le.

Finally, sincere thanks to my parents, my father Youjun Hu and my mother Yumin Cai, and thanks to all supporting from my family, especially Yu Hu.

All work presented has been financially supported by the Chengdu University of Technology (grant no. 10800-18Z0102), China Scholarship Council (grant no. 202008510177), and University of Tübingen. The field work in LongMen mountain was funded by the Chengdu University of Technology, and in Cap de Creus and Molinos by the University of Tübingen.

Table of Contents

Introduction

1 Background of fold

The study of rock deformation is one of the main topics in Structural Geology and Microtectonics, which is of high importance of analysing with respect to geometries (e.g., structural orientation, shape, layering, scale, etc.), kinematics (displacement, velocity, sense of shear, etc.) and even dynamics (stress, strain, endotectonic, exogenetic and their relations), to investigate historical development, especially the deformation stages and tectonic secquences along this development. The mentioned factors are not individual but inter-relevant and mutually accomplished.

Deformation structures, such as folds, lineations, are typically used by geologists to understand how rocks deform and their quantification in related to the describing parameters. Rocks can deform in different ways depending on their (i) physical environment where the objective rocks located, such as pressure P, temperature T related to the depth and, in Geology, as metamorphic rocks in orogens and fold-thrust belts, volcanic rocks in strike-slip systems, and sediments in the margin of divergent / convergent massifs or continents, etc. (ii) rheological properties, which are related to rock types with different mineral compositions, such as elasticity E, viscosity μ, viscosity contrast R, cohesion C, intrinsic anisotropy A, like hexagonal crystal system has different habit with tetragonal crystal system, and (iii) boundary conditions b, etc., both these four main factors contributing to get into different tectonic environment or form various structural geometries. The geometric parameters of folds can be used to qualify and quantify rheological properties and strain during deformation (e.g., Hudleston and Lan, 1993; Lan and Hudleston, 1995), so they have a relation that,

$$\varepsilon = f(P, T, E, \mu, R, C, A, b \ldots) \tag{1}$$

and also, a detailed relation (Glen, 1952; 1955) between strain rate and other parameters as

$$\dot{\varepsilon} = A_0 \, exp^{\left(\frac{-Q}{R\,T}\right)} \, \frac{\sigma^n}{g^m} \tag{2}$$

where the A_0 is pre-exponential factor material property of deformation material, Q is activation energy, R is universal gas constant, T is temperature, n is stress exponent (typically 1 to 5), g is grain size and m is grain size exponent (usually 1 to 3.).

1.1 Folds and crenulations undergoing simple shear / pure shear deformation

Folds are common deformation structures in deformed rocks distributed almost all tectonic related places, leading layered and foliated rocks to the curved planer structures, and giving information on shortening direction, kinematics, rheological properties, deformation histories, etc. (Sherwin and Chapple, 1968; Treagus, 1982; Hudleston, 1986; Ramsay and Huber, 1987; Hudleston and Lan, 1993; Lan and Hudleston, 1995; Bobillo-Ares et al., 2004; Passchier and Trouw, 2005; Hudleston and Treagus, 2010; Adamuszek et al., 2011; Llorens et al., 2013a, 2013b; Schmalholz and Mancktelow, 2016; Llorens, 2019b; Nabavi & Fossen, 2021). The review papers of the different equations for the dominant wavelength and amplitude can be found in Hudleston and Treagus (2010), Schmalholz and Mancktelow (2016), the fold geometries clarification can be found in review of Nabavi and Fossen (2021).

Here in this study, the mechanisms of deformation behaviours are assumed to be ductile in viscous and plastic states. The deformation processes are assumed to deform under rheological circumstances as a power-law fluid (Price and Cosgrove, 1990; Johnson and Fletcher, 1994; Pollard and Fletcher, 2005; Hudleston and Treagus, 2010; Burov, 2011; Cloetingh and Burov, 2011), so the brittle deformation is not much considered. In strength of the crust, the viscous deformation always occurs under the “Brittle-Ductile transition”, where the deformation environment is higher pressure and higher temperature within deeper crust by ductile flow. But there are still exceptions, some rocks can also deform in ductile at shallow crust which depend on their material properties, and also ice, who has a special lattice structure like ice 1h with respect to its typical environment, deforms in ductile at earth surface in e.g., Antarctic and Greenland, as ice sheets or glaciers.

The deformation structures of crenulations (micro-folds) and folds have numerous of different geometries, which also could be clarified by different describing parameters, such as interlimb angle, asymmetry, harmony, surface shape, cylindrical degree, etc., details can be found in detail in Nabavi and Fossen (2021). The thin plate theory for single layer folding (Biot, 1957, 1961; Ramberg, 1962, 1963, 1964; Fig. 1) and multilayer folding (Biot, 1964a, 1964b, 1965a; Ramberg, 1962, 1970; Ramsay and Huber, 1987; Price and Cosgrove, 1990; Fig. 1) has a dominate positions on number of research of layer-parallel shortening models with rocks or materials assumed at least are two phases. But later, geologists also found the different characters on various kinematics, such as synthetic movement and antithetic movement of high strain localised areas / domains within one model and forming crenulations, which could deform locally and simultaneously by single phase or multi-phase in a simple shear boundary condition of the whole model or natural outcrops. These high strain localised areas / domains

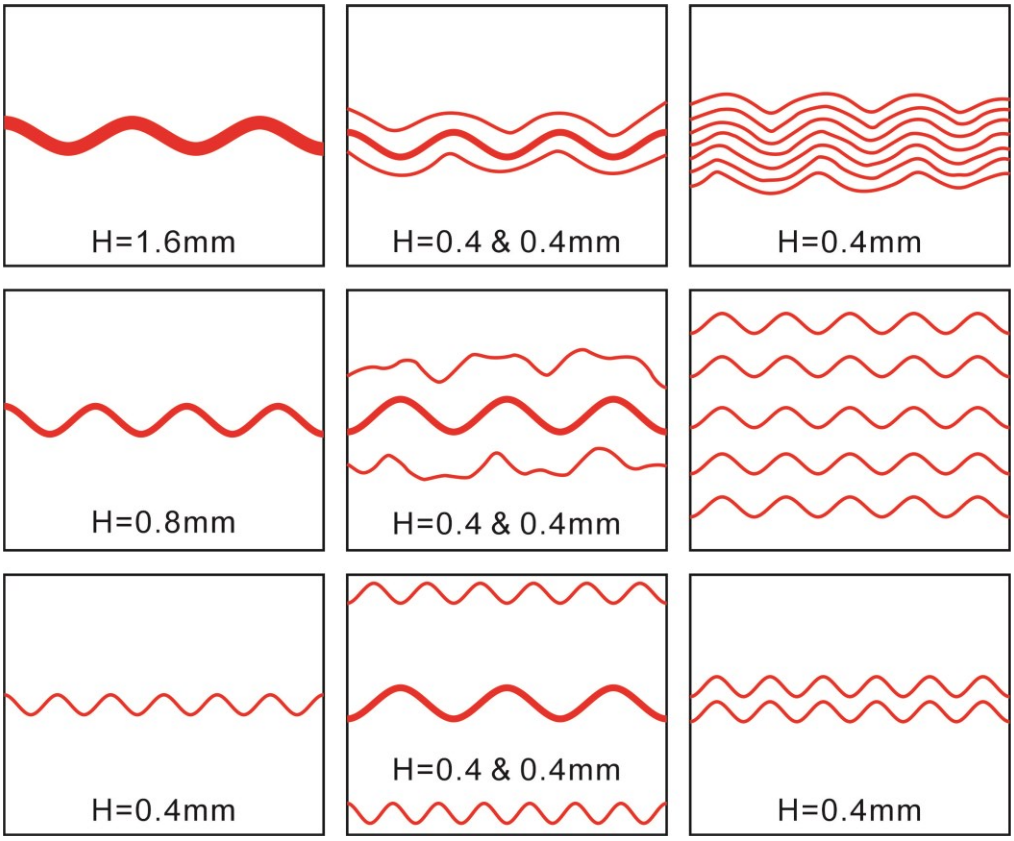

Fig.1 Buckling of single layer and multilayer that infer effects of layer thickness and layer spacing on fold geometries (from Currie et al., 1962, after Nabavi and Fossen, 2021, Fig.3.r)

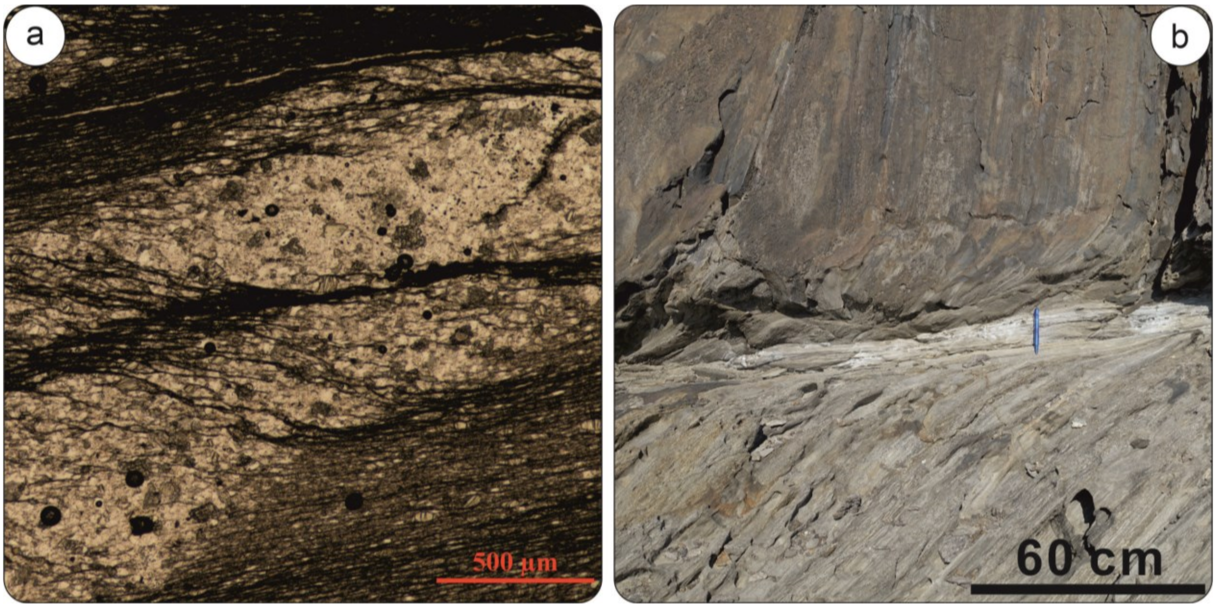

Fig.2 Shear localisation on all scales. (a) Shear bands in deformed metapelite at LongMen Mountain structural belt, China. (b) Shear zone in meta-turbidites at Cap de Creus, Spain.

deform together with the low strain areas / domains, where low strain areas / domains have less or very little deformation (Marshak et al., 2006; Carreras et al., 2010, 2013; Ponce et al., 2013; Llorens et al., 2013a, 2013b; Tanner, 2016; de Riese et al., 2019; Finch et al., 2020; 2022; Fig. 2).

Folds are indeed useful when investigating tectonic cycles because they experienced at least one or more stages of tectonic processes and formed over the whole range of geological scales (Schmalholz and Mancktelow, 2016). The deformation of folds probably recorded the information to (i) determine tectonic shortening directions, (ii) calculate the amount of tectonic shortening, (iii) interpret the geometry of lithospheric structures, (iv) identification of boundary conditions, and (v) investigate the rheological properties of the folded rocks (Nabavi and Fossen, 2021). Folds themselves bring the information about the deformation circumstances where they settled, and prediction of deep crust structures and relations to regional geological settings.

Nabavi and Fossen (2021) came up with that "…Several questions about folds should be raised to identify, analyse and interpret of fold structure. … Which parameters exert the greatest control on the observed fold geometry and folding mechanism? Which parameters need to be analysed? … How can fold analysis provide an estimate of strain? How did the fold evolve? What is needed to improve the mapping, analysis and understanding of folds and folding in the future? ...". Here I want to focus on several factors which are contribute to these processes and resulting geometries by using numerical simulation.

Complementary to field studies (e.g., Quinquis et al., 1978; Ramsay and Huber, 1987; Ormond and Hudleston, 2003; Alsop and Carreras, 2007; Alsop and Holdsworth, 2007; Torremans et al., 2014; Pérez-Alonso et al., 2016; Tanner, 2016) and analogue experiments (e.g., Biot et al., 1961; Ghosh, 1966; Hudleston, 1973; Cobbold, 1975; Manz and Wickham, 1978; Abassi and Mancktelow, 1990, 1992; Bons and Urai, 1996; Hunt et al., 1997; Tikoff and Peterson, 1998), numerical simulations have been applied to investigate how and by what mechanisms fold structures that we observe in nature form. The deformation simulated in this thesis is assumed to be within viscous flow that the stress depends on the invariable strain rate increment. And the strain can be redistributed randomly within a system or can concentrate locally (Llorens, 2015), e.g., the tip of the shear band (Bordignon et al., 2015).

Using numerical studies on folding research is a tendency not only to reveal the tectonic histories by using the constitutive equations, but also to find out the potential area for economy related objects as well as to predict of changing some inherent thoughts on previous studies. Here the numerical studies of folds have included many parameters, but the main parameters in this study concentrate on the effects of mechanical anisotropy (Lan and Hudleston, 1996;

Kocher et al., 2006; Ran et al. 2018; de Riese et al., 2019), which is the one of most important rheological parameter, then non-linear rheology (Parrish, 1973; Lan and Hudleston, 1991; Mancktelow, 1999; Schmalholz and Podladchikov, 2000; Kocher et al., 2006; Llorens et al., 2013a, 2013b), and viscoplastic behaviour (Zhang et al., 1996; Mancktelow, 1999; Schmalholz et al., 2001) of rocks, ice, or other assumed materials.

1.2 Single layer folding

The single layer folding theory beginning with the work of Biot (1957, 1961), Ramberg (1963, 1964) and Currie et al. (1962), who developed the theory and equations for single layer embedded in viscous, elastic or viscoelastic media, these base studies made fold describing by using rheological parameters based on layer-parallel shortening.

Biot (1957) created the describing equations on sinusoidal waveform folding structures, these procedures are concluded by the field observation (Biot, 1957, 1961, 1965c; Fletcher, 1977; Treagus, 1982; Ramsay and Huber, 1987; and abovementioned), analogue physics experiment (references abovementioned) and computing numerical modelling (Parrish, 1973; Parrish et al., 1976; Anthony and Wickham, 1978; Lan and Hudleston, 1991; Hudleston and Lan, 1994; Zhang et al., 1996, 2000; Mühlhaus et al., 1998; Mancktelow, 1999; Schmalholz and Podladchikov, 2000; Schmalholz et al., 2001; Viola and Mancktelow, 2005; Frehner and Schmalholz, 2006; Schmalholz, 2008; Hobbs et al., 2008; Kocher et al., 2006, 2008; Llorens et al., 2013a, 2013b; Griera et al., 2018; Llorens, 2019b). The studies on folds involves more parameters in the processes of formation variable geometries and forms different moving characteristics, which gave information back to researchers.

Based on the field studies and analogue experiments, layers become folded because of the amplification of instabilities that arise from the layer-parallel shortening competent (strong) layers and surrounding incompetent (weak) layers or a matrix. For Newtonian (linear) viscous layer and matrix in layer-parallel shortening, the dominant wavelength (λ_d) is depends on the viscosity of two layered materials ($\mu_L$and μ_M) and the layer thickness (H):

$$\lambda_d = 2\pi \mathrm{H} \left(\frac{\mu_L}{6\,\mu_M}\right)^{1/3} \tag{3}$$

Later, geologists carried out relevant describing equations of elastic materials (Currie et al., 1962; Jeng and Huang, 2008), elastic-viscous materials (Biot, 1961; Turcotte and Schubert, 1982).

A layer will shorten without folding if this thin plate layer is perfect, this process requires much work. However, folding is the preferred deformation procedures and results because they minimise the mechanical work required to shorten mechanically layered rock or even other materials from microscale to macroscale (England and McKenzie, 1982; Schmalholz et al., 2002; Schmalholz and Mancktelow, 2016). An initial perturbation of this thin plate layer would lead to the layer folding under layer-parallel shortening, or in Geology, layer-parallel pure shear. These kinds of perturbation would influence the fold geometries along the shortening process or stage (Abbassi and Mancktelow, 1990, 1992; Mancktelow, 1999; Griera et al., 2018). This process results from initial instabilities or perturbations of competent layer embedded in elastic, plastic, and viscous material by layer-parallel compression (Abbassi and Mancktelow, 1990, 1992; Mancktelow, 1999; Hudleston and Treagus, 2010; Schmalholz and Mancktelow, 2016) or layer-isocline simple shear (Llorens et al., 2013a, 2013b).

After Fletcher (1974), mechanical anisotropy and non-linearity are taken into consider as parameters that can largely affect fold geometries. What has not yet been deeply investigated is how the orientation of a mechanical anisotropy due to a Crystallographic Preferred Orientation (CPO) (as in a cleavage in a micaceous rock) that can affect the developing folding geometries with different initial settings under different boundary condition, such as (i) a perfect, relatively competent planar structure, such as a layer, vein or dyke as well as layered ice, under layer-parallel shortening (PAPER II, III and IV) and (ii) single phase planar structure undergoing simple shear deformation (PAPER I).

Using numerical simulations in thesis, some disharmonious fold geometries are discovered, e.g., big amplitude fold with small wavelength, or large wavelength with small amplitude. And the different stages of fold growth by using the amplification rate and layer thickness. Schmalholz and Mancktelow (2016) carried out three situations of amplification: (i) if the initial irregularities is small and/or dynamic amplification rate is low, the layer would shortening and thickening, (ii) if the dynamic amplification rate increase there would be a quickest amplification (Ramsay, 1967; Schmalholz and Podladchikov, 2001), and then (iii) after previous amplification, the amplification rate would decrease to ≈0, the amplification remains little with compression in matrix.

1.3 Multilayer folding

For multilayers consisting of many alternating competent and incompetent layers, with parameters such as (i) basic settings: layer thickness, layer spacing (the spacing interval of alternative competent and incompetent layers), number of layers, (ii) rheological properties: viscosity, elasticity, mechanical anisotropy, and (iii) boundary conditions, etc. of both competent layers and soft layered matrix, that have different contact relationships carry out resulting folds geometries vary like similar or disharmonic etc. (Ramberg, 1963; Ramsay and

Huber, 1987; Price and Cosgrove, 1990; Johnson and Fletcher, 1994; Schmid and Podladchikov, 2006; Hudleston and Treagus, 2010; de Riese, 2014; Schmalholz and Mancktelow, 2016), Johnson and Pfaff (1989) also came up with three end-member forms in multilayers: parallel, constrained and similar folds.

Biot (1964a, b, 1965a, b) developed a theory with functions to describe and to quantity the folding geometries, with realisation the importance of anisotropy, both the intensity of anisotropy and orientation of anisotropy, of rocks or materials. Previous study concluded several more questions or parameters that controlling multilayer folding (Hudleston and Treagus, 2010): (i) Layer spacing, which have an impaction that whether the “multilayer” can be considered as a package “single layer” or real multiple layers (Schmid and Podladchikov, 2006). (ii) Thick layers with relative thinner matrix, or can be considered as incompetent layer surrounded by competent matrix (Biot, 1964b). (iii) Large layer spacing, no layer interactions in between, with different viscous properties between each layer with matrix (Ramberg, 1964). (iv) Internal buckling of laminated medium (Biot, 1964a, 1965a). Johnson and Fletcher (1994) showed that the amplification rate of multilayer folds having free slip interfaces between each layer is indeed greater than for multilayers having no slip interfaces. This is a similar property of crystal slip system, which involves the definition of how to make the mechanical anisotropy as a parameter involving. The instability of multilayer folding is discussed by Biot (1965b), Schmid and Podladchikov (2006), as the multilayer folding geometries are dependence on each of their amplification rate.

2 Motivation of this thesis

From the Alps and Pyrenees to Andes, and to Tibet plateau, the orogenic structural belts attract geologists to progressively understand earth. As mentioned before, the necessity for further investigation on the fold structures that related to the rock physics benefits this quantitively earth-understanding. The fantastic fold geometries (Fig. 3) at field observations offer only the current dependent information and state of rocks, and cannot backtrack the microtectonics development over time or strain, or one want to know the initial state and process. The requirement of numerical simulation offers a selection to reveal the micro-dynamic processes, give potential possibilities with variable beginning settings to the final geometries.

The ongoing work on variable folds with surrounding schistosity from meta-turbidite of Cap de Creus, Spain (Fig. 3. a-e) and schist of Long-Men Mountain structural belt, China (Fig. 3. f-h) may provide a different way to understand how rocks evolved. The folds here have at least one or several characteristics among: (i) Folding with cleavage and microlithon are widely distributed in ductile deformation, but the foliations in surrounding matrix have different angles respect to the layers (PAPER II), foliations parallel to the layer (Fig. 3. a, b, f), foliations incline to the layer (Fig. 3. c, d) and foliations normal to the layer (Fig. 3. e). (ii) Folds unfolding (Llorens et al., 2013a, 2013b). (iii) Folds are distributed in all scale levels, from thin sections to km-scale (de Riese et al., 2019). (iv) Folds / crenulations deform differently, forming a variety of widths and even shapes. The folds are disharmonic, as axial planes cannot be traced for over more than a few times the fold wavelength at the most (PAPER I, II, III, IV). (v) Progressive deformation is identified to be more than one tectonic cycle, but intrinsic anisotropy of material may lead different geometries within one cycle (Fig. 3. g, h; PAPER I). (vi) During rock flow leads to an evolving of CPO, which lead a shear localisation within it (PAPER I, II). The flow of rock related a rheological process (PAPER I, II, III, IV).

Numerical modelling with given deformation conditions, provide time-independent microstructural evolution with fold amplification, planner rotation, and insights into micro-dynamics with strain, strain-rate distribution, stress evolving, which are nice complementary to the field observations and better interpretation corresponding to the natural examples. In this thesis, these processes are investigated by the multi-process numerical simulations based on the full-field platform Elle (Bons et al., 2008).

Several general objectives of this thesis:

(i) Fold geometry and rheology. The shapes of folds are generally and directly the first impression for observers. Accurately describing the fold geometries provides the base to identify the folding kinematics and folding mechanisms. Folding description with amplitudes, thickness, dominate wavelength, arclength, waveform etc. give out the relations to the rheological properties, e.g., viscosity ratio, elasticity ratio, which could be estimated, as well as some microstructures can be used as an indicator for sense of shear and deformation condition. The thesis analysis the fold shapes and get related rheology properties with the previously published constitutive equations, but the comparison with the initial setting of simulations is quite different. This supports the intrinsic properties of material, in this thesis the CPO, cannot be independent to the other rheological properties.

(ii) CPO evolving. Systematically analyse the influence of the initially different intensity of anisotropy and the variable initial angle between the CPO and deformation circumstances related to the boundary conditions. The CPO evolving along the simulation process observed by frequencies of c-axes evolving, that is of basal plane activities.

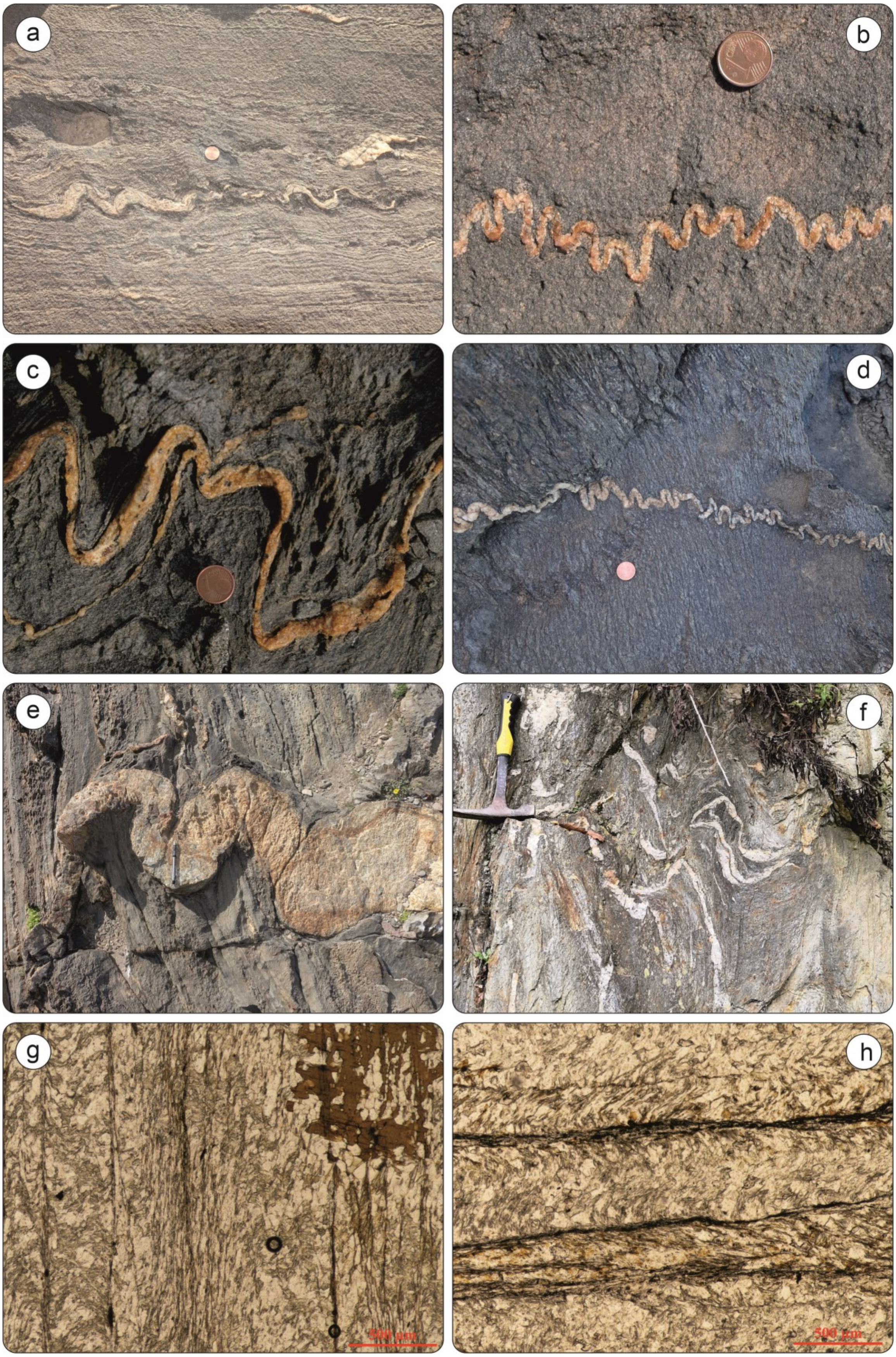

Fig. 3: The natural fold geometries at field observations and thin sections at east Pyrenees, Cap de Creus, Spain (a-e), and east margin of Tibet, LongMen mountain structural belt, China (f-h).

(iii) Stress evolving and strain-rate field. The von Mises stress and von Mises strain-rate field are used to relate to the progressive stages of fold geometries variation. This helps the investigation of strain distributions and stress reactions, which indicates an influence of the variable rheological parameters not only affect the fold geometries, but also make a difference between stages (periods) along the progressive (simulated) deformation.

(iv) Link with natural examples. Comparison between the simulated results and natural examples (both rocks and ice) gives potential approaches to the final fold geometries. All kinds of simulated results should be clarified to several deformed mechanisms with respect to their processes and final shapes, this helps on scientific identification on folding mechanism and the (relatively) physical properties of field objects in future field observation.

(v) Identification on periods of tectonic. Due to anisotropy applied into the simulations lead to resulting folding with different strain localisation behaviours and distributions, both which simultaneously deform the high strain area and low strain area in one tectonic period. Study about the characteristic on identify tectonic period on microstructures.

3 Rheological properties

The deformation behaviour of rock depends on the environment where the rock placed, the temperature, confining stress, pressure, as well as the rock physics itself, all of which affect the rocks or materials behave in brittle or in ductile, so the effects of elasticity or viscosity are considered (Mancktelow, 1999). The previous studies have summarised by Jeng et al. (2002) that the different groups of material models which consist of elastic properties, viscous properties and elasto-viscous properties of layer and matrix, respectively, are behave variably.

The initial stage along the deformation of a rock is firstly behave on its elastic property (Price and Cosgrove, 1990), which relative to the Young's modulus (E) of materials. A rock placed at relatively low temperature and low stress environment, like shallow crust, would behave brittlely while the stress beyond the limitation of elastic property. The deformation of folds is always taking place at a relatively deep crust or even deeper to lower crust where has a high temperature and high confining stress environment that makes the rock deforms viscously in ductility, so the Eq.(1) (Biot, 1957, 1961; Ramberg, 1963, 1964) is considered to use with their dynamic viscosities, especially for a long wavelengths, harmonious waveform folding which the thin plate theory is appropriate (BIot, 1961; Fletcher, 1974, 1977). An exception that ice can deform on earth surface as ice sheet or glacier in ductility.

The equations for elastic and viscous folding are linear, and the output planar foliations are periodic that can be expressed with trigonometric functions such as sinusoidal function or cosine function, and reflect as constant relation between dominate wavelength, thickness and viscosity ratio such as the Biot's folding equation (Biot, 1961). However, due to the composite differences the natural fold geometries are always not strictly periodic but irregular, discontinuous and form strain localisations (Hunt et al., 1996; Whiting and Hunt, 1997; Hobbs and Ord, 2012; Schmalholz and Mancktelow, 2016). The reason for irregular fold geometries with different strain localisation behaviours has been controversially discussed and modelled (e.g., Zhang et al., 1996; Hunt et al., 1997; Mancktelow, 1999; Hobbs and Ord, 2012, Llorens et al., 2013a, 2013b, 2013c). There are essentially two fundamental rheological parameters of materials that affecting fold geometries discussed in this thesis: (1) viscosity and (2) mechanical anisotropy.

3.1 Viscosity and non-linearity of viscous material

For power-law non-linear fluids it is not meaningful to talk about a single viscosity contrast between two rock types because viscosities are dynamic which varies as function of stress or strain rate, and thus viscosity ratio will vary as stress or strain-rate vary (Treagus, 1993), affects the dominate wavelength and amplification rate of the resulting fold geometries (Fletcher, 1974; Schmalholz and Mancktelow, 2016). Furthermore, a non-linearity of viscous materials leads the strain rate is exponential to the stress to the power n, which also resulting fold geometries vary (Fletcher, 1974; Abassi and Mancktelow, 1992; Hudleston and Lan, 1994; Schmalholz and Schmid, 2012).

The folding theory for ductile deformation under rheological conditions, are based on the mechanical and rheological properties of natural rocks or ice, suggests that these materials would deform following non-linear flow laws (Heard and Raleigh, 1972; Smith, 1977; Watkinson, 1983; Carter and Tsenn, 1987; Mühlhaus et al., 1998; Llorens et al, 2013a, 2013b; Hudleston and Treagus, 2010; Kocher et al., 2008) suggested by introduction the rheology of the lithosphere (Kirby, 1983; Kirby and Kronenberg, 1987; Rutter, 1993; Kohlstedt et al., 1995; Hirth et al., 2001; Burov, 2011), and some tried to quantity the value of non-linearity of materials (Bayly, 1970; Fletcher, 1974; Schmalholz and Mancktelow, 2008; Bons et al., 2018). Power-law rheology of the layer deformation both enhances the amplification rate, growth rate and decreases the dominant wavelength compared to linear behaviour (Hudleston and Treagus, 2010).

A resulting fold with a non-Newtonian material form to cylindricity increases with amplification rate and is stronger than a Newtonian layer (Fletcher, 1995; Hudleston and Treagus, 2010), and even higher non-linearity. The folding amplitude grows more rapid with increasing stress exponent under shortening (Kaus and Schmalholz, 2006), but not linear.

3.2 Mechanical anisotropy

Another key factor investigated in thesis in rheological process that controlling strain localisation is the anisotropy, as anisotropy of the matrix increases both the amplification rate and the dominant wavelength of folds, and the intensity to which the amplification rate and dominant wavelength are affected obviously depends on the intensity of anisotropy (Hudleston and Treagus, 2010). Rocks and materials are generally anisotropic in both their brittle and ductile properties. In case of planar mineral mica, the anisotropy is very strong (Kronenberg et al., 1990; Mares and Kronenberg, 1993; Shea and Kronenberg, 1993; Aslin et al., 2019; Finch et al., 2020).

Two types of anisotropy including composite and intrinsic anisotropy in geological materials are usually in consider. Composite anisotropy is an anisotropy due to layers of different composition or material properties (Dabrowski et al., 2012; Wang et al., 2022), or stratigraphic layers, veins, dykes are always be considered as composite anisotropy. Here each individual material may be isotropic, or anisotropic. Another type of anisotropy is the intrinsic anisotropy (Griera et al., 2011; 2013), which is a single composition material due to a crystallographic preferred orientation (CPO), which produced after plastic flow with or without recrystallisation, or after viscous flow and anisotropic crystal growth (Mainprice and Nicolas, 1989), such as pure ice, shale, schist, of alignment of minerals.

A rock as a whole can become anisotropic when crystallographic orientations align in a CPO (Mainprice and Nicolas, 1989; Passchier and Trouw, 2005). Tectonic foliations are often formed by the alignment of micas so that tectonically foliated rocks can be expected to be highly anisotropic.

Anisotropy has been recognised as a factor in the formation of geological structures and a cause for strain localisation (Cobbold et al., 1971; Ramsay, 1980; Passchier and Trouw. 2005; Kocher et al., 2006, 2008; Naus-Thijssen, et al., 2010; Griera et al., 2013; Bordignon et al., 2015; Steinbach et al., 2016; Gardner et al., 2017; Ran et al., 2019; de Riese et al., 2019; Torvela and Kurhila, 2020). In progressive deformation, mechanical anisotropy causes heterogeneity, then forming shear localisation by making shear bands, which are influenced by the intensity of anisotropy (A), the nature property of the anisotropy, the initial orientation of the anisotropy (CPO) etc. (Cosgrove, 1976; Carreras et al., 2013; Steinbach et al., 2016; Llorens et al., 2017; de Riese et al., 2019; Griera et al., 2020). All above properties of anisotropy controlling the kinematics of shear bands, which performing two distinct types of kinematical behaviours in rocks are (1) synthetic shearing (Berthé et al., 1979; Lister and Snoke, 1984; Bell, 1986; Ramsay and Huber, 1987; Ham and Bell, 2004; Mandal et al., 2004; Passchier and Trouw, 2005; Ponce et al., 2013) and (2) antithetic shearing (Carreras et al., 2010, 2013; Ponce et al., 2013; Tanner, 2016). Both types show that from initial angle between layers and shear plane together with duration of shearing give strong influence on the final geometries of crenulation. Unfortunately, relatively few studies are only concentrated on the issue that about shear localised behaviours controlling deformation geometries.

Anisotropy is properties depend on direction in crystal. The anisotropy can be understood in this thesis by using the transverse isotropy. "… A transversely isotropic material is one with physical properties that are symmetric about an axis that is normal to a plane of isotropy. This transverse plane has infinite planes of symmetry and thus, within this plane, the material properties are the same in all directions. Hence, such materials are also known as 'polar anisotropic' materials …" (wikipedia/Transverse_isotropy). This is often good approximation of mechanical anisotropy of foliated rock.

Anisotropy was achieved by glide of dislocations along slip planes of crystal system, which is assumed have basal plane, prismatic plane, and pyramidal plane of a hexagonal crystal. The intensity of anisotropy in this thesis was defined as shear resistances, that related to the critical resolved shear stress (Gottstein, 2004), in times between basal plane and non-basal planes gliding system.

4 Numerical simulations with software platform Elle

4.1 Numerical procedures association with Elle

As for the purpose of numerical modelling for shortening or extension of rocks and ice, the applications of both (i) single phase or polyphase setting and (ii) regarding rheological parameters are required certainly. To investigate these different parameters, series of numerical simulations were chosen to be done with the modelling platform Elle. Elle is an open-source full-filed modelling platform used to simulate the development of deformation structures during microtectonic and microdynamic processes in rocks and ice (http://www.elle.ws; Bons et al. 2008). Numerous microtectonic processes have been done with Elle, such as dynamic recrystallisation (Montagnat et al., 2014, Jansen et al., 2016; Llorens et al., 2016a, 2016b, 2017, 2019a; Steinbach et al., 2016), grain growth (Jessell et al., 2001, 2003; Jessell, 2004; Roessiger et al., 2014), porphyroclasts / porphyroblasts rotation (Griera et al., 2013; Ran et al., 2018, 2022), strain localisation (Griera et al., 2011; Steinbach et al., 2016; Gardner et al., 2017; de Riese et al., 2019), and deformation of poly-phase materials (Finch et al., 2009, 2022). Elle is a 2D platform, which could be recognised as a section of structures.

Elle (Bons et al., 2008) runs simulations as a progressively stepping with incremental strain, every step is a loop which the object simulated system must go through all processes (Steinbach, 2017). Every pixel in Elle platform can be treated as a single crystal or a mineral, termed "*unode*", a group of pixels is a grain or cluster, termed "*flynn*", and the node sits at the grain boundary is termed "*bnode*". One *bnode* can be connected to either two or three neighbour *bnodes* depend on the position it placed, so the *unode* is the unconnected node. The properties of objects can be added to the *unodes* or *flynns* so that crystals or grains can be different with their neighbours. Elle can be coupled with different codes to achieve different simulated goals, such as BASIL (Houseman et al., 2008), FFT (Griera et al., 2011), etc.

4.2 Numerical simulation with VPFFT+ELLE method

To introduce the anisotropy of material property (glide system of lattices) into the Elle, the Viscoplastic Fast Fourier (VPFFT) (Lebensohn, 2001, Lebensohn et al., 2008, Lebensohn and Rollett, 2020) crystal plasticity code, is coupled by Griera et al. (2013) with the modelling platform Elle (Griera et al., 2013; Llorens et al., 2016a; Steinbach et al., 2016; Llorens et al., 2017; Piazolo et al., 2019; Ran et al., 2018; de Riese et al., 2019), based on the Full-Field Theory. VPFFT assumes deformation by dislocation glide including the CPO re-orientation and using a non-linear viscous rate-dependent law (Llorens, 2015; Steinbach, 2017).

As the setting of simulations are bulk strain-rate constant, the distribution of stress field and strain-rate fields are initially unknown, an iterative solver in order to minimise the calculating errors is based on Fast Fourier Transformation is implemented as number of corrections of calculation. Addition to the mechanical fields, VPFFT predicts dislocation glide, strain-rate and stress field, lattice re-orientation and dislocation densities following the model by Brinckmann et al. (2006). In the Elle file (*.elle), the *bnode* and *flynns* were updated according to the local strain-rate field after each deformation step by VPFFT.

The constitutive equation (Eq. 4) of Elle process predicts the strain rate $\dot{\varepsilon}_{ij}(x)$ at each *unode* position in the grid x as a function of the deviatoric stress (σ'_{ij}), a reference shear strain rate ($\dot{\gamma}_0$) and the sum of the shear strain rates ($\dot{\gamma}^s$) on *N* individual slip systems.

$$\dot{\varepsilon}_{ij}(x) = \sum_{s=1}^{N_S} m_{ij}^{s}(x)\dot{\gamma}^{s}(x) = \dot{\gamma}_0 \sum_{s=1}^{N_S} m_{ij}^{s}(x) \left|\frac{m^s : \sigma'(x)}{\tau^s(x)}\right|^n sgn\big(m^s(x) : \sigma'(x)\big) \qquad (4)$$

In VPFFT, each individual slip system s is defined by a shear resistance or critical resolved shear-stress (τ^s) and its orientation is dependent the symmetric Schmidt tensor (m_{ij}^s). This equation can be simplified to:

$$\dot{\gamma}_s = \dot{\gamma}_0 \left(\frac{\sigma_s}{\tau_s}\right)^n \tag{5}$$

A symmetrical hexagonal crystal lattice of ice 1h is used as an analogue for anisotropic minerals, such as of alignment of mica, quartz, ice 1h, etc. (as in Griera et al. 2013; Ran et al., 2019; de Riese et al., 2019). Deformation assumed to be accommodated by dislocation glide along the basal, prismatic and pyramidal slip systems only for hexagonal crystal lattice. Here the intensity of anisotropy (A) is defined by the ratio of the shear resistance of the non-basal and basal slip systems:

$$A = \frac{\tau^{(non-basal)}}{\tau^{(basal)}} \tag{6}$$

If A = 1, which makes the material is effectively isotropic (Griera et al, 2013). If $A \neq$ 1, the material is anisotropic. Here we choose to use A = 64, A = 16, A = 4 which simulates a highly or moderately anisotropic rock or material with an approximately transverse isotropy, in which shear deformation along the basal plane is much softer than non-basal planes.

As the boundary of Elle simulations is infinite, the results can be repeated to their surroundings infinitely, which has been introduced by e.g., Ran et al. (2018), Finch et al. (2020), Hu et al. (PAPER I). The von Mises strain rate ($\dot{\varepsilon}_{vm}$) and von Mises stress (σ_{vm}) is defined as:

$$\dot{\varepsilon}_{vm} = \sqrt{\frac{2}{3}\,\dot{\varepsilon}_{ij}\,\dot{\varepsilon}_{ij}} \tag{7}$$

and

$$\sigma_{vm} = \sqrt{\frac{3}{2}\,\sigma'_{ij}\,\sigma'_{ij}} \tag{8}$$

where $\dot{\varepsilon}_{ij}$ is the strain-rate tensor, σ'_{ij} is the stress tensor, and i and j summation indices.

The numerical simulations in this thesis are made by the VPFFT + Elle to investigate the fold geometries and strain-field differences resulting from an intrinsically mechanical material. The theoretically infinite AIR phase is numerically described as a mechanically anisotropic material with relatively lower viscosity, while the ICE phase is numerically described as a mechanically isotropic or anisotropic material with relatively high viscosity, depends on the basic settings of our simulated goals in several papers.

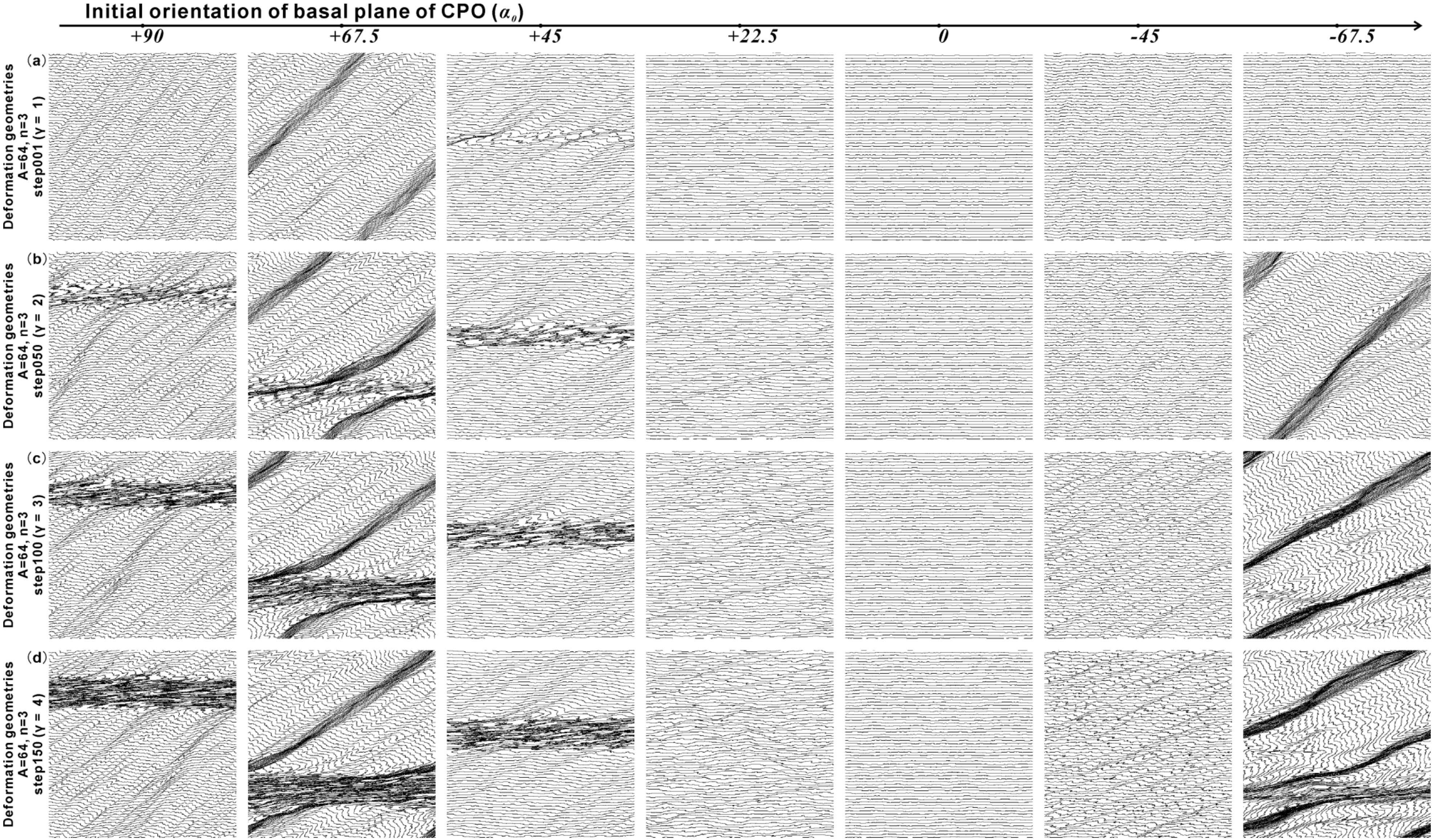

Fig.4: Preliminary simulation in dextral simple shear deformation with an initial CPO (intensity of anisotropy A = 64, stress exponent n = 3, and different initial angles α_0 of basal planes) in γ = 1, 2, 3 and 4, notice that all passive mark lines (black curved lines) are initially horizontal. Initial state with passive mark lines shows in Fig.6.

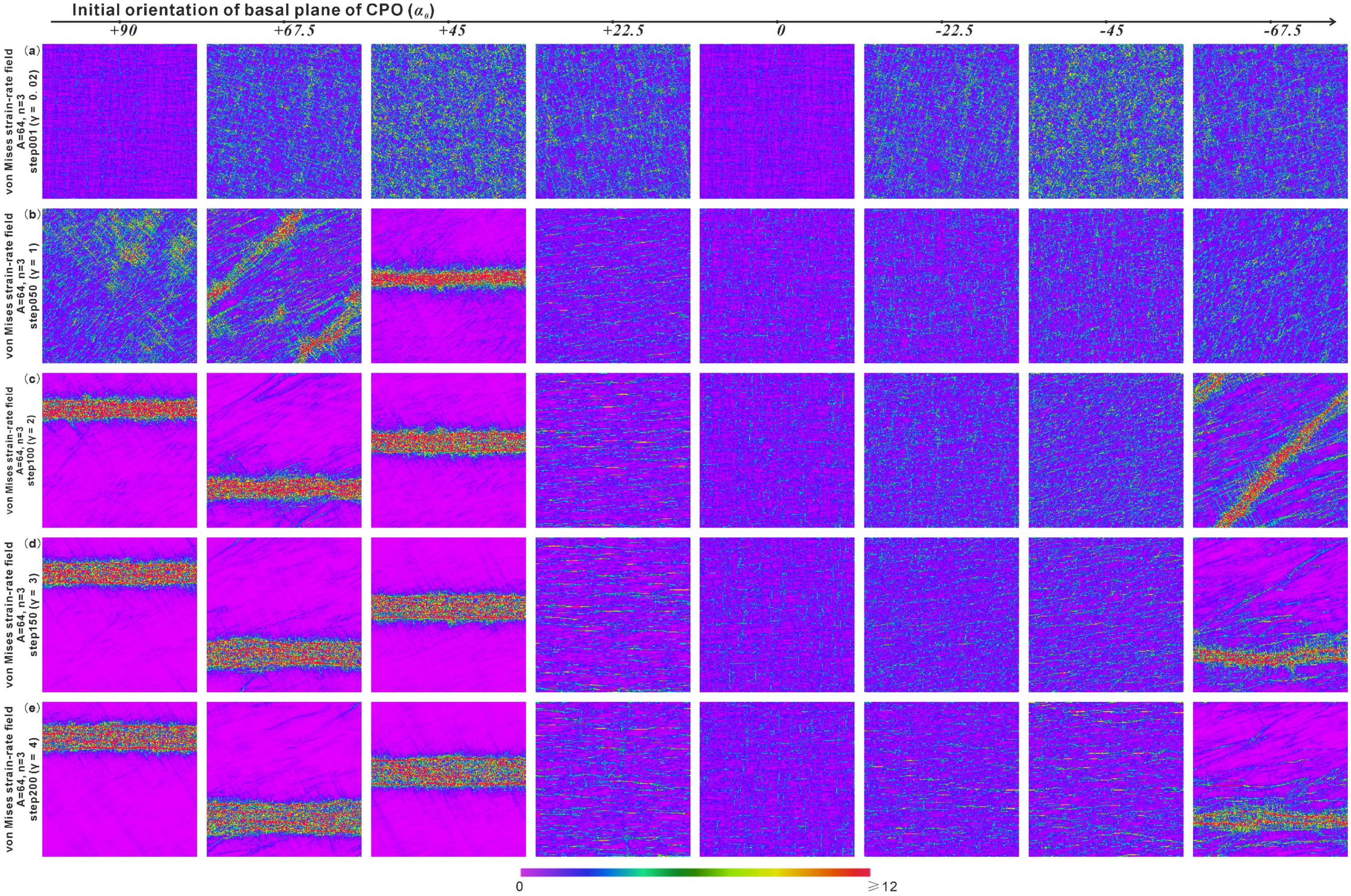

Fig.5: von Mises strain-rate filed of preliminary simulation in dextral simple shear deformation with an initial CPO (same as Fig.4) in γ = 0.02, 1, 2, 3 and 4.

4.3 Preliminary simulation results

Attempts simulations have been done with the in both dextral simple shear (Fig. 4 and Fig. 5) and pure shear (Fig. 7) with a mechanical anisotropic material.

Initial simulated setting for dextral simple shear deformation includes the intensity of anisotropy A = 64, power law stress exponent of material n = 3, initial orientation of anisotropy (basal plane) α_0 = 0°, +11.25°, +22.5°, …, +78.75°, +90° and -11.25°, -22.5°, …, -78.75° (a horizontal layer is 0° respect to the *x*-axis, the layer rotate anticlockwise means the layer has a positive angle respect to the *x*-axis, while rotate clockwise means the layer has a negative angle), the simple shear strain rate is $\dot{\gamma}$= 0.02 per step in Elle. Fig. 6 gives the initial state for this series of simple shear simulation. Fig. 5 shows von Mises strain-rate field of partial simulated results. The geometrical differences in Fig. 4 are due to different strain rate distribution in Fig. 5, which are caused by the initial setting of CPO.

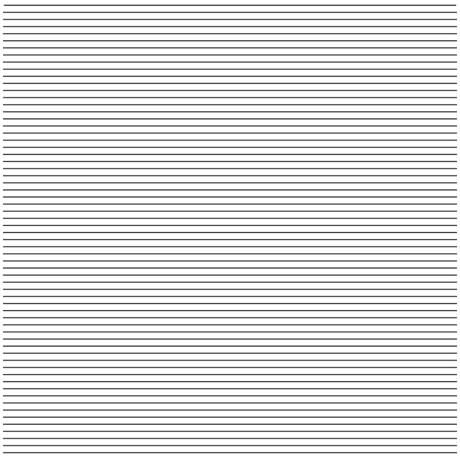

Fig. 6: Initial state for simple shear simulation, black lines are passive marker layer without any physical property and meaning. The relative simulated results are displayed in Fig. 4 and Fig. 5, controlled the strain redistribution.

Initial simulated setting for pure shear deformation includes the intensity of anisotropy A = 64, power law stress exponent of material n = 3, initial orientation of anisotropy (basal plane) α_0 = 0° and +90°. The pure shear strain rate is $\dot{\varepsilon}$= 0.01 both for horizontal compression and vertical extension per step in Elle. The deformation geometries displayed in Fig. 7 also indicates a difference of strain rate distributions lead two diverse kinds of deformation behaviours and two folding processes.

The two series simulations verify the influence of CPO and can be compared with Ran et al. (2018), de Riese et al. (2019), and Finch et al. (2020) that strain-rate field and deformation geometries are CPO dependent.

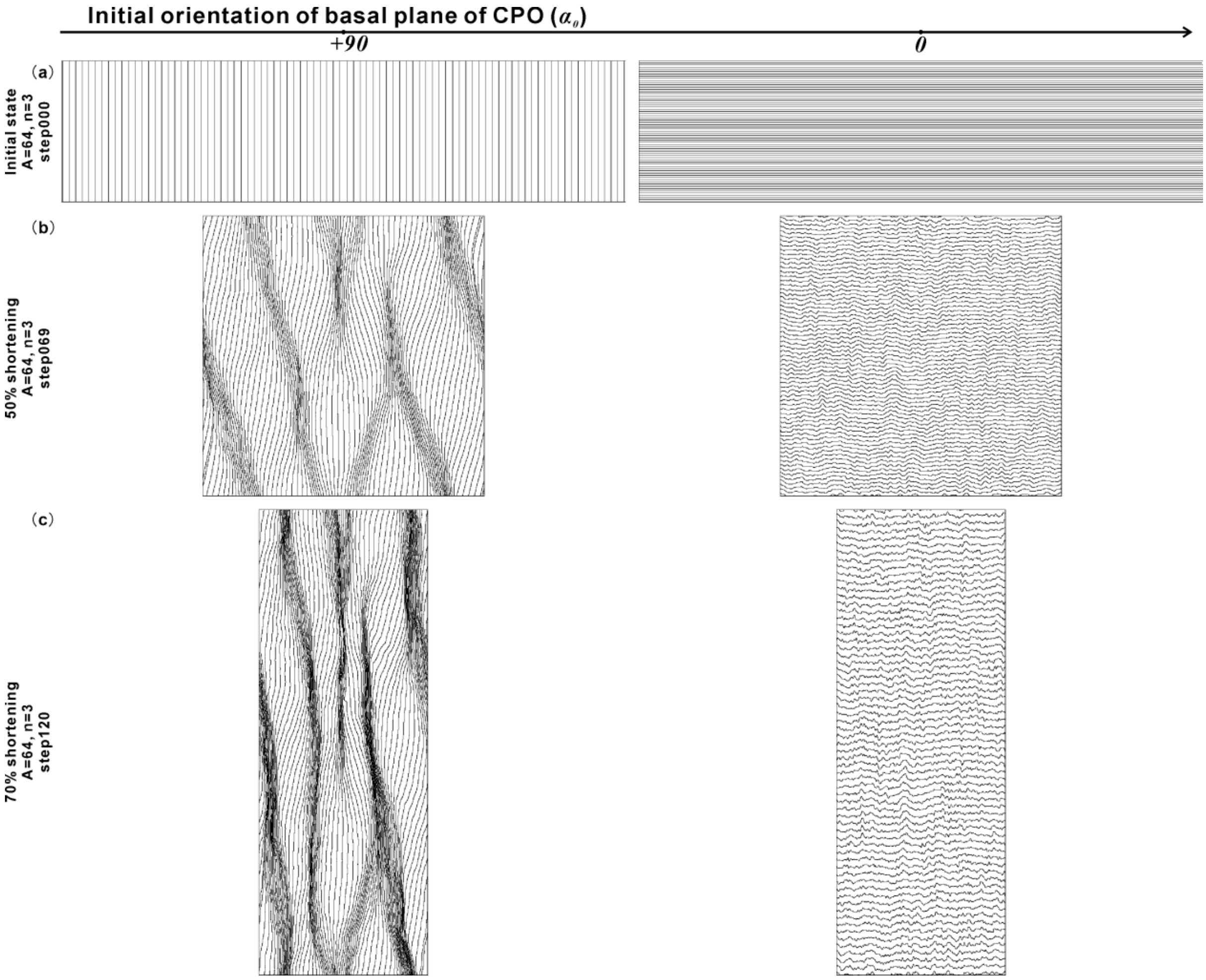

Fig. 7: Preliminary simulation in pure shear deformation with an initial CPO (intensity of anisotropy A = 64, stress exponent n = 3, and basal planes orientation α_0 = 0° and 90°) in 50% and 70% shortening, note that all passive mark lines (black curved lines) are initially parallel to the initial CPO (basal plane), reflect the CPO rotations.

Driving from these simulated results, this thesis further invests the influence on deformation structures in rocks and ice by systematically controlling the anisotropy in simple shear and pure shear deformations.

In PAPER I, the Elle simulations are made with boundary condition of dextral simple shear to investigate how a single-phase material (ICE phase, here using ice 1h, please see Appendix for further information) with an intrinsic mechanical anisotropy affect the strain rate field, which could be roughly divided to the high strain domains with strain localisation and low strain domains with crenulation geometries.

In PAPER II, III and IV, the Elle simulations are made with layer parallel shortening, to study (i) the processes of folding geometries evolution that growth together with the matrix deformation, made by an initial setting of a competent, isotropic layer (ICE phase, please see Appendix for further information) embedded in a viscos, mechanically anisotropic matrix (AIR phase) (PAPER II), (ii) how a single-phase ice 1h (ICE phase) with mechanically anisotropy induce to a folding geometries to a low value of dominate wavelength against layer thickness compared to the cloudy bands in polar ice (EGRIP ice drill core, PAPER III), and (iii) a single-phase ice 1h (ICE phase) with mechanically anisotropy undergoing pure shear that leads a rotation of CPO and fold amplification related to the northeast Greenland icesheet NEGIS (PAPER IV).

5 Outcome and conclusion of the thesis

This thesis investigates the how (i) mechanical anisotropy, includes the intensity of anisotropy and the orientation of initial anisotropy, (ii) viscous properties, contains viscosity differences and stress exponent related to the non-linearity of materials, affect from microstructures to macro tectonic structures. By using the simulated method, the processes of simulation results reflect the evolutions of structural geometries, kinematics, and even strain-rate fields and stress evolutions, which influence strain distribution with different deformation characteristics, localisation behaviours, rheological processes difference in pure polycrystalline material or polyphase competent and incompetent materials.

1. For simple shear simulation, the results crenulation (micro-folds) geometries are strongly dependent on the abovementioned parameters which are the set initial intensity of anisotropy (CPO, A), the initial orientation of initial anisotropy (basal plane, α_0). Simple shear simulation within foliated single-phase material, the CPO controls the shear localisation behaviours which would lead different shearing movement respect to the simple shear boundary condition that lead to extensional fields. The shear bands, or in some cases the high strain areas, can move synthetically, antithetically, or first antithetically then synthetically, with different velocities and rotation rates (PAPER I). There are big differences of shear localisation behaviours between $\alpha_0 < 45°$ and $\alpha_0 >= 45°$, and resulting various crenulation geometries.

2. For layer-parallel shortening, except the initial intensity of anisotropy (A) and the initial orientation of initial anisotropy (α_0), the initial set viscosity ratio (R) and the non-linearity (n) in

a certain range also has tiny influence on folding geometries. Two basic end-member types of behaviour and resulting fold geometries in both the competent layer and matrix are compressed buckle folds and extensional folds (PAPER II). Strain localisation behaviours also largely vary with α_0 < 45° and α_0 > 45°. Within matrix, Low α_0 cases cause the formation of random, tiny, discontinuous strain localisation related to the α_0. High α_0 cases cause the formation of strain localisation together with lenticular microlithons on the scale of the fold wavelength.

3. A single phase material with CPO and non-linearity property also leads the development of self-similar folds with a power-law power spectrum (PAPER III, IV), which could compare with the folded biotite schist and the cloudy bands in ice drill core. The small cloudy bands in micro-scale and lithospheric ice fold in large-scale resulted in a self-affine trend, that amplify the fold in several times on their amplitudes, while elongate the fold in thousand times on their arclengths where largest folds are relatively flat.

4. Deformation of the CPO foliations may also develop crenulations and folds within low strain domains, where the geometries controlled by the kinematics of high strain domains (PAPER I, II). Apart from the obvious behaviours in high strain localisation domains, the foliations preferred to keep relatively constant geometries within low strain domains. When strain concentrate in high strain rate area, only little strain distributed in the low strain domains with little rotation driven by shear movement of high strain area. These low strain areas may rotate as a whole cluster like a bubble / grain, or rotate with different velocities between the edges and centres. The rotation velocities of edges are sometimes quicker than centres, lead to a crenulation not only between edges and centres but also between edges and high strain localised bands.

5. Evolving of CPO relies on the boundary condition of deformation system, and influences the micro dynamic processes. Boundary condition of simple shear and layer-parallel pure shear carry out different stress evolving can be compared with de Riese et al. (2019) and PAPER II in this thesis, as the bulk stress variations until the material yields and stresses drop due to the formation of the shear bands, so that geometrical softening and hardening forms at different deformation stages of simple shear and pure shear. Anisotropy dominates both endmembers and processes. By plotting the C-axes of basal plane, the two routines of CPO evolve, one is single point-maximum shifting to the fabric attractor, another is from one point-maximum split to two sub-symmetrical point-maximum and reunion.

Reference

Abbassi, M.R., Mancktelow, N.S., (1990). The effect of initial perturbation shape and symmetry on fold development. Journal of Structural Geology, 12(2), 273–282. doi: https://doi.org/10.1016/0191-8141(90)90011-m

Abbassi, M.R., Mancktelow, N.S., (1992). Single layer buckle folding in non-linear materials - I. Experimental study of fold development from an isolated initial perturbation. J. Struct. Geol. 14, 85–104. DOI: https://doi.org/10.1016/0191-8141(92)90147-O

Adamuszek, M., Schmid, D. W., Dabrowski, M., (2011). Fold geometry toolbox – Automated determination of fold shape, shortening, and material properties. Journal of Structural Geology, Volume 33, Issue 9, September 2011, Pages 1406-1416. DOI: https://doi.org/10.1016/j.jsg.2011.06.003

Alsop, G.I., Carreras, J., (2007). Three dimensional sheath folds in quartz mylonite, Cap de Creus. J. Struct. Geol. 31 (1), 1–2. DOI: https://doi.org/10.1016/j.jsg.2007.09.010

Alsop, G.I., Holdsworth, R.E., (2007). Flow perturbation folding in shear zones. Geological Society, London, Special Publications. 272 (1), 75–101. DOI: https://doi.org/10.1144/GSL.SP.2007.272.01.06

Anthony, M., Wickham, John., (1978). Finite-element simulation of asymmetric folding. Tectonophysics, 47(1-2), 1–14. doi: https://doi.org/10.1016/0040-1951(78)90148-8

Aslin, J., Mariani, E., Dawson, K., Barsoum M.W., (2019). Ripplocations provide a new mechanism for the deformation of phyllosilicates in the lithosphere. Nature Communication 10, 686. https://doi.org/10.1038/s41467-019-08587-2

Bayly, M.B., (1970). Viscosity and anisotropy estimates from measurements on chevron folds. Tectonophysics, Volume 9, Issue 5, May 1970, Pages 459-474. DOI: 10.1016/0040-1951(70)90058-2

Bell, T.H. (1986). Foliation development and refraction in metamorphic rocks: reactivation of earlier foliations and decrenulation due to shifting patterns of deformation partitioning. Journal of Metamorphic Geology, 4(4), 421–444. doi: https://doi.org/10.1111/j.1525-1314.1986.tb00362.x

Berthé, D., Choukroune, P., Jegouzo, P., (1979). Orthogneiss, mylonite and non coaxial deformation of granites: the example of the South Armorican Shear Zone. Journal of Structural Geology 1(1), 31-42. Doi: https://doi.org/10.1016/0191-8141(79)90019-1

Biot, M.A., (1957). Folding Instability of a Layered Viscoelastic Medium under Compression. Proceedings of the Royal Society A: Mathematical, Physical and Engineering Sciences, 242(1231), 444–454. DOI: 10.1098/rspa.1957.0187

Biot, M.A., (1961). Theory of folding of stratified viscoelastic media and its implications in tectonics and orogenesis. Geological Society of America Bulletin, v. 72, p. 1595-1620. DOI: 10.1130/0016-7606(1961)72[1595:TOFOSV]2.0.CO;2

Biot, M.A., Odé, H., Roever, W.L. (1961). Experimental Verification of the Theory of Folding of Stratified Viscoelastic Media. Geological Society of America Bulletin, 72(11), 1621-1631. https://doi.org/doi:10.1130/0016-7606(1961)72[1621:EVOTTO]2.0.CO;2

Biot, M.A. (1964a). Theory of internal buckling of a confined multi-layered structure, Geological Society of America Bulletin, 75, 563–568. Doi: https://doi.org/10.1130/0016-7606(1964)75[563:TOIBOA]2.0.CO;2

Biot, M.A. (1964b). Theory of viscous buckling of multilayered fluids undergoing finite strain, Physics of Fluids 7, 855–861. Doi: https://doi.org/10.1063/1.1711296

Biot, M.A., (1965a). Further Development of the Theory of Internal Buckling of Multilayers. Geological Society of America Bulletin, 76 (7): 833–840. DOI: 10.1130/0016-7606(1965)76[833:FDOTTO]2.0.CO;2

Biot, M.A., (1965b). Theory of similar folding of first and second kind, Geological Society of America Bulletin, 76, 251–258. Doi: https://doi.org/10.1130/0016-7606(1965)76[251:TOSFOT]2.0.CO;2

Biot, M.A., (1965c), Mechanics of incremental deformations: New York, Wiley, 504 p.

Bobillo-Ares, N.C., Toimil, N.C., Aller, J., Bastida, F., (2004). FoldModeler: a tool for the geometrical and kinematical analysis of folds. Computers & Geosciences, 30, Pages 147-159. DOI: https://doi.org/10.1016/j.cageo.2003.09.008

Bons, P.D., Urai, J.L., (1996). An apparatus to experimentally model the dynamics of ductile shear zones. Tectonophysics 256, 145–164. DOI: https://doi.org/10.1016/0040-1951(95)00161-1

Bons, P.D, Koehn, D, Jessell, M.W (Eds) (2008) Microdynamic Simulation. Lecture Notes in Earth Sciences 106, Springer, Berlin. 405 pp. ISBN 978-3-540-44793-1

Bordignon, N., Piccolroaz, A., Dal Corso, F., Bigoni, D., (2015). Strain localization and shear band propagation in ductile materials. Frontiers in Materials 2(22), 1-13. DOI: 10.3389/fmats.2015.00022

Brinckmann, S., Siegmund, T., Huang, Y., (2006). A dislocation density based strain gradient model. International Journal of Plasticity, 22(9), 1784–1797. https://doi.org/doi:10.1016/j.ijplas.2006.01.005

Burov, E. (2011): Rheology and strength of the lithosphere. Marine and Petroleum Geology 28, 1402-1443. https://doi.org/doi:10.1016/j.marpetgeo.2011.05.008

Carreras, J., Druguet, E., Griera, A., Soldevila, J., (2004). Strain and deformation history in a syntectonic pluton. The case of the Roses granodiorite (Cap de Creus, Eastern Pyrenees), vol. 224. Geological Society, London, Special Publications, pp. 307–319. Doi: https://doi.org/10.1144/GSL.SP.2004.224.01.19

Carreras, J., Czeck, D. M., Druguet, E., Hudleston, P. J. (2010). Structure and development of an anastomosing network of ductile shear zones. Journal of Structural Geology, 32(5), 656–666. doi: https://doi.org/10.1016/j.jsg.2010.03.013

Carreras, J., Cosgrove, J.W., Druguet, E., (2013). Strain partitioning in banded and/or anisotropic rocks: Implications for inferring tectonic regimes. Journal of Structural Geology, 50, 7–21. doi: https://doi.org/10.1016/j.jsg.2012.12.003

Cloetingh, S., Burov, E. (2011): Lithospheric folding and sedimentary basin evolution: a review and analysis of formation mechanisms, Basin Research., 23, 257–290. Doi: https://doi.org/10.1111/j.1365-2117.2010.00490.x

Cobbold, P.R., Cosgrove, J.W., Summers, J.M., (1971). Development of internal structures in deformed anisotropic rocks. Tectonophysics, 12: 23-53. DOI: 10.1016/0040-1951(71)90065-5

Cobbold, P.R., (1975). Fold propagation in single embedded layers. Tectonophysics 27 (4), 333–351. DOI: https://doi.org/10.1016/0040-1951(75)90003-7

Cosgrove, J.W., (1976). The formation of crenulation cleavage. Journal of the Geological Society, 132(2), 155–178. doi: https://doi.org/10.1144/gsjgs.132.2.0155

Currie, J.B., Patnode, H.W., Trump, R.P. (1962). Development of Folds in Sedimentary Strata. Geological Society of America Bulletin, 73(6), 655–673. doi: https://doi.org/10.1130/0016-7606(1962)73[655:DOFISS]2.0.CO;2

Dabrowski, M., Schmid, D. W., Podladchikov, Y. Y. (2012). A two-phase composite in simple shear: Effective mechanical anisotropy development and localization potential. Journal of Geophysical Research, 117(B8), B08406. doi: https://doi.org/10.1029/2012jb009183

de Riese, T., (2014). Numerical modelling of multilayer folding. Eberhard Karls University Tübingen, Master thesis

de Riese, T., Evans, L., Gomez-Rivas, E., Griera, A., Lebensohn, R.A., Llorens, M.-G., Ran, H., Sachau, T., Weikusat, I., Bons, P.D. (2019). Shear localisation in anisotropic, non-linear viscous materials that develop a CPO: A numerical study. J. Struct. Geol. 124, 81-90. DOI: https://doi.org/10.1016/j.jsg.2019.03.006

Druguet, E., Passchier, C.W., Carreras, J., Victor, P., Den Brok, S., (1997). Analysis of a complex high-strain zone at Cap de Creus, Spain. Tectonophysics 280, 31–45. Doi: https://doi.org/10.1016/S0040-1951(97)00137-6

England, P., McKenzie, D. (1982): A thin viscous sheet model for continental deformation, Geophysical Journal International, Volume 70, Issue 2, August 1982, Pages 295–321, https://doi.org/10.1111/j.1365-246X.1982.tb04969.x

Finch, M.A., Bons, P.D., Steinbach, F., Griera, A., Llorens, M.-G., Gomez-Rivas, E., Ran, H., de Riese, T., (2020). The ephemeral development of C′ shear bands: A numerical modelling approach, Journal of Structural Geology, DOI: https://doi.org/10.1016/j.jsg.2020.104091

Finch, M.A., Bons, P.D., Weinberg, R.F., Llorens, M.G., Griera, A., Gomez-Rivas, E., (2022). A dynamic atlas of interference patterns in superimposed, opposite sense ductile shear zones, Journal of Structural Geology, 165, 104739, doi: https://doi.org/10.1016/j.jsg.2022.104739

Fletcher R.C., (1974). Wavelength selection in the folding of a single layer with power-law rheology. American Journal of Science November 1974, 274 (9) 1029-1043. DOI: https://doi.org/10.2475/ajs.274.9.1029

Fletcher R.C., (1977). Folding of a single viscous layer: Exact infinitesimal-amplitude solution. Tectonophysics, 39(4), 593–606. doi: https://doi.org/10.1016/0040-1951(77)90155-x

Fletcher, R.C., (1995). Three-dimensional folding and necking of a power-law layer: are folds cylindrical, and, if so, do we understand why? Tectonophysics 247, 65-83. DOI: https://doi.org/10.1016/0040-1951(95)00021-E

Frehner, M., Schmalholz, S. M. (2006). Numerical simulations of parasitic folding in multilayers. Journal of Structural Geology, 28(9), 1647–1657. doi: https://doi.org/10.1016/j.jsg.2006.05.008

Gardner, R., Piazolo, S., Lynn, E., Nathan, D., (2017). Patterns of strain localization in heterogeneous, polycrystalline rocks – a numerical perspective. Earth and Planetary Science Letters, 463, 253–265. doi: https://doi.org/10.1016/j.epsl.2017.01.039

Ghosh, S.K., (1966). Experimental tests of buckling folds in relation to strain ellipsoid in simple shear deformations. Tectonophysics, 3, 169–185. DOI: https://doi.org/10.1016/0040-1951(66)90001-1

Glen, J.W. (1952). Experiments on the Deformation of Ice, Journal of Glaciology, 2(12), 111–114, doi: https://doi.org/10.3198/1952JoG2-12-111-114

Glen, J.W. (1955). The Creep of Polycrystalline Ice, Proc R Soc Lond A Math Phys Sci, 228(1175), 519, doi: https://doi.org/10.1098/rspa.1955.0066

Gottstein G., (2004). Physical Foundations of Materials Science, Springer, 2004, pp 227.

Griera, A., Bons, P.D., Jessell, M.W., Lebensohn, R.A., Evans, L., Gomez-Rivas, E., (2011). Strain localization and porphyroclast rotation. Geology, 39(3), 275–278. doi: https://doi.org/10.1130/G31549.1

Griera, A., Llorens, M.-G., Gomez-Rivas, E., Bons, P. D., Jessell, M. W., Evans, L. A., Lebensohn, R., (2013). Numerical modelling of porphyroclast and porphyroblast rotation in anisotropic rocks. Tectonophysics, 587, 4–29. DOI: 10.1016/j.tecto.2012.10.008

Griera, A., Gomez-Rivas, E., Llorens, M.-G., (2018). The influence of layer-interface geometry on single-layer folding. Geological Society, London, Special Publications, 487 (1): 59. DOI: 10.1144/SP487.4

Ham, A.P., Bell, T.H. (2004). Recycling of foliations during folding. Journal of Structural Geology, 26(11), 1989–2009. doi: 10.1016/j.jsg.2004.04.003

Hirth, G., Teyssier, C., Dunlap, W.J., (2001). An evaluation of quartzite flow laws based on comparisons between experimentally and naturally deformed rocks. International Journal of Earth Sciences, 90, 77-87. DOI: 10.1007/s005310000152

Hobbs. B.E, Regenauer-Lieb., K., Ord. A., (2008). Folding with thermal–mechanical feedback. Journal of Structural Geology, 30(12), 1572–1592. doi: https://doi.org/10.1016/j.jsg.2008.09.002

Hobbs, B.E., Ord, A., (2012). Localized and chaotic folding: the role of axial plane structures. Philosophical Transactions of the Royal Society A: Mathematical, Physical and Engineering Sciences, 370(1965), 1966–2009. doi: https://doi.org/10.1098/rsta.2011.0426

Heard, H.C., Raleich, C.B. (1972). Steady-State Flow in Marble at 500° to 800°C. Geological Society of America Bulletin, 83(4), 935–956. doi: https://doi.org/10.1130/0016-7606(1972)83[935:sfimat]2.0.co;2

Houseman, G., Barr, T., Evans, L., (2008). Basil: Stress and Deformation in a Viscous Material. Microdynamics Simulation. Springer-Verlag, Berlin, pp. 139–154.

Hudleston, P.J., (1973). An analysis of “Single-layer” folds developed experimentally in viscous media, Tectonophysics, Volume 16, Issues 3–4, Pages 189-214. Doi: https://doi.org/10.1016/0040-1951(73)90012-7

Hudleston, P.J., (1986). Extracting information from folds in rocks. Journal of Geological Education 34, 237-245. Doi: https://doi.org/10.5408/0022-1368-34.4.237

Hudleston, P.J., Lan, L., (1993). Information from fold shapes. Journal of Structural Geology. 15, 253–264. https://doi.org/10.1016/0191-8141(93)90124-S

Hudleston, P.J., Lan L., (1994). Rheological controls on the shapes of single-layer folds. Journal of Structural Geology, 16(7), 1007–1021. doi: https://doi.org/10.1016/0191-8141(94)90082-5

Hudleston, P.J., Treagus, S.H., (2010). Information from folds: a review. Journal of Structural Geology. 32(12), 2042–2071. DOI: 10.1016/j.jsg.2010.08.011

Hunt G., Mühlhaus H., Hobbs B., Ord A., (1996). Localized folding of viscoelastic layers. Geologische Rundschau volume 85, pages58–64. doi: https://doi.org/10.1007/bf00192061

Hunt, G. W., Muhlhaus, H., Whiting, A.I.M. (1997). Folding processes and solitary waves in structural geology. Philosophical Transactions of the Royal Society A: Mathematical, Physical and Engineering Sciences, 355(1732), 2197–2213. doi: https://doi.org/10.1098/rsta.1997.0118

Jansen, D., Llorens, M.-G., Westhoff, J., Steinbach, F., Kipfstuhl, S., Bons, P. D., Griera, A., and Weikusat, I. (2016): Small-scale disturbances in the stratigraphy of the NEEM ice core: observations and numerical model simulations, The Cryosphere, 10, 359–370, https://doi.org/10.5194/tc-10-359-2016

Jeng, F.S., Lin M.L., Lai Y.C., Teng M.H., (2002). Influence of strain rate on buckle folding of an elasto-viscous single layer. J. Struct. Geol. 24, 501-516. Doi: 10.1016/S0191-8141(01)00073-6

Jeng, F.S., Huang, K.P., (2008). Buckling folds of a single layer embedded in matrix – Theoretical solutions and characteristics. Journal of Structural Geology, 30(5), 633–648. doi: https://doi.org/10.1016/j.jsg.2008.01.009

Jessell, M., Bons, P.D., Evans, L., Barr, T., Stüwe, K., (2001). Elle: the numerical simulation of metamorphic and deformation microstructures. Computers and Geosciences, 27(1), 17–30. doi: https://doi.org/10.1016/s0098-3004(00)00061-3

Jessell, M.W., Kostenko, O., Jamtveit, B., (2003). The preservation potential of microstructures during static grain growth. Journal Metamorphic Geology, 21(5), 481–491. doi: https://doi.org/10.1046/j.1525-1314.2003.00455.x

Jessell, M.W. (2004). Grain Growth Microstructures as Indicators of Sample Evolution. Materials Science Forum, 467-470 (2004), 1051–1056. doi: https://doi.org/10.4028/www.scientific.net/MSF.467-470.1051

Johnson, A.M., Pfaff, V.J., (1989). Parallel, similar and constrained folds. Engineering Geology, 27(1-4), 115–180. doi: https://doi.org/10.1016/0013-7952(89)90032-x

Johnson, A.M. and Fletcher, R.C. (1994): Folding of Viscous Layers, Columbia University Press, New York.

Kaus, B.J.P., Schmalholz, S.M., (2006). 3D finite amplitude folding: Implications for stress evolution during crustal and lithospheric deformation. GEOPHYSICAL RESEARCH LETTERS, VOL. 33, L14309, doi: https://doi.org/10.1029/2006GL026341

Kirby, S.H. (1983). Rheology of the lithosphere. Reviews of Geophysics, 21(6), 1458-1487. doi: https://doi.org/10.1029/rg021i006p01458

Kirby, S.H., Kronenberg, A.K., (1987). Rheology of the lithosphere: Selected topics. Reviews of Geophysics, 25(6), 1219–1244. doi: https://doi.org/10.1029/rg025i006p01219

Kocher, T., Schmalholz, S.M., Mancktelow, N.S. (2006). Impact of mechanical anisotropy and power-law rheology on single layer folding. Tectonophysics 421 71–87. DOI: https://doi.org/10.1016/j.tecto.2006.04.014

Kocher, T., Mancktelow, N.S., Schmalholz, S.M., (2008). Numerical modelling of the effect of matrix anisotropy orientation on single layer fold development. Journal of Structural Geology 30 (2008) 1013–1023. DOI: https://doi.org/10.1016/j.jsg.2008.04.006

Kohlstedt, D.L., Evans, B., Mackwell, S.J., (1995). Strength of the lithosphere: Constraints imposed by laboratory experiments. Journal of Geophysical Research 100, 17,587-17,602 DOI: https://doi.org/10.1029/95JB01460

Kronenberg, A. K., Kirby, S. H., Pinkston J., (1990). Basal slip and mechanical anisotropy of biotite. Journal of Geophysical research Solid Earth, 95, 19257-19278. DOI: https://doi.org/10.1029/JB095iB12p19257

Lan, L., Hudleston, P.J., (1991). Finite-element models of buckle folds in non-linear materials. Tectonophysics 199, 1-12. DOI: https://doi.org/10.1016/0040-1951(91)90115-9

Lan, L., Hudleston, P.J., (1995). The effects of rheology on the strain distribution in single layer buckle folds. Journal of Structural Geology. 17, 727–738. https://doi.org/10.1016/0191-8141(94)00095-H

Lan, L., Hudleston, P.J., (1996). Rock rheology and sharpness of folds in single layers. Journal of Structural Geology, Vol. 18, No. 7, pp. 925-931. Doi: https://doi.org/10.1016/0191-8141(96)00018-1

Lebensohn, R.A., (2001). N-site modeling of a 3D viscoplastic polycrystal using Fast Fourier Transform. Acta Materialia, 49, 2723-2737. Doi: 10.1016/S1359-6454(01)00172-0

Lebensohn, R.A., Brenner, R., Castelnau, O., Rollett, A. D. (2008). Orientation image-based micromechanical modelling of subgrain texture evolution in polycrystalline copper. Acta Materialia, 56, 3914-3926. Doi: 10.1016/j.actamat.2008.04.016

Lebensohn, R.A., Rollett, A.D. (2020). Spectral methods for full-field micromechanical modelling of polycrystalline materials. Computational Materials Science, 173, 109336. Doi: 10.1016/j.commatsci.2019.109336

Llorens, M.-G., Bons, P. D., Griera, A., Gomez-Rivas, E. (2013a). When do folds unfold during progressive shear? GEOLOGY, May 2013, v. 41, no. 5, p. 563–566. DOI:10.1130/G33973.1

Llorens, M.-G., Bons, P. D., Griera, A., Gomez-Rivas, E., Evans, L. A. (2013b). Single layer folding in simple shear. Journal of Structural Geology 50, 209-220. DOI: 10.1016/j.jsg.2012.04.002

Llorens, M.-G. Bons, P.D., Griera. A., Gomez-Rivas. E. (2013c). Pardo-Igúzquiza, E., Guardiola-Albert, C., Heredia, J., Moreno-Merino, L., Durán, J.J. and Vargas-Guzmán, J.A. (Editors). Mathematics of Planet Earth. Lecture Notes in Earth System Sciences, pp. 763-766. Springer. Doi: http://www.springer.com/gb/book/9783642324079

Llorens, M.-G. (2015). Numerical simulation of deformation microstructures and folds in polar ice and ductile rocks. Eberhard Karls University Tübingen, PhD Dissertation

Llorens, M.-G., Griera, A., Bons, P.D., Roessiger, J., Lebensohn, R.A., Evans, L.A., Weikusat, I. (2016a). Dynamic recrystallisation of ice aggregates during co-axial viscoplastic deformation: A numerical approach. Journal of Glaciology, 62(232), 359-377. DOI: https://doi.org/10.1017/jog.2016.28

Llorens, M.-G., Griera, A., Bons, P.D., Lebensohn, R.A., Evans, L.A., Jansen, D., Weikusat, I. (2016b). Full-field predictions of ice dynamic recrystallisation under simple shear conditions. Earth and Planetary Science Letters, 450 (2016), 233–242. doi: https://doi.org/10.1016/j.epsl.2016.06.045

Llorens, M.-G., Griera, A., Steinbach, F., Bons, P.D., Gomez-Rivas, E., Jansen, D., Roessiger, J., Lebensohn, R.A., Weikusat, I. (2017). Dynamic recrystallization during deformation of polycrystalline ice: insights from numerical simulations. Philosophical Transactions of the Royal Society A: Mathematical, Physical and Engineering Sciences, 375, 20150346. https://doi.org/10.1098/rsta.2015.0346

Llorens, M.-G., Gomez-Rivas, E., Ganzhorn, A.-C., Griera, A., Steinbach, F., Roessiger, J., Labrousse, L., Walte, N.P., Weikusat, I., Bons, P.D., (2019a). The effect of dynamic recrystallisation on the rheology and microstructures of partially molten rocks. Journal of Structural Geology, (118), 224-235. doi: https://doi.org/10.1016/j.jsg.2018.10.013

Llorens, M.-G. (2019b). Stress and strain evolution during single-layer folding under pure and simple shear, Journal of Structural Geology, Volume 126, Pages 245-257, DOI: https://doi.org/10.1016/j.jsg.2019.06.009

Mainprice, D., Nicolas, A. (1989). Development of shape and lattice preferred orientations: application to the seismic anisotropy of the lower crust. Journal of Structural Geology, 11(1-2), 175–189. doi: https://doi.org/10.1016/0191-8141(89)90042-4

Mancktelow, N.S., (1999). Finite-element modelling of single-layer folding in elastoviscous materials; the effect of initial perturbation geometry. Journal of Structural Geology 21, 161-177. DOI: https://doi.org/10.1016/S0191-8141(98)00102-3

Mandal, N., Samanta, S.K., Chakraborty, C., (2004). Problem of folding in ductile shear zones: a theoretical and experimental investigation. Journal of Structural Geology, 26(3), 475–489. doi: https://doi.org/10.1016/j.jsg.2003.07.004

Manz, R., Wickham, J., (1978). Experimental analysis of folding in simple shear. Tectonophysics 44, 79–90. DOI: https://doi.org/10.1016/0040-1951(78)90064-1

Mares V. M., Kronenberg A. K., (1993). Experimental deformation of muscovite. Journal of Structural Geology. Volume 15, Issues 9–10, September–October 1993, Pages 1061-1075. DOI: 10.1016/0191-8141(93)90156-5

Marshak, S., Alkmim, F.F., Whittington, A., Pedrosa-Soares A.C., (2006). Extensional collapse in the Neoproterozoic Araçuaí orogen, eastern Brazil: a setting for reactivation of asymmetric crenulation cleavage, Journal of Structural Geology 28 (2006) 129–147. Doi: https://doi.org/10.1016/j.jsg.2005.09.006

Montagnat, M., Castelnau, O., Bons, P.D., Faria, S.H., Gagliardini, O., Gillet-Chaulet, F., Grennerat, F., Griera, A., Lebensohn, R.A., Moulinec, H., Roessiger, J., Suquet, P. (2014). Multiscale modeling of ice deformation behavior. Journal of Structural Geology, 61, 78–108. https://doi.org/doi:10.1016/j.jsg.2013.05.002

Mühlhaus, H.-B., Sakaguchi, H., Hobbs, B.E. (1998). Evolution of three-dimensional folds for a non-Newtonian plate in a viscous medium. Proceedings of the Royal Society A: Mathematical, Physical and Engineering Sciences, 454(1980), 3121–3143. doi: https://doi.org/10.1098/rspa.1998.0294

Nabavi, S.T., Fossen, H., (2021). Fold geometry and folding – a review. Earth-Science Reviews, 222, 103812. DOI: https://doi.org/10.1016/j.earscirev.2021.103812

Naus-Thijssen, F.M.J., Johnson, S.E., Koons, P.O. (2010). Numerical modeling of crenulation cleavage development: A polymineralic approach. Journal of Structural Geology, 32(3), 330–341. DOI: https://doi.org/10.1016/j.jsg.2010.01.004

Ormand, C.J., Hudleston, P.J., (2003). Strain paths of three small folds from the Appalachian Valley and Ridge, Maryland. Journal of Structural Geology 25, 1841-1854 doi: https://doi.org/10.1016/S0191-8141(03)00042-7

Parrish, D.K., (1973). A nonlinear finite element fold model. American Journal of Science April 1973, 273 (4) 318-334; DOI: https://doi.org/10.2475/ajs.273.4.318

Parrish, D.K., Krivz, A.L., Carter, N.L. (1976). Finite-element folds of similar geometry. Tectonophysics, 32(3-4), 183–207. doi: https://doi.org/10.1016/0040-1951(76)90062-7

Passchier, C.W., Trouw, R.A., (2005). Microtectonics. Springer Science & Business Media.

Pérez-Alonso, J., Fuertes-Fuente, M., Bastida, F., (2016). Quartz veining in slates and Variscan deformation: Insights from the Luarca sector (NW Spain). Tectonophysics, Volume 671, 7 March 2016, Pages 24-41. https://doi.org/10.1016/j.tecto.2016.01.019

Piazolo, S, Bons, P.D., Griera, A., Llorens, M.-G., Gomez-Rivas, E., Koehn, D., Wheeler, J., Gardner, R., J.R.A. Godinho, J.R.A., Evans, L., Lebensohn, R.A., Jessell, M.W. (2019). A review of numerical modelling of the dynamics of microstructural development in rocks and ice: Past, present and future. J. Struct. Geol. 125, 111-123. DOI: https://doi.org/10.1016/j.jsg.2018.05.025

Pollard, D. D. and Fletcher, R. C. (2005): Fundamentals of Structural Geology, Cambridge University Press, Cambridge.

Ponce, C., Druguet, E., Carreras, J. (2013). Development of shear zone-related lozenges in foliated rocks. Journal of Structural Geology, 50, 176–186. doi: https://doi.org/10.1016/j.jsg.2012.04.001

Price, N.J., Cosgrove, J.W., (1990). Analysis of Geological Structures. Cambridge University Press, Great Britain

Quinquis, H., Audren, CL., Brun, J.P., Cobblod, P.R., (1978). Intense progressive shear in Ile de Groix blueschists and compatibility with subduction or obduction. Nature 273, 43–45. Doi: https://doi.org/10.1038/273043a0

Ramberg, H., (1961). Relationship between concentric longitudinal strain and concentric shearing strain during folding of homogeneous sheets of rocks. American Journal of Science May 1961, 259 (5) 382-390, DOI: https://doi.org/10.2475/ajs.259.5.382

Ramberg, H., (1962). Contact strain and folding instability of a multilayered body under compression. Geologische Rundschau, 51, 405–439. DOI: 10.1007/BF01820010

Ramberg, H., (1963). Fluid Dynamics of Viscous Buckling Applicable to Folding of Layered Rocks. AAPG Bulletin (1963) 47 (3): 484–505. DOI: 10.1306/BC743A5B-16BE-11D7-8645000102C1865D

Ramberg, H., (1970). Folding of laterally compressed multilayers in the field of gravity, I., 2(4), 0–232. doi: https://doi.org/10.1016/0031-9201(70)90010-5

Ramsay, J.G., (1967): Folding and Fracturing of Rocks, McGraw-Hill, New York.

Ramsay, J.G., (1980). Shear zone geometry: A review. Journal of Structural Geology, 2(1-2), 83–99. DOI: https://doi.org/10.1016/0191-8141(80)90038-3

Ramsay J.G. Huber M. I., (1987). The Techniques of Modern Structural Geology. Volume 2: Folds and Fractures. Academic Press.

Ran, H., Bons, P.D., Wang, G., Steinbach, F., Finch, M., Griera, A., Gomez-Rivas, E Llorens, M.-G., Ran, S., Liang, X., Zhou, J., (2018). High-strain deformation of conglomerates: Numerical modelling, strain analysis, and an example from the Wutai Mountains, North China Craton. Journal of Structural Geology, Volume 114, September 2018, Pages 222-234. doi: https://doi.org/10.1016/j.jsg.2018.06.018

Ran, H., de Riese, T., Llorens, M.-G., Finch, M.A., Evans, L.A., Gomez-Rivas, E., Griera, A., Jessell, M.W., Lebensohn, R.A., Piazolo, S., Bons, P.D., (2019). Time for anisotropy: The significance of mechanical anisotropy for the development of deformation structures. J. Struct. Geol. 125, 41-47. DOI: https://doi.org/10.1016/j.jsg.2018.04.019

Ran, H., Bons, P.D., Wang, G., Griera, A., de Riese, T., Gomez-Rivas, E., Llorens, M.-G., Ran, S., Wang, Y., Wang, S., (2022). Folds inside pebbles: When do they form during conglomerate deformation? Numerical modelling and comparison with the Hutuo Group conglomerates, North China Craton. Journal of Structural Geology, Volume 160, July 2022, Article number 104620. Doi: https://doi.org/10.1016/j.jsg.2022.104620

Roessiger, J., Bons, P.D., Faria, S.H., (2014). Influence of bubbles on grain growth in ice. Journal of Structural Geology, 61 (2014), 123–132. doi: https://doi.org/10.1016/j.jsg.2012.11.003

Rutter, E.H., (1993). Experimental rock deformation, techniques, results and applications to tectonics. Geology Today 9, 61-65. DOI: https://doi.org/10.1111/j.1365-2451.1993.tb00982.x

Schmalholz, S.M., Podladchikov, Y.Y., (1999). Buckling versus folding: Importance of viscoelasticity. Geophysical Research Letters, 26(17), 2641–2644. doi: https://doi.org/10.1029/1999gl900412

Schmalholz, S.M., Podladchikov, Y.Y., (2000). Finite amplitude folding: transition from exponential to layer length controlled growth. Earth and Planetary Science Letters 181, 619-633. DOI: https://doi.org/10.1016/S0012-821X(00)00193-X

Schmalholz, S.M., Podladchikov, Y.Y. (2001). Strain and competence contrast estimation from fold shape. Tectonophysics, 340(3-4), 0–213. doi: https://doi.org/10.1016/s0040-1951(01)00151-2

Schmalholz, S.M., Podladchikov, Y.Y., Schmid, D.D., (2001). A spectral/finite difference method for simulating large deformations of heterogeneous, viscoelastic materials. Geophysical Journal International 145, 199-208. DOI: https://doi.org/10.1046/j.0956-540x.2000.01371.x

Schmalholz, S.M., Podladchikov, Y.Y., Burg, J.-P. (2002): Control of folding by gravity and matrix thickness: implications for large-scale folding, J. Geophys. Res., 107, doi: https://doi.org/10.1029/2001JB000355

Schmalholz, S. M. (2008). 3D numerical modeling of forward folding and reverse unfolding of a viscous single-layer: Implications for the formation of folds and fold patterns. Tectonophysics, 446(1-4), 0–41. doi:10.1016/j.tecto.2007.09.005

Schmalholz, S.M., Mancktelow, N.S., (2008). Estimation of palaeo-rheology from buckle fold geometries. Bollettino Della Società Geologica Italiana 127, 227-230.

Schmalholz, S.M., Schmid, D.W., (2012). Folding in power-law viscous multi-layers. Philosophical Transactions of the Royal Society A: Mathematical, Physical and Engineering Sciences, 370(1965), 1798–1826. doi: https://doi.org/10.1098/rsta.2011.0421

Schmalholz. S. M., Mancktelow. N.S., (2016): Folding and necking across the scales: a review of theoretical and experimental results and their applications. Solid Earth, 7, 1417–1465, 2016. DOI: 10.5194/se-7-1417-2016

Schmid, D.W., Podlachikov, Y.Y. (2006): Fold amplification rates and dominant wavelength selection in multilayer stacks, Philos. Mag., 86, 3409–3423. Doi: https://doi.org/10.1080/14786430500380175

Shea Jr., W.T., Kronenberg, A.K., (1993). Strength and anisotropy of foliated rocks with varied mica contents. Journal of Structural Geology. Volume 15, Issues 9–10, September–October 1993, Pages 1097-1121. https://doi.org/10.1016/0191-8141(93)90158-7

Sherwin, J.-A., Chapple. W.M., (1968). Wavelengths of single-layer folds; a comparison between theory and observation. American Journal of Science March 1968, 266 (3) 167-179; DOI: 10.2475/ajs.266.3.167

Smith, R.B., (1977). Formation of folds, boudinage, and mullions in non-Newtonian materials. Geological Society of America Bulletin, 88 (2): 312–320. Doi: https://doi.org/10.1130/0016-7606(1977)88<312:FOFBAM>2.0.CO;2

Steinbach, F., Bons, P.D., Griera, A., Jansen, D., Llorens, M.-G., Roessiger, J., Weikusat, I. (2016): Strain localization and dynamic recrystallization in the ice–air aggregate: a numerical study, The Cryosphere, 10, 3071–3089, https://doi.org/10.5194/tc-10-3071-2016

Steinbach, F. (2017). Numerical modelling of deformation and recrystallisation mechanics in ice and ice-air aggregates. Eberhard Karls University Tübingen, Doktorat Dissertation

Tanner, G.P.W., (2016). A new model for the formation of a spaced crenulation (shear band) cleavage in the Dalradian rocks of the Tay Nappe, SW Highlands, Scotland. Journal of Structural Geology, 84, 120–141. doi: https://doi.org/10.1016/j.jsg.2015.11.007

Tikoff, B., Peterson, K., (1998). Physical experiments of transpressional folding. Journal of Structural Geology. 20, 661–672. DOI: https://doi.org/10.1016/S0191-8141(98)00004-2

Torremans, K., Muchez, P., Sintubin, M., (2014). Mechanisms of flexural flow folding of competent single-layers as evidenced by folded fibrous dolomite veins. Journal of Structural Geology, Volume 69, Part A, Pages 75-90. Doi: https://doi.org/10.1016/j.jsg.2014.10.002

Treagus, S.H., (1982). Strain refraction in layered systems, Journal of Structural Geology Volume 10, Issue 5, 1988, Pages 517-527, doi: https://doi.org/10.1016/0191-8141(88)90038-7

Turcotte, D.L. and Schubert, J. (1982). Geodynamics, Cambridge University Press, Cambridge

Viola, G., Mancktelow, N.S., (2005). From XY tracking to buckling: axial plane cleavage fanning and folding during progressive deformation. Journal of Structural Geology, 27(3), 409–417. doi: https://doi.org/10.1016/j.jsg.2004.10.011

Wang, W., Ye, Y., Wang, Q., Hu, N., (2022). Experimental Study on Anisotropy of Strength, Deformation and Damage Evolution of Contact Zone Composite Rock with DIC and AE Techniques, Rock Mechanics and Rock Engineering, 55, pages837–853. doi: https://doi.org/10.1007/s00603-021-02682-x

Watkinson, A.J., (1983). Patterns of folding and strain influenced by linearly anisotropic bands. Journal of Structural Geology, 5(3-4), 449–454. doi: https://doi.org/10.1016/0191-8141(83)90031-7

Whiting, A.I.M., Hunt, G.W. (1997). Evolution of nonperiodic forms in geological folds. Mathematical Geology, volume 29, 705–723. doi: https://doi.org/10.1007/bf02769652

Zhang, Y., Hobbs, B.E., Ord, A.M., Mühlhaus, H.B., (1996). Computer simulation of single layer buckling. Journal of Structural Geology 18, 643-655. DOI: https://doi.org/10.1016/S0191-8141(96)80030-7

Zhang, Y., Mancktelow, N.S., Hobbs, B.E., Ord, A.M., Mühlhaus, H.B., (2000). Numerical modelling of single-layer folding: clarification of an issue regarding the possible effect of computer codes and the influence of initial irregularities. Journal of Structural Geology 22, 1511-1522. DOI: https://doi.org/10.1016/S0191-8141(00)00063-8

Contributions to scientific publications

PAPER I

Hu, Yuanbang, de Riese, T., Bons, P. D., Liu, S.-G., Griera, A., Llorens, M.-G., Gomez-Rivas, E., Finch, M., Cai, X.-L.: Crenulation geometries developed in anisotropic materials undergoing simple shear deformation. *(In preparation).*

Scientific ideas	**Data generation**	**Analysis and Interpretation**	**Paper writing**
50%	**60%**	**60%**	**70%**
Initial scientific idea of crenulation by PDB and HY. Initial idea for models on strain localisation and crenulation by HY, TdR and PDB.	Numerical modelling data presented in the paper by TdR and HY, substantial work on program code together with PDB.	All analysis and interpretation by HY and PDB with contribution of TdR and MGL.	All paper writing. Proof-reading and comments by PDB

PAPER II

Hu, Yuanbang, Bons, P. D., de Riese, T., Liu, S.-G., Llorens, M.-G., Cai, X.-L.: Folding of a single layer in an anisotropic viscous matrix under layer-parallel shortening. *(In preparation).*

Scientific ideas	**Data generation**	**Analysis and Interpretation**	**Paper writing**
50%	**90%**	**70%**	**70%**
Initial scientific idea and models of layer-parallel folding with CPO by HY and PDB.	Generation of all numerical modelling data presented in the paper, including substantial work on program code together with PDB.	All analysis and interpretation by HY and PDB.	All paper writing. Proof-reading and comments by PDB

PAPER III

Bons, P. D., **Hu, Yuanbang**, Llorens, M.-G., Zhang, Y., Westhoff, J., Franke, S., Stoll, N.: Folding due to anisotropy in ice, from cm-scale cloudy bands to the km-scale. *(In preparation).*

Scientific ideas	**Data generation**	**Analysis and Interpretation**	**Paper writing**
20%	**40%**	**20%**	**20%**
Initial scientific idea from PDB. Contributing ideas on the layer-parallel shortening model for comparing the fold geometries.	Generation of all data from VPFFT+Elle method related to folding simulations in the paper.	Most analysis and interpretation made by PDB. Contribution to analysis of fold geometries.	Most paper writing by PDB. Part of Method and fold by HY. Proof-reading and comments by all co-authors.

PAPER IV

Jansen, D., Franke, S., Bauer, C. C., Binder, T., Dahl-Jensen, D., de Riese, T., Eichler, J., Eisen, O., **Hu, Yuanbang**, Llorens, M.-G., Kerch, J., Miller, H., Neckel, N., Paden, J., Sachau, T., Stoll, N. Weikusat, I., Wilhelms, F., Zhang, Y., Bons, P. D.: Folded ice reveals: North East Greenland Ice Stream was fully established only 2000 years ago. *(In preparation).*

Scientific ideas	**Data generation**	**Analysis and Interpretation**	**Paper writing**
5%	**10%**	**5%**	**5%**
Initial scientific idea by DJ, SF and PDB. No significant contribution. Come up with the model for comparing the fold geometries.	Generation of all data from VPFFT+Elle method related to folding simulations in the paper.	Analysis related to anisotropic ice from Elle made by PDB and minor contribution by HY. Stereonet projection by PDB and HY.	Part of anisotropic ice related to results from Elle, with crystal rotation and fold amplification by PDB and HY.

PAPER I

Crenulation geometries developed in anisotropic materials undergoing simple shear deformation

Yuan-bang Hu[1,2], Tamara de Riese[1], Paul D. Bons[1], Shu-gen Liu[2,3,4], Albert Griera[5], Maria-Gema Llorens[6], Enrique Gomez-Rivas[7], Melanie Finch[1,8], Xue-lin Cai[2] (Preliminary author list; Only edited by YH and PDB now)

[1] *Department of Geosciences, Eberhard Karls Universität Tübingen, Tübingen, Germany*

[2] *College of Earth Science, Chengdu University of Technology, Chengdu, China*

[3] *State Key Laboratory of Oil and Gas Reservoir Geology and Exploitation, Chengdu University of Technology, Chengdu, China*

[4] *Xihua University, Chengdu, China*

[5] *Departament de Geologia, Universitat Autònoma de Barcelona, Barcelona, Spain*

[6] *Institute of Earth Sciences Jaume Almera (ICTJA-CSIC), Barcelona, Spain.*

[7] *Department of Mineralogy, Petrology and Applied Geology, University of Barcelona, Barcelona, Spain*

[8] *School of Earth, Atmosphere and Environment, Monash University, Clayton, Victoria, Australia*

Abstract

Deformation of foliated rocks commonly leads to crenulation or micro-folding, with the development of cleavage domains and microlithons. We here consider the effect of mechanical anisotropy due to a crystallographic preferred orientation (CPO) that defines the foliation, for example by of alignment of micas. Mechanical anisotropy induces shear localisation, resulting in low-strain domains (with microlithons) and high-strain shear bands or cleavage domains. We investigate the crenulation patterns that result from moderate strain in dextral simple shear deformation, varying the initial orientation of the mechanical anisotropy (CPO) relative to the shear plane of an anisotropic single-phase material by using the numerical simulation. An initially point-maximum CPO at variable angles to the shear plane defines the initial straight localised bands at different angles to the shear plane, limiting themselves to orientations in which the localised bands are in the stretching field. The resulting crenulation geometries strongly depend on the orientation of the foliation (CPO) and we observe four types of localisation behaviour: (1) synthetic shear localisation, (2) antithetic shear localisation, (3) initial formation of antithetic shear localisation and subsequent development of synthetic shear localisation, and (4) distributed, approximately shear-margin parallel and normal strain localisation. The numerical simulations not only show the evolving strain-rate field, but also the predicted finite strain pattern of existing visible layers or foliations. We display the results for passive layers parallel to the orientation of anisotropy (CPO), together with passive layers parallel to the shear plane (e.g., the case of sedimentary layers and a cleavage that controls the mechanical anisotropy). A wide range of crenulation geometries form as a function of the initial orientation of the visible layering and mechanical anisotropy. Most importantly, some of these may be highly misleading and may easily be interpreted as indicating the opposite sense of shear.

Keywords: Crenulation geometries, Micro-fold, Anisotropy, Crystallographic preferred orientation, Strain-rate redistribution, Extensional field.

1 Introduction

Most rocks are foliated in the sense that they have some compositional or stratigraphic layering, or a planar anisotropy, such as cleavages or schistosity. Ductile shortening of such foliations typically leads to folding (Ramsay and Huber, 1987). Folds can vary in scale, depending on what foliation is folded (Biot, 1961). Fine foliations form micro-folds, also termed 'crenulations' (Rickard, 1961; Passchier and Trouw, 2005). Crenulations, similar to folds, are very useful structures to unravel the history and evolution of deformation in rocks (Hudleston, 1986; Ramsay and Huber, 1987; Hudleston and Lan, 1993; Passchier and Trouw, 2005; Hudleston and Treagus, 2010; Adamuszek et al., 2011; Llorens et al., 2013a, 2013b; Schmalholz and Mancktelow, 2016). Many studies have investigated fold development based on theory (Biot, 1961; Ramberg, 1961), field studies (Ramsay and Huber, 1987; Passchier and Trouw, 2005; and relevant references therein), laboratory models (Ghosh, 1966; Cobbold, 1975; Dubey and Cobbold, 1977; Manz and Wickham, 1978), or numerical simulation (Ramsay, 1974; Casey and Huggenberger, 1985; Hudleston and Lan, 1994; Mancktelow, 1999; Frehner and Schmalholz, 2006; Schmid and Podladchikov, 2006; Naus-Thijssen et al., 2010; Llorens et al, 2013a, 2013b).

According to the classical fold theory of Biot (1957, 1961, 1964a, b, 1965a, b), layers become folded because of the amplification of instabilities that arise from the layer-parallel shortening of one or more competent (strong) layers and surrounding incompetent (weak) layers or a matrix (Fig.1a, b). The wavelength of the folds is determined by relative strength or competence of the layers and their thickness. Other authors have since further developed and refined the basic fold theory, including factors such as non-linearity of materials (Cobbold, 1975; Gray, 1979; Schmid and Podladchikov, 2006; Schmalholz and Podladchikov, 1999, Llorens et al, 2013a, 2013b).

Folds and crenulations can also form in rocks without layering, but with a planar anisotropy instead. For example, the ice sheets of Greenland and Antarctica are probably among the most homogeneous mono-mineralic rocks on earth, consisting of almost pure of ice 1h. However, folds occur on mm to 100-m scales (Wolovick et al., 2014; Leyinger Vieli et al., 2011; Jansen et al., 2016; Bons et al., 2016; Westhoff et al., 2021), which can be explained by the strong mechanical anisotropy - a *foliation* - due to alignment of the easy-glide basal planes (Jansen et al., 2016; Bons et al., 2016). There is no fully developed theory for folding or crenulation due to intrinsic mechanical anisotropy (Griera et al., 2013), although several studies have recognised and addressed the issue (Ran et al., 2019; de Riese et al., 2019). Folds and crenulations, however, do not only form by Biot-type folding. Folding is essentially caused by heterogeneous deformation in which an originally planar surface becomes non-planar. Heterogeneous strain, or strain localisation, can thus also produce folds or crenulations in both compressional and extensional circumstances.

Strain localisation can result from many processes, such as shear heating (Brun and Cobbold, 1980; Tullis and Yund, 1985; Hirth and Tullis, 1992; Montési, 2013), strain and geometrical hardening and/or softening weakening (White et al., 1980; Hobbs et al., 1990; Hirth and Tullis, 1992), grain-size reduction (Tullis and Yund, 1985; Braun et al., 1999; de Bresser et al., 2001; Warren and Hirth, 2006; Platt and Behr, 2011), etc. Mechanical anisotropy can also play an important role in causing strain localisation (Cobbold et al., 1971; Cosgrove, 1976, 1989; Williams and Price, 1990; Carreras, 2001; Dabrowski et al., 2012; Ponce et al., 2013; Llorens et al., 2017; Bons et al., 2016; Gardner et al., 2017; Ran et al., 2019; de Riese et al., 2019).

Minerals are generally (intrinsically) anisotropic both in their brittle and ductile properties if deformation is by dislocation glide on crystallographic planes. In case of micas, this anisotropy is very strong (Kronenberg et al., 1990; Mares and Kronenberg, 1993; Shea and Kronenberg, 1993; Aslin et al., 2019; Finch et al., 2020). A rock as a whole can become anisotropic when crystallographic orientations align in a crystallographic preferred orientation (CPO). Tectonic foliations are often formed by the alignment of micas so that tectonically foliated rocks can be expected to be highly anisotropic. Anisotropy has been recognised as a key factor in the formation of geological structures and a cause for strain localisation (Cobbold et al., 1971; Ramsay, 1980; Passchier and Trouw. 2005; Naus-Thijssen, et al., 2011; Griera et al., 2013; Tanner, 2016; Ran et al., 2019; de Riese et al., 2019; Torvela and Kurhila, 2020) in crenulations, folds and other micro-structures.

Shear localisation tends to result in low-strain domains and high-strain domains in both pure shear and simple shear by strain rate redistribution (de Riese et al., 2019). Strain localisation zones can have different characteristics of movement, rotation and velocity, while these also affect the movements and rotations in low-strain areas. This can happen on all scales (Carreras, 2001; Ponce et al., 2013; Steinbach et al., 2016, de Riese et al., 2019). On the small scale the localisation leads to the formation of so-called 'microlithons' (low-strain domains) and 'shear bands' (high strain zones) (Berthé et al, 1979, Passchier and Trouw, 2005). The localised high-strain domains form conjugated shear bands in pure shear (Steinbach et al., 2016), and form C, C' (synthetic, Fig.1c, Berthé et al., 1979; Lister and Snoke, 1984; Ramsay and Huber, 1987; Mandal et al., 2004; Passchier and Trouw, 2005) and C'' (antithetic, Fig.1d, Carreras et al., 2005; Carreras et al., 2013; Ponce et al., 2013; Ran et al., 2019; Finch et al., 2020, 2022) shear bands in simple shear.

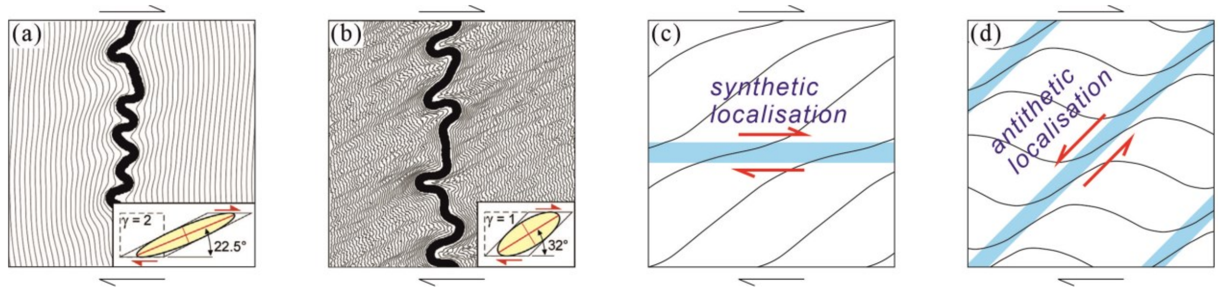

Fig.1 Three types of formation of crenulations or folds under dextral simple shear. (a) & (b) Competent layers embedded in soft matrix from (figure from Ran et al., 2019, Fig.1). (a) Under progressive shearing the competent layer folds, and the isotropic matrix mimics this folding close to the competent layer. Deformation in the matrix is realtively homogeneous. (b) Heterogeneous deformation resulting in crenulation of the matrix foliation develops in an anisotropic matrix. (c) Synthetic shearing and (d) antithetic shearing results in extensional field crenulations that are the topic of this study.

Generally, structural geologists analyse geometries and patterns in rocks to determine the deformation these rocks experienced, and to relate these with, for example, tectonic events or phases. In case of shear zones or shear bands, the sense of shear is an important parameter that is, unfortunately, not always easily determined. When rocks are foliated, the patterns we see are often folds and crenulations of the foliation (Ez, 2000; Carreras et al., 2005). In that case it is not always clear if an observed sense of shear is synthetic (Fig.1c) or antithetic (Fig.1d) to the overall, larger-scale kinematics (Carreras et al., 2005; Carreras et al., 2013; Ponce et al., 2013; Tanner, 2016; Carreras and Druguet, 2019).

de Riese et al. (2019) investigated the amount and patterns of shear localisation in simple shear due to an intrinsic mechanical anisotropy in power-law viscous materials. They simulated the deformation of an initially non-foliated material. In de Riese et. al (*In preparation*) they systematically investigated the effect of an initial CPO on the localisation and deformation behaviour in an anisotropic material and the role of passive material markers on the development of deformation structures. This contribution presents a part of this set of simulations. The aim of the paper is to determine the effects of anisotropy on patterns of crenulations or folds. We present a series of numerical simulations in simple shear in which the orientation of the anisotropy relative to the shear plane is varied. The focus here is not on the mechanical aspects of such shearing (see de Riese et al. *In preparation*), but the visible patterns that develop in a foliated rock at a low shear strain of up to about 2. Layering that is visible in a rock can, but must not be parallel to the mechanical anisotropy. This may be the case when the visible layering is bedding, but the mechanical anisotropy is dominated by a cleavage at an angle to bedding. We not only consider fold patterns for when the visible layering is parallel to the anisotropy, but also cases where the visible layering is originally oriented differently, in particular parallel to the shear direction. We restrict ourselves here to foliation orientations that are always in the stretching field. This way, Biot-type buckling can be excluded as a cause of folding. In the absence of any other localisation mechanisms (shear heating, hardening/softening, etc.) all folding that does arise is now purely due to the mechanical anisotropy (A) of the material. We use the same numerical approach to model an intrinsically anisotropic material as in Griera et al. (2013), Llorens et al. (2017), Piazolo et al. (2019), Ran et al. (2019, 2022), de Riese et al. (2019), Finch et al., (2020, 2022).

2 Method

We use the full-field, Viscoplastic Fast-Fourier Transform (VPFFT, Lebensohn, 2001; Lebensohn et al., 2008; Lebensohn and Rollett, 2020) crystal plasticity code coupled with the modelling platform ELLE (http://www.elle.ws; Griera et al., 2013; Steinbach et al., 2016; Llorens et al., 2017; Piazolo et al., 2019; Ran et al., 2019; de Riese et al., 2019) to simulate the deformation of an anisotropic single-phase material with an intrinsic mechanical anisotropy due to an initial CPO.

ELLE is an open-source modelling platform and aims to provide a generalized framework for the numerical simulation of the evolution of microstructures during deformation and metamorphism. The VPFFT + ELLE code has been used for the numerical simulation of the deformation and recrystallisation of polycrystalline ice (Steinbach et al., 2016; Llorens et al., 2017; Gomez-Rivas et al., 2017), development of porphyroclasts /-blasts or hard inclusions (Griera et al., 2011, 2013; Ran et al., 2018, 2022), shear band development (Ran et al., 2019; de Riese et al., 2019; Finch et al., 2020, 2022). etc. The numerical procedure used in this study is identical to that of de Riese et al. (2019) and Finch et al. (2020), and is therefore described only briefly here.

The 2D models consist of a square grid of so-called *unodes* (Bons et al., 2008). The *unodes* effectively represent crystallites or single grains with a constant internal crystal orientation, defined by three Euler angles. All simulations were run with a resolution of 256 x 256 *unodes*. Deformation is assumed to occur by slip on crystallographic planes. Such slip produces simple-shear deformation parallel to the slip plane. The shear-strain rate ($\dot{\gamma_s}$) along a slip plane of a slip system is related to shear stress (σ_s) and the shear-stress component (τ) parallel to that plane with a power law:

$$\dot{\gamma}_s = \dot{\gamma}_0 \left(\frac{\tau}{\tau_s}\right)^n \qquad (1)$$

Here $\dot{\gamma_0}$ is a reference shear rate that is set at the same value for all simulations. n is the stress exponent, always set to n = 3. A mechanical anisotropy is achieved by assigning a different value for τ_s to each slip system. This is the resistance to slip, also referred to as the critical resolved shear stress. The strain rate of one unode is the sum of the shear rates along the individual slip planes, taking into consideration their orientations.

For given boundary conditions, the code calculates the stress and strain rate field that minimises the work rate and obeys compatibility requirements between unodes. In all simulations velocities are applied to the boundaries such that the average deformation is dextral simple shear along the horizontal axis. Boundaries are wrapping in both directions: material leaving the model on one side enters it on the opposite side. The velocity field that is derived from the strain rate field is linearly integrated for a small time step to obtain the displacement field. The time step is set such that each deformation step is a shear increment of $\Delta\gamma$ = 0.02. Each unode is first displaced according to the displacement field and its lattice orientation is updated according to its strain rate. As the FFT spectral solver requires an orthogonal grid of unodes, the deformed grid is remapped every calculation step. The displacement field is further used to track passive markers to visualise finite strain and the deformation of originally straight layers.

We use the crystal symmetry of ice 1h with a hexagonal lattice as an analogue for highly anisotropic minerals, such as micas, as in Ran et al. (2019) and de Riese et al. (2019). Deformation is assumed to be accommodated by glide along the basal and non-basal prismatic and pyramidal slip systems only. The intensity of anisotropy (A) is defined by the ratio between the critical resolved shear stresses of the non-basal and the basal slip systems:

$$A = \frac{\tau_s^{(non-basal)}}{\tau_s^{(basal)}} \tag{2}$$

If A=1, the material is effectively isotropic (Griera et al., 2011). Here we use A=64, which simulates a highly anisotropic material with an approximately transverse isotropy, in which shear deformation along the basal plane is much easier than any other deformation.

de Riese et al. (2019) started simulations with random initial lattice orientations assigned to the unodes. Here the basal-plane orientations are initially aligned within ±5° to a plane rotated anticlockwise by an angle α_0 relative to the shear plane (Fig.2). We refer to these aligned basal planes as the foliation. We present simulation for α_0 = 0°, 33°, 45° and 73° as it was found that these represent the four basic types of behaviour that we describe below. In all these four cases, the initial foliation is in the extensional field.

The initial orientation of layers is defined by the angle θ_0, also taken anticlockwise relative to the shear plane (Fig.2). Note that the layers are deforming passively and that, therefore, one simulation with a set initial angle for the foliation can be used to calculate the resulting deformation patters in layers with varying initial angle θ_0.

Results are presented in the form of maps of the Von Mises strain rate field and of images of the deformed passive layers. As the boundaries in the model are wrapping, the sheared model can always be remapped onto a square and is presented as such (Fig.3). The Von Mises strain rate ($\dot{\varepsilon}_{vm}$) is defined as:

$$\dot{\varepsilon}_{vm} = \sqrt{\frac{2}{3}\dot{\varepsilon}_{ij}\dot{\varepsilon}_{ij}} \tag{3}$$

where $\dot{\varepsilon}_{ij}$ is the strain-rate tensor and i and j summation indices. To better visualise the patterns in the deformed layers, images are composed of 2x2 or 3x3 tiles of the result of a simulation, again using the wrapping in both directions (Fig.2d, e).

Table.1 Symbols in use presented in this study

θ	Orientation of passive marker layering, we assume a horizontal layering is θ=0°, a rotation in anticlockwise of the layering is a positive value
α	Crystallographic preferred orientation (CPO, lattice preferred orientation, basal plane orientation, the orientation of foliation in this paper), we assume a horizontal plane is α=0° to the *x*-axis, a rotation in anticlockwise of the plane is a positive value
β	Orientation of localised band, we assume a horizontal plane is β=0° to the x-axis, a rotation in anticlockwise of the plane is a positive value. β_S is the angle between localised bands and x-axis, always equal to 0°, using in initially synthetic shearing, β_A is the angle between antithetic localised bands and x-axis, using in initially antithetic shearing
τ	The shear component of strain, τ_S is the shear component of strain in synthetic localised bands, τ_A is the shear component of strain in antithetic localised bands
γ	Value of strain, we discuss the strain from 0-2 in this paper
λ	Layering in the microlithons relative to β

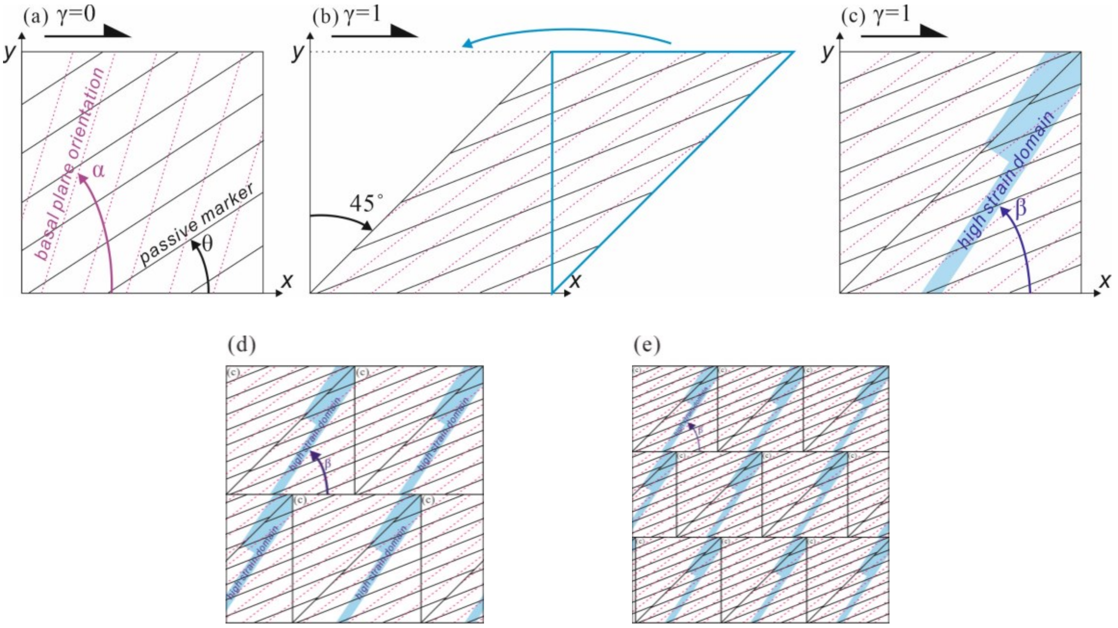

Fig.2 (a) A grid of 256 × 256 unconnected *unodes* was used in our 2D models to define the deforming square unit cell in Elle. A simulation is defined by the given CPO (basal plane orientation (α_0), the purple dashed lines) and the orientation of visualised passive marker layers (θ, the black line). (b) The Elle data structure allows for wrapping of the boundaries (Bons et al., 2008). When material moves outside of the square box, it is moved to within the box according to the finite strain. This is illustrated for γ=1, but is in reality done every time step of γ=0.02. (c) high strain domains may form and rotate during deformation. Their orientation is defined by the angle β. (d) and (e) Because of the wrapping boundaries, the map of a single simulation can be tiled to make 2x2 or 3x3 images that better illustrate the developing structure.

3 Results

3.1 Strain localisation in shear bands

The normalised von Mises strain rate fields for the four simulations and at 3 deformation stages up to a shear strain of 2 are shown in Fig.3. The four simulations show remarkably different strain-rate fields (Fig.3).

There is no discernible shear localisation up to γ =2 when the *foliation* is initially parallel to the shear plane (α_0=0°).

A shear-plane parallel high-strain rate zone forms when α_0=33° (Fig.4b). Von Misses strain rates inside this zone, which we will refer to as a shear band, are >10 times higher than in the remainder of the model. The shear band is stable up to γ =2, as it does not rotate, nor does the strain-rate localisation change significantly. Deformation inside the shear band is approximately simple shear, i.e., it has the same kinematics as the bulk deformation. The shear band can thus be classified as a synthetic, C-type shear band (Berthé et al., 1979; Passchier and Trouw, 2005; Finch et al., 2020, 2022). We define the orientation of the shear band with the angle β, measured anticlockwise from the shear plane. In this case β remains zero.

A shear band also forms at α_0 =45°, but originally at an angle of β≈90° and then rotating clockwise with increasing shear strain (Fig.4c). As it rotates it stretches and thins, and the localisation of strain rate inside the shear band decreases. It should be noted that the thin shear bands at γ =2 are in fact the same shear band if one considers the wrapping boundaries. Deformation inside the shear band is initially simple shear, but antithetic with respect to the bulk sense of shear, making it a C''-type shear band (Finch et al., 2020, 2022).

Finally, α_0 =73° results in the most complex type of strain-localisation evolution (Fig.4d). Shear bands first develop at high angles to the shear plane. Contrary to the previous two cases, the shear bands are more diffuse. The dominant localisation is initially in an antithetic, C''-type shear band with β >90°. As it rotates with the applied bulk simple shear its activity decreases and at a shear strain of about one there is a transition to synthetic shear parallel the shear plane. A synthetic, C-type shear band is fully established by γ =2.

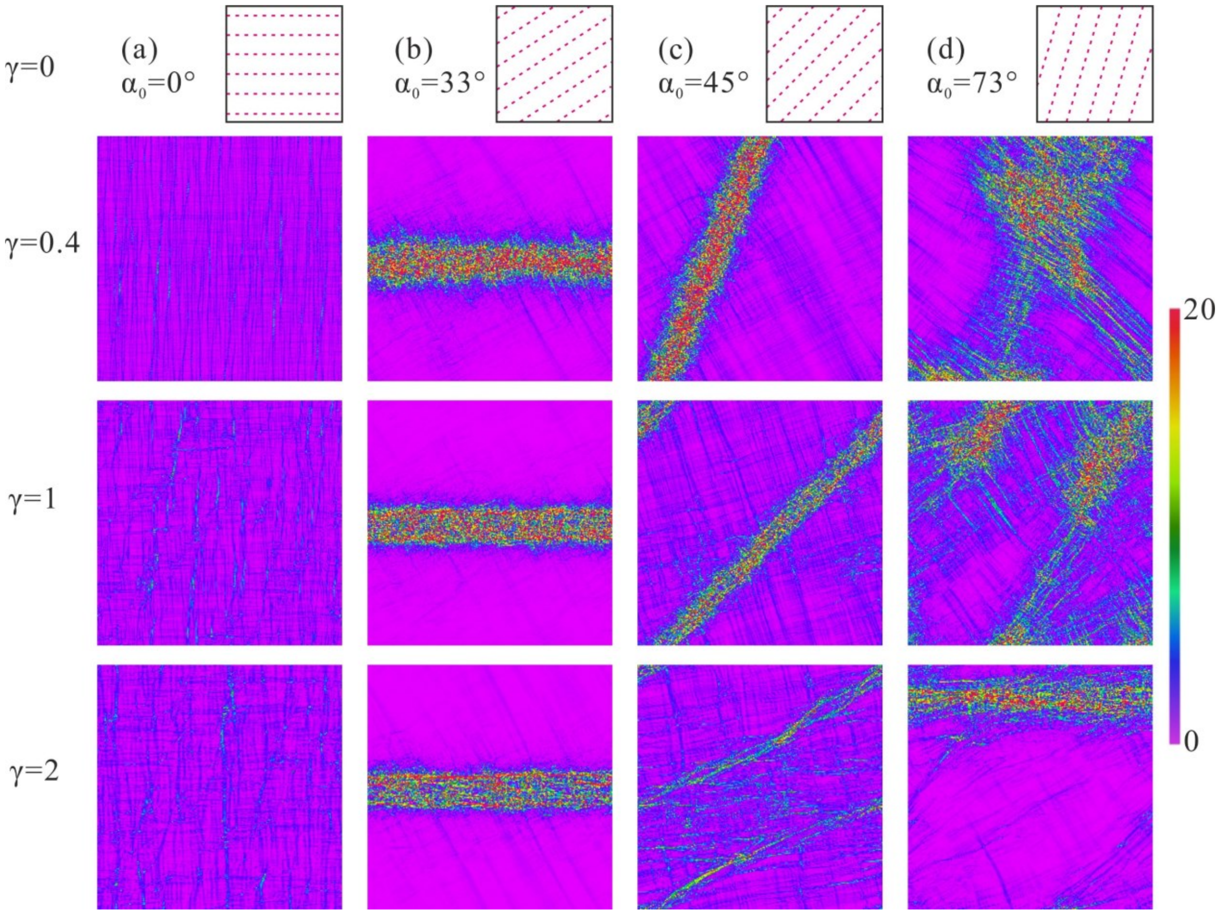

Fig.3 Normalised von Mises strain rate field of the simulations shown in Figs. 4 and 5 for top-to-the-right simple shear. (a) Random distributed bands with no distinct localisation are observed for α_0=0°. (b) At α_0=33° a single zone with highly localised strain rate forms. This shear band is synthetic with persistent dextral shearing. (c) Initially antithetic shear localisation is observed when α_0=45°, which then rotates until the shear sense reverses to synthetic shearing. (d) Finally, α_0=73° shows the initial formation of antithetic shear localisation. The C''-shear band deactivates with rotation, while another shear band with synthetic shear localisation develops. In (b), (c), and (d), strain is strongly localised in high strain domains, showing that the initial CPO has a strong influence on the formation of high strain domains.

3.2 Deformation of the foliation

3.2.1. Visible foliation parallel to foliation (α_0 =θ_0)

The deformation patterns that result if the visible layering is initially parallel to the mechanical foliation (α_0 =θ_0) reflects the four very different types of strain localisation behaviour (Fig. 4). In case α_0 = θ_0=0° the layers remain unchanged due to the absence of significant localisation and because planes parallel to the shear plane do not rotate, nor stretch in simple shear. An S-C structure geometry forms at α_0 = θ_0=33° with the foliation remaining at approximately α=45° in the microlithons, e.g., the low-strain zones between the shear bands. Inside the C-type shear bands the foliation quickly rotates towards a =0°. As a result, there is little change in the structure once the shear bands have developed.

The cases where α_0 = θ_0=45° or 73° are the most dynamic with a rapidly changing structure at low shear strain. At α_0 = θ_0=45° the antithetic C''-type shear bands offset the layering to parallelism with the shear bands (Fig. 4c). Layering in the microlithons makes an initial angle of $\lambda = \beta - \theta = 45°$. As the shear bands and microlithons rotate in the dextral simple-shear field, they get stretched parallel to the shear bands. This leads to a rapid rotation of the layering inside the microlithons towards the shear plane and a decrease in λ. Antithetic C''-type shear bands are also visible in case α_0 = θ_0=73° (Fig. 4d), but the finite shear strain in these bands is much less than in the cases α_0 = θ_0= 45°. Synthetic, C-type shear-band activity already starts to dominate the finite-strain geometry at γ ≈1. By γ =2 the interaction of the early antithetic shear bands and the later synthetic ones creates a pattern of lozenge-shaped microlithons.

3.2.2. Visible foliation parallel to the shear plane (θ_0 =0°)

The deformation patterns that result if the visible layering is initially parallel to the shear plane (θ_0 = 0°) also reflects the four very different types of strain localisation behaviour (Fig. 5). The case α_0 = θ_0=0° is already mentioned, and Fig. 5a is the same as Fig. 4a. A similar geometry forms at α_0 =33° with the visible foliation remaining at θ ≈0°. The β=0° shear zones are hardly visible, as they are parallel to the visible layering. The shear bands only cause minor, but increasing disturbances of the layering.

The cases α_0 =45° or 73° with constant θ_0=0° are the most dynamic and rotational structure at low shear strain. At α_0 =45° the antithetic C''-type shear bands are now clearly visible in the structure as they form at a high angle to the layering (Fig. 5c). Layering in the microlitons makes an angle $\lambda = \theta = 0°$. As the shear bands and microlitons rotate in the dextral simple-shear field, they get stretched parallel to the shear bands. This leads to a rapid rotation of the layering inside the microlithons offset the shear plane and an increase in λ. Flattening of the microlithons leads to folding of the layering that becomes visible by γ =2. Antithetic C''-type shear bands are initially the most prominent at α_0 =73° (Fig. 5d), but not as distinct as for the α_0 =45° case as the finite shear strain in these bands is much less than in the cases α_0 =33 and 45°. The synthetic, C-type shear-band activity already starts to take over the finite-strain geometry at γ ≈1. Relative shifting of the crenulations due to the antithetic shearing leads to complex fold patterns by γ =2.

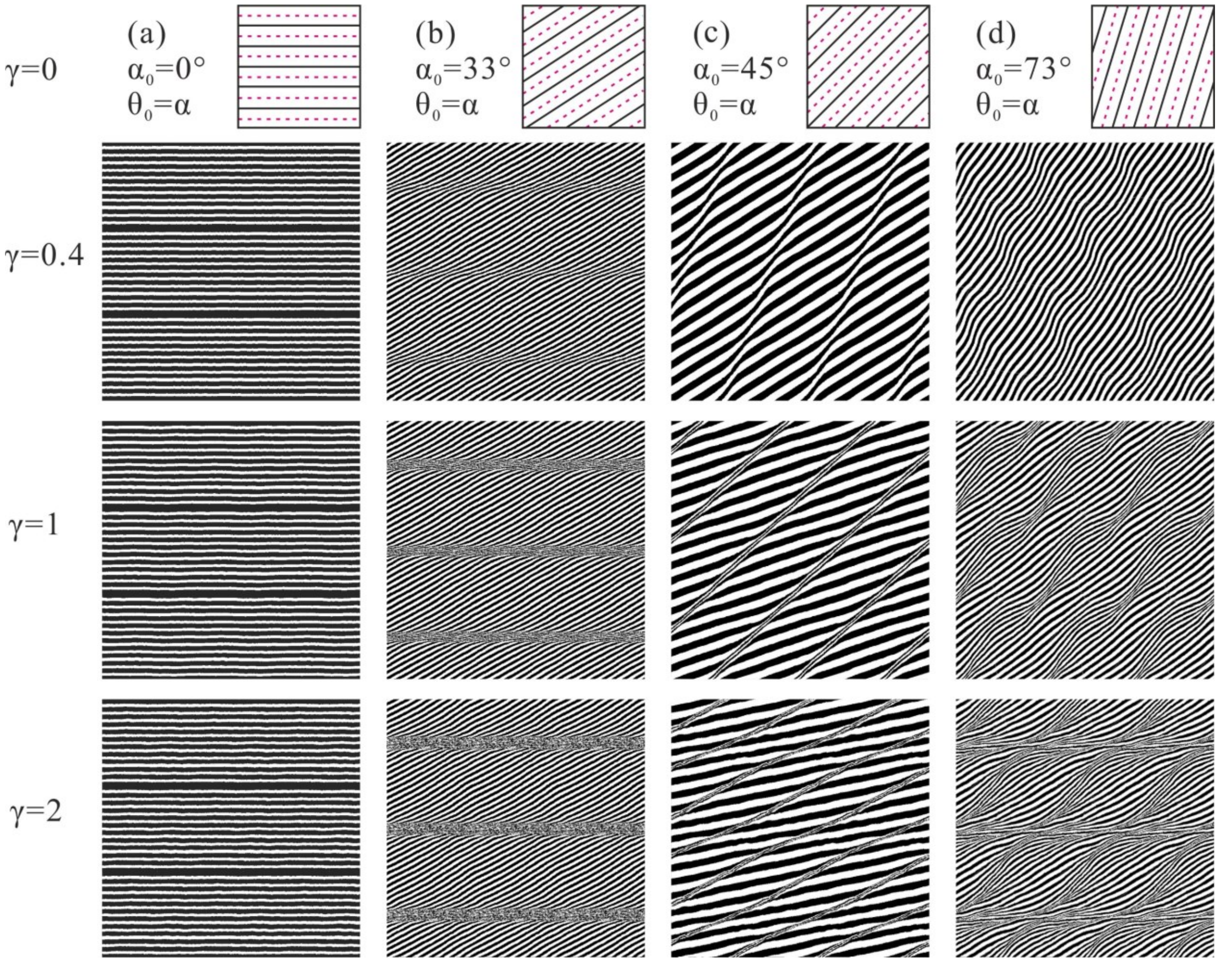

Fig.4 Results for passive marker layers parallel to the given CPO (θ_0 = α_0), as illustrated at the top of the image, where purple dashed lines show the orientation of the CPO and solid black lines that of the visible passive marker layers. (a) When CPO and marker layers parallel to shear plane (α_0=θ_0=0°) the visible structure remains unchanged. (b) At (α_0=θ_0=33°) the developing structure is dominated by straight localised synthetic (C-type) shear bands. Passive marker layers rotate rapidly in the shear bands, but only very slowly in the low-strain domains. (c) When α_0=45°, high-β shear bands form. These have an antithetic sense of shear for γ <1, when β_A decreases from 90° to 45°. These are thus C''-type shear bands. However, there sense-of shear reverses and becomes synthetic when γ >1. Low and high strain domains rotate together and flatten with increasing strain. (d) At α_0=73°, antithetic localised-shear bands are observed up to about γ<1.5. These rotate rapidly with β_A decreasing from about 130° to 45°. After about γ ≥1.5, new synthetic shear bands form, while the antithetic one become deactivated.

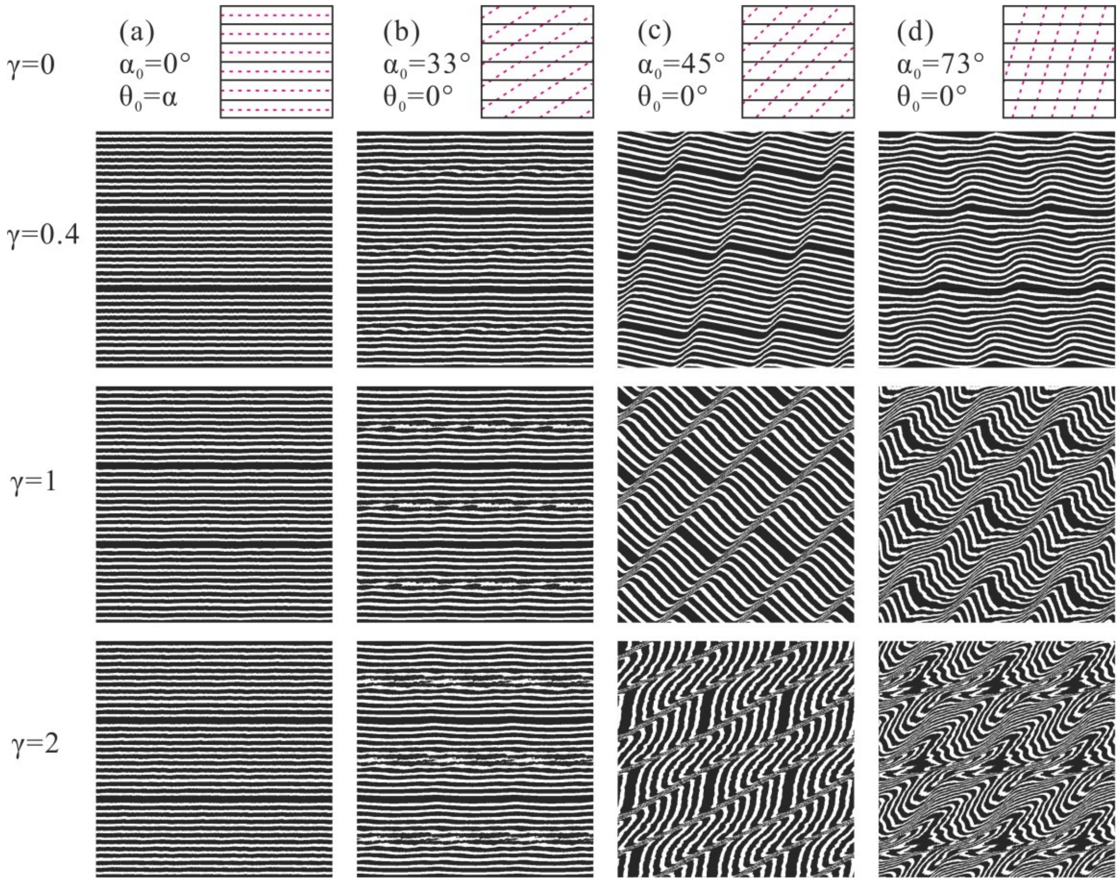

Fig.5 Results for passive marker layers parallel to the shear plane (θ_0 = 0 ≠ α_0), as illustrated at the top of the image, where purple dashed lines show the orientation of the CPO and solid black lines that of the visible passive marker layers. (a) When CPO and marker layers parallel to shear plane (α_0= θ_0 =0°), same to Fig.4 a. (b) When α_0=33° & θ=0°, high strain localised bands behaved synthetically with β_S=0°, passive marker layers subparallel to the straight localised synthetic (C-type), micafish structures form within localised bands, no instinct crenulation. (c) When α_0=45°, high-β shear bands form, initially passive maker layers vertical to localised bands, which have an antithetic sense of shear for γ <1, when β_A decreases from 90° to 45°. These are thus C''-type shear bands. However, there sense-of shear reverses and becomes synthetic when γ >1. Low and high strain domains rotate together, due to the high strain domains getting close, passive marker layers in low strain domains are locally in a pure shear circumstances and form subfolds. (d) At α_0=73°, antithetic localised-shear bands are observed up to about γ<1.5. These rotate rapidly with β_A decreasing from about 130° to 45°. After about γ ≥1.5, new synthetic shear bands form, while the antithetic one become deactivated. Low strain domains rotate with a velocity depend on the movement of high strain localised bands. Deformation of marker layering in low strain domains get refolding due to the localised behaviour of high stain domains and the big angle between the marker layering and antithetic localised bands.

4 Discussion

4.1 Shear band types and shear localised behaviour in anisotropic materials

The Normalised von Mises strain rate fields in Fig.3 illustrate the main shear localisation types that develop as a function of the two setting of simulations here are under the same boundary condition relate to the initial foliation (CPO). As we mentioned in early section, foliations and passive marker layers and shear bands gets into competition to be shearing and rotation in movement direction and velocity. Mechanical anisotropy induces shear localisation (Ran et al., 2019; de Riese et al., 2019), resulting in low-strain domains (microlithons) and high-strain shear bands or cleavage domains. The formation of localised, high-strain domains in a single material is affected by the development of foliation in anisotropic materials or the presence of a foliation already at the start of the (next) deformation event. The latter is here simulated with an initially point-maximum CPO (defining the foliation perpendicular to it at α_0) at variable angles to the shear plane. We limit ourselves to orientations in which the foliation is in the stretching field, thus excluding buckling as a result of shortening (see Chapter 3). The resulting extensional field crenulation geometries strongly depend on the orientation of the localised bands. Their orientation is defined by the angle β. We observe four types of localisation behaviour: (1) distributed, approximately shear-margin parallel strain localisation (β≈0°); (2) synthetic shear localisation (β≈0°); (3) antithetic shear localisation starting at β≥90°, and (4) initial formation of antithetic shear localisation at high β, and subsequent development of synthetic shear localisation at low β, and.

4.1.1 Distributed shear bands

When α_0=0°, the easy, foliation parallel glide direction is on average parallel to the overall shear direction. This is close to the CPO that develops at very high finite shear strain when starting with a random CPO (de Riese et al. 2019). The α_0=0° CPO is therefore the most stable and we indeed observe much more homogenous deformation (Fig.3a, Fig.4a, Fig.5a) than for the other starting CPOs. Diffuse and small-scale localisation that is both parallel and perpendicular to the shear plane is observed (Fig. 3a) but does not lead to significant variability of the finite strain field. These minor shear bands may be related to the variability of the initial 5° noise in the CPO.

4.1.2 Synthetic shear bands

The simulation with α_0=33° results in a classical S-C structure with synthetic shear bands parallel to the shear plane (Fig.4b & Fig.5b, α_0=33°; Berthé et al., 1979; Lister and Snoke, 1984; Ramsay and Huber, 1987; Mandal et al., 2004; Passchier and Trouw, 2005). Clockwise rotation of the CPO from α_0=33° towards 0° softens the material. The shear bands thus experience geometrical softening and can increasingly accommodate a larger fraction of the total shearing. This reduces the shear strain in the low-strain zones in between, where the foliation remains at a distinct angle to the shear plane (Fig. 4b). As the synthetic, C-type shear bands at β_S=0° are in the orientation of both zero rotation and zero stretching, they are stable (Fig. 3b).

When α_0=73°, we also observe the formation of C-type shear bands, but only after some strain (γ>1). At this stage the foliation in the microlithons has rotated to α≤45°, which makes the material comparable to the initial α_0=33° simulation.

4.1.3 Antithetic shear bands

At high α_0 shear localises in antithetic, C''-type shear bands that form at low strain at angles β_A≥90°. The rotation rate is highest for lines and planes at a high angle to the shear plane and these antithetic shear bands thus show a rapid clockwise rotation towards the shear plane (Ponce et al., 2013). However, as the shear bands are antithetic, the foliation within the shear bands rotates anticlockwise relative to the shear bands. This is in contrast to synthetic shear bands, where both rotations are clockwise.

Localised shear bands form with β_A≈90° (Fig.6a), then rotate clockwise with progressive deformation to finally become approximately horizontal, synthetic shear bands (β_A→0°) (Ponce et al., 2013). This behaviour is illustrated in Fig. 6a. The solid orange line shows the rotation rate of a passive line that starts at β_A=90°, which is the maximum rotation rate. The dashed orange line shows the resolved shear stress τ_A. This is the shear stresss component of the overall stress field, here assumed to be with the maximum compressive stress at 45° to the shear plane. At first τ_A is negative (antithetic) and the layering is offset by an anticlockwise sense of shear. The shear bands quickly rotate to β_A=45° (at γ =1) when the resolved shear stress τ_A is zero and then changes sign. At this point the principal compressive stress is approximately perpendicular to the shear bands. In this stage, shear bands and the low-strain domains in between experience an approximately a pure shear environment with stretching for both. This is reflected by the thin and conjugate shear bands that are distributed within the low-strain domains (Fig.3c, γ=1 and γ=2). With continuing of rotation β becomes <45° and τ_A increases further but at a decreasing rate. This is because the rotation rate of the shear bands decreases with decreasing β. The sense of shear of the shear bands is now reverses to synthetic shearing.

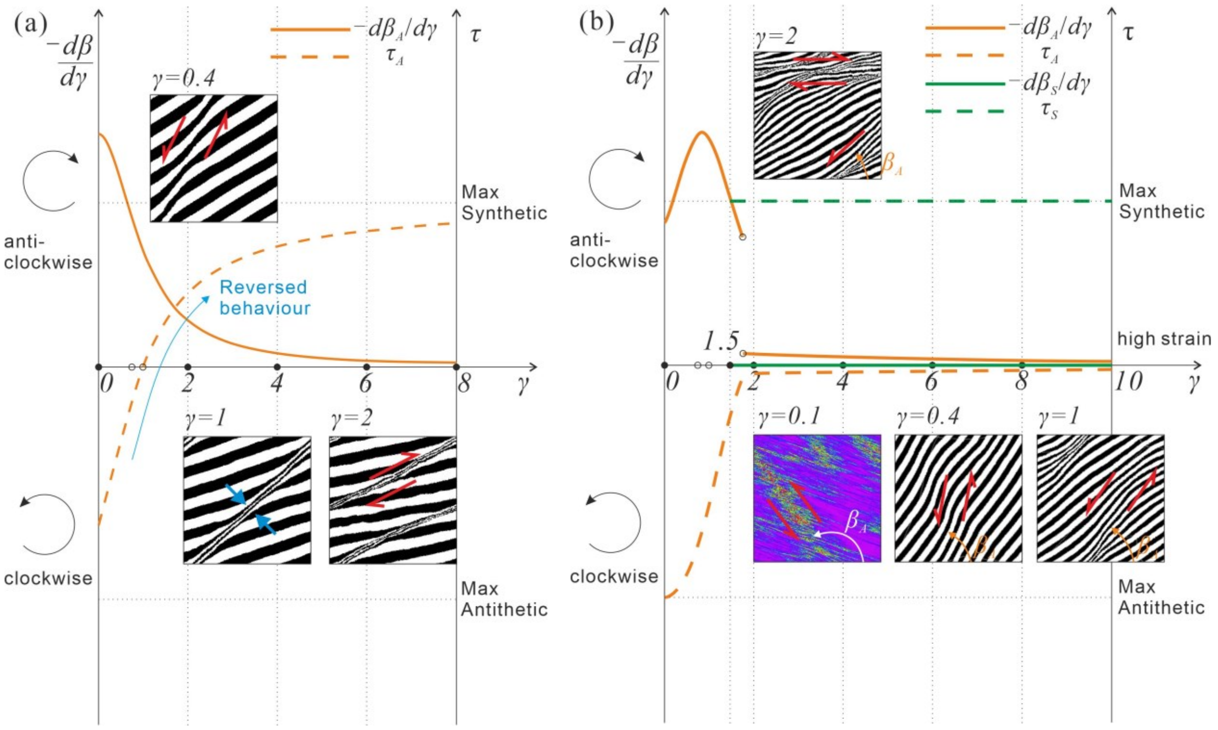

Fig.6 Rotation of localised bands divided by incremental strain ($-d\beta_A/d\gamma$) and shear stress component (τ) along the increasing strain, relative to the two types of shear bands that initial formation of antithetic shear localisation (Fig. 3. c & d, Fig. 4. c & d, Fig. 5. c & d). Note that we only discuss strain from 0 to 2 in this study. (a) α_0=45°, Initially antithetic shear localisation, then rotating and reversing to synthetic (orange lines), with decreasing rotation rate $-d\beta_A/d\gamma$ and variable shear stress τ_A of localised bands. Localised bands initially vertical to the shear plane, with maximum anticlockwise rotation rate and antithetic movement. When γ =0.4, continually rotating and antithetically moving, with decreasing rotating rate and shear stress. When γ =1 and now β_A=45°, only normal stress contributes to the localised bands with no shear stress component, so current τ_A=0. When γ >1, the opposite shear stress τ_A drives the localised bands move synthetically, then shear stress increases along the incremental strain. When the $-d\beta_A/d\gamma$ →0° and β_A →0°, the localised bands reach approximately maximum synthetic velocity. (b) α_0=73°, Initial formation of antithetic shear localisation with rotation (orange lines), and subsequent development of another synthetic shear localisation (green lines), with decreasing rotation rate $-d\beta_A/d\gamma$ and shear stress τ_A of antithetic localised bands and a new constant β_S=0° and τ_S of synthetic localised bands, simultaneously and respectively. Localised bands initially have an angel β_{A0}≈130° to the simple shear plane (normal *x*-axis), with increasing anticlockwise rotation rate $-d\beta_A/d\gamma$ (orange line) and approximately maximum antithetic shear stress (orange dash line). when γ =0.4, continually rotating and antithetically moving, with beginning of both rotating rate and shear stress decrease. When γ =1 and now β_A≈70°, continually rotating and antithetically moving, with rotating rate and shear stress decrease. When γ ≈1.5, β_A≈45°, only normal stress contributes to the antithetic localised bands with no shear stress (τ_A=0), meanwhile, system staring forming another synthetic localised bands with β_S=0° with no rotation (green lines) but maximum shear stress (green dash line), and most strain concentrate on the new localised bands. When γ >1.5, the former antithetic bands tend

to deactivate, the shear stress τ_S drives the localised bands move synthetically. The strain in former localised bands extinct with bands absence.

4.1.4 Initial antithetic shear bands and subsequent development of synthetic shear bands

The simulation with α_0=73° shows development of both antithetic (C'') and synthetic (C') shear bands as has also been observed in natural rocks (Marshak et al., 2006; Carreras et al., 2010, 2013; Ponce et al., 2013). The initially antithetic localised shear bands form with β_A≈130° at beginning. In this orientation τ_A is small, but negative and the sense of shear is antithetic (Fig. 6b). Rotation of the shear bands initially increases, while shear bands and low-strain domains in between shorten until β_A=90°. As a result, the angle between shear band and microlithon foliation increases during this stage. From β_A=90°, rotation rate and resolved shear stress both decrease and microlithons start stretching again. At γ ≈1.5, while activity of the shear bands at β_S>45° is still anticlockwise, the foliation inside the microlithons is already rotated to α>45°, i.e., a situation similar to the start of the α_0=33° simulation. As the antithetic shear bands become deactivated because resolved shear stress on the shear bands approaches zero, the CPO outside them in the microlithons becomes amenable to the development of synthetic, C-type shear bands parallel to the shear plane. This means that the rotation rate of the antithetic shear bands drops to close to zero and the resolved shear stress remains close to zero (Fig. 6b).

4.2 The resulting crenulation geometries

The simulation results provide instructive examples on how mechanical anisotropy redistributes the strain rate and rotation rate of high- and low-strain domains (Fig.3). The relationships between crenulation and shear band are not isolated parts but simultaneously form by strain redistribution. How materials behave to redistribute strain under a variety of conditions with an intrinsic anisotropy (CPO) is discussed above. These numerical simulations demonstrate that strain rate distribution depends on the orientation of the initial CPO relative to the shear plane (Fig.3). However, the visible passive marker layers may show different finite strain structures even for one and the same strain-rate field under simple shear (Figs. 4 & 5).

4.2.1 First foliation parallel to layering

Shearing parallel to layering (θ_0= α_0=0°) is very difficult to recognise as there are no offset marker lines. Strain localisation may be overlooked in such a situation.

Cases θ_0= α_0=33° or 45° result in almost identical geometries, but rotated and mirrored relative to the bulk sense of shear (the boundary condition). Both conform to the classical S-C geometry. Classical sense-of-shear analysis (Ramsay and Huber, 1987; Passchier and Trouw, 2005; Fossen, 2016) would result in opposite sense of shear: top to the right in case of θ_0= α_0=33° (Fig. 4b) and top-left moving down in case of θ_0= α_0=45° (Fig. 4c). This is because in both cases the angle λ between shear bands and microlithon layers is <45°. This angle is relatively constant in case of synthetic shear bands, because there is less flattening of the passive layers within microlithons. If bulk shear strain varies, little variation in angle λ is therefore expected if the shear bands are synthetic, while more variation is to be expected if they are antithetic, due to flattening of the rotating microlithons (Fig.4c, α_0=45°).

Case θ_0= α_0=73° is the most complex. After γ >1.5, the microlithons are sigma-clast or lozenge shaped, and surrounded by the four shear localisation bands, two synthetic bands above and below and two antithetic bands on either side (Marshak et al., 2006; Carreras et al., 2010, 2013; Ponce et al., 2013). Layering inside the low-strain microlithons pinches towards the tips of the domains and is subparallel to the antithetic shear bands (Fig.4d) (Marshak et al., 2006). The antithetic shear bands may thus be difficult to recognise. The structure could also be mistaken for a case with two deformation stages with different kinematics. The sigma-clast shape of the low-strain domains forms the only reliable indicator of the sense of shear, but only develops after a shear strain of γ≈1.5. At low strain the antithetic shear movement may be erroneously mistaken for top-right moving up shear if the shear bands are not recognised as C''-type bands. At γ≈1, just before the onset of synthetic shear-band activity, the structure suggests pure-shear SW-NE stretching with foliation boudinage (Platt and Vissers, 1980).

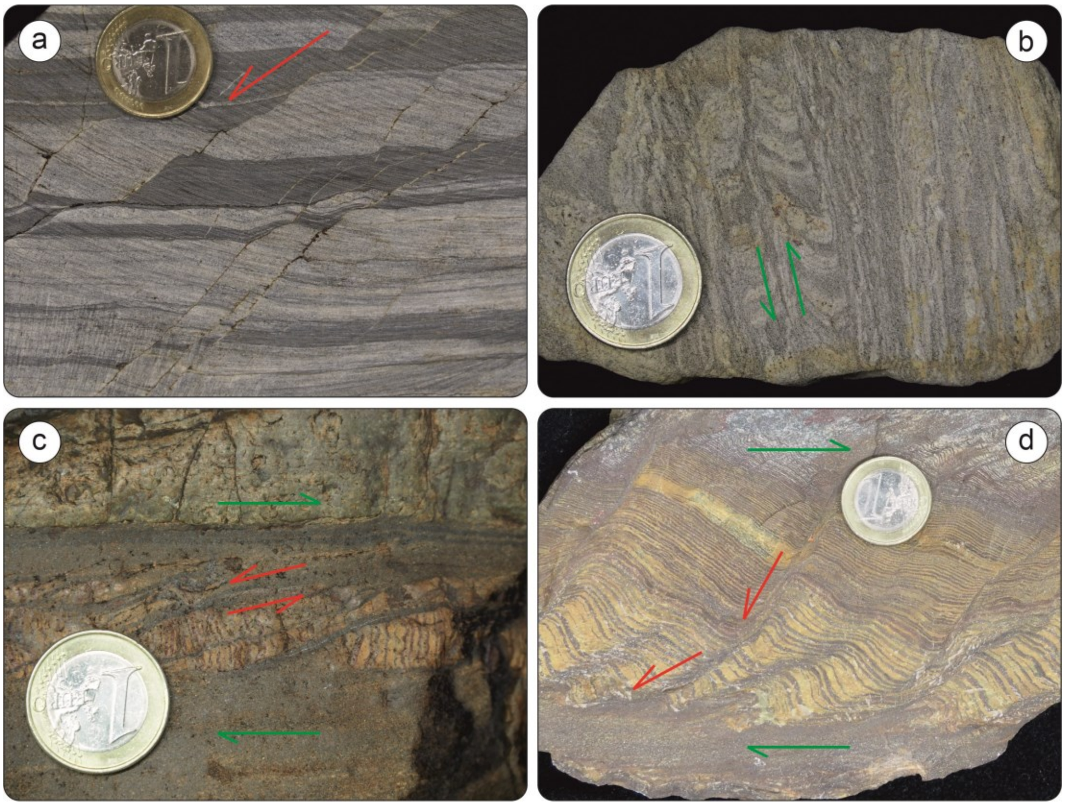

Fig.7 Natural examples, in correspond to the simulated results respectively. Green arrows are synthetic shearing, while red arrows are antithetic shearing. (a) Antithetic shear bands: This sample was first interpreted as faults with associated drag folds in brittle-ductile banded quartzite (at Cap de Creus, Spain) with the sense of shear that is top to the right by Gomez-Rivas et al. (2007). Even this sample is come from a brittle-ductile geological setting, we can assume the small-scale fractures as high-strain localised bands which have antithetic movement. (b) Synthetic bands with crenulation: High strain domains are subparallel to the shear plane, which is sinistral shear. No instinct antithetic shear localisation. The crenulation in low strain domains remain relatively parallel to each other. (c) Initial antithetic bands then form synthetic bands with crenulation: In this sample we observed two localised bands, the waved bands with crenulations show antithetic movement and low moving rate, which are obviously up to left, and the horizontal bands illustrate the synthetic shearing character. Crenulations in low strain domains remain relatively parallel to each other, but the crenulations about vertical to the shear bands. In our discussion in section 4.1.4, the surrounded crenulation domains are very controlled by the movement of antithetic shear bands with not only shearing but also rotating in stretching field, due to the geometry in this sample reserved well and not deformed much, which indicating the quick and property strain concentration shifting from antithetic to synthetic ones. (d) Initial antithetic bands then form synthetic bands with crenulation: On this sample we observed two localised bands, the (ironed) inclined bands with crenulations show antithetic movement, which are obviously up to left, and the horizontal bands illustrate the synthetic shearing character. The synthetic localised bands indicate real sense of shear.

4.2.2 Layering parallel to the shear plane

If layering is parallel to the shear bands, as in both α_0=0° and α_0=33°, shear localisation is almost completely masked, for lack of offset marker lines. No distinct geometries to be expected and shear localisation may not be detected.

The initial crenulations in the α_0=45° case are wave-like (Fig.5c, γ=0.4), or in α_0=73° resemble ripple marks (Fig.5d, γ=0.4). With increasing strain the offsets along the antithetic shear bands becomes distinct. Because of the rotation of the shear bands from their original steep orientation, the microlithons in between also rotate and get flattened. Because the initial angle between passive layers and initially formed shear bands is much greater than 45° the pattern is not consistent with a proper S-C structure. This may help to properly identify the shear band as antithetic or C''-type. Figure 8a may be an example of this geometry with C'' shear bands. Here Gomez-Rivas et al. (2007) could show that these structures formed in top-to-the-right simple shear because shear bands with decreasing angle with the visible layering showed increasing offset. However, flattening of the microlithons at a high angle to the internal visible layering may also lead to passive folding, making the structure look like trans-compression with a sinistral shear component. This structure is similar to the one shown in Fig. 7d from Cap de Creus, Spain. It should therefore be considered that it may have formed by dextral simple shear in which sinistral C''-type shear bands formed. As the microlithons rotate with the shear bands, this angle λ remains high (Tanner, 2016). Examples are the sheared banded iron formation samples (BIF, Fig.7 c & d). The antithetic shear bands are rotated together with the layering inside the microlithons. The overall sense of shear is clear from the layer parallel dextral shear bands that overprint the antithetic shears. Superposition of early antithetic and late synthetic shear band activity leads to complex patterns at case α_0=73°. In this case, the lozenge shape is masked and the structure at γ =2 could easily be interpreted as pure shear shortening at about 45° to the x-axis.

In summary, a first visible layering or foliation that is not parallel to the CPO shows that a wide range of structures can develop, even in only one event of perfect simple shear (Ez, 2000; Carreras et al., 2005). These structures may be ambiguous and very difficult to interpret (Tanner, 2016). We only provided one example of $\alpha_0 \neq \theta_0$. It is to be expected that other relative orientations of the visible layering may result in an even larger, and possibly confusing, range of structures. This will even be more so when pure or general shear and CPOs initially in the shortening field are considered.

5 Conclusions

We simulated the deformation of an anisotropic material in simple shear for different orientations of the anisotropy. We also considered the structures that develop in passive layers parallel to the anisotropy and parallel to the shear plane.

(1) The resulting crenulation geometries strongly depend on the orientation of the anisotropy (CPO), and we observe four types of localisation behaviour: (1) synthetic shear bands, (2) antithetic shear bands, (3) initial formation of antithetic shear bands and subsequent development of synthetic shear bands, and (4) distributed, approximately shear-margin parallel strain localisation.

(2) Synthetic shear bands are expected at an initial CPO orientation of ≤45°. Initial antithetic shear bands are expected at initial CPO orientation ≥45°. Antithetic shear bands become deactivated as they rotate towards the extensional field. Depending on the orientation of the CPO inside the microlithons, synthetic shear bands may also develop later and overprint the initial antithetic ones.

In addition to the classical interpretation of shear sense of S-C structures, we suggest two additional classes of localisation behaviour controlling the crenulation geometries which are (1) crenulation with no rotation of shear bands and (2) crenulation with rotation of the shear bands. When correctly recognised, these can also be used to determine the sense of shear.

(3) Layering in low-strain domains deforms contemporaneously with the strain localisation in the high-strain shear bands to form crenulations. Both synthetic and antithetic localised bands contribute to the formation of crenulations, but patterns can differ. Especially in case of antithetic shear bands that rotate and stretch, folds can develop inside the microlithons due to flattening of these low-strain domains.

(4) The visible microstructure depends strongly on the orientation of visible layers or foliations relative to the CPO. The same kinematic conditions, here simple shear, can thus lead to very different structures.

Reference

Adamuszek, M., Schmid, D.W., Dabrowski, M., (2011). Fold geometry toolbox – Automated determination of fold shape, shortening, and material properties. Journal of Structural Geology, Volume 33, 1406-1416. DOI: https://doi.org/10.1016/j.jsg.2011.06.003

Aslin, J., Mariani, E., Dawson, K., Barsoum M.W., (2019). Ripplocations provide a new mechanism for the deformation of phyllosilicates in the lithosphere. Nature Communication 10, 686. https://doi.org/10.1038/s41467-019-08587-2

Berthé, D., Choukroune, P., Jegouzo, P., (1979). Orthogneiss, mylonite and non coaxial deformation of granites: the example of the South Armorican Shear Zone. Journal of Structural Geology 1(1), 31-42. Doi: https://doi.org/10.1016/0191-8141(79)90019-1

Biot, M.A., (1957). Folding Instability of a Layered Viscoelastic Medium under Compression. Proceedings of the Royal Society A: Mathematical, Physical and Engineering Sciences, 242(1231), 444–454. DOI: 10.1098/rspa.1957.0187

Biot, M.A., (1961). Theory of folding of stratified viscoelastic media and its implications in tectonics and orogenesis. Geological Society of America Bulletin, v. 72, p. 1595-1620. DOI: 10.1130/0016-7606(1961)72[1595:TOFOSV]2.0.CO;2

Biot, M.A. (1964a). Theory of internal buckling of a confined multi-layered structure, Geological Society of America Bulletin, 75, 563–568. Doi: https://doi.org/10.1130/0016-7606(1964)75[563:TOIBOA]2.0.CO;2

Biot, M.A. (1964b). Theory of viscous buckling of multilayered fluids undergoing finite strain, Physics of Fluids 7, 855–861. Doi: https://doi.org/10.1063/1.1711296

Biot, M.A., (1965a). Further Development of the Theory of Internal Buckling of Multilayers. Geological Society of America Bulletin, 76 (7): 833–840. DOI: 10.1130/0016-7606(1965)76[833:FDOTTO]2.0.CO;2

Biot, M.A., (1965b). Theory of similar folding of first and second kind, Geological Society of America Bulletin, 76, 251–258. Doi: https://doi.org/10.1130/0016-7606(1965)76[251:TOSFOT]2.0.CO;2

Bons, P.D, Koehn, D, Jessell, M.W (Eds) (2008) Microdynamic Simulation. Lecture Notes in Earth Sciences 106, Springer, Berlin. 405 pp. ISBN 978-3-540-44793-1

Bons, P.D., Jansen, D., Mundel, F., Bauer, C.C., Binder, T., Eisen, O., Jessell, M.W., Llorens, M.G., Steinbach, F., Steinhage, D., Weikusat, I., (2016). Converging flow and anisotropy cause large-scale folding in Greenland's ice sheet. Nature Communication. 7, 11427 (2016). https://doi.org/10.1038/ncomms11427

Braun, J., Chery, J., Poliakov, A., Mainprice, D., Vauchez, A., Tommasi, A., Daignieres, M., (1999). A simple parameterization of strain localization in the ductile regime due to grain size reduction: a case study for olivine. Journal of Geophysical Research, 104, 25,167–25,181. https://doi.org/10.1029/1999JB900214

Brun, J.P., Cobbold, P.R., (1980). Strain heating and thermal softening in continental shear zones: a review. Journal of Structural Geology. Vol 2: 149-158. https://doi.org/10.1016/0191-8141(80)90045-0

Carreras, J., (2001). Zooming on Northern Cap de Creus shear zones. JSG, 23(9), 1457–1486. doi: https://doi.org/10.1016/s0191-8141(01)00011-6

Carreras, J., Druguet, E., Griera, A., (2005). Shear zone-related folds. Journal of Structural Geology, 27(7), 1229–1251. Doi: https://doi.org/10.1016/j.jsg.2004.08.004

Carreras, J., Czeck, D.M., Druguet, E., Hudleston, P.J. (2010). Structure and development of an anastomosing network of ductile shear zones. Journal of Structural Geology, 32(5), 656–666. doi: https://doi.org/10.1016/j.jsg.2010.03.013

Carreras, J., Cosgrove, J.W., Druguet, E., (2013). Strain partitioning in banded and/or anisotropic rocks: Implications for inferring tectonic regimes. Journal of Structural Geology, 50, 7–21. doi: https://doi.org/10.1016/j.jsg.2012.12.003

Carreras, J., Druguet, E., (2019). Complex fold patterns developed by progressive deformation. Journal of Structural Geology. Vol 125: 195-201. https://doi.org/doi:10.1016/j.jsg.2018.07.015

Carter, N.L. and Tsenn, M.C., (1987). Flow properties of continental lithosphere. Tectonophysics 136, 27-63. DOI: https://doi.org/10.1016/0040-1951(87)90333-7

Casey, M., Huggenberger, P., (1985). Numerical modelling of finite-amplitude similar folds developing under general deformation histories. Journal of Structural Geology, 7(1), 103–114. doi: https://doi.org/10.1016/0191-8141(85)90118-x

Cobbold, P.R., Cosgrove, J.W., Summers, J.M., (1971). Development of internal structures in deformed anisotropic rocks. Tectonophysics, 12: 23-53. DOI: 10.1016/0040-1951(71)90065-5

Cobbold, P.R., (1975). Fold propagation in single embedded layers. Tectonophysics 27 (4), 333–351. DOI: https://doi.org/10.1016/0040-1951(75)90003-7

Cosgrove, J.W., (1976). The formation of crenulation cleavage. Journal of the Geological Society, 132(2), 155–178. doi: https://doi.org/10.1144/gsjgs.132.2.0155

Cosgrove, J.W., (1989). Cleavage, folding and the finite strain ellipsoid. Proceedings of the Geologists Association, 100(4), 461–479. doi: https://doi.org/10.1016/s0016-7878(89)80022-7

Dabrowski, M., Schmid, D. W., Podladchikov, Y. Y. (2012). A two-phase composite in simple shear: Effective mechanical anisotropy development and localization potential. Journal of Geophysical Research, 117(B8), B08406. doi: https://doi.org/10.1029/2012jb009183

de Bresser, J.H.P., ter Heege, J.H., Spiers, C.J., (2001). Grain size reduction by dynamic recrystallization: can it result in major rheological weakening? International Journal of Earth Sciences volume 90, pages28–45. Doi: https://doi.org/10.1007/s005310000149

de Riese, T., Evans, L., Gomez-Rivas, E., Griera, A., Lebensohn, R.A., Llorens, M.-G., Ran, H., Sachau, T., Weikusat, I., Bons, P.D. (2019). Shear localisation in anisotropic, non-linear viscous materials that develop a CPO: A numerical study. J. Struct. Geol. 124, 81-90. DOI: https://doi.org/10.1016/j.jsg.2019.03.006

Dubey, A.K., Cobbold, P.R. (1977). Noncylindrical flexural slip folds in nature and experiment. Tectonophysics, 38(3-4), 223–239. doi: https://doi.org/10.1016/0040-1951(77)90212-8

Ez, V., (2000), When shearing is a cause of folding: Earth-Science Reviews, v. 51, p. 155–172, doi: https://doi.org/10.1016/S0012-8252(00)00020-9

Finch, M.A., Bons, P.D., Steinbach, F., Griera, A., Llorens, M.-G., Gomez-Rivas, E., Ran, H., de Riese, T., (2020). The ephemeral development of C′ shear bands: A numerical modelling approach, Journal of Structural Geology, DOI: https://doi.org/10.1016/j.jsg.2020.104091

Finch, M.A., Bons, P.D., Weinberg, R.F., Llorens, M.G., Griera, A., Gomez-Rivas, E., (2022). A dynamic atlas of interference patterns in superimposed, opposite sense ductile shear zones, Journal of Structural Geology, 165, 104739, doi: https://doi.org/10.1016/j.jsg.2022.104739

Fossen, H., (2016). Structural Geology (second edition). Cambridge University Press (Publisher), 978-1-316-47427-3 (ISBN)

Frehner, M., Schmalholz, S. M. (2006). Numerical simulations of parasitic folding in multilayers. Journal of Structural Geology, 28(9), 1647–1657. doi: https://doi.org/10.1016/j.jsg.2006.05.008

Gardner, R., Piazolo, S., Lynn, E., Nathan, D., (2017). Patterns of strain localization in heterogeneous, polycrystalline rocks – a numerical perspective. Earth and Planetary Science Letters, 463, 253–265. doi: https://doi.org/10.1016/j.epsl.2017.01.039

Ghosh, S.K., (1966). Experimental tests of buckling folds in relation to strain ellipsoid in simple shear deformations. Tectonophysics, 3, 169–185. DOI: https://doi.org/10.1016/0040-1951(66)90001-1

Gomez-Rivas, E., Bons, P.D., Griera, A., Carreras, J., Druguet, E., Evans, L., (2007). Strain and vorticity analysis using small-scale faults and associated drag folds. jsg, 29(12), 1882–1899. doi: https://doi.org/10.1016/j.jsg.2007.09.001

Gomez-Rivas, E., Griera, A., Llorens, M.-G., Bons, P.D., Lebensohn, R.A., Piazolo, S., (2017). Subgrain rotation recrystallization during shearing: Insights from full-field numerical simulations of halite polycrystals. J. Geophys. Res. Solid Earth. Doi: 10.1002/2017JB014508.

Gray, D.R., (1979). Geometry of crenulation-folds and their relationship to crenulation cleavage. Journal of Structural Geology, 1(3), 187–205. DOI:10.1016/0191-8141(79)90039-7

Griera, A., Bons, P.D., Jessell, M.W., Lebensohn, R.A., Evans, L., Gomez-Rivas, E., (2011). Strain localization and porphyroclast rotation. Geology, 39(3), 275–278. doi: https://doi.org/10.1130/G31549.1

Griera, A., Llorens, M.-G., Gomez-Rivas, E., Bons, P. D., Jessell, M. W., Evans, L. A., Lebensohn, R., (2013). Numerical modelling of porphyroclast and porphyroblast rotation in anisotropic rocks. Tectonophysics, 587, 4–29. DOI: 10.1016/j.tecto.2012.10.008

Hirth, G., Tullis, J., (1992). Dislocation creep regimes in quartz aggregates. Journal of Structural Geology. 14, 145–159. Doi: https://doi.org/10.1016/0191-8141(92)90053-Y

Hobbs, B.E., Mülhaus, H.B., Ord, A., (1990). Instability, softening and localization of deformation. Geological Society London Special Publications 54(1):143-165. DOI: https://doi.org/10.1144/GSL.SP.1990.054.01.15

Hudleston, P.J., (1986). Extracting information from folds in rocks. Journal of Geological Education 34, 237-245. Doi: https://doi.org/10.5408/0022-1368-34.4.237

Hudleston, P.J., Lan, L., (1993). Information from fold shapes. Journal of Structural Geology . 15, 253–264. https://doi.org/10.1016/0191-8141(93)90124-S

Hudleston, P.J., Lan L., (1994). Rheological controls on the shapes of single-layer folds. Journal of Structural Geology, 16(7), 1007–1021. doi: https://doi.org/10.1016/0191-8141(94)90082-5

Hudleston, P.J., Treagus, S.H., (2010). Information from folds: a review. Journal of Structural Geology. 32(12), 2042–2071. DOI: 10.1016/j.jsg.2010.08.011

Jansen, D., Llorens, M.-G., Westhoff, J., Steinbach, F., Kipfstuhl, S., Bons, P. D., Griera, A., and Weikusat, I. (2016): Small-scale disturbances in the stratigraphy of the NEEM ice core: observations and numerical model simulations, The Cryosphere, 10, 359–370, https://doi.org/10.5194/tc-10-359-2016

Kronenberg, A. K., Kirby, S. H., Pinkston J., (1990). Basal slip and mechanical anisotropy of biotite. Journal of Geophysical research Solid Earth, 95, 19257-19278. DOI: https://doi.org/10.1029/JB095iB12p19257

Lebensohn, R.A., (2001). N-site modeling of a 3D viscoplastic polycrystal using Fast Fourier Transform. Acta Materialia, 49, 2723-2737. Doi: 10.1016/S1359-6454(01)00172-0

Lebensohn, R.A., Brenner, R., Castelnau, O., Rollett, A. D. (2008). Orientation image-based micromechanical modelling of subgrain texture evolution in polycrystalline copper. Acta Materialia, 56, 3914-3926. Doi: 10.1016/j.actamat.2008.04.016

Lebensohn, R.A., Rollett, A.D. (2020). Spectral methods for full-field micromechanical modelling of polycrystalline materials. Computational Materials Science, 173, 109336. Doi: 10.1016/j.commatsci.2019.109336

Leysinger Vieli, G.J.-M. C., Hindmarsh, R.C.A., Siegert, M.J., Bo, S., (2011). Time-dependence of the spatial pattern of accumulation rate in East Antarctica deduced from isochronic radar layers using a 3-D numerical ice flow model. Journal of Geophysical Research, 116(F2), F02018. doi: https://doi.org/10.1029/2010jf001785

Lister, G.S. Snoke, A.W. (1984). S-C mylonites. Journal of Structural Geology. 6, 617-638. Doi: https://doi.org/10.1016/0191-8141(84)90001-4

Llorens, M.-G., Bons, P. D., Griera, A., Gomez-Rivas, E. (2013a). When do folds unfold during progressive shear? GEOLOGY, May 2013, v. 41, no. 5, p. 563–566. DOI:10.1130/G33973.1

Llorens, M.-G., Bons, P. D., Griera, A., Gomez-Rivas, E., Evans, L. A. (2013b). Single layer folding in simple shear. Journal of Structural Geology 50, 209-220. DOI: 10.1016/j.jsg.2012.04.002

Llorens, M.-G., Griera, A., Steinbach, F., Bons, P.D., Gomez-Rivas, E., Jansen, D., Roessiger, J., Lebensohn, R.A., Weikusat, I. (2017). Dynamic recrystallization during deformation of polycrystalline ice: insights from numerical simulations. Philosophical Transactions of the Royal Society A: Mathematical, Physical and Engineering Sciences, 375, 20150346. https://doi.org/10.1098/rsta.2015.0346

Mancktelow, N.S., (1999). Finite-element modelling of single-layer folding in elastoviscous materials; the effect of initial perturbation geometry. Journal of Structural Geology 21, 161-177. DOI: https://doi.org/10.1016/S0191-8141(98)00102-3

Mandal, N., Samanta, S.K., Chakraborty, C., (2004). Problem of folding in ductile shear zones: a theoretical and experimental investigation. Journal of Structural Geology, 26(3), 475–489. doi: https://doi.org/10.1016/j.jsg.2003.07.004

Manz, R., Wickham, J., (1978). Experimental analysis of folding in simple shear. Tectonophysics 44, 79–90. DOI: https://doi.org/10.1016/0040-1951(78)90064-1

Mares V. M., Kronenberg A. K., (1993). Experimental deformation of muscovite. Journal of Structural Geology. Volume 15, Issues 9–10, September–October 1993, Pages 1061-1075. DOI: 10.1016/0191-8141(93)90156-5

Marshak, S., Alkmim, F.F., Whittington, A., Pedrosa-Soares A.C., (2006). Extensional collapse in the Neoproterozoic Araçuaí orogen, eastern Brazil: a setting for reactivation of asymmetric crenulation cleavage, Journal of Structural Geology 28 (2006) 129–147. Doi: https://doi.org/10.1016/j.jsg.2005.09.006

Montési, L.G.J., (2013). Fabric development as the key for forming ductile shear zones and enabling plate tectonics. Journal of Structural Geology, 254–266. https://doi.org/10.1016/j.jsg.2012.12.011

Naus-Thijssen, F.M.J., Johnson, S.E., Koons, P.O. (2010). Numerical modeling of crenulation cleavage development: A polymineralic approach. Journal of Structural Geology, 32(3), 330–341. DOI: https://doi.org/10.1016/j.jsg.2010.01.004

Naus-Thijssen, F.M.J., Goupee, A.J., Johnson, S.E., Vel, S.S., Gerbi, C., (2011). The influence of crenulation cleavage development on the bulk elastic and seismic properties of phyllosilicate-rich rocks. Earth and Planetary Science Letters, 311(3-4), 212–224. DOI: https://doi.org/10.1016/j.epsl.2011.08.048

Passchier, C.W., Trouw, R.A., (2005). Microtectonics. Springer Science & Business Media.

Piazolo, S, Bons, P.D., Griera, A., Llorens, M.-G., Gomez-Rivas, E., Koehn, D., Wheeler, J., Gardner, R., J.R.A. Godinho, J.R.A., Evans, L., Lebensohn, R.A., Jessell, M.W. (2019). A review of numerical modelling of the dynamics of microstructural development in rocks and ice: Past, present and future. J. Struct. Geol. 125, 111-123. DOI: https://doi.org/10.1016/j.jsg.2018.05.025

Platt, J.P., Vissers, R.L.M. (1980). Extensional structures in anisotropic rocks. Journal of Structural Geology, 2(4), 397–410. doi: https://doi.org/10.1016/0191-8141(80)90002-4

Platt, J.P., Behr, W.M., (2011). Grainsize evolution in ductile shear zones: implications for strain localization and the strength of the lithosphere. Journal of Structural Geology. 33, 537–550 doi: https://doi.org/10.1016/j.jsg.2011.01.018

Ponce, C., Druguet, E., Carreras, J. (2013). Development of shear zone-related lozenges in foliated rocks. Journal of Structural Geology, 50, 176–186. doi: https://doi.org/10.1016/j.jsg.2012.04.001

Ramberg, H., (1961). Relationship between concentric longitudinal strain and concentric shearing strain during folding of homogeneous sheets of rocks. American Journal of Science May 1961, 259 (5) 382-390, DOI: https://doi.org/10.2475/ajs.259.5.382

Ramsay, J.G., (1974). Development of Chevron Folds. Geological Society of America Bulletin, 85(11), 1741. doi: https://doi.org/10.1130/0016-7606(1974)85<1741:docf>2.0.co;2

Ramsay, J.G., (1980). Shear zone geometry: A review. Journal of Structural Geology, 2(1-2), 83–99. DOI: https://doi.org/10.1016/0191-8141(80)90038-3

Ramsay, J.G. Huber, M.I., (1987). The Techniques of Modern Structural Geology. Volume 2: Folds and Fractures. Academic Press.

Ran, H., Bons, P.D., Wang, G., Steinbach, F., Finch, M., Griera, A., Gomez-Rivas, E Llorens, M.-G., Ran, S., Liang, X., Zhou, J., (2018). High-strain deformation of conglomerates: Numerical modelling, strain analysis, and an example from the Wutai Mountains, North China Craton. Journal of Structural Geology, Volume 114, September 2018, Pages 222-234. doi: https://doi.org/10.1016/j.jsg.2018.06.018

Ran, H., de Riese, T., Llorens, M.-G., Finch, M.A., Evans, L.A., Gomez-Rivas, E., Griera, A., Jessell, M.W., Lebensohn, R.A., Piazolo, S., Bons, P.D., (2019). Time for anisotropy: The significance of mechanical anisotropy for the development of deformation structures. J. Struct. Geol. 125, 41-47. DOI: https://doi.org/10.1016/j.jsg.2018.04.019

Ran, H., Bons, P.D., Wang, G., Griera, A., de Riese, T., Gomez-Rivas, E., Llorens, M.-G., Ran, S., Wang, Y., Wang, S., (2022). Folds inside pebbles: When do they form during conglomerate deformation? Numerical modelling and comparison with the Hutuo Group conglomerates, North China Craton. Journal of Structural Geology, Volume 160, July 2022, Article number 104620. Doi: https://doi.org/10.1016/j.jsg.2022.104620

Rickard, M.J. (1961). A Note on Cleavages in Crenulated Rocks. Geological Magazine, 98(04), 324 - 332. doi: https://doi.org/10.1017/s0016756800060659

Schmalholz, S.M., Podladchikov, Y.Y., (1999). Buckling versus folding: Importance of viscoelasticity. Geophysical Research Letters, 26(17), 2641–2644. doi: https://doi.org/10.1029/1999gl900412

Schmalholz, S.M., (2006). Scaled amplification equation: A key to the folding history of buckled viscous single-layers. Tectonophysics, 419(1-4), 0–53. doi: https://doi.org/10.1016/j.tecto.2006.03.008

Schmalholz. S. M., Mancktelow. N.S., (2016): Folding and necking across the scales: a review of theoretical and experimental results and their applications. Solid Earth, 7, 1417–1465, 2016. DOI: 10.5194/se-7-1417-2016

Schmid, D.W., Podlachikov, Y.Y. (2006): Fold amplification rates and dominant wavelength selection in multilayer stacks, Philos. Mag., 86, 3409–3423. Doi: https://doi.org/10.1080/14786430500380175

Shea Jr., W.T., Kronenberg, A.K., (1993). Strength and anisotropy of foliated rocks with varied mica contents. Journal of Structural Geology. Volume 15, Issues 9–10, September–October 1993, Pages 1097-1121. https://doi.org/10.1016/0191-8141(93)90158-7

Steinbach, F., Bons, P.D., Griera, A., Jansen, D., Llorens, M.-G., Roessiger, J., Weikusat, I. (2016): Strain localization and dynamic recrystallization in the ice–air aggregate: a numerical study, The Cryosphere, 10, 3071–3089, https://doi.org/10.5194/tc-10-3071-2016

Tanner, G.P.W., (2016). A new model for the formation of a spaced crenulation (shear band) cleavage in the Dalradian rocks of the Tay Nappe, SW Highlands, Scotland. Journal of Structural Geology, 84, 120–141. doi: https://doi.org/10.1016/j.jsg.2015.11.007

Torvela, T., Kurhila, M., (2020). How does orogenic crust deform? Evidence of crustal-scalecompetent behaviour within the partially molten middle crust during orogenic compression, Precambrian Research, DOI: https://doi.org/10.1016/j.precamres.2020.105670

Tullis, J., Yund, R.A., (1985). Dynamic recrystallization of feldspar: a mechanism for ductile shear zone formation. Geology (1985), 13 (4): 238–241. https://doi.org/10.1130/0091-7613(1985)13<238:DROFAM>2.0.CO;2

Warren, J.M., Hirth, G., (2006). Grain size sensitive deformation mechanisms in naturally deformed peridotites. Earth and Planetary Science Letters. 248, 438–450. Doi: https://doi.org/10.1016/j.epsl.2006.06.006

Westhoff, J., Stoll, N., Franke, S., Weikusat, I., Bons, P., Kerch, J., Jansen, D., Kipfstuhl, S., Dahl-Jensen, D. (2021). A stratigraphy-based method for reconstructing ice core orientation. Annals of Glaciology 62, 191-202. Doi:10.1017/aog.2020.76.

White, S.H., Burrows, S.E., Carreras, J., Shaw, N.D., Humphreys, F.J., (1980). On mylonites in ductile shear zones. Journal of Structural Geology, 175–187. Doi: https://doi.org/10.1016/0191-8141(80)90048-6

Williams P.F., Price G.P. (1990). Origin of kinkbands and shear-band cleavage in shear zones: an experimental study. JSG 12(2), 145–164. doi: https://doi.org/10.1016/0191-8141(90)90001-f

Wolovick, M.J., Creyts, T.T., Buck, W.R., Bell, R.E., (2014). Traveling slippery patches produce thickness-scale folds in ice sheets. Geophysical Research Letters, 41, 8895–8901, doi: https://doi.org/10.1002/2014GL062248

PAPER I

PAPER II

Folding of a single layer in an anisotropic viscous matrix under layer-parallel shortening

Yuan-bang Hu[1,2], Paul D. Bons[1], Tamara de Riese[1], Shu-gen Liu[2,3,4], Maria-Gema Llorens[5], Xue-lin Cai[2] (Preliminary author list; Only edited by YH and PDB now)

[1] *Department of Geosciences, Eberhard Karls Universität Tübingen, Tübingen, Germany.*

[2] *College of Earth Science, Chengdu University of Technology, Chengdu, China.*

[3] *State Key Laboratory of Oil and Gas Reservoir Geology and Exploitation, Chengdu University of Technology, Chengdu, China*

[4] *Xihua University, Chengdu, China*

[5] *Geosciences Barcelona (GEO3BCN-CSIC), Barcelona, Spain.*

Abstract

Folds are common structures in deformed rocks and give information on kinematics, stress, strain, rheological properties, etc. While Biot's thin plate folding theory applies to isotropic materials, rocks can have cleavages and foliations that make them intrinsically anisotropic in their rheology. We here consider the effect of a mechanical anisotropy due to a foliated viscous matrix, for example by the of alignment of micas. Mechanical anisotropy can enhance shear localisation, resulting in low-strain microlithon domains and localised high-strain shear domains. We investigate the evolving fold geometries, stress field and strain-rate field differences and redistributions resulting from layer-parallel shortening deformation of an isotropic, competent layer embedded in an anisotropic, incompetent matrix, systematically varying the initial mechanical anisotropy and other rheological properties of the weak viscous matrix by using the Viscoplastic Fast-Fourier Transform code coupled with the modelling platform ELLE. The simulated results illustrate that localisation behaviour, and hence fold geometry, depends on (i) the initial orientation of the anisotropy (here is the initial crystallographic preferred orientation, CPO), (ii) the intensity of anisotropy, and (iii) the viscous property of materials. Variation in localisation behaviour that results from different strain-rate distributions lead to two end-member geometries, ranging from (1) buckle folding and thickening of the layer, while the matrix forms a new axial-plane crenulation cleavage, to (2) layer extensional folding with great amplification of amplitude while matrix form conjugate, localised bands with lenticular areas. Other geometries are in between. Classical buckle folds dominate at initial CPO parallel or subparallel to shortening direction, while extensional folds dominate when initial CPO normal or subnormal to shortening direction.

Keywords: Fold geometries, Layer-parallel pure shear, Anisotropy, Crystallographic preferred orientation, Strain-rate redistribution, Extensional folding.

1 Introduction

Folds are common structures in deformed rocks that can give information on strain, rheology, kinematics, material properties, deformation histories, etc. (Hudleston, 1986; Ramsay and Huber, 1987; Hudleston and Lan, 1993; Passchier and Trouw, 2005; Hudleston and Treagus, 2010; Bobillo-Ares et al., 2004; Adamuszek et al., 2011; Llorens et al., 2013a, 2013b; Schmalholz and Mancktelow, 2016; Llorens, 2019b; Nabavi and Fossen, 2021). Much of this information stems from developments in fold theory and simulations over the last several decades, beginning with the work of Biot (1957, 1961, 1964a, b, 1965a, b), who developed the basic theories for single- and multi-layer folding in elastic-viscous medias and between viscous medias. According to this theory, folds initiate from tiny instabilities or perturbations in the folding layer or layers (e.g., Ramberg, 1962; Ghosh, 1966; Sherwin and Chapple, 1968; Fletcher, 1974; Smith, 1977; Abbassi and Mancktelow, 1992; Griera et al., 2018) and follow an exponential growth (Biot, 1961; Johnson and Fletcher, 1994). Note that we here use the term 'layer' for any initially planar, sheet-like rock body, which can be a sedimentary layer, but also a mineral vein or an igneous dyke or sill.

Layers become folded because of the amplification of these perturbations during layer-parallel shortening of competent (strong) layers and surrounding incompetent (weak) layers or a matrix. Biot's theory predicts that if the layer is given small sinusoidal perturbations of different wavelengths, one such perturbation will amplify at a greater rate than all others. This leads to folds with a dominant wavelength (λ_d). For a single competent layer of thickness h and with linear viscosity μ_L that is embedded in a less competent matrix with viscosity μ_M, λ_d is expected to be (Biot, 1957, 1961; Ramberg, 1962; Nabavi and Fossen, 2021):

$$\frac{\lambda_d}{h} = 2\pi\left(\frac{\mu_L}{6\,\mu_M}\right)^{1/3} \qquad (1)$$

As a result, the length scale or wavelength of folds increases with thickness of the folding layer and with the viscosity contrast between layer and matrix. This basic rule remains when other factors are taken into account, such as elastic properties (Biot, 1961; Currie et al., 1962), multi-layers (Biot, 1964a, b, 1965a, b; de Riese, 2014), slip along layer-interfaces (Ramberg, 1961, Griera et al., 2018), or non-linear viscosity (Bayly, 1970). Reviews of the different equations for the dominant wavelength can be found in Hudleston and Treagus (2010) and Schmalholz and Mancktelow (2016), Adamuszek et al. (2011) using these equations in Fold Geometry Toolbox. Ductile rocks are usually assumed to have a power-law rheology (e.g., Carter and Tsenn, 1987).

Multilayers consist of alternating competent and incompetent layers, with parameters such as (i) layer thickness, spacing and distributions, (ii) rheological properties, and (iii) boundary conditions (Ramberg, 1963; Ramsay and Huber, 1987; Johnson and Pfaff, 1989; Price and Cosgrove, 1990; Johnson and Fletcher, 1994; Schmid and Podlachikov, 2006; de Riese, 2014;). Because multilayer folding is depends on many more parameters, we in this study first focus on single-layer folding.

Power-law rheology of the folding rock both enhances the growth rate and decreases the dominant wavelength compared to linear behaviour (Fletcher, 1974; Smith, 1977; Fletcher, 1995; Mühlhaus et al., 1998; Kaus and Schmalholz, 2006; Kocher et al., 2006, 2008; Schmalholz and Schmid, 2012). The analysis of natural folds can thus be used to get an indication of the rheology of the folding layer(s) (Llorens et al., 2013b).

Another important rock property that affects folding is anisotropy. Minerals are generally mechanically anisotropic when they deform by dislocation creep (Linker et al., 1984). In case of micas, this anisotropy is very strong as shearing parallel to their basal plane is much easier than deformation in any other direction (Kronenberg et al., 1990; Mares and Kronenberg, 1993; Shea and Kronenberg, 1993; Fan and El-Awady, 2015; Aslin et al., 2019; Finch et al., 2020).

A rock as a whole can become anisotropic when crystallographic orientations align in a crystallographic preferred orientation (CPO). Tectonic foliations or cleavages are often formed by the alignment of micas so that tectonically foliated rocks can be expected to be anisotropic. Anisotropy has been recognised as an important factor in the formation of geological structures and a cause for strain localisation (Cobbold et al., 1971; Ramsay, 1980; Lan and Hudleston, 1995; Passchier and Trouw. 2005; Kocher et al., 2006, 2008; Naus-Thijssen, et al., 2011; Griera et al., 2013; Bordignon et al., 2015; Steinbach et al., 2016; Gardner et al., 2017; Ran et al., 2019; de Riese et al., 2019; Torvela and Kurhila, 2020).

Many fold structures that are observed in the field are in foliated rocks. For example (quartz) veins can form a competent layer embedded in an anisotropic matrix with an arbitrary angle between the layer and the anisotropy. The effect of anisotropy on folding must therefore be considered (Kocher et al, 2006; Ran et al., 2019). Mechanical anisotropy can enhance shear localisation (Ran, et al., 2018; de Riese et al., 2019), resulting in low-strain domains and high-strain domains. If strain localisation occurs in the matrix of a layer folds can be expected to form.

Numerical simulations have been applied to investigate how and by what mechanisms structures that we observe in nature form. These simulations complement field studies (e.g., Quinquis et al., 1978; Ramsay and Huber, 1987; Ormand and Hudleston, 2003; Alsop and Carreras, 2007; Alsop and Holdsworth, 2007; Mukherjee, 2014; Torremans et al., 2014; Pérez-Alonso et al., 2016) and analogue experiments (e.g., Hudleston, 1973; Cobbold, 1975; Manz and Wickham, 1978; Abbassi and Mancktelow, 1992; Bons and Urai, 1996; Tikoff and Peterson, 1998), numerical simulations have been applied to investigate how and by what mechanisms structures that we observe in nature form.

Numerical studies of single-layer folds have included the effects of non-linear rheology (Parrish, 1973; Lan and Hudleston, 1991; Mancktelow, 1999; Schmalholz and Podladchikov, 2000; Kocher et al., 2006; Llorens et al., 2013a, 2013b), anisotropy (Lan and Hudleston, 1996; Kocher et al., 2006; Ran et al. 2019), and viscoelastic behaviour (Zhang et al., 1996; Mancktelow, 1999; Schmalholz et al., 2001). Numerical simulations of folding in a rock with an anisotropic rheology are few (e.g., Kocher et al. 2008; Ran et al., 2019). What has not yet been investigated is how the orientation of a mechanical anisotropy due to an CPO (as in a cleavage in a micaceous rock) relative to the shortening direction affects the developing folds in a competent planar structure, such as a layer, vein or dyke.

In this numerical study we systematically investigate the controlling parameters on fold geometries of a single layer in a power-law rheology, anisotropic matrix under layer-parallel shortening. For this purpose, we vary (i) the orientation of the initial anisotropy (α_0), (ii) the intensity of the anisotropy of the matrix (A_M), (iii) rheological contrast between competent layer and its surrounding matrix (R_η), and (iv) the power-law exponent of the viscous matrix (n).

Table.1 Frequently used symbols presented in this study.

Symbol	Meaning
α	Angle of crystallographic preferred orientation (CPO, orientation of basal plane), we assume a horizontal crystallographic basal plane is α = 0° to the *x*-axis, a rotation in anticlockwise of the plane is positive value. The orientation of the initial anisotropy is α_0.
β	Orientation of localised band, we assume a horizontal band is β = 0° to the x-axis, a rotation in anticlockwise of the plane is a positive value.
τ	The shear component of stress σ.
ε	Value of strain, we discuss the strain from 0.0 - ~3.0 in this paper.
$\dot{\varepsilon}$	Strain rate
σ	Total stress
λ	Wavelength is twice the distance between two inflection points
L	Arclength is determined along the interface as the length of the competent layer. The initial length is 2.0
H	Thickness of competent layer
Amp	Classical definition amplitude of fold structure
Amp_{max}	Measured as the vertical distance between the highest point and the lowest point in our simulation
A	Intensity of anisotropy, controlled by the intrinsically mechanical properties of minerals and materials, we use A_M and A_L which represent the intensity of anisotropic matrix and competent layer, respectively. If A = 1 means an isotropic material.
μ	Reference viscosity of material, influenced by the material property and environment parameters, We use μ_M and μ_L which represent the intensity of anisotropic matrix and competent layer, respectively
R	Viscosity ratio, viscosity of competent layer verse viscosity of matrix ($\tau^{(layer)}$/ $\tau^{(non-basal,matrix)}$).
n	Power-law stress exponent (n), controlled by the intrinsically mechanical properties of minerals and materials

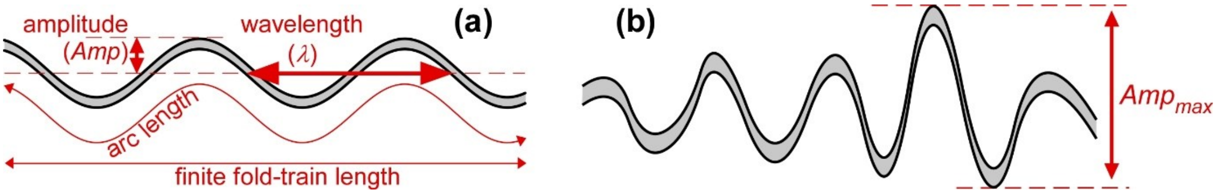

Fig.1 Fold parameters for describing the fold geometries, corresponding to the Table.1.

2 Method

2.1 Numerical simulation

The numerical simulations in this study are carried out with the Viscoplastic Fast Fourier Transform (VPFFT, Lebensohn, 2001; Lebensohn et al., 2008; Lebensohn and Rollett, 2020) crystal plasticity code, which is a full-field model, coupled with the modelling platform Elle (http://www.elle.ws; Bons et al., 2008; Griera et al., 2011, 2013; Llorens et al., 2016; Steinbach et al., 2016; Llorens et al., 2017; Piazolo et al., 2019; Ran et al., 2019, 2022; de Riese et al., 2019, Llorens et al., 2019a; Finch et al., 2020, 2022) to investigate the fold geometries and strain-fields resulting from pure shear, layer-parallel shortening (up to 75%) of an isotropic competent layer surrounded by a weaker matrix with an intrinsic mechanical anisotropy.

The 2D models consist of a rectangular grid of so-called *undoes* (Bons et al., 2008). The *unodes* effectively represent crystallites with a constant internal-crystal orientation, defined by three Euler angles. The simulations are run at a resolution of 256 * 256 *unodes*. The initial model size is 0.5 in the vertical (*y*) direction, and 2 in the horizontal (*x*) direction. Each simulation starts with a horizontal competent and isotropic layer embedded in a less-competent anisotropic matrix. The initial layer is eight *unodes* wide, corresponding to a width of 1/32.

The FFT-code assumes that deformation is achieved by slip along crystallographic lattice planes. The strain rate $\dot{\varepsilon}_{ij}(x)$ at a *unode* position (*x*) is the sum of the shear strain rates ($\dot{\gamma}_s$) on the *N* available individual lattice planes (*s*). with $m^s_{ij}(x)$ the symmetric Schmid tensor, this can be expressed as:

$$\dot{\varepsilon}_{ij}(x) = \sum_{s=1}^{N_S} m^s_{ij}(x)\dot{\gamma}_s(x) \qquad (2)$$

The shear strain rate parallel to a slip direction is a power-law function of the shear stress (σ_s) acting on that plane in the direction of slip:

$$\dot{\gamma}_s = \dot{\gamma}_0 \left(\frac{\sigma_s}{\tau_s}\right)^n \qquad (3)$$

Here $\dot{\gamma}_0$ is a reference shear rate that is set to unity for all slip systems in the model materials. The stress exponent *n* is set to three or four in this study. Differences in rheology between layer and matrix, and as a function of direction in case of the mechanically anisotropic matrix are set through the slip system-dependent critical resolved shear stress or shear-resistance parameter τ_s.

We use the hexagonal crystal lattice of ice 1h as an analogue for anisotropic minerals, such as mica (as in Griera et al. 2013; Ran et al., 2019; de Riese et al., 2019). Deformation assumed to be accommodated by slipping the basal, prismatic and pyramidal slip systems only. The intensity of anisotropy (A) is defined by the ratio of the shear resistance of the non-basal and basal slip systems:

$$A = \frac{\tau_s{}^{(non-basal)}}{\tau_s{}^{(basal)}} \tag{4}$$

For the layer we use A = 1, which makes the material is effectively isotropic (Griera et al, 2013. If $A \neq$ 1, the material is anisotropic. Here we use A = 64 and A = 16, which simulates a highly or moderately anisotropic matrix with an approximately transverse isotropy, in which shear deformation along the basal plane is much easier than along non-basal planes.

In all starting models, basal planes of all *unodes* are oriented at an angle α_0 ($\pm 10°$ standard deviation) to the horizontal shortening direction. We refer to these aligned basal planes as the *foliation*. We present simulation for α_0 = 0°, 11.25°, 22.5°, 33.75°, 45°, 56.25°, 67.5°, 78.75° and 90°, with anticlockwise rotation taken as positive.

We apply velocity boundary conditions where the velocities along the boundaries on average comply with 2% horizontal shortening and 2% vertical stretching per time step. The model is fully wrapping, meaning that a material point that moves out of the rectangular model on one side, comes into the model at the opposite side.

Results are presented in the form of maps of the von Mises strain rate field and of model with passively deformed grid lines that are initially parallel to the foliation. As the boundary of Elle simulations is infinite, the results can be repeated to their surroundings infinitely, which has been introduced by e.g., Finch et al., 2020. The von Mises strain rate ($\dot{\varepsilon}_{vm}$) and von Mises stress (σ_{vm}) is defined as:

$$\dot{\varepsilon}_{vm} = \sqrt{\frac{2}{3}\,\dot{\varepsilon}_{ij}\,\dot{\varepsilon}_{ij}} \tag{5}$$

and

$$\sigma_{vm} = \sqrt{\frac{3}{2}\,\sigma'_{ij}\,\sigma'_{ij}} \tag{6}$$

where $\dot{\varepsilon}_{ij}$ is the strain-rate tensor, σ'_{ij} is the stress tensor, and *i* and *j* summation indices.

2.2 Fold geometry analysis

Fold geometry can be described with a number of parameters (Ramsay and Huber 1987, Adamuszek et al. (2011). The folding layer has a thickness (H) and a length that can be measured as the distance (L) of a straight line that connects the beginning and end of the fold train, or as the arclength (L'), which is the length measured along the fold train. In the models, both equal the original layer length L_0 = 2. The normalised arclength is the arclength divided by the original length (L'/L_0). When a layer does not fold, but only thickens to accommodate the shortening, L'/L_0 decreases steadily. When it does not thicken but only folds, L' remains equal to L_0. The different length parameters are determined with a C-script that measures this for a passive marker line in the middle of the competent layer, deformed according to the velocity field that is calculated by the FFT-routine.

Amplitude (Amp') is measured as half the distance, normal to the fold train direction, between two inflection points at the extremities of the fold. Wavelength (λ) is twice the distance between two inflection points (Ramsay and Huber, 1987). When folds are irregular, the determination of these parameters is not trivial. For a few example cases we therefore used the Fold Geometry Toolbox (FGT) of Adamuszek et al. (2011) and the update by Adamuszek (2022). In all other cases we used the maximum amplitude (A_{max}), which we define as the difference between the maximum and minimum height of the fold line, measured in the vertical direction of extension.

3 Results

3.1 Series I: non-linear viscous, highly anisotropic intensity, high viscosity ratio deformation simulations

Simulations of series I (Fig.2.a & Fig.3.a) have a starting configuration of a single layer in the matrix, which has a stress exponent of n = 3, an intensity of anisotropy (A_M) is 64, and a viscosity ratio (R_η) of 125. The initial foliation orientation or CPO (α_0) of the matrix ranges between α_0 = +0° and α_0 = +90° with respect to the x-axis (Table 2). Deformation is layer-parallel pure shear up to 75% of shortening. The resulting folds and matrix-foliation patterns are shown in Fig. 2.a for 50% shortening and in Fig. 3.a for ~70% shortening. These figures show that the folding in the strong layer changes significantly as a function of the foliation orientation α_0. One also sees that this is accompanied by different patterns in the matrix foliation.

The Amp_{max}-curves (Fig. 4.a) show that all layers hardly fold the first 10% of shortening. For case I-1 (α_0 = 0°) to I-4 (α_0 = 33.75°), Amp_{max} smoothly increases to 75% shortening percentage, as small-wavelength folds develop and the competent layers keeps thickening. At α_0 = 0° a regular and symmetric axial-planar crenulation cleavage develops in the anisotropic matrix. Up to α_0 = 33.75° folds in the competent layer look qualitatively similar but become increasingly oblique and irregular with increasing α_0. An increasing asymmetry is also observed in the crenulation cleavage that develops in the matrix. In addition we observe small oblique zones of strain localisation in the matrix at α_0 = 22.5°, and especially at α_0 = 33.75°. A dramatic change in fold pattern is observed for α_0 ≥45°. Case I-5 (α_0 = 45°) and case I-6 (α_0 = 56.25°) have a similar increase rate of Amp_{max} as case I-4 (α_0 = 33.75°) in the early stage on their folding, but the amplitude then increases much faster from 45% and 25% shortening, respectively. After initial layer thickening, the rapid amplification of the folds leads to extension and thinning of the layer. The anisotropic matrix does not form small-scale crenulations, but instead shows a general reorientation of the foliation and the development of localised shear bands. Case I-7 (α_0 = 67.5°), case I-8 (α_0 = 78.75°) and case I-9 (α_0 = 90°) have an initially faster increase of their fold amplitude, accompanied by the layer thinning throughout the deformation. Competent layers in these cases deform into folds with stretched limbs and large amplitudes. The foliation in the matrix is reorientated and develops obvious strain localisation in shear bands that enclose lenticular low-strain areas.

Wavelengths of folds in the different simulations vary strongly. For the cases that have an initial orientation of CPO α_0 ≤ 22.5°, competent layers deform as classical buckling folds, and the

Table 2 Simulation setup. In all simulations the strong layer is isotropic (A_L=1). All simulations are run to a maximum shortening of 75%.

Series name	Simulation name	Initial CPO orientation (α_0)	Initial viscosity ratio (μ_L/μ_M)	Intensity of matrix's anisotropy (A_M)	Stress exponent (n)
I	I-1	0°	125	64	3
	I-2	11.25°	125	64	3
	I-3	22.5°	125	64	3
	I-4	33.75°	125	64	3
	I-5	45°	125	64	3
	I-6	56.25°	125	64	3
	I-7	67.5°	125	64	3
	I-8	78.75°	125	64	3
	I-9	90°	125	64	3
II	II-1	0°	125	16	3
	II-2	11.25°	125	16	3
	II-3	22.5°	125	16	3
	II-4	33.75°	125	16	3
	II-5	45°	125	16	3
	II-6	56.25°	125	16	3
	II-7	67.5°	125	16	3
	II-8	78.75°	125	16	3
	II-9	90°	125	16	3
III	III-1	0°	125	16	4
	III-2	11.25°	125	16	4
	III-3	22.5°	125	16	4
	III-4	33.75°	125	16	4
	III-5	45°	125	16	4
	III-6	56.25°	125	16	4
	III-7	67.5°	125	16	4
	III-8	78.75°	125	16	4
	III-9	90°	125	16	4
IV	IV-1	0°	66.7	64	3
	IV-2	11.25°	66.7	64	3
	IV-3	22.5°	66.7	64	3
	IV-4	33.75°	66.7	64	3
	IV-5	45°	66.7	64	3
	IV-6	56.25°	66.7	64	3
	IV-7	67.5°	66.7	64	3
	IV-8	78.75°	66.7	64	3
	IV-9	90°	66.7	64	3

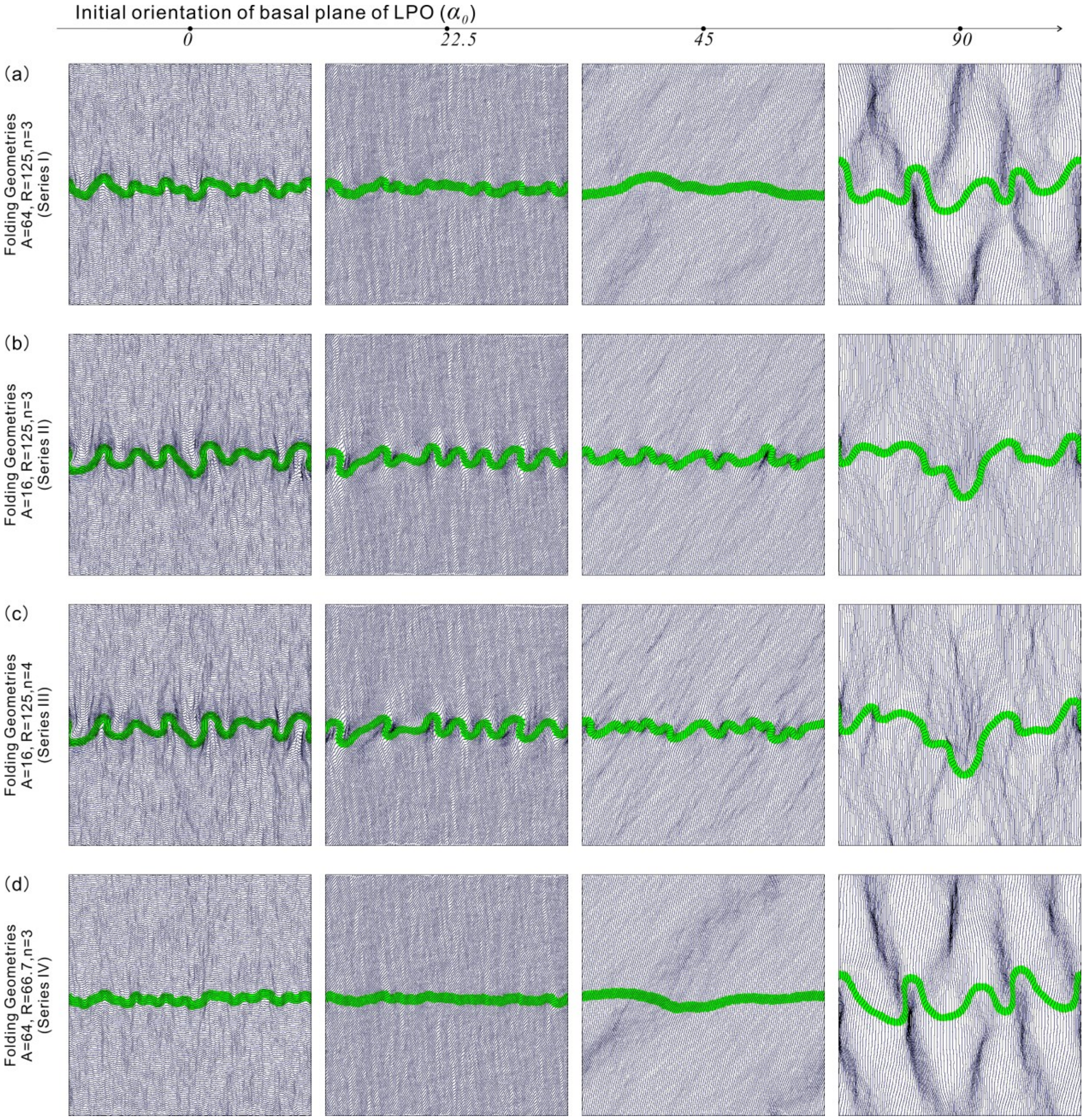

Fig.2: Cases with structural geometries of Series **I** (a), **II** (b), **III** (c), **IV** (d) with α_0 = 0°, 22.5°, 45°, 90° at the 50% shortening percentage (step 069). The controlling parameter of structural geometries is obviously the CPO, both the intensity and orientation. Anisotropy of matrix is A = 64 (a, d) could make the glide system benefit the basal plane sliding in both layer-parallel shortening and layer-vertical extending, these make competent layers deform either thicken layer or buckle folds in different scales. Matrix with low anisotropy A = 16 (b, c) lead to a more classical buckle folding geometry. The viscosity ratio also has influence on structural geometries while anisotropy in low value.

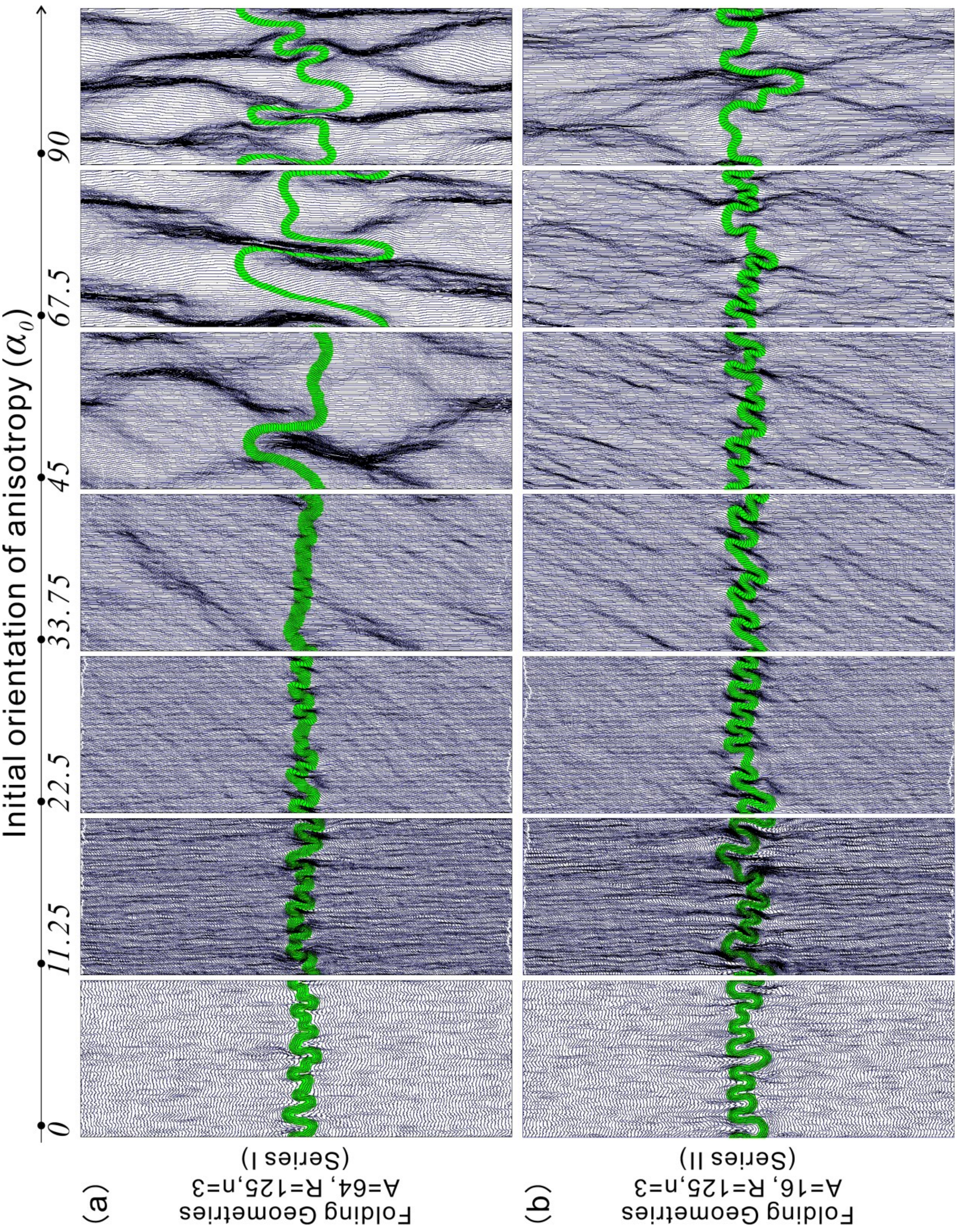

Fig.3: (a-d) Structural geometries of different intensity of anisotropy of matrix verse different initial orientation of anisotropy of Series I, II, III and IV at almost 70% shortening (step 120).

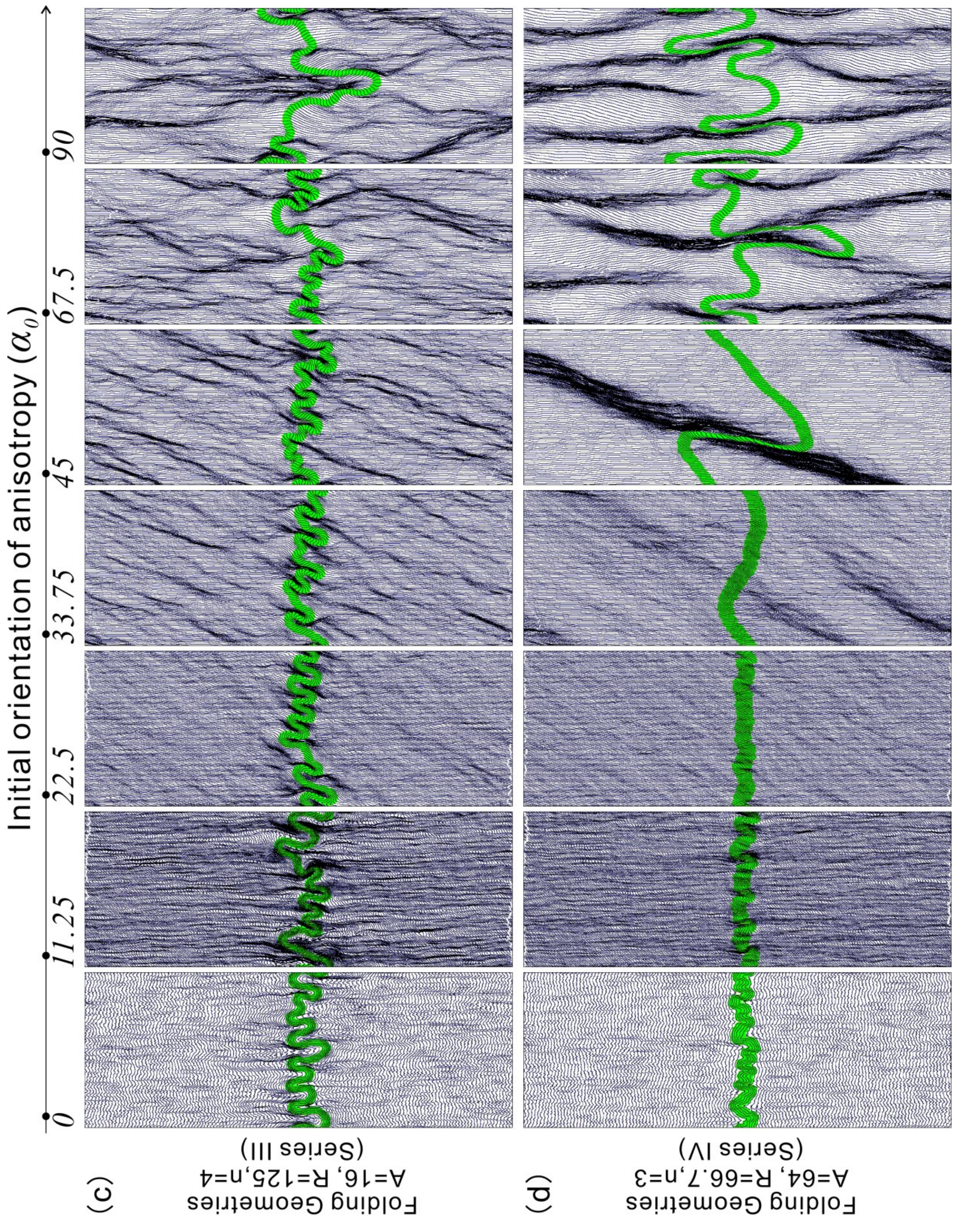

Fig.3 continue: (a-d) Structural geometries of different intensity of anisotropy of matrix verse different initial orientation of anisotropy of Series I, II, III and IV at almost 70% shortening (step 120).

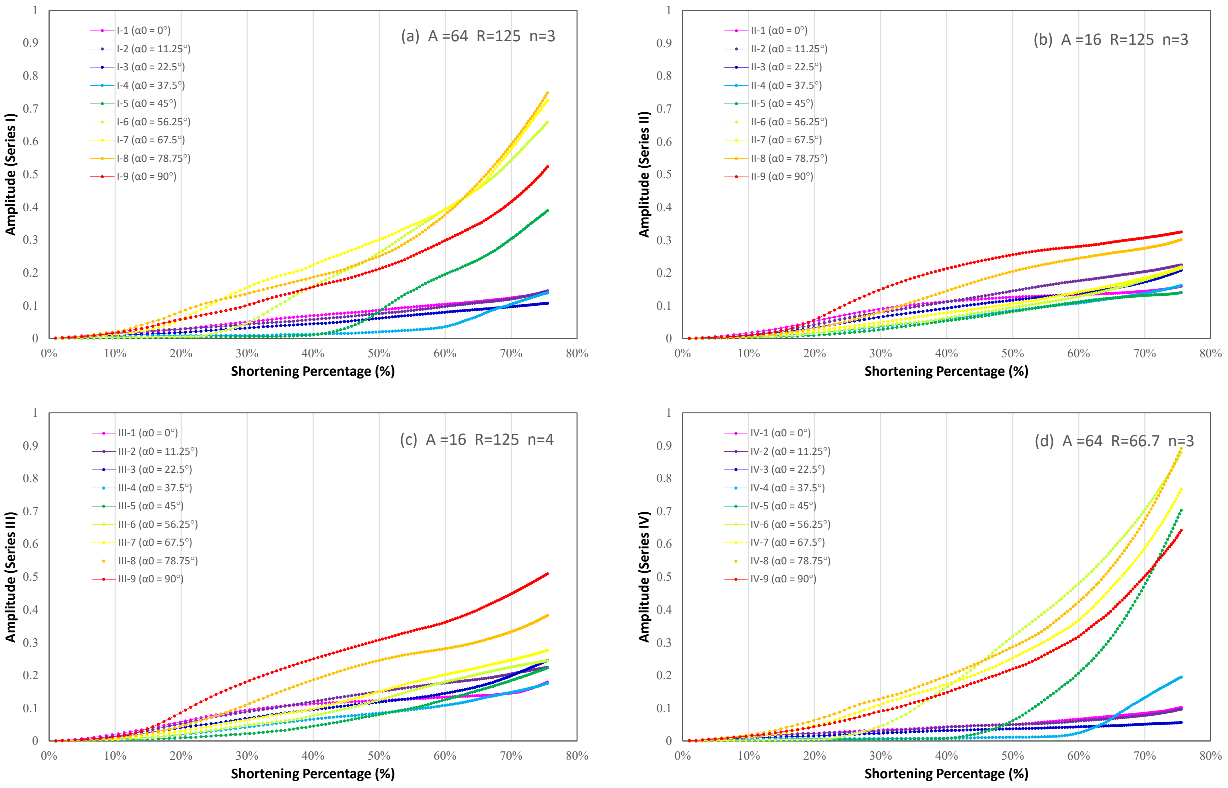

Fig.4: The vertical distance between the highest point and the lowest point (Amp_{max}) along the layer-parallel shortening, which here we use this distance as the amplitudes of deformed competent layers in our simulations. Figures are amplitude verse shortening percentage, shown the variation of amplitudes, maximal amplitude, amplification rate (the slope) for series **I** (a), **II** (b), **III** (c) and **IV** (d) from initial state to 75% shortening percentage. One could easily find out big differences in variation in amplitudes between the cases have an initial orientation of CPO are less than 45°, or greater than 45°, or equal 45°, while these cases have the same tendency of vary at the point of shortening percentage with the figures of von Mises stress and of slip system activities.

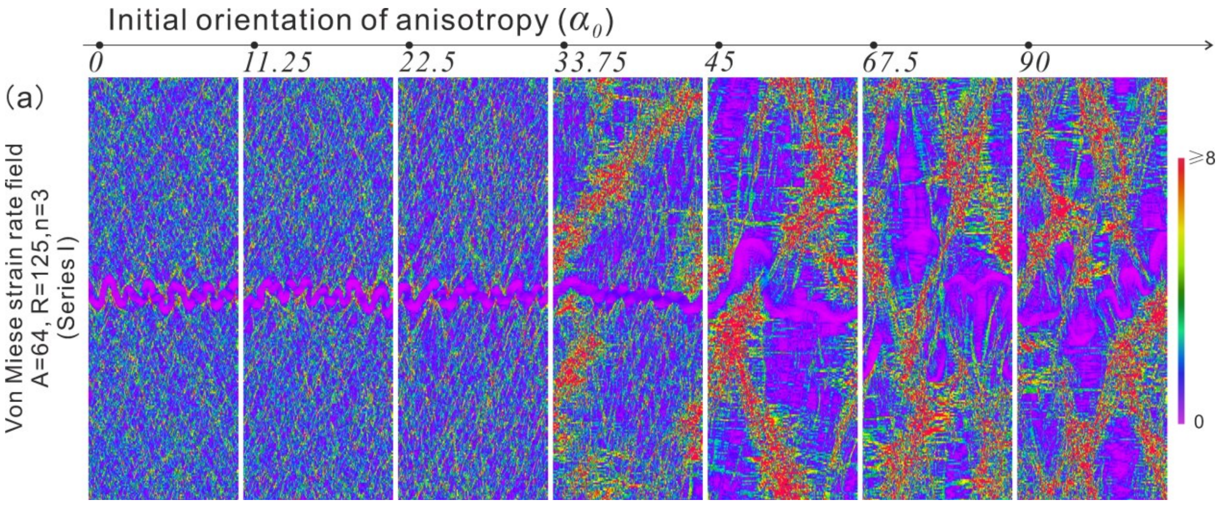

Fig.5: von Mises strain rate field of series I simulation at ~ 70% shortening (step 120). The competent layers always stay at low strain rate, while the matrix always has a spectrum of strain rates. For the low α_0 cases that have no obvious high strain domains, strain rate is distributed over the whole matrix. For the high α_0 cases that have distinct high strain domains, the strain rate is concentring related to the axial planes of the folds.

ratio between wavelength and thickness is moderate. However, the cases that have an initial foliation orientation of $\alpha_0 \geq 45°$, both the fold wavelengths and amplitudes increase dramatically, resulting in a much large ratio of wavelength and thickness. As a result their arclengths are also much larger than for low α_0. (Fig.7).

The difference in behaviour between low and high α_0 is also distinctly visible in the distribution of von Mises strain rates (Fig. 5). $\alpha_0 \leqslant 22.5°$ shows no distinct localisation in the matrix and highest strain rates rarely exceed four times the average. This changes for $\alpha_0 \geq 33.75°$ where large-scale shear bands develop with strain rates that exceed eight times the average strain rate. Except for $\alpha_0=33.75°$, the high strain domains for a conjugate set.

3.2 Series II: non-linear viscous, moderately anisotropic intensity, high viscosity ratio deformation simulations

Simulations of series II (Fig.2.b & Fig.3.b) have a starting configuration of a single layer in the matrix, which has a stress exponent (n) is 3, an intensity of the anisotropy (A_M) is 16, the viscosity ratio (R_η) is 125. The initial foliation orientation or CPO (α_0) of the matrix again ranges between α_0 = +0° and α_0 = +90° with respect to the x-axis (Table 2), and it is again deformed in layer-parallel pure shear up to 75% of shortening. The only difference with series I is thus the lower anisotropy, which also affects the viscosity ratio.

The competent layer folds and thickens in all cases. The anisotropic matrix forms axial-planar crenulation cleavages related to the folded competent layer in case of low α_0. These crenulations become increasingly asymmetric with increasing α_0. Whereas deformation in both layer and matrix is quite similar in series I and II for $\alpha_0 \leq 22.5°$, the deformation patterns become distinct at higher α_0. Although shear localisation in shear bands does develop in series two at high α_0, it is far less pronounced. There are more shear bands that envelope diffuse lenticular low strain domains. Fold amplitudes (Fig.4.b) and wavelengths are therefore much smaller than in series I, especially for $45° \leq \alpha_0 \leq 67.5°$.

3.3 Series III: higher non-linear viscous deformation simulations

Simulation series III (Fig.2.c & Fig.3.c) has identical setting to series II, except that the stress exponent (n) is set to four instead of three. The matrix rheology with n = 4 is thus similar to that of ice 1h (Bons, et al., 2018).

Resulting deformation patterns (Fig.2.c & Fig.3.c) are very similar to those of series II. Main differences are that fold amplitudes (Fig.4.c) are slightly larger than series II, especially at high α_0, and that strain localisation in the matric is more distinct, but still diffuse as in series II and not as strong as in series I.

3.4 Series IV: non-linear viscous, highly anisotropic intensity, moderate viscosity ratio deformation simulations

The settings for simulation series IV (Fig.2.d & Fig.3.d) are identical to those of series I (n = 3, A_M = 64), except for the viscosity ratio that is halved to R_η = 66.7.

With the decreased viscosity ratio, the competent layer in the low-α_0 cases IV-1 to IV-4 tends to thicken more than cases I-1 to I-4. Deformation of the anisotropic matrix is very similar to that of series I. From case IV-5 to IV-9 (α_0 = 45° to 90°) the competent layer large folds with even larger amplitudes than in series I form, which reflected by the Amp_{max}-trends of series IV (Fig.4.d). Wide strain-localisation zones form in matrix that shear and extend the competent layer to form the irregular folds in that layer. The general behaviour at high-α_0 is comparable with that of series I, but the effects of shear localisation appear more intense.

4 Information from fold geometries

4.1 Folding analysis by FGT

The Fold Geometries Toolbox (FGT, Adamuszek, et al, 2011, updated by Adamuszek, 2022) allows to analyse folds according to a range of fold models from the literature (e.g., Biot, 1961, 1965c; Currie, et. al., 1962; Fletcher, 1974, 1977; Sherwin and Chapple, 1968). The basic idea of the FGT is acquiring useful parameters, such as for example viscosity ratio between layer and matrix, by analysing the fold geometries. The test its applicability to folding in an anisotropic matrix, we applied the FGT to two basic setting, α_0= 0° and α_0= 90° of series I, to estimate the viscosity ratio between competent layer and surrounding less-competent matrix.

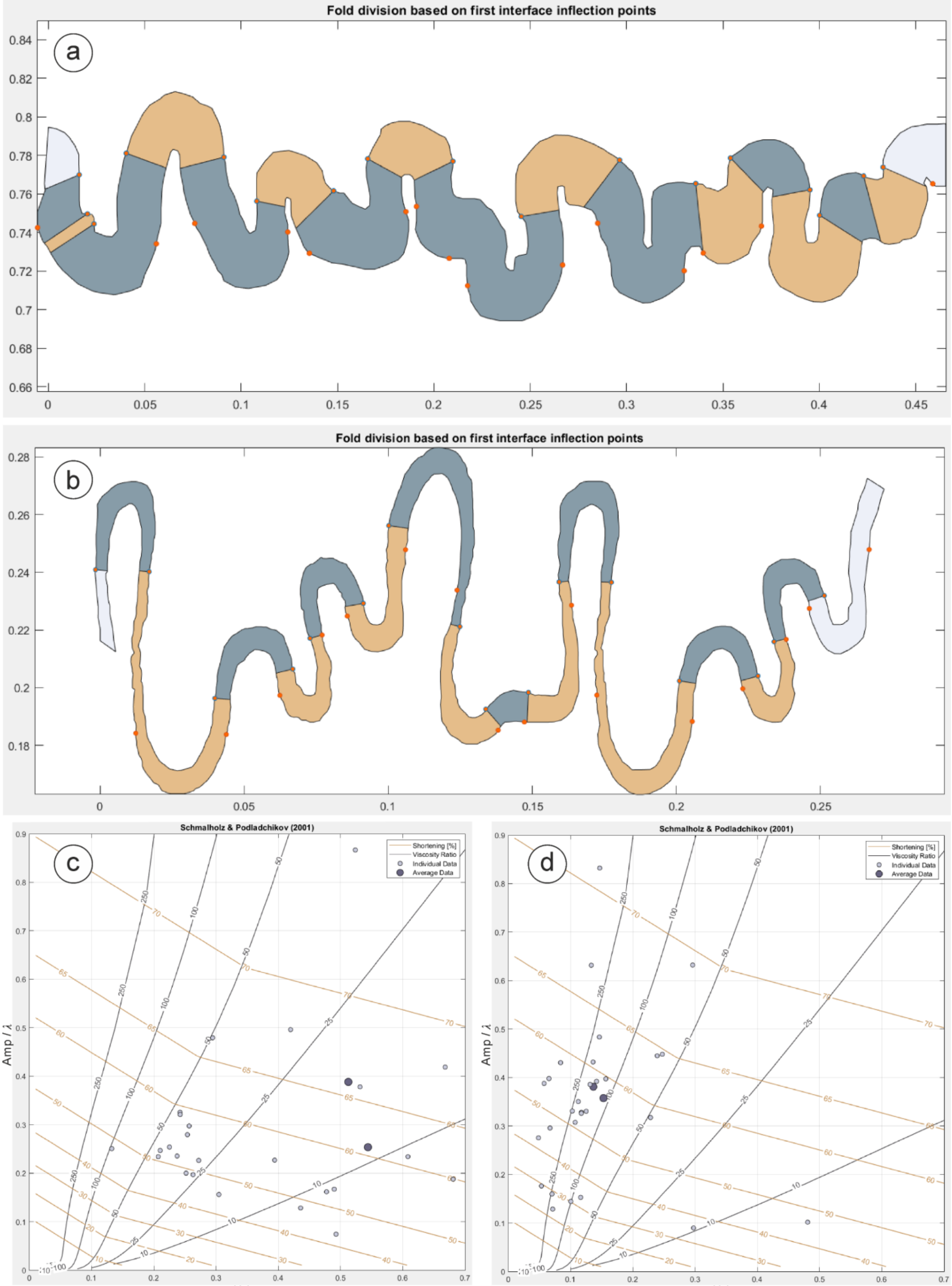

Fig.6 The position of hinges and inflection points determined by FGT about case I-1 (a, α_0 = 0°) and I-9 (b, α_0 = 90°) of fold geometries in series I, the grey and yellow areas represent the antiform structure and synform structure of the folds. Plot of data by analysing of fold shapes of case I-1 (c, α_0 = 0°) and I-9 (d, α_0 = 90°) with the equations by Schmalholz and Podladchikov (2001), Amp is amplitude, λ is

dominate wavelength, H is the thickness of competent layer, the orange lines show the amount of shortening in per cents, while the black lines are the variable viscosity ratio between layer and matrix. Light grey dots are the individual data for every single antiformal and synform structure of fold train. The black dots are the average data of all antiformal and synform structures of (a) and (b) taken separately.

Figure 6.a-b shows the two end-member fold trains at 70% shortening, divided into antiforms and synforms. We see that each of these is different in shape within one fold train. It is also not always trivial to determine the inflexion points, as can be seen in the middle of each fold train. We chose to plot the amplitude/wavelength ratio (Amp/λ) against the thickness/wavelength ratio (H/λ) to obtain the apparent viscosity ratio and finite strain according to Schmalholz and Podladchikov (2001) (Fig. 6.c-d).

In both examples the data of individual antiforms and synforms show a very large spread, as can be expected from the highly variable shape of individual folds in the simulations. Most individual data underestimate the total strain, as do the averages of all antiforms and synforms, especially for α_0=90° (Fig. 6.d). The viscosity ratio between the competent layer and the soft direction in the matrix was set to 125~~.~~ For α_0 = 0°, individual folds give apparent viscosity ratios up to about 50, while for α_0 = 90° the ratios vary from <10 to >>250. The analysis would thus tend to underestimate the true viscosity ratio, although it should be clear that in case of anisotropy no such single ratio exists.

4.2 Variation of arclengths along the competent layers

The arclength which is used to identify the layer states of our simulated competent layers. Here we use the normalised arclength (L_{norm} = arclength divided by original length) of competent layer to study whether it is in compressional or extensional situation at any shortening percentage. In case of no folding, but only thickening of the layer, L_{norm}, as a function of shortening strain, steady decreases according to the finite shortening down to 0.25 at 75% shortening. When the layer does not thicken nor thin it keeps is original arclength and L_{norm} remains unity. A sharp increase in L_{norm} means that the layer is stretching.

In all cases we see a decreasing trend of L_{norm} from initial state to ~20% shortening, indicating that the simulated layers are shortened and thickened at the early stages, with only minor variations between the different simulations. The low anisotropy series II and III show a flattening of the curves between 20 and 40% shortening and no distinct increase in L_{norm} . This implies a low rate of fold amplification. This is in stark contrast to the high-anisotropy

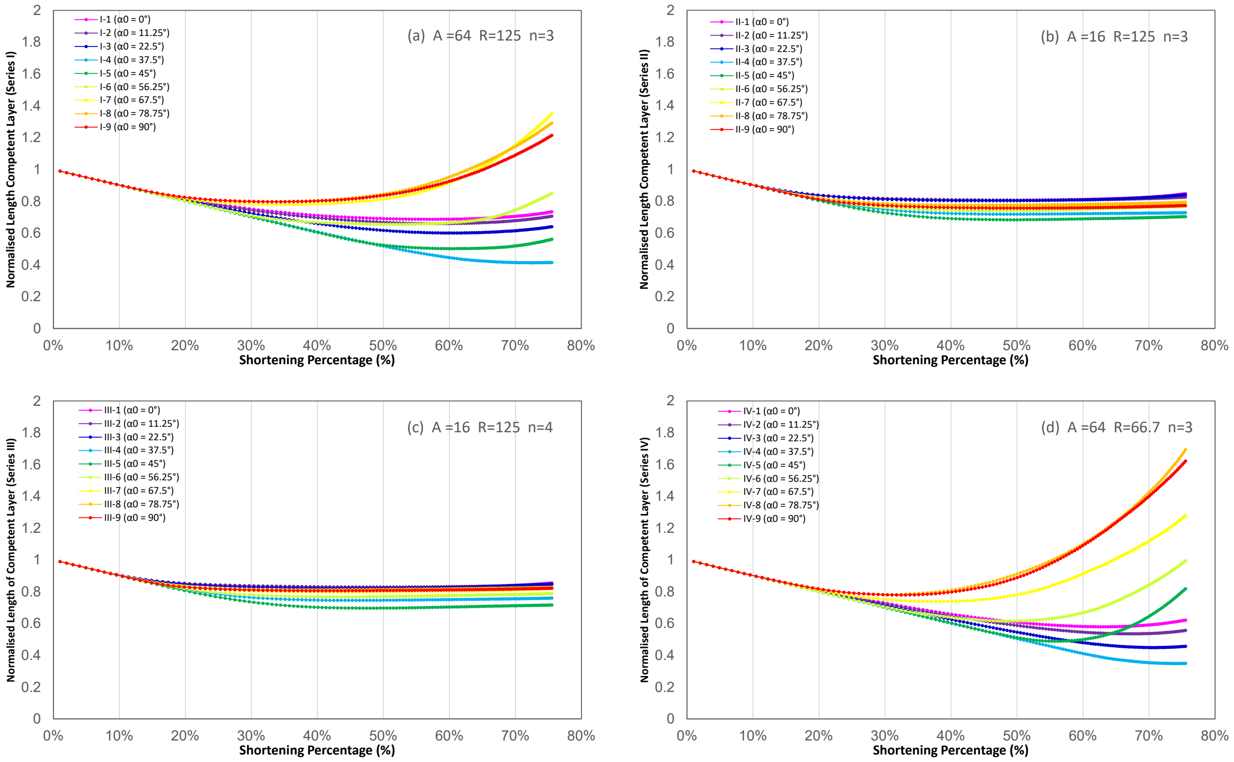

Fig.7: Normalised arclengths (L_{norm}) along the central line of the competent layer for all simulations of series I (a), II (b), III (c) and IV (d) from initial state to 75% shortening percentage. The arclength trends correspond to the amplification character (Fig.4).

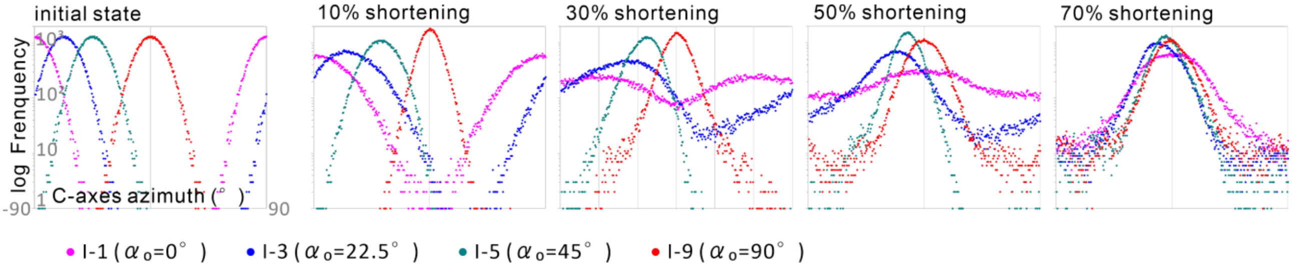

Fig.8: C-axes azimuth frequency distributions for *unodes* aligned with a Gaussian distribution (±10°) for initial state, 10%, 30%, 50% and 70% shortening percentage on the stress curve for case I-1 (purple), I-3 (navy), I-5 (green) and I-9 (red) are shown in boxes. The initial state of c-axes azimuth distribution before deformation is shown at the left box, which also contains data labelling for all boxes.

simulations (series I and IV; Fig.7.a, d), especially for high α_0. Here we see strong increases in L_{norm} , meaning the layer starts to stretch again. In Fig.3 we have already seen that this is associated with the development of large-scale shear bands in the matrix that stretch the limbs of the competent layer. There is almost no difference between the n = 3 and n = 4 cases

(Fig.7.b, c) and the viscosity ratio also seems to have little effect (Fig.7.a, d). It appears that the anisotropy has to strongest effect on the developing fold patterns, especially at high α_0.

4.3 Evolution of the lattice orientations (CPO)

The evolution of the orientation of the mechanical anisotropy can be seen in Figs. 2 and 3 as the change in orientation of passive marker lines that were originally parallel to the foliation or mean weak direction (basal planes). However, these passive marker lines show the finite displacement field, and their orientation may start to deviate for the local lattice orientation with increasing strain. We therefore show the CPO development in the form of azimuth graphs at five shortening stages for Series I and α_0 = 0°, 22.5°, 45° and 90° (Fig.8). Note that the c-axis is at 90° to the basal plane: they are at ±90° for α_0 = 0°. For case I-1, c-axes are initially aligned at ±90°. The single maximum then evolves to a bimodal distribution with weaker peaks at -60° and +60° at 30% shortening. This means that the c-axes rotate in two, opposite directions. Finally, the c-axes align to a new and strong single maximum at ~0°, which is parallel to the maximum shortening direction. The alignment of c-axes is initially already parallel to the maximum shortening direction for case I-9 with α_0 = 90°. The c-axes maximum at 0° remains stable, although it decreases in intensity from about 30% shortening.

For case I-3 (α_0 = 22.5°), c-axes alignment starts with a -67.5° maximum. The maximum then shifts and weakens until about 40%-50% shortening. From 50% shortening the c-axes to align again at a maximum at -9° at 70% shortening. The c-axes distribution of case I-3 is always asymmetric. For case I-5 (α_0 = 45°), c-axes are aligned at -45° initially. The single maximum subsequently rotates to -4.5° at 70% shortening. The single maximum remains strong throughout the whole processes.

At high strain, c-axes align parallel to the maximum finite shortening direction at in all cases. This direction is the fabric attractor of Passchier et al. (1997). However, we see two end-member paths to achieve this final alignment. The first is through a bi-modal distribution, where the single c-axes maximum splits into two maxima that rotate towards and finally join at the fabric attractor (low α_0). In Figs. 2 and 3 this behaviour leads to small crenulations in the foliation. In the second path, the single maximum remains, but rotates towards the fabric attractor (high α_0).

4.4 Stress evolution

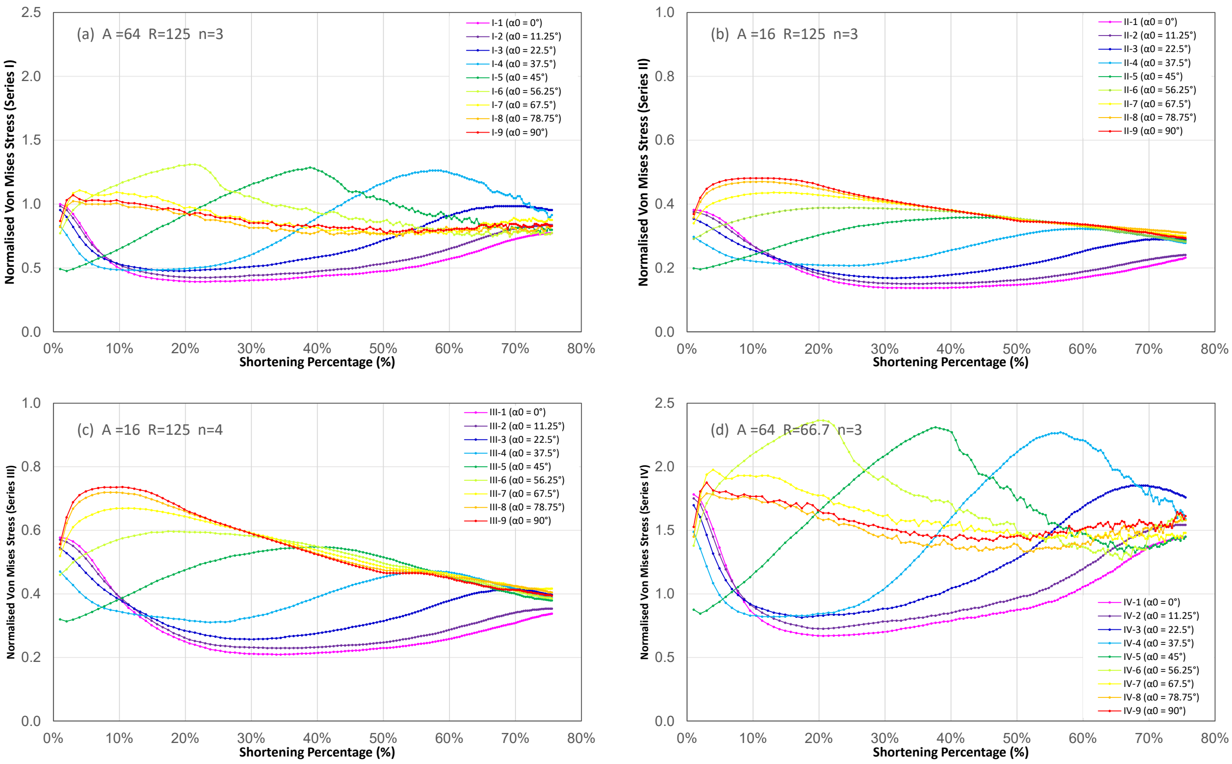

Fig.9: Plot of bulk von Mises stress (σ_{vm} normalised to initial σ_{vm} at step001 of case I-1, the absolute value is 0.129 from calculation of Elle platform) versus shortening percentage for series I (a), series II (b), series III (c) and series IV (d). The curvatures show different tendencies and different hardening and softening stages for variable anisotropy (A_M), viscosity ratio (R) and orientation of initial CPO (α_0). For all series we set the same rheological property to isotropic competent layer, the less viscosity ratio of series IV is made by increased viscosity of soft direction in the matrix.

Folding changes the geometry of the system and therefore typically leads to geometric softening or hardening with increasing strain (e.g., Schmalholz et al., 2005; Schmalholz and Schmid, 2012; Llorens, 2019b) by changing CPO (Takeda and Griera, 2006; Dabrowski et al., 2012; Llorens et al., 2016a; de Riese et al., 2019). As the strain rate in the simulations is a constant boundary condition, we plot the normalized von Mises stress (σ_{vm}) in Fig. 9. For better comparison of the four series, all von Mises stresses are normalized relative to the initial σ_{vm} of simulation Series I-1 (α_0 = 0°).

For series I (Fig.9a), the normalised von Mises stress show similar trends for α_0 = 0° to 33.75°, with buckling of the competent layer at the beginning that causes a ~50% decrease in stress, as the folding requires less mechanical work to shorten the system (Schmalholz and Mancktelow, 2016). After that folds only getting tighter and stresses do not change much (Fig. 2.a). Finally, the stress increases back towards the original stress as it becomes harder to compress the by now tight folds (Fig. 3.a). For the cases α_0 = 22.5 and 33.75° the stresses start to increase again at an earlier strain to reach a maximum that is equal or higher than the initial stress and finally decreases again.

Case I-5 with α_0 = 45°, requires the least initial stress. At this orientation the CPO in the matrix is at an optimal orientation of horizontal shortening at 45° to the alignment of the basal planes. From the onset of the simulation, stresses steadily increase to a maximum at about 40% shortening (Fig. 2.a) after which stresses decrease again.

Case I-6 with α_0 = 56.25° shows a similar trend, but with a stress maximum at lower finite shortening.

The cases with α_0 = 67.5° to 90° are remarkably similar with the highest stress at the beginning and a steady decrease to ~80% the initial stress at 70% shortening. For series II, III and IV the tendencies (Fig.9b, c and d) are quite similar except for the absolute stress values.

Summarizing, we can recognize three basic trends. At low α_0 stress decreases first and then rises again. The opposite is the case at high α_0, where the stress increases at very beginning then decreases slowly but steadily with increasing strain. In between stresses first decrease, then rise again to finally drop again. The amount of shortening at peak stress decreases with increasing α_0.

5 Discussion

The numerical simulations of single-layer folding in an anisotropic matrix with various initial orientations of the anisotropy resulted in a rich variation of fold geometries (Figs. 2 and 3). Comparison of the cases α_0=0° (anisotropic foliation parallel to layer and shortening direction) and α_0=90° (foliation normal to shortening direction) best illustrate the basic end-member types of folding behaviour.

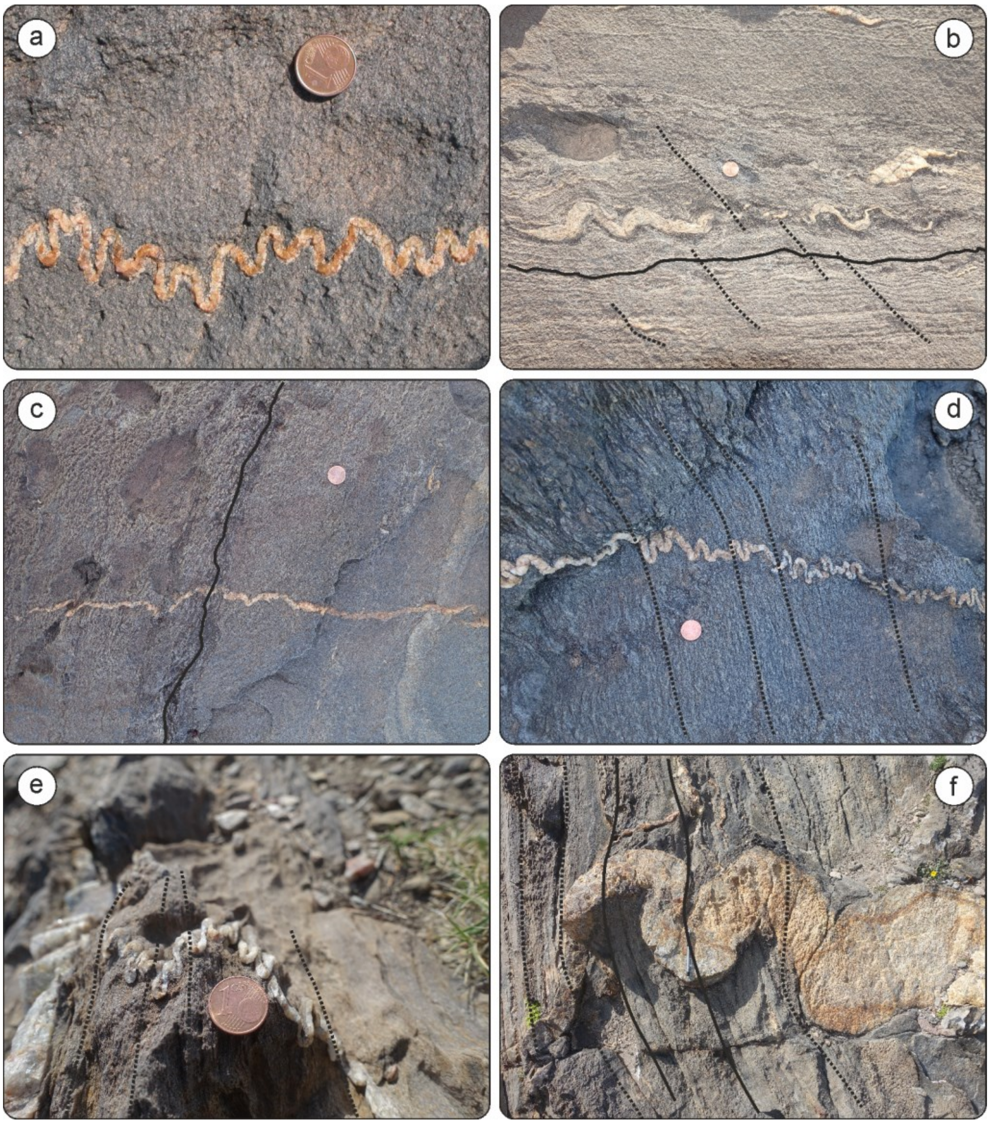

Fig.10: Natural examples, in correspond to the simulated results respectively. Black curvatures follow the foliations within the matrix, black dash lines are newly formed overprinting cleavages which representing the highly strain-localised zones. (a) Thin competent layer deforms compressional buckle folding, typical ptygmatic folds (e.g., Llorens et al. 2013b). Both samples (b) and (c) competent layers deform compressional folding, and forming isocline folds, the anisotropic matrix forms cleavages parallel to the axial plane of folded layer, all cleavages have the equally inclined angle. (d) competent layer deforms extensional folding with larger amplitudes, part of layer in low strain zone only experiences little deforming, cleavages in matrix are almost vertical to the layer. Both samples (e) and (f) competent layers deform extensional folding with larger rations about amplitude vs. wavelength, both foliation and cleavages in matrix are vertical to the layer. The outcrop (e) is shortening more than our maximum shortening percentage.

5.1 Initial CPO α_0=0°

Ptygmatic folds form in the competent layer and an axial planar crenulation cleavage in the matrix (Figs. 2 and 3). Fold wavelengths are typically less than five times the layer thickness. The layer also shows significant thickening. The folds in the layer are similar to those modelled for an isotropic matrix (Parrish et al., 1976; Anthony and Wickham, 1978; Hudleston and Lan, 1994; Zhang et al., 1996, 2000; Mancktelow, 1999; Viola and Mancktelow, 2005; Frehner and Schmalholz, 2006; Kocher et al., 2006, 2008; Hobbs et al., 2008; Llorens et al. 2013b; Llorens, 2019b). As such they appear to follow classical Biot-type theories (Biot, 1957, 1961; Ramberg, 1961; Hudleston and Treagus, 2010; Adamuszek et al., 2011; Schmalholz and Mancktelow, 2016). However, applying these theories to obtain a viscosity contrast (Fig. 6.c) can only result in an effective or apparent viscosity contrast, as there is no single viscosity contrast with the anisotropic matrix. At α_0=0° the foliation in the matrix would form crenulation folds with axial planes normal to the finite shortening direction (Kocher et al., 2006, 2008; Bons et al., 2018; Chapter 3 of this thesis) as is commonly observed in natural rocks (Fig. 10.a) (Ramsay and Huber, 1987; Passchier and Trouw, 2005). This crenulation is observed in the c-axes azimuth distributions (Fig. 8) where the single maximum divides into two maxima that then each rotate in opposite directions towards the fabric attractor.

Folding of the matrix foliation and of the hard layer act in concert. Initially, both are at their strongest orientation relative to the layer and foliation-parallel shortening. Buckling of the competent layer and rotation of the basal planes in the matrix both result in a decrease in required stress to achieve the constant shortening rate (Fig. 9.a). Strain rate within the matrix is distributed relatively homogeneously (Fig. 5), with only small variations on the scale of the individual folds in both layer and foliation.

5.2 Initial CPO α_0=90°

Fold geometries in both competent layer and matrix are completely different at α_0=90° (Figs. 2 and 3). Here we observe much less thickening of the competent layer and fold wavelength / thickness ratios are in the order of ten or more, suggesting a very high apparent viscosity ratio (Fig. 3). The different fold geometry is accompanied by a very different pattern of the deformed foliation in the matrix. Instead of a small-scale shortening crenulation observed for α_0=0°, we see extension of the foliation by the development of shear bands on a larger length scale. These shear bands can be regarded as an extensional crenulation (Carreras, 2001; Carreras et al., 2010, 2013; Ponce et al., 2013; Tanner, 2016; de Riese et al., 2019) or foliation boudinage (Platt and Vissers, 1980; Arslan et al., 2008). The shear bands are clearly visible as zones of high strain rate (Fig. 3). Folds in the competent layer and shear bands are closely related, with the shear bands shearing and stretching the layer to form the fold limbs. The low-strain domains between the shear bands shift up or down relative to each other and form the fold hinges in the competent layer. Fig. 10.e and f show natural examples of this type of folding. As the folds are mostly passive products of the matrix deformation, their geometry is different from that for Biot-type competent-layer buckling (Biot, 1957, 1961).

5.3 Intermediate Initial CPO α_0

Intermediate initial foliation angles behave between the two end members. Clearly, small α_0 is closer to α_0=0°, while large α_0 resembles α_0=90° more. An important aspect is that the mean orientation of the foliation rotates when α_0≠90°. At low α_0 deformation of the foliation is still dominated be shortening by crenulation that becomes increasingly asymmetric. As α_0 increases towards 45°, the initial foliation-parallel shortening decreases, while the mean rotation rate increases. This suppresses crenulation and at high enough α_0 the mean foliation can rotate beyond 45° to enter the stretching field.

From α_0=45° the foliation is in the stretching field. Close to 45° stretching is minor and rotation fast. The matrix is relatively weak, as the foliation is optimally oriented for shear parallel to the foliation to accommodate the deformation. However, the stretching rate parallel to the foliation increases with increasing rotation that foliation. This leads to an increase in the bulk von Mises stress (Fig. 9) until yield when shear bands form and the stress decreases again. These shear bands accommodate the stretching of the foliation and allow the 'microlithons' in between to shift relative to each other. Strain rate in these microlithons themselves decreases, which also decreases the rotation rate of the foliation inside of these. This results in minor folding of the competent layer within the microlithons, but the formation of long fold limbs where the shear bands intersect the layer.

From α_0=0° to 90° we see a gradual transition in behaviour from the one to the other end member. Classical buckle folds dominate at low α_0 as along as the anisotropy does not rotate into the stretching field before crenulation of the foliation has set in. When α_0≥45°, the foliation is stretching from the onset and buckling of the foliation does not occur. The main transition in behaviour thus occurs at α_0 below 45° where the foliation rotates into the stretching field before significant foliation buckling can destroy the single maximum of the c-axis distribution (Fig.8).

5.4 Effect of viscosity contrast and stress exponent

Many more simulation series would be needed to explore the effect of the viscosity contrast and the stress exponent. Series II to IV only give a glimpse of the effects.

The most notable effect of reducing the intensity of anisotropy in the matrix from A=64 (Series I) to A=16 (Series II) is the suppression of the formation of shear bands at high α_0. Shear localisation is more distributed and less intense. This is not surprising as these shear bands are the result of the anisotropy. Raising the stress exponent from n=3 (Series II) to n=4 (Series III) has relatively little effect compared to the intensity of the anisotropy. Deformation patterns (Fig. 2 and 3), but also the evolution of the arclengths (Fig. 7) and the von Mises stresses (Fig. 9) are almost identical between the two series. The intensity of shear localisation is slightly more intense for Series III (with n=4) than for Series II, which is consistent with the observation that an increase in stress exponent makes the material less stable and more prone to strain localisation (Smith, 1977; Lan and Hudleston, 1995). Finally, halving the viscosity contrast (Series IV) while keeping A and n the same as Series I mostly affects the folding of the strong layer at low α_0 (Fig. 3.a and d). This is in line with the observation that at high α_0 the deformation pattern is dominantly controlled by the anisotropy. The effect of viscosity contrast therefore only comes into play at low α_0 where folding of the layer is partly controlled by Biot-type buckling.

6 Conclusions

We modelled folding due to layer-parallel pure-shear shortening of a competent layer that is embedded in an anisotropic matrix with various initial orientations (α_0) of that anisotropy. We observed two basic end-member types of behaviour and resulting fold geometries in both the competent layer and matrix. The difference in behaviour is primarily determined by whether the foliation, defined as the strong direction, is initially in the shortening (α_0<45°) or stretching field (α_0>45°).

At low α_0=45°, both the competent layer and foliation buckle. Folds in the layer resemble 'classical' buckle folds. Buckling of the foliation leads to the development of an axial planar crenulation cleavage with the new cleavage domains defined by aligned limbs of the small-scale folds. The initial single-maximum distribution of c-axes (perpendicular to the strong direction or foliation) splits up into two weak maxima that both rotate in opposite directions towards the final fabric attractor parallel to the finite shortening direction. The strength of the bulk material initially decreases and subsequently increases gradually as folds tighten.

Anisotropy dominates the deformation patterns in both competent layer and matrix at high α_0. Here the foliation is in the stretching field and cannot accommodate the stretching by buckling. Instead, shear bands form that envelope low strain-rate lenses. Folds in the competent layer mostly result from passive shearing by the shear bands. The resulting folds are very irregular and have much higher wavelength/thickness ratios than at low α_0. The initial single-maximum c-axis distribution does not split into two but shifts towards the fabric attractor. The stress evolution is also different from the low α_0 cases, as the bulk stress first increases until the material yields and stresses drop again due to the formation of the shear bands.

Reference

Abbassi, M.R., Mancktelow, N.S., (1992). Single layer buckle folding in non-linear materials - I. Experimental study of fold development from an isolated initial perturbation. J. Struct. Geol. 14, 85–104. DOI: https://doi.org/10.1016/0191-8141(92)90147-O

Adamuszek, M., Schmid, D.W., Dabrowski, M., (2011). Fold geometry toolbox – Automated determination of fold shape, shortening, and material properties. Journal of Structural Geology, Volume 33, 1406-1416. DOI: https://doi.org/10.1016/j.jsg.2011.06.003

Adamuszek, M., (2022). FGT - Fold Geometry Toolbox (https://www.mathworks.com/matlabcentral/fileexchange/31694-fgt-fold-geometry-toolbox), MATLAB Central File Exchange. Retrieved August 31, 2022.

Alsop, G.I., Carreras, J., (2007). Three dimensional sheath folds in quartz mylonite, Cap de Creus. J. Struct. Geol. 31 (1), 1–2. DOI: https://doi.org/10.1016/j.jsg.2007.09.010

Alsop, G.I., Holdsworth, R.E., (2007). Flow perturbation folding in shear zones. Geological Society, London, Special Publications. 272 (1), 75–101. DOI: https://doi.org/10.1144/GSL.SP.2007.272.01.06

Anthony, M., Wickham, John., (1978). Finite-element simulation of asymmetric folding. Tectonophysics, 47(1-2), 1–14. doi: https://doi.org/10.1016/0040-1951(78)90148-8

Arslan, A., Passchier, C.W., Koehn, D., (2008). Foliation boudinage. Journal of Structural Geology, 30(3), 291–309. doi: https://doi.org/10.1016/j.jsg.2007.11.004

Aslin, J., Mariani, E., Dawson, K., Barsoum M.W., (2019). Ripplocations provide a new mechanism for the deformation of phyllosilicates in the lithosphere. Nature Communication 10, 686. https://doi.org/10.1038/s41467-019-08587-2

Bayly, M.B., (1970). Viscosity and anisotropy estimates from measurements on chevron folds. Tectonophysics, Volume 9, Issue 5, May 1970, Pages 459-474. DOI: 10.1016/0040-1951(70)90058-2

Biot, M.A., (1957). Folding Instability of a Layered Viscoelastic Medium under Compression. Proceedings of the Royal Society A: Mathematical, Physical and Engineering Sciences, 242(1231), 444–454. DOI: 10.1098/rspa.1957.0187

Biot, M.A., (1961). Theory of folding of stratified viscoelastic media and its implications in tectonics and orogenesis. Geological Society of America Bulletin, v. 72, p. 1595-1620. DOI: 10.1130/0016-7606(1961)72[1595:TOFOSV]2.0.CO;2

Biot, M.A. (1964a). Theory of internal buckling of a confined multi-layered structure, Geological Society of America Bulletin, 75, 563–568. Doi: https://doi.org/10.1130/0016-7606(1964)75[563:TOIBOA]2.0.CO;2

Biot, M.A. (1964b). Theory of viscous buckling of multilayered fluids undergoing finite strain, Physics of Fluids 7, 855–861. Doi: https://doi.org/10.1063/1.1711296

Biot, M.A., (1965a). Further Development of the Theory of Internal Buckling of Multilayers. Geological Society of America Bulletin, 76 (7): 833–840. DOI: 10.1130/0016-7606(1965)76[833:FDOTTO]2.0.CO;2

Biot, M.A., (1965b). Theory of similar folding of first and second kind, Geological Society of America Bulletin, 76, 251–258. Doi: https://doi.org/10.1130/0016-7606(1965)76[251:TOSFOT]2.0.CO;2

Biot, M.A., (1965c), Mechanics of incremental deformations: New York, Wiley, 504 p.

Bobillo-Ares, N.C., Toimil, N.C., Aller, J., Bastida, F., (2004). FoldModeler: a tool for the geometrical and kinematical analysis of folds. Computers & Geosciences, 30, Pages 147-159. DOI: https://doi.org/10.1016/j.cageo.2003.09.008

Bons, P.D., Urai, J.L., (1996). An apparatus to experimentally model the dynamics of ductile shear zones. Tectonophysics 256, 145–164. DOI: https://doi.org/10.1016/0040-1951(95)00161-1

Bons, P.D, Koehn, D, Jessell, M.W (Eds) (2008) Microdynamic Simulation. Lecture Notes in Earth Sciences 106, Springer, Berlin. 405 pp. ISBN 978-3-540-44793-1

Bons, P.D., Kleiner, T., Llorens, M.-G., Prior, D.J., Sachau, T., Weikusat, I., Jansen, D., (2018). Greenland Ice Sheet: Higher nonlinearity of ice flow significantly reduces estimated basal motion. Geophysical Research Letters, 45, 6542–6548. 10.1029/2018GL078356

Bordignon, N., Piccolroaz, A., Dal Corso, F., Bigoni, D., (2015). Strain localization and shear band propagation in ductile materials. Frontiers in Materials 2(22), 1-13. DOI: 10.3389/fmats.2015.00022

Burov, E. (2011): Rheology and strength of the lithosphere. Marine and Petroleum Geology 28, 1402-1443. https://doi.org/doi:10.1016/j.marpetgeo.2011.05.008

Carreras, J., (2001). Zooming on Northern Cap de Creus shear zones. JSG, 23(9), 1457–1486. doi: https://doi.org/10.1016/s0191-8141(01)00011-6

Carreras, J., Czeck, D.M., Druguet, E., Hudleston, P.J. (2010). Structure and development of an anastomosing network of ductile shear zones. Journal of Structural Geology, 32(5), 656–666. doi: https://doi.org/10.1016/j.jsg.2010.03.013

Carter, N.L. and Tsenn, M.C., (1987). Flow properties of continental lithosphere. Tectonophysics 136, 27-63. DOI: https://doi.org/10.1016/0040-1951(87)90333-7

Cobbold, P.R., Cosgrove, J.W., Summers, J.M., (1971). Development of internal structures in deformed anisotropic rocks. Tectonophysics, 12: 23-53. DOI: 10.1016/0040-1951(71)90065-5

Cobbold, P.R., (1975). Fold propagation in single embedded layers. Tectonophysics 27 (4), 333–351. DOI: https://doi.org/10.1016/0040-1951(75)90003-7

Currie, J.B., Patnode, H.W., Trump, R.P. (1962). Development of Folds in Sedimentary Strata. Geological Society of America Bulletin, 73(6), 655–673. doi: https://doi.org/10.1130/0016-7606(1962)73[655:DOFISS]2.0.CO;2

Dabrowski, M., Schmid, D. W., Podladchikov, Y. Y. (2012). A two-phase composite in simple shear: Effective mechanical anisotropy development and localization potential. Journal of Geophysical Research, 117(B8), B08406. doi: https://doi.org/10.1029/2012jb009183

de Riese, T., (2014). Numerical modelling of multilayer folding. Eberhard Karls University Tübingen, Master thesis

de Riese, T., Evans, L., Gomez-Rivas, E., Griera, A., Lebensohn, R.A., Llorens, M.-G., Ran, H., Sachau, T., Weikusat, I., Bons, P.D. (2019). Shear localisation in anisotropic, non-linear viscous materials that develop a CPO: A numerical study. J. Struct. Geol. 124, 81-90. DOI: https://doi.org/10.1016/j.jsg.2019.03.006

Fan, H., El-Awady, J.A., (2015). Towards resolving the anonymity of pyramidal slip in magnesium. Materials Science and Engineering: A, Volume 644, 318–324. DOI: 10.1016/j.msea.2015.07.080

Finch, M.A., Bons, P.D., Steinbach, F., Griera, A., Llorens, M.-G., Gomez-Rivas, E., Ran, H., de Riese, T., (2020). The ephemeral development of C′ shear bands: A numerical modelling approach, Journal of Structural Geology, DOI: https://doi.org/10.1016/j.jsg.2020.104091

Finch, M.A., Bons, P.D., Weinberg, R.F., Llorens, M.G., Griera, A., Gomez-Rivas, E., (2022). A dynamic atlas of interference patterns in superimposed, opposite sense ductile shear zones, Journal of Structural Geology, 165, 104739, doi: https://doi.org/10.1016/j.jsg.2022.104739

Fletcher R.C., (1974). Wavelength selection in the folding of a single layer with power-law rheology. American Journal of Science November 1974, 274 (9) 1029-1043. DOI: https://doi.org/10.2475/ajs.274.9.1029

Fletcher, R.C., (1995). Three-dimensional folding and necking of a power-law layer: are folds cylindrical, and, if so, do we understand why? Tectonophysics 247, 65-83. DOI: https://doi.org/10.1016/0040-1951(95)00021-E

Frehner, M., Schmalholz, S. M. (2006). Numerical simulations of parasitic folding in multilayers. Journal of Structural Geology, 28(9), 1647–1657. doi: https://doi.org/10.1016/j.jsg.2006.05.008

Gardner, R., Piazolo, S., Lynn, E., Nathan, D., (2017). Patterns of strain localization in heterogeneous, polycrystalline rocks – a numerical perspective. Earth and Planetary Science Letters, 463, 253–265. doi: https://doi.org/10.1016/j.epsl.2017.01.039

Ghosh, S.K., (1966). Experimental tests of buckling folds in relation to strain ellipsoid in simple shear deformations. Tectonophysics, 3, 169–185. DOI: https://doi.org/10.1016/0040-1951(66)90001-1

Griera, A., Bons, P.D., Jessell, M.W., Lebensohn, R.A., Evans, L., Gomez-Rivas, E., (2011). Strain localization and porphyroclast rotation. Geology, 39(3), 275–278. doi: https://doi.org/10.1130/G31549.1

Griera, A., Llorens, M.-G., Gomez-Rivas, E., Bons, P. D., Jessell, M. W., Evans, L. A., Lebensohn, R., (2013). Numerical modelling of porphyroclast and porphyroblast rotation in anisotropic rocks. Tectonophysics, 587, 4–29. DOI: 10.1016/j.tecto.2012.10.008

Griera, A., Gomez-Rivas, E., Llorens, M.-G., (2018). The influence of layer-interface geometry on single-layer folding. Geological Society, London, Special Publications, 487 (1): 59. DOI: 10.1144/SP487.4

Hobbs. B.E, Regenauer-Lieb., K., Ord. A., (2008). Folding with thermal–mechanical feedback. Journal of Structural Geology, 30(12), 1572–1592. doi: https://doi.org/10.1016/j.jsg.2008.09.002

Hudleston, P.J., (1973). An analysis of “Single-layer” folds developed experimentally in viscous media, Tectonophysics, Volume 16, Issues 3–4, Pages 189-214. Doi: https://doi.org/10.1016/0040-1951(73)90012-7

Hudleston, P.J., (1986). Extracting information from folds in rocks. Journal of Geological Education 34, 237-245. Doi: https://doi.org/10.5408/0022-1368-34.4.237

Hudleston, P.J., Lan, L., (1993). Information from fold shapes. Journal of Structural Geology . 15, 253–264. https://doi.org/10.1016/0191-8141(93)90124-S

Hudleston, P.J., Lan L., (1994). Rheological controls on the shapes of single-layer folds. Journal of Structural Geology, 16(7), 1007–1021. doi: https://doi.org/10.1016/0191-8141(94)90082-5

Hudleston, P.J., Treagus, S.H., (2010). Information from folds: a review. Journal of Structural Geology. 32(12), 2042–2071. DOI: 10.1016/j.jsg.2010.08.011

Johnson, A.M., Pfaff, V.J., (1989). Parallel, similar and constrained folds. Engineering Geology, 27(1-4), 115–180. doi: https://doi.org/10.1016/0013-7952(89)90032-x

Johnson, A.M., Fletcher, R.C. (1994): Folding of Viscous Layers, Columbia University Press, New York.

Kaus, B.J.P., Schmalholz, S.M., (2006). 3D finite amplitude folding: Implications for stress evolution during crustal and lithospheric deformation. GEOPHYSICAL RESEARCH LETTERS, VOL. 33, L14309, doi: https://doi.org/10.1029/2006GL026341

Kocher, T., Schmalholz, S.M., Mancktelow, N.S. (2006). Impact of mechanical anisotropy and power-law rheology on single layer folding. Tectonophysics 421 71–87. DOI: https://doi.org/10.1016/j.tecto.2006.04.014

Kocher, T., Mancktelow, N.S., Schmalholz, S.M., (2008). Numerical modelling of the effect of matrix anisotropy orientation on single layer fold development. Journal of Structural Geology 30 (2008) 1013–1023. DOI: https://doi.org/10.1016/j.jsg.2008.04.006

Kronenberg, A. K., Kirby, S. H., Pinkston J., (1990). Basal slip and mechanical anisotropy of biotite. Journal of Geophysical research Solid Earth, 95, 19257-19278. DOI: https://doi.org/10.1029/JB095iB12p19257

Lan, L., Hudleston, P.J., (1991). Finite-element models of buckle folds in non-linear materials. Tectonophysics 199, 1-12. DOI: https://doi.org/10.1016/0040-1951(91)90115-9

Lan, L., Hudleston, P.J., (1995). The effects of rheology on the strain distribution in single layer buckle folds. Journal of Structural Geology. 17, 727–738. https://doi.org/10.1016/0191-8141(94)00095-H

Lan, L., Hudleston, P.J., (1996). Rock rheology and sharpness of folds in single layers. Journal of Structural Geology, Vol. 18, No. 7, pp. 925-931. Doi: https://doi.org/10.1016/0191-8141(96)00018-1

Lebensohn, R.A., (2001). N-site modeling of a 3D viscoplastic polycrystal using Fast Fourier Transform. Acta Materialia, 49, 2723-2737. Doi: 10.1016/S1359-6454(01)00172-0

Lebensohn, R.A., Brenner, R., Castelnau, O., Rollett, A. D. (2008). Orientation image-based micromechanical modelling of subgrain texture evolution in polycrystalline copper. Acta Materialia, 56, 3914-3926. Doi: 10.1016/j.actamat.2008.04.016

Lebensohn, R.A., Rollett, A.D. (2020). Spectral methods for full-field micromechanical modelling of polycrystalline materials. Computational Materials Science, 173, 109336. Doi: 10.1016/j.commatsci.2019.109336

Linker, M.F., Kirby, S.H., Ord, A., Christie, J.M., (1984). Effects of compression direction on the plasticity and rheology of hydrolytically weakened synthetic quartz crystals at atmospheric pressure. Journal of Geophysical Research, 89, 4241–4255. Doi: https://doi.org/10.1029/JB089iB06p04241

Llorens, M.-G., Bons, P. D., Griera, A., Gomez-Rivas, E. (2013a). When do folds unfold during progressive shear? GEOLOGY, May 2013, v. 41, no. 5, p. 563–566. DOI:10.1130/G33973.1

Llorens, M.-G., Bons, P. D., Griera, A., Gomez-Rivas, E., Evans, L. A. (2013b). Single layer folding in simple shear. Journal of Structural Geology 50, 209-220. DOI: 10.1016/j.jsg.2012.04.002

Llorens, M.-G., Griera, A., Bons, P.D., Roessiger, J., Lebensohn, R.A., Evans, L.A., Weikusat, I. (2016). Dynamic recrystallisation of ice aggregates during co-axial viscoplastic deformation: A numerical approach. Journal of Glaciology, 62(232), 359-377. DOI: https://doi.org/10.1017/jog.2016.28

Llorens, M.-G., Griera, A., Steinbach, F., Bons, P.D., Gomez-Rivas, E., Jansen, D., Roessiger, J., Lebensohn, R.A., Weikusat, I. (2017). Dynamic recrystallization during deformation of polycrystalline ice: insights from numerical simulations. Philosophical Transactions of the Royal Society A: Mathematical, Physical and Engineering Sciences, 375, 20150346. https://doi.org/10.1098/rsta.2015.0346

Llorens, M.-G., Gomez-Rivas, E., Ganzhorn, A.-C., Griera, A., Steinbach, F., Roessiger, J., Labrousse, L., Walte, N.P., Weikusat, I., Bons, P.D., (2019a). The effect of dynamic recrystallisation on the rheology and microstructures of partially molten rocks. Journal of Structural Geology, (118), 224-235. doi: https://doi.org/10.1016/j.jsg.2018.10.013

Llorens, M.-G. (2019b). Stress and strain evolution during single-layer folding under pure and simple shear, Journal of Structural Geology, Volume 126, Pages 245-257, DOI: https://doi.org/10.1016/j.jsg.2019.06.009

Mancktelow, N.S., (1999). Finite-element modelling of single-layer folding in elastoviscous materials; the effect of initial perturbation geometry. Journal of Structural Geology 21, 161-177. DOI: https://doi.org/10.1016/S0191-8141(98)00102-3

Manz, R., Wickham, J., (1978). Experimental analysis of folding in simple shear. Tectonophysics 44, 79–90. DOI: https://doi.org/10.1016/0040-1951(78)90064-1

Mares V. M., Kronenberg A. K., (1993). Experimental deformation of muscovite. Journal of Structural Geology. Volume 15, Issues 9–10, September–October 1993, Pages 1061-1075. DOI: 10.1016/0191-8141(93)90156-5

Mukherjee, S., (2014). Review of flanking structures in meso-and micro-scales. Geological Magazine. 151 (6), 957–974. DOI: https://doi.org/10.1017/S0016756813001088

Mühlhaus, H.-B., Sakaguchi, H., Hobbs, B.E. (1998). Evolution of three-dimensional folds for a non-Newtonian plate in a viscous medium. Proceedings of the Royal Society A: Mathematical, Physical and Engineering Sciences, 454(1980), 3121–3143. doi: https://doi.org/10.1098/rspa.1998.0294

Nabavi, S.T., Fossen, H., (2021). Fold geometry and folding – a review. Earth-Science Reviews, 222, 103812. DOI: https://doi.org/10.1016/j.earscirev.2021.103812

Naus-Thijssen, F.M.J., Johnson, S.E., Koons, P.O. (2010). Numerical modeling of crenulation cleavage development: A polymineralic approach. Journal of Structural Geology, 32(3), 330–341. DOI: https://doi.org/10.1016/j.jsg.2010.01.004

Ormand, C.J., Hudleston, P.J., (2003). Strain paths of three small folds from the Appalachian Valley and Ridge, Maryland. Journal of Structural Geology 25, 1841-1854 doi: https://doi.org/10.1016/S0191-8141(03)00042-7

Parrish, D.K., (1973). A nonlinear finite element fold model. American Journal of Science April 1973, 273 (4) 318-334; DOI: https://doi.org/10.2475/ajs.273.4.318

Parrish, D.K., Krivz, A.L., Carter, N.L. (1976). Finite-element folds of similar geometry. Tectonophysics, 32(3-4), 183–207. doi: https://doi.org/10.1016/0040-1951(76)90062-7

Passchier, C.W. (1997). The fabric attractor. Journal of Structural Geology, Vol. 19, No. 1, pp. 113-127. DOI: https://doi.org/10.1016/S0191-8141(96)00077-6

Passchier, C.W., Trouw, R.A., (2005). Microtectonics. Springer Science & Business Media.

Pérez-Alonso, J., Fuertes-Fuente, M., Bastida, F., (2016). Quartz veining in slates and Variscan deformation: Insights from the Luarca sector (NW Spain). Tectonophysics, Volume 671, 7 March 2016, Pages 24-41. https://doi.org/10.1016/j.tecto.2016.01.019

Piazolo, S, Bons, P.D., Griera, A., Llorens, M.-G., Gomez-Rivas, E., Koehn, D., Wheeler, J., Gardner, R., J.R.A. Godinho, J.R.A., Evans, L., Lebensohn, R.A., Jessell, M.W. (2019). A review of numerical modelling of the dynamics of microstructural development in rocks and ice: Past, present and future. J. Struct. Geol. 125, 111-123. DOI: https://doi.org/10.1016/j.jsg.2018.05.025

Platt, J.P., Vissers, R.L.M. (1980). Extensional structures in anisotropic rocks. Journal of Structural Geology, 2(4), 397–410. doi: https://doi.org/10.1016/0191-8141(80)90002-4

Ponce, C., Druguet, E., Carreras, J. (2013). Development of shear zone-related lozenges in foliated rocks. Journal of Structural Geology, 50, 176–186. doi: https://doi.org/10.1016/j.jsg.2012.04.001

Price, N.J., Cosgrove, J.W., (1990). Analysis of Geological Structures. Cambridge University Press, Great Britain

Quinquis, H., Audren, CL., Brun, J.P., Cobblod, P.R., (1978). Intense progressive shear in Ile de Groix blueschists and compatibility with subduction or obduction. Nature 273, 43–45. Doi: https://doi.org/10.1038/273043a0

Ramberg, H., (1961). Relationship between concentric longitudinal strain and concentric shearing strain during folding of homogeneous sheets of rocks. American Journal of Science May 1961, 259 (5) 382-390, DOI: https://doi.org/10.2475/ajs.259.5.382

Ramberg, H., (1962). Contact strain and folding instability of a multilayered body under compression. Geologische Rundschau, 51, 405–439. DOI: 10.1007/BF01820010

Ramberg, H., (1963). Fluid Dynamics of Viscous Buckling Applicable to Folding of Layered Rocks. AAPG Bulletin (1963) 47 (3): 484–505. DOI: 10.1306/BC743A5B-16BE-11D7-8645000102C1865D

Ramsay, J.G., (1980). Shear zone geometry: A review. Journal of Structural Geology, 2(1-2), 83–99. DOI: https://doi.org/10.1016/0191-8141(80)90038-3

Ramsay J.G. Huber M. I., (1987). The Techniques of Modern Structural Geology. Volume 2: Folds and Fractures. Academic Press.

Ran, H., de Riese, T., Llorens, M.-G., Finch, M.A., Evans, L.A., Gomez-Rivas, E., Griera, A., Jessell, M.W., Lebensohn, R.A., Piazolo, S., Bons, P.D., (2019). Time for anisotropy: The significance of mechanical anisotropy for the development of deformation structures. J. Struct. Geol. 125, 41-47. DOI: https://doi.org/10.1016/j.jsg.2018.04.019

Ran, H., Bons, P.D., Wang, G., Griera, A., de Riese, T., de Riese, T., Llorens, M.-G., Ran, S., Wang, Y., Wang, S., (2022): Folds inside pebbles: When do they form during conglomerate deformation? Numerical modelling and comparison with the Hutuo Group conglomerates, North China Craton, Journal of Structural Geology, Volume 160, 104620. Doi: https://doi.org/10.1016/j.jsg.2022.104620

Schmalholz, S.M., Podladchikov, Y.Y., (2000). Finite amplitude folding: transition from exponential to layer length controlled growth. Earth and Planetary Science Letters 181, 619-633. DOI: https://doi.org/10.1016/S0012-821X(00)00193-X

Schmalholz, S.M., Podladchikov, Y.Y. (2001). Strain and competence contrast estimation from fold shape. Tectonophysics, 340(3-4), 0–213. doi: https://doi.org/10.1016/s0040-1951(01)00151-2

Schmalholz, S.M., Podladchikov, Y.Y., Schmid, D.D., (2001). A spectral/finite difference method for simulating large deformations of heterogeneous, viscoelastic materials. Geophysical Journal International 145, 199-208. DOI: https://doi.org/10.1046/j.0956-540x.2000.01371.x

Schmalholz, S.M., Podladchikov, Y.Y., Jamtveit, B., (2005). Structural softening of the lithosphere. Terra Nova, 17(1), 66–72. doi: https://doi.org/10.1111/j.1365-3121.2004.00585.x

Schmalholz, S.M., (2006). Scaled amplification equation: A key to the folding history of buckled viscous single-layers. Tectonophysics, 419(1-4), 0–53. doi: https://doi.org/10.1016/j.tecto.2006.03.008

Schmalholz, S.M., Schmid, D.W., (2012). Folding in power-law viscous multi-layers. Philosophical Transactions of the Royal Society A: Mathematical, Physical and Engineering Sciences, 370(1965), 1798–1826. doi: https://doi.org/10.1098/rsta.2011.0421

Schmalholz. S. M., Mancktelow. N.S., (2016): Folding and necking across the scales: a review of theoretical and experimental results and their applications. Solid Earth, 7, 1417–1465, 2016. DOI: 10.5194/se-7-1417-2016

Schmid, D.W., Podlachikov, Y.Y. (2006): Fold amplification rates and dominant wavelength selection in multilayer stacks, Philos. Mag., 86, 3409–3423. Doi: https://doi.org/10.1080/14786430500380175

Shea Jr., W.T., Kronenberg, A.K., (1993). Strength and anisotropy of foliated rocks with varied mica contents. Journal of Structural Geology. Volume 15, Issues 9–10, September–October 1993, Pages 1097-1121. https://doi.org/10.1016/0191-8141(93)90158-7

Sherwin, J.-A., Chapple. W.M., (1968). Wavelengths of single-layer folds; a comparison between theory and observation. American Journal of Science March 1968, 266 (3) 167-179; DOI: 10.2475/ajs.266.3.167

Smith, R.B., (1977). Formation of folds, boudinage, and mullions in non-Newtonian materials. Geological Society of America Bulletin, 88 (2): 312–320. Doi: https://doi.org/10.1130/0016-7606(1977)88<312:FOFBAM>2.0.CO;2

Steinbach, F., Bons, P.D., Griera, A., Jansen, D., Llorens, M.-G., Roessiger, J., Weikusat, I. (2016): Strain localization and dynamic recrystallization in the ice–air aggregate: a numerical study, The Cryosphere, 10, 3071–3089, https://doi.org/10.5194/tc-10-3071-2016

Takeda, Y., Griera, A., (2006). Rheological and kinematical responses to flow of two-phase rocks. Tectonophysics, 427(1-4), 0–113. doi: https://doi.org/10.1016/j.tecto.2006.03.050

Tanner, G.P.W., (2016). A new model for the formation of a spaced crenulation (shear band) cleavage in the Dalradian rocks of the Tay Nappe, SW Highlands, Scotland. Journal of Structural Geology, 84, 120–141. doi: https://doi.org/10.1016/j.jsg.2015.11.007

Tikoff, B., Peterson, K., (1998). Physical experiments of transpressional folding. Journal of Structural Geology. 20, 661–672. DOI: https://doi.org/10.1016/S0191-8141(98)00004-2

Torremans, K., Muchez, P., Sintubin, M., (2014). Mechanisms of flexural flow folding of competent single-layers as evidenced by folded fibrous dolomite veins. Journal of Structural Geology, Volume 69, Part A, Pages 75-90. Doi: https://doi.org/10.1016/j.jsg.2014.10.002

Viola, G., Mancktelow, N.S., (2005). From XY tracking to buckling: axial plane cleavage fanning and folding during progressive deformation. Journal of Structural Geology, 27(3), 409–417. doi: https://doi.org/10.1016/j.jsg.2004.10.011

Zhang, Y., Hobbs, B.E., Ord, A.M., Mühlhaus, H.B., (1996). Computer simulation of single layer buckling. Journal of Structural Geology 18, 643-655. DOI: https://doi.org/10.1016/S0191-8141(96)80030-7

Zhang, Y., Mancktelow, N.S., Hobbs, B.E., Ord, A.M., Mühlhaus, H.B., (2000). Numerical modelling of single-layer folding: clarification of an issue regarding the possible effect of computer codes and the influence of initial irregularities. Journal of Structural Geology 22, 1511-1522. DOI: https://doi.org/10.1016/S0191-8141(00)00063-8

PAPER III

Folding due to anisotropy in ice, from cm-scale cloudy bands to the km-scale

Paul D. Bons[1,2], **Yuanbang Hu**[1,3], Maria-Gema Llorens[4], Yu Zhang[1], Julien Westhoff[5], Steven Franke[1,6,] Nicolas Stoll[6] (Preliminary author list)

[1]Department of Geosciences, Tübingen University, Tübingen, Germany

[2]China University of Geosciences (Beijing), Beijing, China

[3]College of Earth Science, Chengdu University of Technology, Chengdu, China

[4]Geosciences Barcelona GEO3BCN-CSIC

[5]Niels Bohr Institute, University of Copenhagen, Copenhagen, Denmark

[6]Alfred Wegener Institute, Helmholtz Centre for Polar and Marine Research, Bremerhaven Germany

Abstract

Folds in ice sheets are observed on the cm-scale in cloudy bands in drill cores and on the km-scale in radargrams. We address the question of the folding mechanism for these folds, by analysing the power spectra of fold trains to obtain the amplitude as a function of wavelength signal. Classical Biot-type buckle folds due to a rheological contrast between layers develop a characteristic wavelength, visible as a peak in the power spectrum. Power spectra of ice folds, however, follow a power law with a steady increase of amplitude with wavelength. Such a power spectrum is also observed in a folded, highly anisotropic biotite schist and in a numerical simulation of the deformation of ice Ih with a strong alignment of the basal planes parallel to the shortening direction. This suggests that the folds observed in ice are primarily due to the strong mechanical anisotropy of ice that tends to have a strong lattice preferred orientation in ice sheets.

1 Introduction

Folds are observed on all scales in glaciers and ice sheets. Large-scale folds (100 -1000 m scale) are observed via internal reflection horizons (IRHs) in radargrams (Wolovick et al., 2014; Bell et al., 2014; Leysinger-Vieli et al., 2018; NEEM community members, 2013; Bons et al., 2016; Franke et al., 2022a) and in satellite images of the ice surface in west Greenland. Folds on the intermediate scale (~m scale) are common in glaciers (Hudleston, 2015), but more difficult to observe in ice sheets because of the snow cover. Small scale folds (≤1 cm) in ice cores are visible as undulated cloudy bands, thin layers of high impurity concentration mainly occurring in glacial periods (Alley et al., 1997; Thorsteinsson, 1996; Svensson et al., 2005; Faria et al., 2010; Fitzpatrick et al., 2014; Jansen et al., 2016; Stoll et al., 2023). These folds are the main topic of this paper, using examples from the EGRIP drill core (Westhoff et al., 2021) in the Northeast Greenland Ice Stream (NEGIS) (Fig. 1). Cloudy bands in EGRIP are observed already in the Younger Dryas (Bohleber et al., 2022), but are a recurring stratigraphic feature from a depth of 1375 m (Westhoff et al., 2021, Stoll et al., 2023). Chemical data from these bands show high impurity concentration, partial layering of certain minerals, and more insoluble particles than in the surrounding ice (Bohleber et al., 2022, Stoll et al., 2023). Stoll et al. (2023) define different cloudy band types and discuss their formation, but few is known about the folding of these bands which is observed at various levels throughout the glacial, i.e., below 1375 m at EGRIP. That folds are not always observed can be explained by the orientation of the drill-core section relative to the fold axis. Only sections at a large angle to the drill core will reveal the cloudy bands (Figure 4 in Westhoff et al., 2021).

Nabavi and Fossen (2021) define folds as "curviplanar structures that form by transformation of any tectonic or primary foliation into curved geometries through a non-linear transformation". In geology 'foliation' is used to denote any planar structure in a rock (which includes ice). The primary foliation in glaciers and ice sheets is the original sedimentary layering formed by the deposition of snow layers on the surface. Other foliations can, for example, be healed fractures or fractures filled with frozen water (Hudleston, 2015). Numerous causes for folding in ice sheets have been proposed. Variations in bedrock elevation (Krabbendam, 2016), variable bedrock sliding (Wolovick et al., 2014), basal melting or freeze-on (Leysinger-Vieli et al., 2018) have been proposed to explain large-scale folds of the original stratigraphy. Such external causes for folding cannot apply to small to medium-scale folds that must have an internal response to layer-parallel shortening (NEEM community members, 2013; Hudleston, 2015; Bons et al., 2016; Jansen et al. 2016).

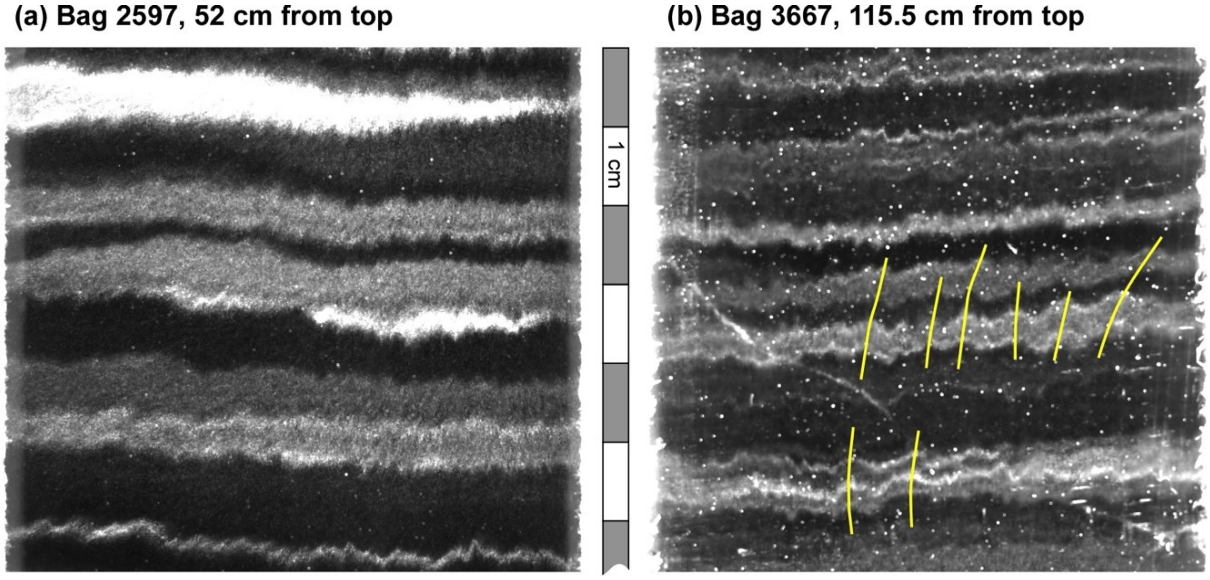

Figure 1. Two visual stratigraphy line scan examples of folded cloudy bands in the EGRIP drill core from a depth of **(a)** 1427.8 m and **(b)** 2017.45 m. Cloudy bands have a variety of widths from about one mm to over one cm. Eight axial planes are drawn as yellow lines in (b). These show that the folds are upright or moderately inclined. The folds are disharmonic, as axial planes cannot be traced for over more than a few times the fold wavelength at the most.

A volume of isotropic and mechanically homogeneous material will not produce folds when subject to deformation. Folds can form when the material has a mechanical layering that forms a 'composite anisotropy' and/or when it is 'intrinsically anisotropic', for example due to a crystallographic preferred orientation (CPO) (Griera et al., 2013; Nabavi and Fossen, 2021). The latter is often the case in ice because ice normally deforms by dislocation creep (Glen, 1955; Weertman, 1983) that results in a CPO that aligns the easy-glide basal planes in certain preferred orientations (Duval et al., 1983; Budd and Jacka, 1989; Faria et al. 2014; Llorens et al., 2017). In both cases the application of a differential stress will normally lead to a heterogenous deformation field, which implies that originally straight planar surfaces get distorted: folds develop. Here we will show, based on fold theory and numerical simulations, that folds observed in cloudy bands in the EGRIP drill core primarily result from an intrinsic anisotropy due to the CPO and not from rheological differences between the individual cloudy bands.

2 Basic fold terminology and theory

Fore detailed reviews of fold geometry and terminology the reader is referred to the textbooks

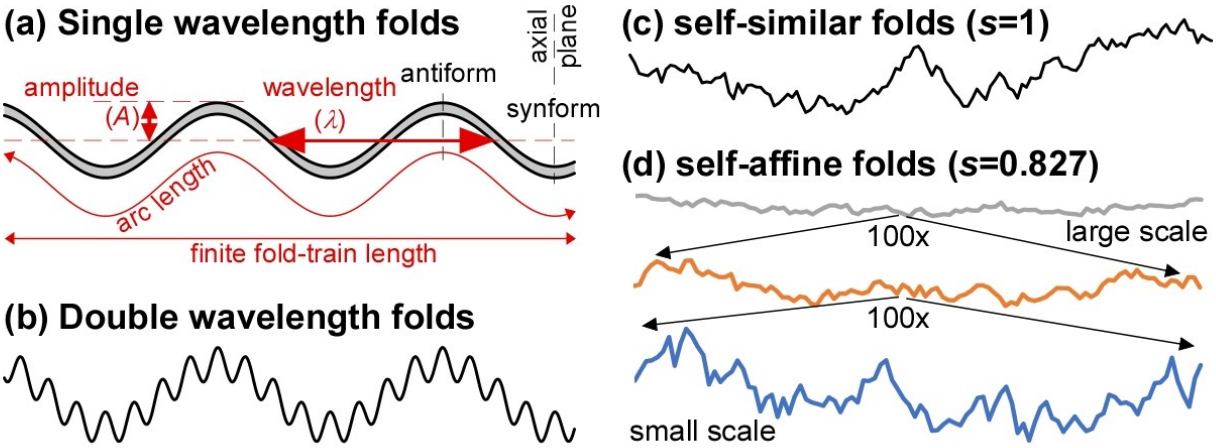

Figure 2. Fold shape and terminology. **(a)** Basic fold with a single wavelength. The arc length is the length of the fold train measured along the fold, while the finite length is the distance between the two ends of the fold train. **(b)** Fold composed of the superposition of two sine waves with different wavelengths and amplitudes. **(c)** Folds consistent of a range of wavelengths $\lambda_N = 1/N$, with N a whole number ranging from 1 to 650. The folds are self-similar as amplitude is linearly proportional to λ_N. The artificial fold train is sampled every 0.5 mm if the whole fold train is 65 mm, comparable to the length of fold trains analysed in the EGRIP drill core. **(d)** Example of a self-affine folds where the amplitude/wavelength ratio systematically decreases with scale (the exponent s is defined in Eq. 2).

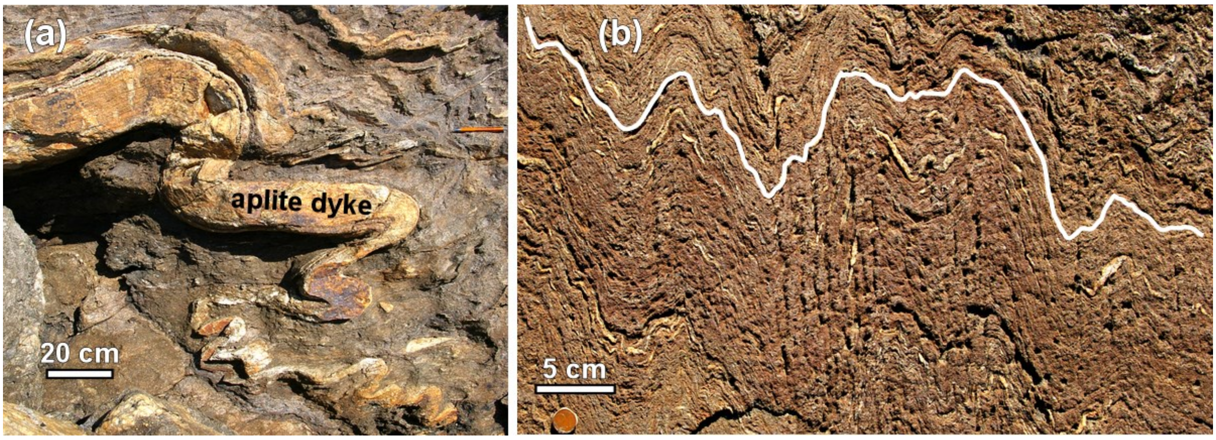

Figure 3. Examples of folds in rocks from Cap de Creus, northeast Catalonia, Spain. **(a)** Biot-type folding of a strong aplite dyke in a weaker granodiorite matrix. The example clearly shows the positive correlation between thickness of the dyke and wavelength that both decrease from the top left to the bottom right (Punta Fallarons; N42°20'25", E3°,15'48"). **(b)** Folded highly anisotropic biotite schist with thin quartz veins showing harmonic multi-wavelength folds. The hand-drawn white line was used for the analysis shown in Fig. 7b (Puig Culip; N42°19'19", E3°18'12").

of Ramsay and Huber (1987) and Twiss and Moores (2007), or to the extensive reviews by Nabavi and Fossen (2021) that also provides an overview of fold theory. Here we only provide a summary of the relevant terminology and theory based on the above publications, unless otherwise referenced.

Most fold trains roughly resemble a sinusoidal wavefunction (Fig. 2a). One individual fold consists of two limbs that meet at the fold hinge, which is the line of maximum curvature. When the fold hinges diverge downwards, the fold is termed an 'antiform', otherwise it is a 'synform'. Antiforms and synforms join at the inflection lines in the fold limbs where the direction of curvature changes sign. The terms 'anticline' and 'syncline' are reserved for folds in a stratigraphic sequence, and therefore apply to folds observed in radargrams or in cloudy bands, as these are assumed to represent sedimentary snow layers. Folds can have shapes that range from rectangular boxes, semi-ellipses, parabolas, sine waves, through to chevron or kink folds (Nabavi and Fossen, 2021). Box folds actually have two fold hinges per fold, but the authors are unaware of any box folds reported in ice. Ideal chevron or kink folds have straight limbs and highly concentrated curvature in the hinges. Such folds were described in ice drill core by Jansen et al. (2016). As most folds resemble a sine wave, the term 'wavelength' (λ) is one metric used to describe the length scale of folds. It is defined as double the distance between inflection lines in the directions of the fold train (Fig. 2a). Accordingly, the 'amplitude' (A) is defined as half the distance between the average antiformal and synformal hinge lines, measured in the direction perpendicular to the fold train. Folds can, however, have multiple wavelengths (Fig. 2b), in which case defining the amplitude becomes difficult. The arc length is the length of a line along the fold trace. The relative arc length ratio is the ratio of the arc length and the length of a straight line along the fold trace. The arc length is the same as the initial length if a layer only folds and does not become thicker or thinner during folding.

Folds may form when a composite material consisting of layers with different rheology is shortened parallel to the layers. The reason for this 'buckle folding' is that it is energetically more favourable to accommodate part of the shortening by bending the stronger layers at intervals (the fold hinges) and rotating the sections in between (the fold limbs). The weaker layers in between need to accommodate this deformation by deforming at a higher rate. Biot (1957) first developed the theory that the final fold wavelength is a function of the amplification rate of an infinite range of wavelengths of initial perturbations in the original layer. The basic idea is that the final wavelength is the one with the highest amplification rate. For a single layer with thickness H and linear viscosity η_l embedded in an infinite matrix with viscosity η_m he derived for the dominant wavelength λ_d:

$$\lambda_d = 2\pi H \left(\frac{\eta_l}{6\eta_m}\right)^{1/3} \tag{1}$$

Since Biot's pioneering work, many authors extended and refined his theory for multilayers, elastic components, slip or no slip between layers, and for non-linear (power-law) rheologies (see Table 2 in Schmalholz and Mancktelow, 2016). All these theories have in common that when the rheological difference between layers approaches zero, the dominant wavelength reduces to approximately the layer thickness. Wavelengths smaller than the layer thickness cannot be explained by Biot-type buckle-fold theory for layers with different rheological properties. It should also be noted that the fold amplification rate decreases with decreasing rheological contrasts (Llorens, 2019). This means that while relatively short wavelengths are possible at low rheological contrast between layers, one would not see the folds as their amplitude would be too small.

Very little work has been done on folding due to an intrinsic anisotropy, for example the alignment of easy-glide basal planes in ice or aligned micas in a schist. Biot-type buckle-fold theory cannot be simply applied as there is no layer thickness to provide a length scale. Without a length scale in the system, folds of all wavelengths should amplify at the same rate. Instead of folds with a dominant wavelength, one would expect folds where the amplitude of each wavelength is proportional to that wavelength (Fig. 2.c). In that case we get:

$$A_{(\lambda)} = \lambda_0 \cdot \lambda^s, \qquad (2)$$

with λ_0 a proportionality constant and s the scaling exponent. When s=1 the folds are self-similar, meaning that folds at all scale look similar because the scaling of amplitude and wavelength is identical (Fig. 2c). When s<1, large folds have relatively smaller amplitudes than small folds (Fig. 2d). When the scaling of amplitudes and wavelengths is not identical, the folds are self-affine.

3 Materials and methods

3.1 Materials

Metamorphic schists are mechanically highly anisotropic due to the alignment of platy mica grains into a foliation. Micas are comparable to ice Ih as the deform most easily along their basal planes (Duval et al., 1983; Finch et al., 2021). Metamorphic schists at Cap de Creus, NE Catalonia, Spain, show folding of the foliation due to Variscan deformation phase (Druguet et al., 1997, Bons et al., 2004). The mechanical anisotropy of the foliated rock is thought to play a dominant role in the deformation of these rocks (Carreras et al., 2013). We therefore use one outcrop as an example of folding of a strongly anisotropic rock in which layering is absent (Fig. 3b).

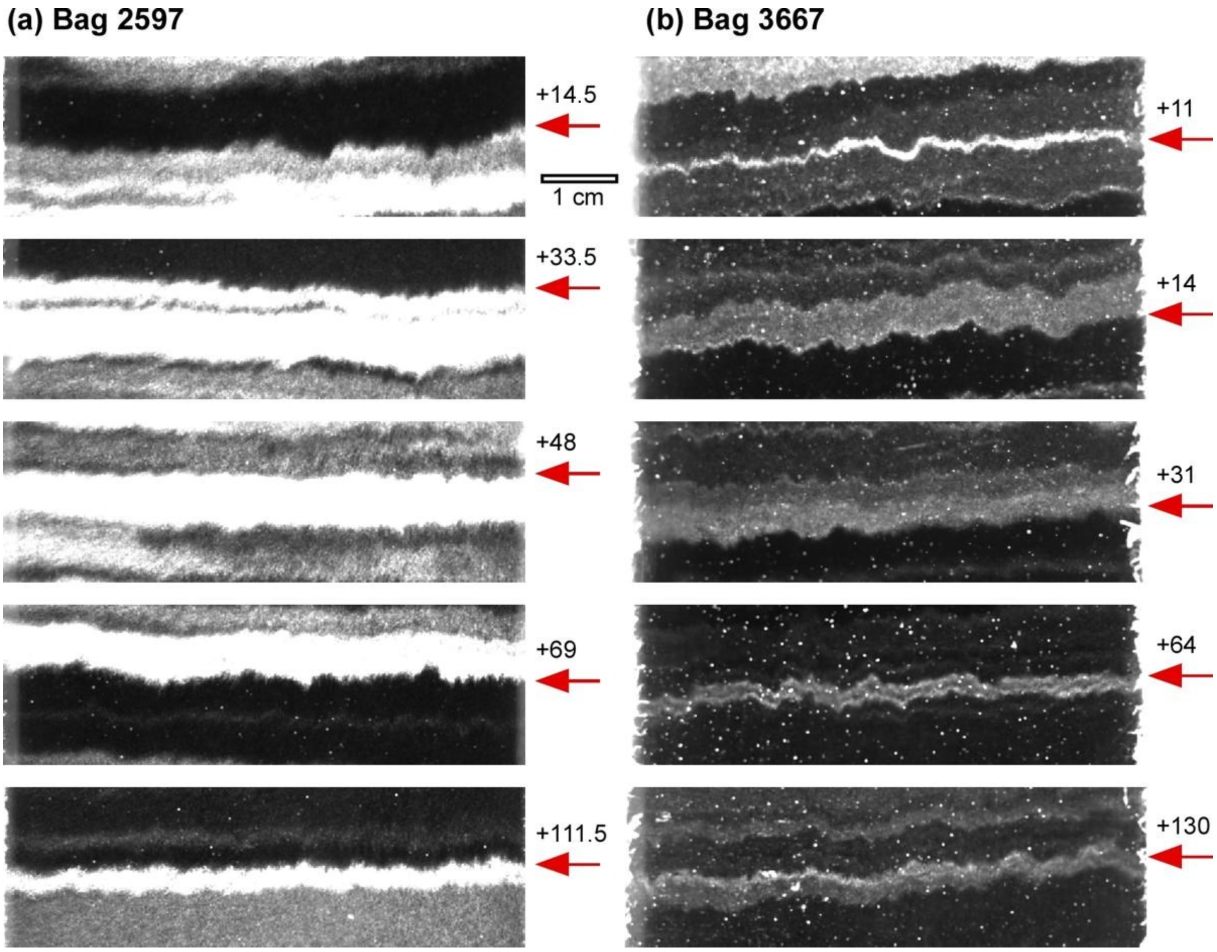

Figure 4. Images of ten of the 15 cloudy-band interfaces (red arrows) that were analysed in this study. Red arrows indicate the analysed cloudy band interface. [Editorial note: images of the third bag 3128 will be added for final submission to the journal]

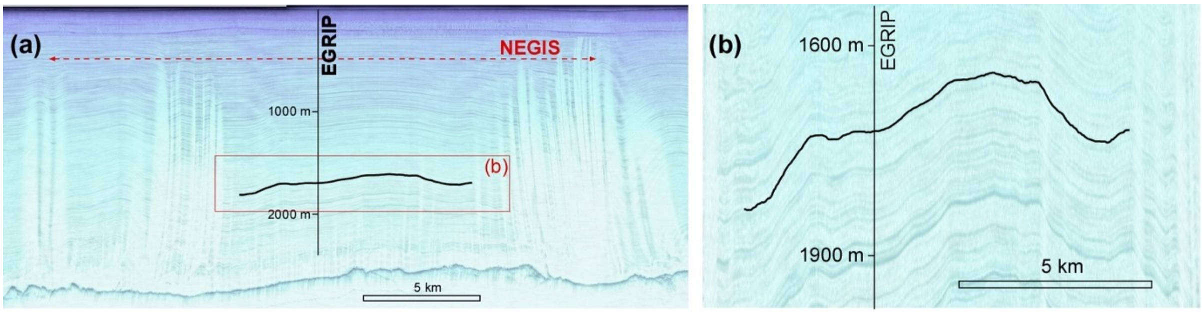

Figure 5. Traced internal reflection horizon (IRH) in a radargram going through NEGIS perpendicular to ice flow (ice flow into the page)- at the location where the EGRIP ice core is drilled. The radargram in **(a)** composed of profiles 20180508_06_004 and 20180514_03_001 (Franke et al., 2022b). **(b)** The same profile showing the centre of NEGIS at the vertical exaggeration at which the layer intersecting EGRIP at 1720 m depth was manually traced.

The East Greenland Ice Core Project (EGRIP) is a deep drilling project located in the middle of the Northeast Greenland Ice Stream (NEGIS) at 75°37.820 N and 35°59.556 W. Line scans of the drill core reveal cloudy bands. When the section of the core is suitably oriented relative to the flow direction, these cloudy bands show folds (Westhoff et al., 2021) (Fig. 2). Line scan images of bags 2597, 3128 and 3677, ranging in depth from 1428 down to 2016 m were used to analyse the folded cloudy bands (Fig. 4).

We use high-resolution radar data from the EGRIP-NOR-2018 survey (Franke et al., 2022b) from the onset region of NEGIS. The radar data were acquired in May 2018 with the AWI's (Alfred Wegener Institute) airborne multichannel ultra-wideband (UWB) radar and have a horizontal resolution of ~ 15 m and vertical resolution of 4.31 m. The radargrams used here are centered at the EGRIP drill site and run perpendicular to ice flow (Figure 5).

3.2 Methods

3.2.1. Numerical modelling

We use the full-field Viscoplastic Fast Fourier Transform (VPFFT) crystal plasticity code (Lebensohn, 2001; Lebensohn et al., 2008; Lebensohn and Rollett, 2020) , coupled with the modelling platform ELLE (http://www.elle.ws; Bons et al., 2008; Griera et al., 2013; Llorens et al., 2016a; Steinbach et al., 2016; Llorens et al., 2017; Piazolo et al., 2019; Ran et al., 2019; de Riese et al., 2019) to illustrate the fold geometries that form when ice Ih with a mechanically anisotropy is shortened. We used the VPFFT-code to simulate deformation of a crystalline material by glide along crystallographic planes. We use the crystallography of ice Ih, which is mechanically highly anisotropic due to much easier glide along its basal planes, compared to glide along the prismatic and pyramidal slip systems (Duval et al. 1983). We use a stress exponent of four (Bons et al., 2018) for the power-law relation between strain-rate and stress and assigned a 16-times higher slip resistance to the non-basal slip systems. At a given strain rate, the stress difference between the basal and non-basal slip systems is thus a factor 16. Details of this modelling approach can be found in Griera et al. (2013) and Llorens et al. (2017).

The 2D models consists of an initially square 256x256 grid of so-called *unodes* (Bons et al., 2008) that store the local lattice orientation. The *unodes* effectively represent crystallites or single grains with a constant internal crystal orientation, defined by three Euler angles. Using a Potts model we created 1995 clusters of identical orientation or grains. On average, each grain is almost 6x6 *unodes* in size. The basal planes of the initial model were aligned, so that the c-axes normal to the basal planes form a point maximum (with a standard deviation of 10°) parallel to the vertical extension direction. Using velocity boundary conditions, the square model was deformed by horizontal shortening of 2% per calculation step up to 40% shortening, accommodated by vertical stretching.

3.2.2. Fold analysis

Between the two end-member fold shapes of box and chevron folds, folds resemble a wave or the addition of multiple waves. Not surprising, Fourier analyses have been applied to folds for about50 years (Hudleston, 1973; Ramsay and Huber, 1987; Schmalholz and Mancktelow, 2016). This can be used to determine whether the fold train has a single dominant wavelength or is composed of folds of different wavelengths (Fig. 2). We therefore applied a Fast Fourier transform to fold contours of both natural and numerical folds.

We used 2044x31550 8-bit images of the line scans with a resolution of 18.6 pixel/mm from three images. Image 'bag 2597' (Fig. 4a) and 'bag 3128' had a suitable contrast, but a ca 2x contrast stretch was applied to 'bag 3677' (Fig. 4b) to achieve a sufficient contrast between dark and bright cloudy bands. In each bag five boundaries between dark and bright cloudy bands were selected that were both sharp and where the adjacent cloudy bands showed no significant lateral variation. A selection of the image was then subjected to a median filter with a 4-pixel radius to reduce small-scale noise and then thresholded to a binary image. The folded trace was subsequently selected by edge detection between the now black and white bands, resulting in the lines shown in Fig. 6a. Only the middle 65 mm of the ca. 70 mm wide drill core image was used to avoid artifacts at the edges of the image. The selection was scaled to 1024 pixels, or 65 mm, width. All this was done with the freeware ImageJ. A script selected the *y*-coordinates of the line for each *x*-coordinate along the trace. The equidistant *x,y*-data were then detrended by subtracting a linear least-squares best fit through the *x,y*-data. The detrended series of 1024 *y*-data was then subjected to a discrete Fourier transform using the routine four1() of Press et al. (1992). The power spectrum was obtained by taking the square root of the sum of the squares of the real and imaginary parts of the transform for each wavelength.

For the power spectrum of the numerical folds of Llorens et al. (2013), we applied the above method to a black-and-white image of one of the modelled folds (Fig 6c) in that paper to convert to upper boundary of the folded layer in a set of 1024 equidistant *x,y*-coordinates. For the large-scale folds in NEGIS, we used a radargram that spans across both shear zones of the NEGIS (Franke et al., 2022b) and is located closely (a few meters) to the EGRIP ice core (Fig. 5) and chose a conspicuous layer at 1720 m depth, close to 'bag 3128'. The layer was traced for 10 km, only within NEGIS to avoid effects of the higher strain in the shear margins. The image on which the layer was traced had a 14.3x vertical exaggeration. For the folded schist we used a 3008x2000 pixel field photograph (Fig3b). In each case the selected folded surface was handtraced in a drawing program (Canvas12) to create a line that was further processed the same way as the cloudy band interfaces.

In case of folds in an anisotropic material, simulated with Elle-FFT, a straight horizontal line, consisting of 102400 nodes, at a chosen level in the model, was subjected to deformation according to the velocity field that Elle-FFT records for each deformation step, up to the strain for which the power spectrum was to be calculated (Fig. 6b). The resulting line was then divided in 256 *x,y*-coordinates that are equidistant in the *x*-direction by interpolating between the original nodes, after which the procedure is the same as for digitised folds in the cloudy bands.

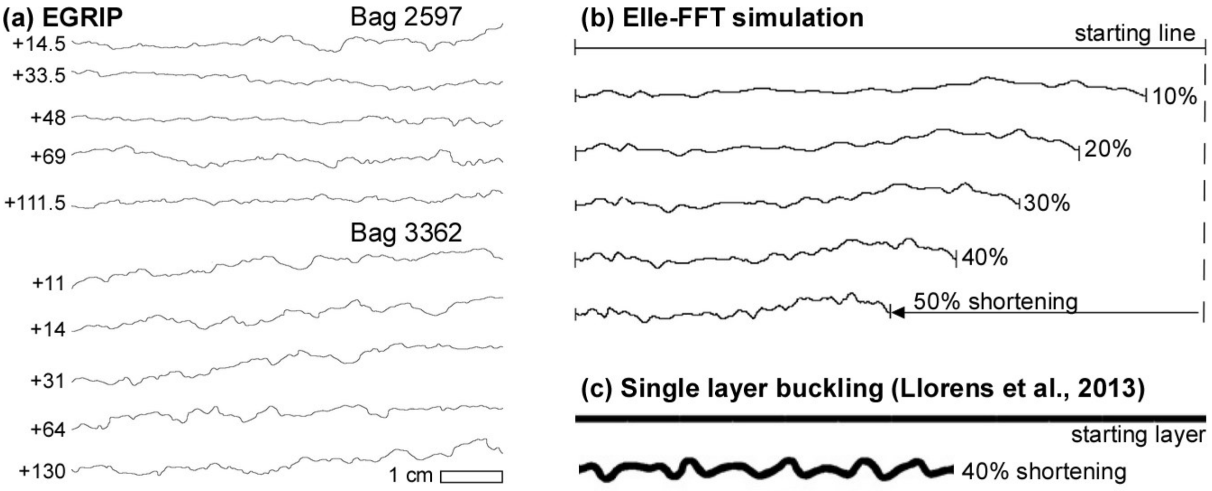

Figure 6. fold traces. **(a)** Traces of folded cloudy-band interfaces in the EGRIP drill core bags 2597 and 3362. Numbers on the left indicate the distance in cm from the top of the core section. **(b)** Traces of an originally horizontal line at different amounts of horizontal shortening in a simulation with Elle-FFT with pure ice Ih and initially a horizontal alignment of basal planes. **(c)** Example from fig 7c in Llorens et al. (2013) of single-layer buckling in a power-law material (*n*=3). [Editorial note: images of the third bag 3128 will be added to (a) for final submission to the journal]

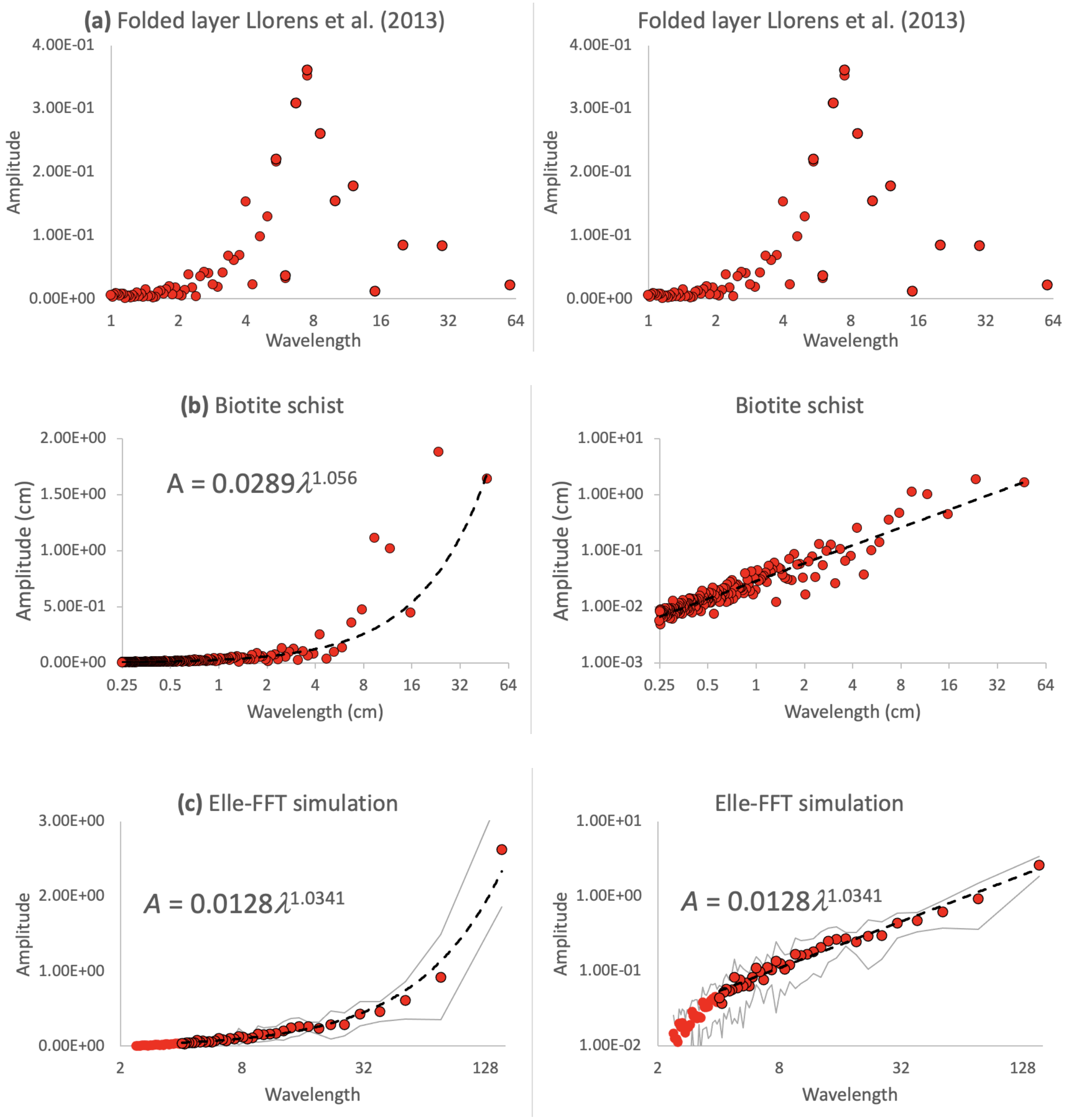

Figure 7. Power spectra of analysed folds. The vertical axis showing the amplitude is linear in the left column and logarithmic in the right column. **(a)** Numerical simulation of a single layer in a softer matrix (Llorens et al. 2013). The power spectrum shows a distinct peak at a wavelength of 8 length units with a total length of the fold train of 60 units. The layer had an initial length of 100 units **(b)** Folded foliation in the Biotite schist from Puig Culip shows an approximately self-similar power-law power-spectrum. **(c)** Numerical simulation with Elle-FFT of the folding of pure ice with an initial strong alignment of basal planes parallel to the shortening direction. Dots are the average of data sets in the model, while grey lines show the one standard deviation variation. The power spectrum follows an approximately self-similar power law from a wavelength of about 4 elements-widths of the initial 256x256 model.

4 Results

4.1 Single-layer buckle folds

Llorens et al. (2013) used finite-element modelling for folding of a competent single layer in a homogeneous softer matrix. They used an isotropic power law rheology relating strain rate ($\dot{\varepsilon}$) to differential stress (s):

$$\dot{\varepsilon} = B \cdot \sigma^{n} \qquad (3)$$

Here *B* is the pre-exponential factor and *n* the stress exponent that was set at *n*=3. We show (Fig. 7a) the power spectrum for 40% layer-parallel shortening of a layer of original length 100 and unit thickness. The layer was made 25 times stronger than the matrix by setting $B_{matrix}=25 \cdot B_{layer}$. The resulting fold (Fig. 6c) shows 8-9 distinct antiforms in the fold train, but no clear folds with other wavelengths. The power spectrum (Fig. 7a) shows a distinct peak at 7.5 times the original layer thickness for a fold-train length of 60 after 40% shortening. The initial wavelength was thus about 11-12 times the layer thickness.

4.2 Folded biotite schist

The folded foliation in the biotite schist from Puig Culip (Fig 3b) shows a power spectrum with a steady increase of the amplitude with the wavelength (Fig. 7b). A power-law best fit results in an exponent of approximately *s*=1, implying that the amplitude is linearly proportional with the wavelength (Eq. 2) and the folds are approximately self-similar.

4.3 Elle-FFT folding

We analysed ten equally spaced originally horizontal lines in the model of folding in ice with aligned basal planes. We chose a finite strain of 40% shortening, as the lines folded to achieve relative arc lengths of 1.14±0.2, comparable to those obtained from the cloudy bands (see below). Initially horizontal lines are folded with various wavelengths. Medium to large folds can be traced along their axial planes over many lines, suggesting that the folds are more harmonic than those in the cloudy bands if the model is assumed to have a comparative width as the EGRIP drill core.

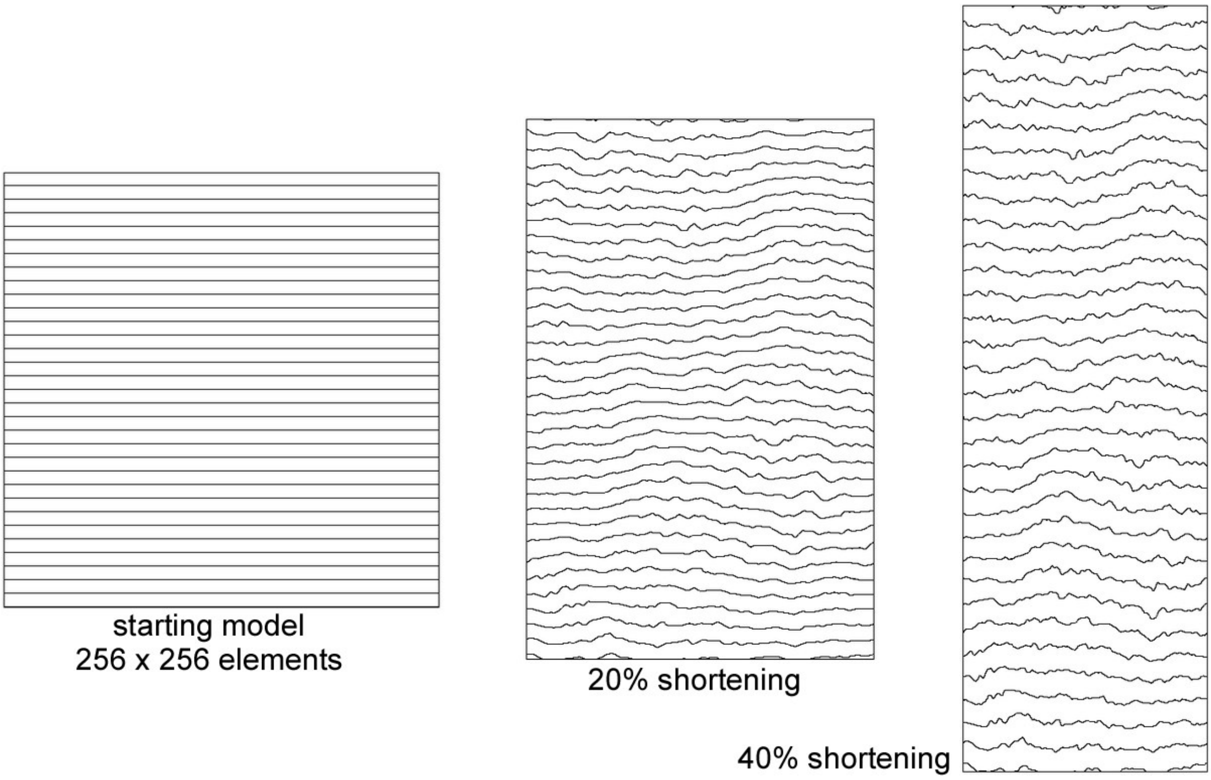
starting model
256 x 256 elements

20% shortening

40% shortening

Figure 8. Result of the Elle-FFT simulation showing the model at 0, 20 and 40% horizontal shortening that is compensated by vertical stretching in plane strain. Lines are passive markers originally aligned to the horizontally aligned basal planes.

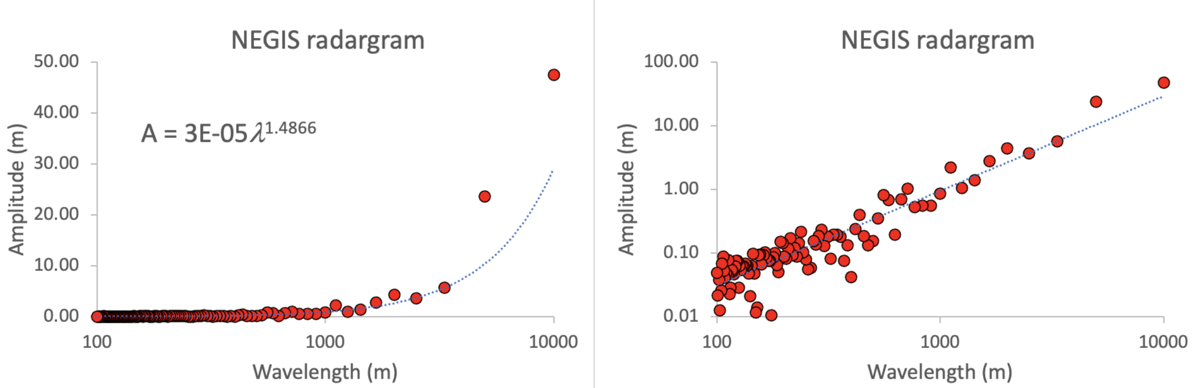

Figure 9. Power spectrum for the internal reflection horizon (IRH) in a radargram that intersects the EGRIP drill core at ca. 1720 m depth (Figure 5) traced over a distance of 10 km perpendicular to NEGIS' flow direction. A power-law best fit for $\lambda \geq 100$ m results in a scaling exponent of $s \approx 1.5$. The vertical amplitude axis is linear in the left column and logarithmic in the right column.

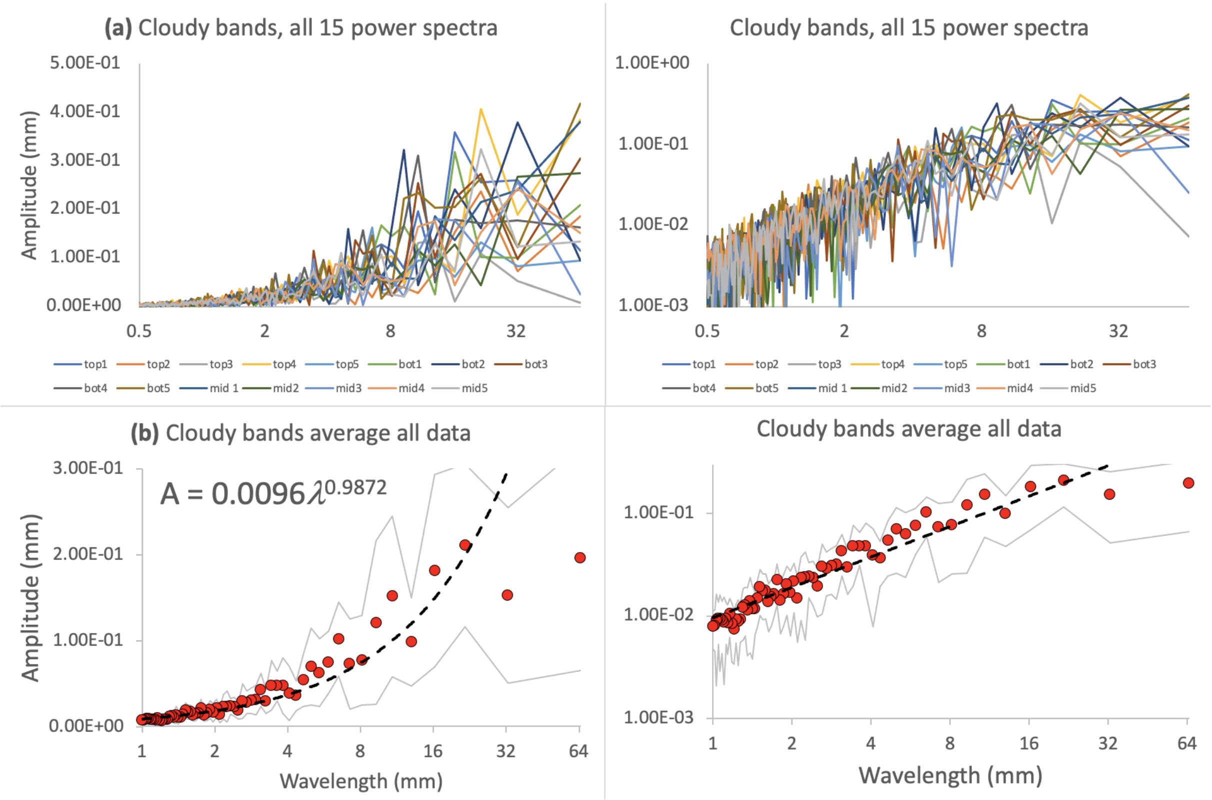

Figure 10. **(a)** Power spectra for all 15 individual cloudy-band interfaces shown in Fig. 4, five each, from bags 2597 (top), 3128 (mid) and 3677 (bot). The vertical axis is linear in the left column and logarithmic in the right column. Note the large spread at the longest wavelengths. **(b)** Power spectrum of the average of the 15 power-spectra, shown together with plus/minus one standard deviation (grey lines) of the variation in powers. Up to $\lambda \approx 20$ mm the data roughly follow a self-similar power law.

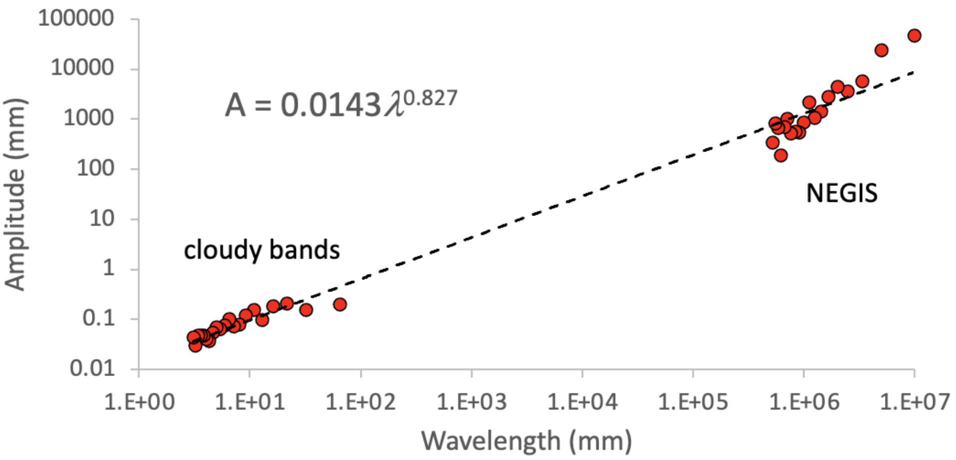

Figure 11. Combined power spectra of cloudy-band interfaces and the internal reflection horizon (IRH), showing the 40 largest wavelengths of each spectrum. A power-law best fit through these data gives an exponent s=0.827, suggesting that folding is self-affine (Fig. 2d), with large folds relatively flat compared to small folds.

The power spectrum shows a steady increase in power with wavelength from λ≈4 initial element widths (Fig. 7c), which is approximately the mean grain width after 40% horizontal shortening $A_{(\lambda)}$ increases approximately linear with λ, i.e., s≈1. This means that the folds are self-similar: their shape is independent of their wavelength.

The 1720 m depth layer in NEGIS shows a power-law amplitude-wavelength trend with s≈1.5 upwards from l=100 m (Fig. 9). This indicates that there is no characteristic wavelength and that small folds are flatter in shape than large folds. However, the fold trace may be too smooth on the small scale to correct for small vertical shifts and steps in reflector depths that are artifacts related to surface elevation variations. A reduction in amplitudes at low wavelengths would increase the exponent s.

4.4 Cloudy bands

Cloudy bands have a variety of widths, ranging from about a mm to a few cm (Fig. 1 and 4). However, it is difficult to define the thickness of one band, as what appears like one dark or bright band may itself be composed of several thinner bands of different brightness (Stoll et al., 2023). All interfaces are folded on the mm to cm scale (Figs. 1 and 4). Folding is most conspicuous in the interfaces of very bright and very dark bands. The folds are upright with mostly vertical axial planes, although some zones with tilted axial planes were observed (Westhoff et al., 2021). Folds are disharmonic, meaning that individual axial planes can rarely be traced from one interface to another, i.e., for more than about 5 mm (Fig. 1). This means that the folds in individual interfaces appear independent of those in the next. Relative arc length ratios of the 15 folded interfaces are on average 1.15 (±0.03 standard deviation).

The individual and average power or amplitude spectra of the 15 folded interfaces at the three selected depths show no significant differences (Fig 10a). We therefore averaged the powers for each wavelength, as shown in Fig. 10b. We see that the amplitudes first increase up to a wavelength of about 2 mm, followed by a shallower, linear (s≈1) increase up to about l=20 mm. The amplitudes of the largest two wavelengths are below the trend, but it cannot be ascertained whether this is significant, or merely due to the large variation in amplitudes. No dominant wavelength well below 65 mm was observed.

5 Discussion

Folds in the cloudy bands do not show a dominant wavelength in the wavelength range shorter than the width of the drill core section (Fig. 10). The power spectra of the 15 sampled fold traces all overlap and show no significant variation between them, although the cloudy bands immediately adjacent vary in thickness from 1 mm to >1 cm. Both observations suggest that the folding has no characteristic length scale. In case of Biot-type buckle folding, this would be the thickness of the layers, here the cloudy bands. For Biot-type buckle folding one would expect shorter wavelength of the folds in the ca. 1 mm thick cloudy band 3667+11 than in the ten times thicker one 3667+14, only 3 cm below in the drill core. Multiple-wavelength folds can develop in multi-layers (e.g., Fig. 11 in Frehner and Schmalholz, 2006). These form by the addition of different characteristic wavelengths of layers with different thickness and or rheology. However, harmonic folds are then expected with axial planes extending across several layers that contributed to the multi-wavelength folds. In case of the analysed cloudy bands this is not the case, as the axial planes rarely extend for more than 5-10 mm. These observations suggest that the folds in the cloudy bands are not the result of Biot-type buckling due to rheological differences between individual cloudy bands, where a high viscosity contrast between layers (>=25) is required for folding (Llorens et al., 2013).

The cloudy band folds resemble folds in the biotite schist (Figs. 3b, 7b) and the numerical ELLE-FFT folds in ice with a strong CPO (Figs. 7c, 8) much more than Biot-type buckle folds (Fig. 3a, 6c, 7a). This holds for both a visual assessment and for the power spectra. Shortening parallel to an intrinsic initial (before onset of folding) mechanical anisotropy due to a CPO is therefore the preferred mechanism to explain the observed folding in the cloudy bands, as was already suggested by Jansen et al. (2016). We observe a similar lack of a characteristic wavelength in the large-scale folds inside NEGIS (Fig. 9). This supports the suggestion by Bons et al. (2016) that such large-scale folding is also due to shortening parallel to the CPO-induced anisotropy.

Folding of an intrinsic anisotropy has no typical length scale, which explains the close to self-similar ($s \approx 1$) power spectra of the cloudy-band interfaces. If the folds were perfectly self-similar and the self-similar range would extend to the 10 km scale that we observe in the traced IRH in the radargram, we would expect folds about seven times taller than the folds we actually observe (Fig. 5).

Unfortunately, we do not have sufficiently detailed observations in the length-scale range from 10 cm to about 100 m. It is therefore possible that the power spectra between the small and large scale show a break. Another possibility is that the scales are related and that the folds are self-affine. A power-law best fit through the cloudy-band and radargram folds results in a scaling exponent of $s \approx 0.8$ (Fig. 11). This would mean that the folds gradually get flatter with increasing scale. Reasons for this could be the effect of the ice-sheet surface, where gravity counteracts the development of surface topography due to folding. An additional effect could be the bedrock topography that imposes a second set of folds on top of the anisotropy-induced folds. Unfortunately, the radargrams are of poor quality for the detailed fold analyses that are applied here. A more systematic analysis of the large-scale folds is needed, but outside the scope of this study.

6 Conclusions

We used power spectra of fold traces to determine the mechanism for folding in ice sheets. Biot-type buckle folds due to rheological contrasts between layers have a characteristic length scale, related to the layer thickness and the rheological contrast between the layers. Numerical simulation of ice with a strong alignment of basal planes parallel to the shortening direction resulted in the development of self-similar folds with a power-law power spectrum. This is to be expected as anisotropy has no length scale. Self-similar folds were also observed in folded biotite schist and in cloudy bands in the EGRIP drill core. We therefore conclude that small-scale folds in cloudy bands are due to shortening parallel to a strong anisotropy as a result of the initial lattice preferred orientation with horizontally aligned basal planes. The spectrum of one 10 km-long traced layer inside NEGIS indicated self-affine folding. Combining the small cloudy band folds and large NEGIS-scale folds resulted in a self-affine trend, where largest folds are relatively flat. This may be caused by additional boundary conditions, such as vertical flattening and bedrock irregularities, that modify the anisotropy-induced folds on the large scale.

References

Alley, R. B., Gow, A. J., Meese, D. A., Fitzpatrick, J. J., Waddington, E. D. and Bolzan, J. F.: Grain-scale processes, folding, and stratigraphic disturbance in the GISP2 ice core, Journal of Geophysical Research: Oceans,102, 26819–26830, doi: https://doi.org/10.1029/96JC03836, 1997.

Bell, R. E., Tinto, K., Das, I., Wolovick, M., Chu, W., Creyts, T.T., Frearson, N., Abdi, A. and Paden, J.D.: Deformation, warming and softening of Greenland's ice by refreezing meltwater. Nature Geoscience, 7(7), pp.497-502, doi: https://doi.org/10.1038/ngeo2179, 2014.

Biot, M. A.: Folding Instability of a Layered Viscoelastic Medium under Compression. Proceedings of the Royal Society A: Mathematical, Physical and Engineering Sciences, 242(1231), 444–454. DOI: https://doi.org/10.1098/rspa.1957.0187, 1957.

Bohleber, P., Stoll, N., Rittner, M., Roman, M., Weikusat, I. and Barbante, C.: Geochemical characterization of insoluble particle clusters in ice cores using two-dimensional impurity imaging. Geochemistry, Geophysics, Geosystems, 24, e2022GC010595. doi:10.1029/2022GC010595, 2022.

Bons, P. D., Druguet, E., Hamann, I., Carreras, J. and Passchier, C.W.: Apparent boudinage in dykes. Journal of Structural Geology, 26, 625-636, doi:10.1016/j.jsg.2003.11.009, 2004.

Bons, P. D., Koehn, D. and Jessell, M.W. (Eds): Microdynamic Simulation. Lecture Notes in Earth Sciences 106, Springer, Berlin. 405 pp. ISBN 978-3-540-44793-1, 2008.

Bons, P. D., Jansen, D., Mundel, F., Bauer, C.C., Binder, T., Eisen, O., Jessell, M.W., Llorens, M.G., Steinbach, F., Steinhage, D. and Weikusat, I.: Converging flow and anisotropy cause large-scale folding in Greenland's ice sheet. Nature communications, 7(1), p.11427, doi: 10.1038/ncomms11427, 2016.

Budd, W. F., and Jacka, T. H.: A review of ice rheology for ice sheet modeling. Cold Regions Science and Technology, 16, 107–144. Doi: https://doi.org/10.1016/0165-232X(89)90014-1. 1989.

Carreras, J., Cosgrove, J. W. and Druguet, E.: Strain partitioning in banded and/or anisotropic rocks: Implications for inferring tectonic regimes. J. Struct. Geol. 50, 7-21. doi:10.1016/j.jsg.2012.12.003, 2013.

Druguet, E., Passchier, C. W., Carreras, J., Victor, P. and den Brok, S. W. J.: Analysis of a complex high-strain zone at Cap de Creus, Spain. Tectonophysics, 280, 31-45, doi: 10.1016/S0040-1951(97)00137-6, 1997.

Duval, P., Ashby, M. F. and Anderman, I.: Rate-controlling processes in the creep of polycrystalline ice. J. Phys. Chem. 87, 4066–4074, doi: https://doi.org/10.1021/j100244a014, 1983.

Faria, S. H., Freitag, J., and Kipfstuhl, S.: Polar ice structure and the integrity of ice-core paleoclimate records, Quaternary Sci. Rev., 29, 338–351, doi: 10.1016/j.quascirev.2009.10.016, 2010

Faria, S. H., Weikusat, I., and Azuma, N.: The microstructure of polar ice. Part II: State of the art. Journal of Structural Geology, 61, 21–49. doi:10.1016/j.jsg.2013.11.003, 2014.

Finch, M.A., P.D.Bons, P.D., Steinbacha, F., Griera, A., Llorens, M.-G, Gomez-Rivase, E. Ran, H. and de Riese, T.: The ephemeral development of C' shear bands: A numerical modelling approach. J. Struct. Geol. 139. Doi: https://doi.org/10.1016/j.jsg.2020.104091, 2020.

Fitzpatrick, J. J., Voigt, D. E., Fegyveresi, J. M., Stevens, N. T., Spencer, M. K., Cole-Dai, J., Alley, R. B., Jardine, G. E., Cravens, E. D., Wilen, L. A., Fudge, T. J., and McConnell, J. R.: Physical Properties of the WAIS Divide ice core, J. Glaciol., 60, 1181–1198, doi:10.3189/2014JoG14J100, 2014.

Franke, S., Bons, P. D., Westhoff, J., Weikusat, I., Binder T., Streng, K., Steinhage, D., Helm, V., Eisen, O., Paden, J. D., Eagles, G. and Jansen, D.: Holocene ice-stream shutdown and drainage basin reorganization in northeast Greenland. Nature Geoscience, 15, 995–1001. https://doi.org/10.1038/s41561-022-01082-2, 2022a

Franke, S., Jansen, D., Binder, T., Paden, J. D., Dörr, N., Gerber, T. A., Miller, H., Dahl-Jensen,D., Helm, V., Steinhage, D., Weikusat, I., Wilhelms, F., and Eisen, O.: Airborne ultra-wideband radar sounding over the shear margins and along flow lines at the onset region of the Northeast Greenland Ice Stream, Earth Syst. Sci. Data, 14, 763–779, doi: https://doi.org/10.5194/essd-14-763-2022, 2022b.

Frehner, M. and Schmalholz, S.M.: Numerical simulations of parasitic folding in multilayers. Journal of Structural Geology 28, 1647-1657, doi: https://doi.org/10.1016/j.jsg.2006.05.008, 2006.

Glen, J. W.: The creep of polycrystalline ice. Proceedings of the Royal Society of London A: Mathematical, Physical and Engineering Sciences, 228(1175), 519–538. The Royal Society, doi: 10.1098/rspa.1955.0066,1955.

Griera, A., Llorens, M.-G., Gomez-Rivas, E., Bons, P. D., Jessell, M. W., Evans, L. A. and Lebensohn, R.: Numerical modelling of porphyroclast and porphyroblast rotation in anisotropic rocks. Tectonophysics, 587, 4–29. DOI: https://doi.org/10.1016/j.tecto.2012.10.008, 2013.

Hudleston, P.J.: An analysis of “single-layer” folds developed experimentally in viscous media. Tectonophysics 16 (3–4), 189–214. doi:10.1016/0040-1951(73)90012-7, 1973.

Hudleston, P.J., Structures and Fabrics in Glacial Ice: A Review, Journal of Structural Geology, 81, 1-27, doi: https://doi.org/10.1016/j.jsg.2015.09.003, 2015.

Jansen, D., Llorens, M.-G, Westhoff, J., Steinbach, F., Kipfstuhl, S., Bons, P.D., Griera, A. and Weikusat, I., Small-scale disturbances in the stratigraphy of the NEEM ice core: observations and numerical model simulations. The Cryosphere 10, 359-370. doi: https://doi.org/10.5194/tc-10-359-2016, 2016.

Krabbendam, M.: Sliding of temperate basal ice on a rough, hard bed: creep mechanisms, pressure melting, and implications for ice streaming. The Cryosphere, 10(5), pp.1915-1932, doi: https://doi.org/10.5194/tc-10-1915-2016, 2016.

Lebensohn, R. A.: N-site modeling of a 3D viscoplastic polycrystal using Fast Fourier Transform. Acta Materialia, 49, 2723-2737. Doi: https://doi.org/10.1016/S1359-6454(01)00172-0, 2001.

Lebensohn, R. A.: Brenner, R., Castelnau, O. and Rollett, A. D.: Orientation image-based micromechanical modelling of subgrain texture evolution in polycrystalline copper. Acta Materialia, 56, 3914-3926. Doi: https://doi.org/10.1016/j.actamat.2008.04.016, 2008.

Lebensohn, R. A. and Rollett, A. D.: Spectral methods for full-field micromechanical modelling of polycrystalline materials. Computational Materials Science, 173, 109336. Doi: https://doi.org/10.1016/j.commatsci.2019.109336, 2020.

Leysinger Vieli, G. M., Martin, C., Hindmarsh, R. C. A. and Lüthi, M. P.: Basal freeze-on generates complex ice-sheet stratigraphy. Nature communications, 9(1), p.4669. doi: https://doi.org/10.1038/s41467-018-07083-3, 2018.

Llorens, M.- G., Bons, P. D., Griera, A., Gomez-Rivas, E. and Evans, L. A.: Single layer folding in simple shear, J. Struct. Geol., 50, 209-220, https://doi.org/10.1016/j.jsg.2012.04.002, 2013.

Llorens, M.- G.: Stress and strain evolution during single-layer folding under pure and simple shear. Journal of Structural Geology, 126, pp.245-257, doi: 10.1016/j.jsg.2019.06.009, 2019

Llorens, M.-G., Griera, A., Steinbach, F., Bons, P. D., Gomez-Rivas, E., Jansen, D., Roessiger, J., Levensohn, R. A. and Weikusat, I.: Dynamic recrystallisation during deformation of polycrystalline ice: insights from numerical simulations. Philosophical Transactions of the Royal Society A, Special Issue on Microdynamics of Ice, 375: 20150346. DOI: https://doi.org/10.1098/rsta.2015.0346, 2017.

Nabavi, S. T., and Fossen, H.: Fold geometry and folding – a review, Earth-Science Reviews, 222, 103812, doi:10.1016/j.earscirev.2021.103812, 2021.

NEEM community members: Eemian interglacial reconstructed from a Greenland folded ice core. Nature 493, 489–494, doi: https://doi.org/10.1038/nature11789, 2013.

Press, W. H., Teukolsky, S. A. and Vetterling, W. T., Flannery, B. P. Numerical recipes in C, 2nd Ed. Cambridge University Press, Cambridge. 994 pp., 1992.

Ramsay, J. G. and Huber, M. I.: The Techniques of Modern Structural Geology: Folds and Fractures, Vol. 2. Academic Press, London, 1987.

Schmalholz, S. M. and Mancktelow, N. S.: Folding and necking across the scales: a review of theoretical and experimental results and their applications. Solid Earth, 7, 1417-1465. doi: https://doi.org/10.5194/se-7-1417-2016. 2016.

Stoll, N., Westhoff, J., Bohleber, P., Svensson, A., Dahl-Jensen, D., Barbante, C., and Weikusat, I.: Chemical and visual characterisation of EGRIP glacial ice and cloudy bands within, The Cryosphere Discuss., doi: https://doi.org/10.5194/tc-2022-250, in review, 2023.

Svensson, A., Wedel Nielsen, S., Kipfstuhl, S., Johnsen, J., Steffensen, J. P., Bigler, M., Ruth, U., and Röthlisberger, R.: Visual Stratigraphy of the North Greenland Ice Core Project (NorthGRIP) ice core during the last glacial period, J. Geophys. Res., 110, D02108, doi:10.1029/2004JD005134, 2005.

Thorsteinsson, T.: Textures and fabrics in the GRIP ice core, in relation to climate history and ice deformation (Thesis), Berichte zur Polarforschung, AWI Bremerhaven, Bremerhaven, 120–133, 1996

Weertman, J.: Creep deformation of ice. Annual Review of Earth and Planetary Sciences, 11(1), 215–240. doi:10.1146/annurev.ea.11.050183.001243, 1983.

Westhoff, J., Stoll, N., Franke, S., Weikusat, I., Bons, P., Kerch, J., Jansen, D., Kipfstuhl, S. and Dahl-Jensen, D.: A Stratigraphy Based Method for Reconstructing Ice Core Orientation. Annals of Glaciology, 62 (85-86), 191-202, https://doi.org/10.1017/aog.2020.76, 2021

Wolovick, M. J., Creyts, T. T., Buck, W. R. and Bell, R. E.: Traveling slippery patches produce thickness-scale folds in ice sheets. Geophysical Research Letters, 41(24), pp.8895-8901, doi: 10.1002/2014GL062248, 2014.

PAPER IV

Folded ice reveals: the North East Greenland Ice Stream was fully established only 2000 years

Daniela Jansen[1], Steven Franke[1,2], Catherine C. Bauer[2], Tobias Binder[1,3], Dorthe Dahl-Jensen[4], Jan Eichler[1], Olaf Eisen[1,5], **Yuanbang Hu[2,6]**, Johanna Kerch[1,7] Maria-Gema Llorens[8], Heinz Miller[1], Niklas Neckel[1], John Paden[9], Tamara de Riese[2], Till Sachau[2], Nicolas Stoll[1], Ilka Weikusat[1,2], Frank Wilhelms[1,7] Yu Zhang[2], Paul D. Bons[2,10]

[1] Alfred Wegener Institute Helmholtz Centre for Polar and Marine Research, Bremerhaven Germany

[2] Department of Geosciences, Tübingen University, Tübingen, Germany

[3] Now at Ibeo automotive Systems, Hamburg, Germany

[4] Niels Bohr Institute, Physics of Ice, Climate and Earth, University of Copenhagen, Copenhagen, Denmark

[5] University of Bremen, Bremen, Germany

[6] College of Earth Science, Chengdu University of Technology, Chengdu, China

[7] Geowissenschaftliches Zentrum, Georg-August University Göttingen, Germany

[8] Geosciences Barcelona - CSIC, Barcelona, Spain

[9] Center for Remote Sensing and Integrated Systems (CReSIS), University of Kansas, Lawrence, KS, USA

[10] School of Earth Science and Resources, China University of Geosciences (Beijing), Beijing, China

Abstract

Only a few localised ice streams drain most ice from the Greenland Ice Sheet. Thus, understanding ice stream behaviour and their temporal variability is crucially important to predict future sea-level change. The interior trunk of the 700 km-long North-East Greenland Ice Stream (NEGIS) is remarkable for the lack of any clear bedrock channel to explain its presence. We present the first-ever 3-dimensional analysis of folding and advection of stratigraphic horizons, which shows that the localised flow and shear margins in the upstream

part were fully developed only ca. 2000 years ago. Our results contradict the assumption that the ice stream has been stable throughout the Holocene in its current form and show that NEGIS-type ice streams can appear suddenly on short time scales, which is a major challenge for realistic mass-balance and sea-level rise projections.

1 Introduction

A significant percentage of discharge of ice into the oceans takes place by solid ice flow via ice streams[1,2]. These are river-like zones where ice flow is significantly faster than in their surroundings, assumed to be triggered by either bedrock properties[3,4], enhanced sliding[2,5], and/or by deformation mechanisms leading to shear localization[6]. The most conspicuous one in Greenland is the North East Greenland Ice Stream (NEGIS; Fig. 1a), which extends for about 700 km inland from its outlets in northeast Greenland, and its catchment area covers 17 % of the ice sheet area[7].

NEGIS reaches up to the central ice divide (Fig. 1a), but while the gates in the coastal mountain range in northeast Greenland clearly determine the location of the coastal outlet, its course in the interior of the ice sheet appears not to be constrained by bed topography[10–12]. The flow velocity increases from about 3 m yr^{-1} close to the divide to 55 m yr^{-1} at the EGRIP drilling camp[8,13], ca 40 m yr^{-1} faster than the ice flow directly adjacent to NEGIS. The present-day shape and surface velocity of NEGIS are well constrained by satellite observations[8], but much less is known about the spatial and temporal evolution of the stream, and the processes which trigger the exceptionally high flow velocities in its upstream region. Satellite and GPS measurements show that NEGIS is accelerating slightly, indicating that the ice-dynamic regime is possibly not in equilibrium[14]. Previously it was assumed that NEGIS existed in its current shape at least during most of the Holocene, and that its presence can be explained by an area of strongly enhanced geothermal heat flux at its upstream end[10] causing substantial basal melting of the ice sheet. To explain the annual layer thickness along the ice column, Fahnestock et al. (2001)[10] suggest a basal ice loss of ~ 0.1 m per year over the last 9 kyrs. This would require an exceptionally high geothermal heat flux of 950 mWm^{2}. However, a comparison with global geothermal heat fluxes shows that the proposed values exceed natural heat fluxes by about an order of magnitude[15].

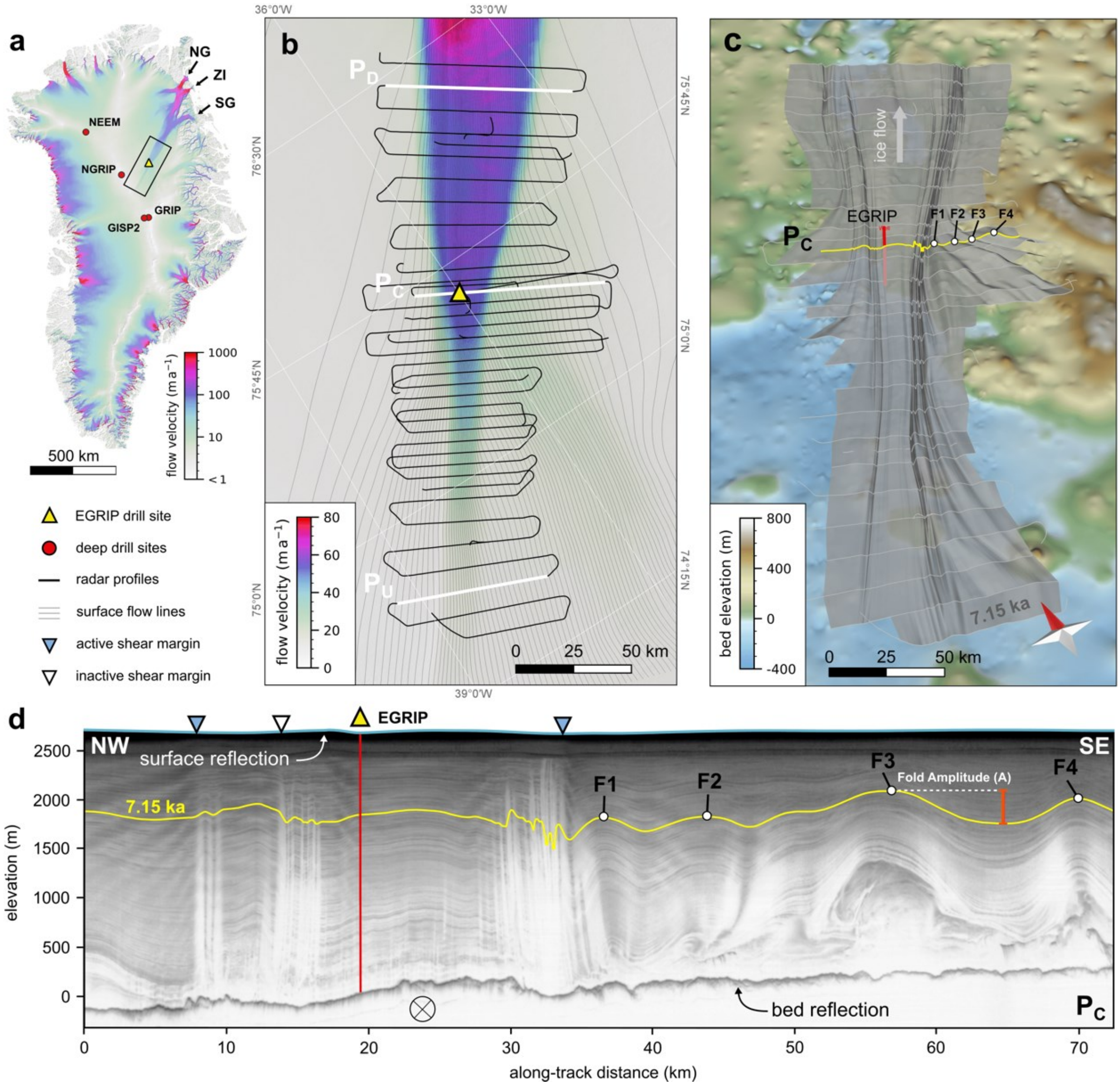

Figure 1: Area and outline of the radar survey. (**a**, **b**) Maps of the survey area and radar lines with ice flow velocity[8]. NG: Nioghalvfjerdsfjorden Glacier, ZI: Zachariae Isstrøm, SG: Storstrømmen Glacier. Radar profile P_C is shown in panel (**d**) and in Figure 2b, P_U and P_D are shown in Figure 2a,c. (**c**) 7150 years BP isochrone horizon as a shaded relief above bedrock[9] (10 times vertical exaggeration). F1-F4 indicate the location of fold anticlines also highlighted in the radar profile P_C in panel (**d**). The location of P_C is indicated by a yellow line. (**d**) Profile P_C across NEGIS in the centre of the survey area. F1-F4 indicate the anticlines highlighted in panel (**c**).

Here we use isochronous radar reflections as passive tracers of ice deformation to reveal the history of NEGIS over the past few thousand years, and show that the shear margins that define it in its present form in the upstream region have been active for only about the last 2000 yrs. This indicates that streaming can be triggered on short time scales, leading to abrupt ice-flow reconfigurations[16], which is contradictory to it being triggered and sustained by a local, long-term heat flow anomaly[10,17].

2 Radar Stratigraphy

The data presented in this study have been derived from an airborne radar survey in May 2018 using an ultra-wide-band radar system (AWI-UWB[18,19]) with an array of 8 transmitters and receivers mounted beneath the fuselage of the AWI aircraft Polar 6[20]. The layout of the survey was designed for mapping radar stratigraphy and bedrock properties in the vicinity of the EGRIP drilling camp, with an area stretching along flow from 150 km upstream of the camp to 150 km downstream. The profiles used in this study were recorded in narrow-band mode, with the frequency range set to 180-210 MHz. Due to the focus on stratigraphy, the radar lines are mostly perpendicular to ice flow in order to best reproduce the deformation pattern in the shear margins. Here we only use data from across-flow profiles (Fig. 1b). The distance between the profiles is 5 km in the central part of the survey region, in the outer area the distance is 10 km.

The ages of distinct layers in the radargrams were derived from tracing to or correlating layers at the EGRIP drill site where ages are known as a function of depth[21]. This results in a set of layers with known depositional ages. In the central profile up to 21 layers < 8 kyrs BP old could be connected to the EGRIP site, while in the downstream profile this number was reduced to at least five. The error in dating of the reference layers is in the order of a few tens of years for the youngest few thousand-year-old layers, increasing to over 100 years towards 8 kyrs BP layers. Most layers within one fold limb cannot be traced all the way to the drill site or can be recognised in the radargram at that site. Their ages are estimated by interpolation (see methods).

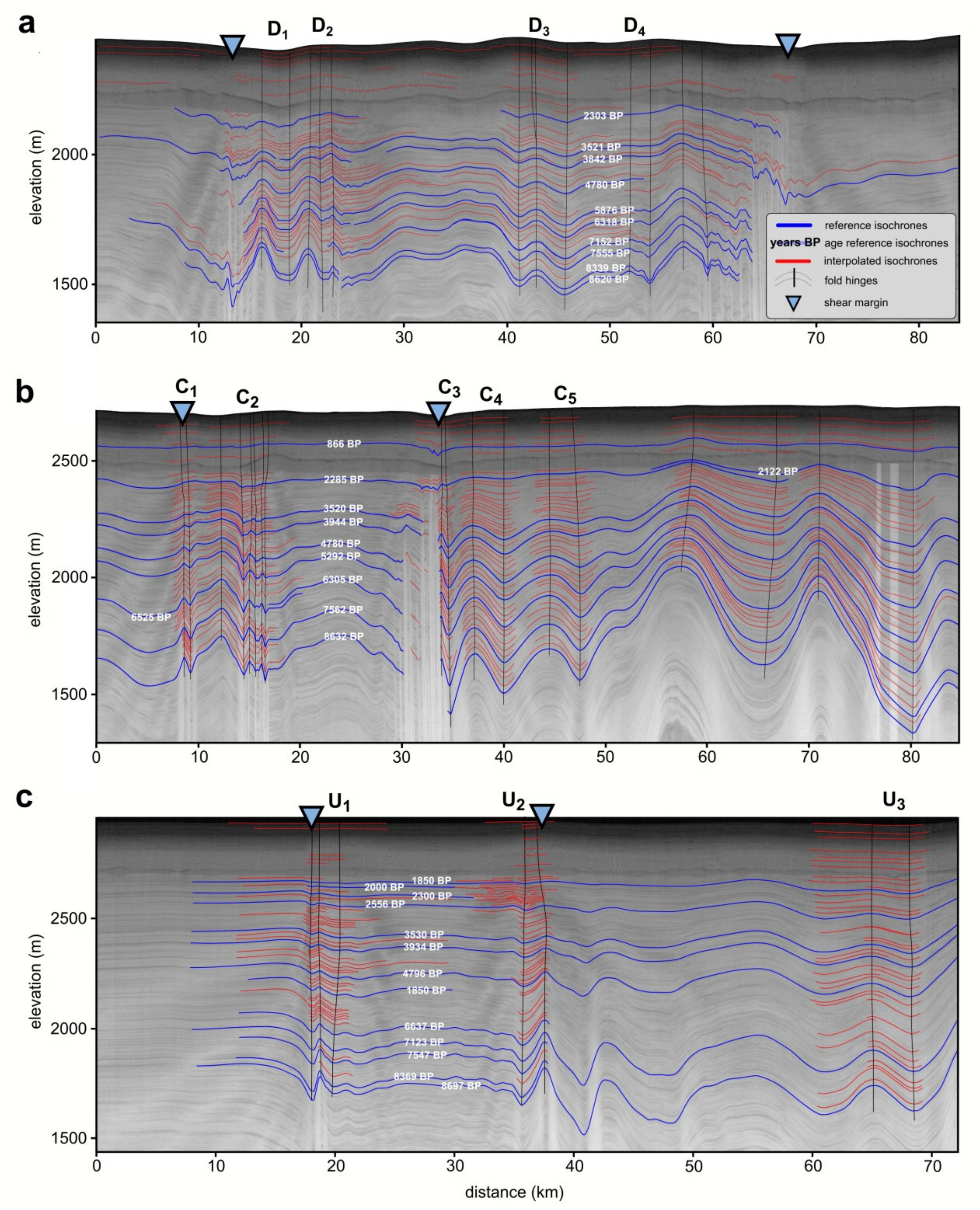

Figure 2: Radar sections with the picked layers for fold analysis and the reference age horizons. Black lines indicate the hinge position of the syn- and anticlines. Letters at the top identify folds in amplitude age plots in Figure 3. **(a)** Upstream radar profile U, composed of one radar track frame (20180514_03_014). **(b)** Central radar profile C, composed of 2 radar tracks (20180508_06_004 and 20180514_03_001). **(c)** Downstream radar profile D, composed of 2 frames (20180509_01_009 and 20180509_01_010).

3 Folds in ice: a record of deformation

Disturbances in radar isochrones have been conclusive to constrain temporal shifts in ice stream flow regimes in Greenland and Antarctica[16,22–24]. New radar systems now make it possible to investigate the processes that influence the shape of the isochrones in great detail[25–30], and, depending on the arrangements of profiles, also in 3D[16,31].

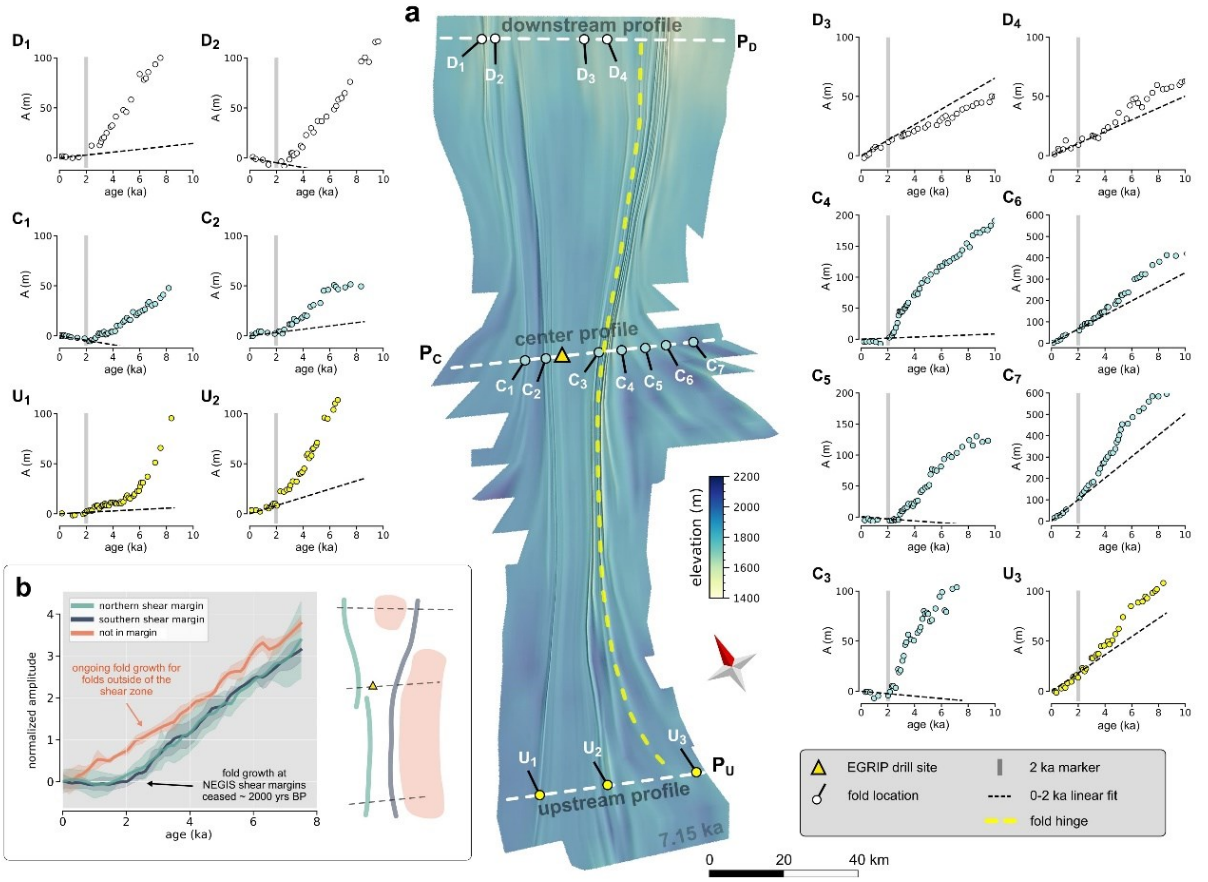

Figure 3: Amplitude-age graphs. (**a**) The centre of the figure shows the 3D visualisation of the 7150 years BP isochrone horizon. (**b**) The graph on the lower left shows the mean normalised fold amplitudes vs age for the two margins and the outside of NEGIS with shaded standard deviation. The sketch to the right shows the origin area of the mean amplitude values. Subfigures show fold amplitude vs. age at fold locations for three selected across-flow radar profiles. Black dotted lines in subfigures represent a linear fit to the data points from 2000 yrs BP until today and then extrapolated to older ages. Letters U, C, and D (Upstream, Central and Downstream) and numbers (increasing from left to right) indicate folds and their locations.

To analyse the overall structure of the distortion of the radar isochrones, we visualised a selected reflector as a 3D horizon (see Methods) in a recently acquired dense array of radargrams (Fig. 1b). We chose one of the deepest layers in the upper half of the ice column, deposited approximately 7150 yrs before present (BP) (EGRIP-core dating[21]) that could still be traced continuously and reliably over the entire survey area (Fig. 1d). The plot of the complete 7150 yr-layer (Fig. 1c) reveals that the ice stream has left a significant imprint on the layer shape over the entire survey area, with complexity, intensity, and number of the folds increasing downstream.

Outside of NEGIS, we find upright, cylindrical folds with wavelengths up to about ten kilometres. Here we define the wavelength as the distance between two adjacent crests or troughs of folds, measured perpendicular to their hinge lines. The amplitude is then defined as the difference in depth of trough and crest. Hinge lines converge on the ice stream in a fan-like pattern (Fig. 1c), with angles relative to NEGIS increasing downstream up to ca. 55° southeast of EGRIP. Here the tallest folds are found with amplitudes (A) that reach up to ca. 500 m in the 7150 yr layer (Fig. 1d). Disturbed ice without a clear stratigraphy is brought up to over a kilometre in the cores of these folds. In the adjacent synclines, the layer of deep disturbed ice is strongly reduced in thickness.

The hinge lines of the folds can be traced from outside of NEGIS into the shear margins and, in some cases, even across the shear margin into the interior of NEGIS (yellow dotted line in Fig. 3). Inside the shear margin, the fold hinges rotate to almost parallel to the shear margin, their wavelengths decrease strongly to < 1 km, and their amplitude is less than outside of NEGIS. It should be noticed that hinge lines are at an angle to flow lines of the surface velocity field.

4 Timescale of fold formation

Dating of the active folding process is essential to constrain fold formation but also to determine the age of the flow perturbations that lead to fold growth, in this case, the formation of NEGIS. Here we address this issue by presenting the results of a novel method, which is based on an analysis of how the fold amplitudes change with the age of the layers, and is introduced in detail in the method section.

The method to date the folding events is based on the principle that a new event leads to a steady increase in fold amplitude with depth in all existing layers. Layers deposited after the folding event are not folded. The timing of the end of the last fold event ended can thus be determined by determining at what age the amplitude-depth trend starts to deviate from zero. Multiple superimposed folding events result in breaks in the amplitude trend, with each break representing a folding event (Methods). Here, however, we are only concerned with the end of fold amplitude growth in the area.

The relationship between depth and age is not exactly, but close to linear in the Holocene ice in the study area, indicating approximately or only gradually changing precipitation rates. In Figure 3, we therefore show amplitude-age, instead of amplitude-depth graphs, for 14 individual crest-through pairs from three radargrams perpendicular to NEGIS. One (labelled C) is at the EGRIP site in the centre of the survey area, one 130 km upstream (U), and one 90 km downstream (D) (Figs. 2, 3 and Methods). Folds well outside of NEGIS ($C_{6\text{-}7}$, and U_3) and inside NEGIS ($D_{3\text{-}4}$) show amplitudes that already start to increase from zero at the surface, which indicates currently active fold amplification. Folds inside the shear margins ($D_{1\text{-}2}$, $C_{1\text{-}3}$, and $U_{1\text{-}2}$) and just adjacent to it southeast of EGRIP ($C_{4\text{-}5}$) show very different amplitude-age trends. Here amplitudes in layers younger than 2 kyrs BP are close to zero, signifying that all these folds stopped growing by about 2 kyrs at the latest. The difference in the fold groups is clearly visible in Figure 3b, which shows the combined-normalised amplitude-age graphs (Methods).

Whereas the end of folding is clearly marked, the onset of the last folding is difficult to determine. The onset of folding would be the age where the amplitude-depth trend reaches a steady slope because layers deposited towards the end of a folding event experienced less folding than those deposited at the beginning. Amplitudes in all folds start to increase steadily with depth and, hence, the age for layers older than ca. 3.5-4 kyrs BP. However, some amplitude-age trends also show bends at other ages, such as ca. 5-6 kyrs (U_1, C_2, $C_{3\text{-}7}$, D_2, D_4, and U_3) and ca. 8 kyrs (D_4 and $C_{4\text{-}7}$). This suggests that the ice sheet here experienced multiple folding events over time, which we cannot resolve here. However, here we are concerned with the final cessation of fold amplification, which was ca. 2 kyrs in and near the shear margins, while fold growth is still ongoing away from the shear margins, both outside NEGIS and in its interior.

5 Folds reveal the history of NEGIS

A conceptual model for the development of the structures in NEGIS that we see in our isochrone horizon is summarised in Figure 4. In the upstream region of NEGIS folding was initiated before 2 kyrs. The fold hinges trend towards the exit gate of the ice stream (Fig. 4a), which is consistent with folding due to convergent flow of ice with a horizontal anisotropy, similar to fold patterns observed at Petermann Glacier[31].

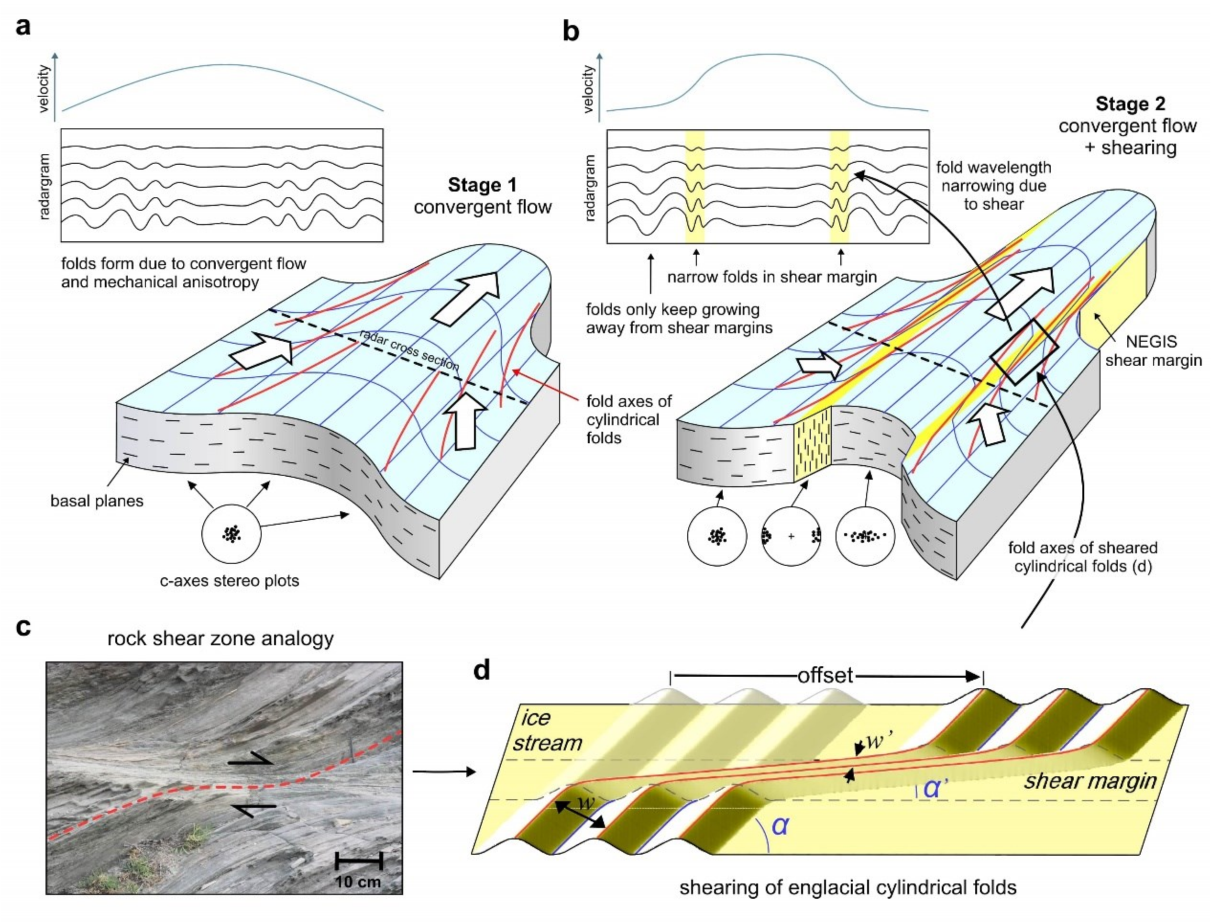

Figure 4: Conceptual model of fold formation. (**a**) Situation before localisation of strain in shear zones. Red lines indicate fold hinges, and white arrows the direction of flow. Below the block diagrams the dominating crystal fabric of the ice is illustrated as Schmidt-plots of c-axed directions. (**b**) After the establishment of shear zones (highlighted in yellow) and a plug-flow like regime in the central part: Inside of the shear margin the fold hinges are rotated towards towards paralellism with the shear margins. (**c**) Shear zone in schistose rock, with the foliation bending into the top-to-the-right shear zone. The picture was taken at Tudela, Cap de Creus, Spain. (**d**) Sketch to illustrate the three strain indicators at the shear margins: (i) reduction of wavelength, (ii) rotation and (iii) offset of fold hinges.

The folds are sheared where they are transected by the shear margins, causing their rotation and tightening (Fig. 4d). This implies that the folds existed before the shear margins developed. Convergent flow implies the development of horizontal velocity and, hence, strain-rate gradients, including zones of non-coaxial strain that are amenable to strain localisation in an anisotropic material such as ice[32,33]. Within the developing shear margins, simple shear along the vertical shear plane dominates over all other strain rate components, such as flattening due to precipitation. This leads to a rotation of the crystal basal planes to vertical and parallel to the shear margins, with concomitant geometric weakening. This kind of fabric has been inferred from airborne radar measurements in the shear margins of Thwaites glacier[34], and NEGIS[35], the latter confirmed by first results from as yet unpublished shallow core measurements. The predominating fabric regimes are indicated in Figure 4a,b as schematic Schmidt-Plots for c-axes orientations. Numerical simulation suggests that the weakening by this change in crystallographic preferred orientation could easily be an increase in shear strain rate of one or two orders of magnitude at a given shear stress (Methods). Figure 4c shows an example of a shear zone in which folds are rotated towards parallelism with the shear zone. Here the anisotropy in metamorphic turbidites is formed by a strong alignment of the highly anisotropic mineral biotite axial planar to folds in a composite bedding and schistosity. As with the shear margins of NEGIS, the rotating anisotropy is thought to have caused localisation of deformation in shear zones[36,37].

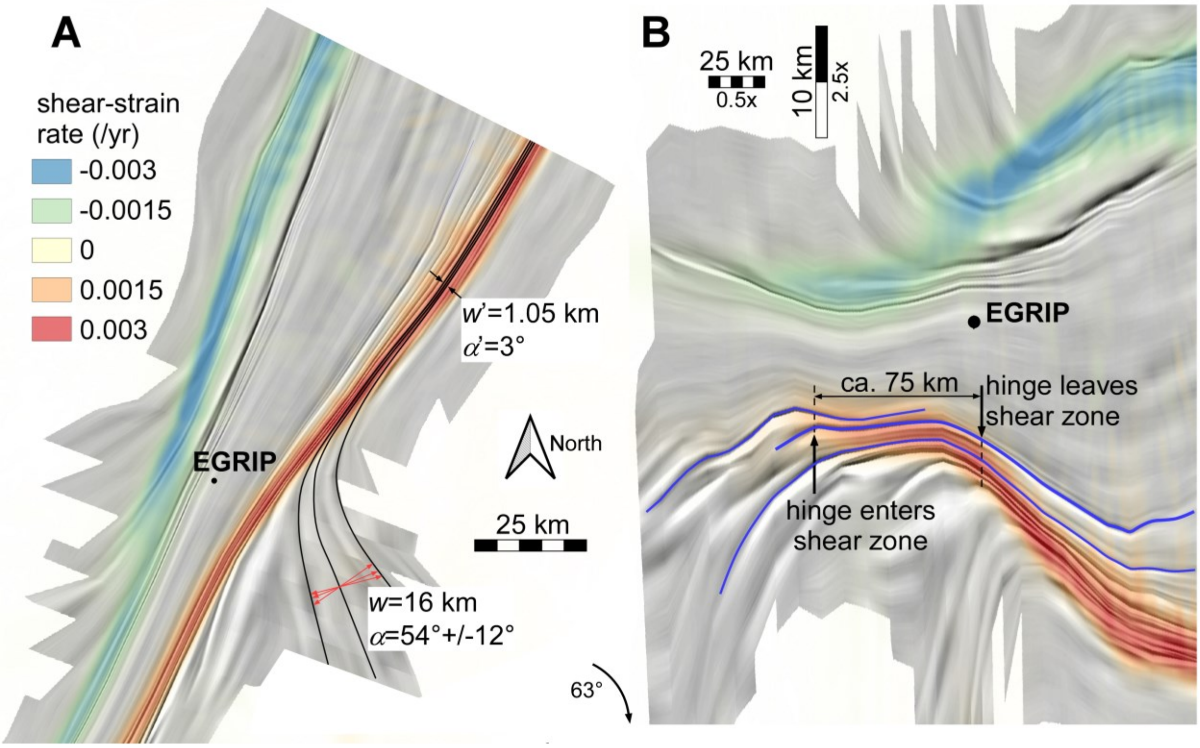

Figure5: (**a**) Folded isochrone horizon with overlay of shear strain rate. Black lines indicate traced fold hinges listed in Suppl. Table 1. Location of EGRIP is shown as the black dot. (**b**) Same image, rotated 63° (long axis of NEGIS) and stretched 5x in the vertical axis of the rotated figure, i.e., perpendicular to the main flow direction, to highlight bends in the hinges.

Numerical simulations with anisotropic ice, with the full-field Elle+VPFFT[38–40] code shows that folds form when basal planes are initially aligned to the shortening direction[41]. However, the shortening quickly rotates the basal planes towards parallelism with the extension direction, which causes a cessation of fold amplification. We thus explain the cessation of fold amplification in and near the shear margins by the rotation of the anisotropy that caused the shear localisation in the shear margins, as compression at a high angle to the planar anisotropy does not lead to folding or fold amplification.

Where the shear margin intersects folds, the hinges of the fold trains rotate towards parallelism with the shear margins (Fig. 4d) as the ice in the ice stream is moving faster, and the fold hinges are advected with the ice flow. This is apparent in the isochrone horizon shown in Figure 1c and the centre panel of Figure 3 but becomes even more apparent when the image is shortened along the flow direction (Figure 5). The observed offset of fold trains southeast of EGRIP is in the order of 75 km. The rotation of the hinges and the resulting shortening of the wavelengths of the folds (Figs. 4d and 5) provide additional indications of the amount of finite strain in the shear margins, resulting in an estimated shear strain of $g \approx 18$ (Methods). The total offset is the product of width of the shear margin and finite shear strain. At a width of 3-4 km, this results in a total offset of ca. 55-75 km. With the current velocity difference of 40 m yr^{-1} across the shear margin, this offset would be achieved in 1375-1875 years. This is underestimated as the velocity difference across the shear margin decreases upstream. Thus, the current flow velocity is consistent with an age of about 2 kyrs BP, which is the time when fold amplification finally ceased in the shear margins (Fig. 3).

From the amplitude graphs and the strain measurements, we can conclude that the upstream part of NEGS and, thus, the present-day NEGIS as an ice stream with distinct shear margins (Fig. 4b) was fully established by about 2 kyrs BP. Geological evidence from the northeast Greenland coast showed that the three major outlets of NEGIS (Fig.1a, the Nioghalvfjerdsfjorden Glacier (NG), the Zachariae Isstrøm (ZI), and the Storstrømmen Glacier (SG) retreated behind their current extent and advanced again at least twice during the last 45 kyrs[42]. During the Holocene Thermal Maximum (HTM) in the early to middle Holocene, temperatures in the Arctic were higher than today[43]. This had a large effect on Greenland ice volume and frontal positions of outlet glaciers[44]. The onset and end of this warm period were regionally different, and there is evidence from geological data that in the area of the three major outlets of the NEGIS that warming started around 8 kyrs BP and ended approximately 4 kyrs BP[43] Accordingly, Nioghalvfjerdsfjorden Glacier was smaller than today in its extent until at least 4.6 kyrs BP[45].

The two-stage process in the upstream NEGIS, with firstly convergent flow and secondly streaming with established shear margins, could be interpreted as a result of increasing discharge from the NEGIS catchment area, following the readvance of the ice front after the HTM, as ice stream activity is linked to the geometry changes of an ice sheet, with increasing intensity of streaming for higher ice volume[46]. Around 4 kyrs BP, a still distributed increase of the outflow led to a drawdown of ice from the flanks and a confluent flow regime due to the geometry of the catchment and the outlet in the northeast. Localisation due to the emerging simple shearing along the vertical plane subsequently led to localised shear and the establishment of the shear margins, which was completed by about 2 kyrs BP, according to our data. Enhanced flow within the ice stream induced ice-stream normal flow in the adjacent ice sheet to compensate for the stretching inside the upstream part of the ice stream, resulting in the typical bottleneck shape of NEGIS, as the shear margins are advected towards the centre of the ice stream[47].

Our observations and dating of folding require a paradigm change in our thinking on NEGIS and, therefore, other ice streams. So far, NEGIS was considered a long-lived structure[4,10] controlled by external boundary conditions, in particular high geothermal heat flux at its upstream end[10,17]. Instead, NEGIS is highly dynamic, only a few thousand years old and still changing. Our results show that an ice sheet is a delicately balanced system in which the whole flow pattern can suddenly and radically change to create major ice streams, such as NEGIS. Together with the study by Franke et al. (2022)[16], we are able to draw a holistic picture of the dynamics of NEGIS-style ice streams, namely that these streams can activate and deactivate within a short time span. Our findings also reveal the time scale on which the ice sheet reacts to changes at the margins by streaming and that these changes are much more likely to trigger the formation and intensification of streaming than local heat flow anomalies[15]. Considering that the ice sheets are now expected to experience massive changes in their boundary conditions[48], it is imperative to include these dynamics in ice-sheet models and predictions of future sea-level rise.

6 Methods

6.1 3D Isochrone horizon

In order to assess the distortion of the radar isochrones in terms of their deformation history to determine the dynamic setting of the ice stream, the 2-dimensional profiles have to be combined to produce a 3-dimensional model of the folded isochrone surfaces[16,31]. For this purpose, we picked selected internal reflections, which are detectable throughout most of the survey area. To ensure spatial continuity, we restrict our analysis to reflections from the upper half of the ice column. By manually assigning profile sections from two neighbouring lines to each other, a surface can be generated in a half-automated way. For this step of the analysis, we used the structural geology modelling software MOVE, a tool for analysis and 3-D visualisation in geosciences and previously employed to visualise folds in Greenland's Petermann Glacier[31] and upstream of Nioghalvfjerdsfjorden Glacier in north-east Greenland. The isochrones are dated by tying them in the depth domain to the age dating of the EGRIP ice core[21] and transferring age in a particular depth to the respective isochrone at that depth. The absolute age and its uncertainty of ca. 90 yrs are of minor importance in our study, as we focus on the overall deformation of the initial flat shape of the considered isochrones.

6.2 Dating of folding events

The method is based on the assumption that a folding event leads to a steady increase in fold amplitude with depth in all layers older than the folding event. Thus, every change in the amplitude-age trend represents a folding event. If this event happened at time t_1, layers younger than t_1 are not folded, i.e., have zero amplitudes. The amplitude trend caused by a subsequent folding event at t_2 will again affect all existing layers. Layers between t_1 and t_2 in age only show the resulting amplitude-depth trend from the second folding event, while older layers show the cumulative effect of both folding events. Every change in the amplitude-age trend thus represents a folding event. It should be borne in mind that folding is not expected to occur at a distinct single point in time but over a certain period and that a change in the amplitude-age trend will be spread out over that period. One should also note that the method is insensitive to changes in precipitation rate or general flow variations over time. These do not show up in amplitude-depth graphs, but may instead create bends in amplitude-age graphs.

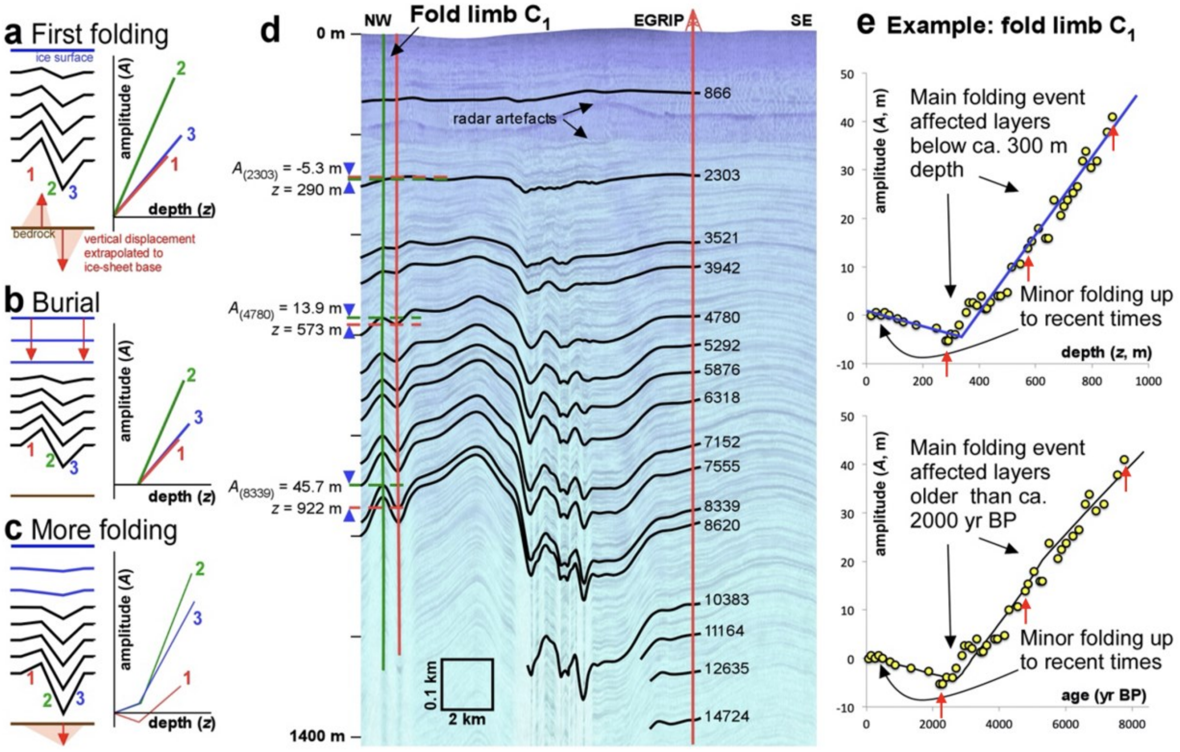

Figure 6: Development of fold amplitudes. (**a-c**) Conceptual sketches for the effect of folding on layer disturbance and development of fold amplitudes (1-3) as a function of depth. (**d**) Part of radargram shown in Figure 2 with traced layers and respective folds. Shown are the uppermost 1400 m y-axes ticks represent 200 m) Numbers on the left show amplitudes and the corresponding reference depth for 3 examples (subscript indicates age of layer), green/red vertical lines on the left indicate the position of the fold hinges of the anti- and synclines. Red vertical line on right indicates EGRIP with each reference layer annotated with its age in years BP. (**e**) Distribution of amplitudes of fold limb C1. The top panel shows amplitude as a function of depth and the bottom amplitude as a function of age The yellow dots indicate the data points derived from the radar layers. Red arrows indicate data points of example folds picked in (**d**). The black and blue lines indicate the trend with a clear kink around 300m depth or 2000 yrs of age.

Folding of stratigraphy causes a change in vertical position of layers, either upwards (anticlines) or downwards (synclines) relative to the undisturbed layer level. This change in height increases downwards from approximately zero at the surface since the surface of ice sheets shows no or little expression of folding (less than a few tens of metres at the most in the study area). We may assume[49,50] that the vertical flattening or thickening strain is approximately constant throughout most of the ice sheet, except in the bottom-most layers. This assumption is not dependent on the cause of the folding, as it essentially states that folding is caused by vertical movements that increase towards the base of the ice sheet. This could be because of basal melting or freezing[27,29], variable slip rates[30], folding due to lateral shortening[31] or even due to flow over bedrock bumps or depressions[51]. The vertical displacement can be described with the parameter:

$$z = \varepsilon \cdot z_0 \qquad (1)$$

A problem is that ε can only be determined if the original depth z_0 of a layer is known. As this is usually not the case, we can compare two adjacent vertical sections with strain ε_1 and ε_2. The difference *A* in depth for a layer is now given by:

$$A = z_1 - z_2 \qquad (2)$$

As long as positions 1 and 2 are close to each other (as in the hinges of a single fold), the pre-fold depths (z_0) of a layer at both locations are expected to be approximately the same. This results in a linear relationship between the amplitude *A* and the mean depth of a layer $<z>=(z_1+z_2)/2$:

$$\frac{z_1}{\varepsilon_1} = \frac{z_2}{\varepsilon_2} \Leftrightarrow \left\langle z' \right\rangle = \frac{z_1 + z_2}{2} = \frac{\left(\varepsilon_1^{-1} + \varepsilon_2^{-1}\right)}{2\left(\varepsilon_2^{-1} - \varepsilon_1^{-1}\right)} A \qquad (3)$$

To determine the amplitude-depth curves, as many layers in a radargram as possible were manually traced for anticline-syncline pairs. Axial planes are constructed as lines that connect the fold hinges. Near the ice surface, folds may die out upwards, in which case the axial planes are extended vertically towards the surface. Depth (z) of a stratigraphic layer is now defined as the vertical distance between a hinge of that layer and the ice surface at the point where it is intersected by the axial plane. Comparison of independent depth determinations by two of the authors (PDB and YZ) showed differences in z up to 3 m, with a standard deviation of the differences of 0.9 m. For each anticline-syncline pair, referred to as a fold limb, this results in a set of $z_{anti}(i)$ and $z_{syn}(i)$ data for each layer *(i)* that was deposited at time *t(i)*. The fold-limb amplitude is now defined as $A(i)=z_{syn}(i)-z_{anti}(i)$, with associated mean depth $<z(i)>=(z_{syn}(i)+z_{anti}(i))/2$.

Ages of layers were derived from tracing to or correlating layers at the EGRIP drill site where ages are known as a function of depth[21]. This results in a set of layers with known depositional ages. In the central profile up to 21 layers < 8 kyrs BP old could be connected to the EGRIP site, while in the downstream profile this number was reduced to at least five. The error in dating of the reference layers is in the order of a few tens of years for the youngest few thousand-year-old layers, increasing to over 100 years towards 8 kyrs BP layers. Most layers within one fold limb cannot be traced all the way to the drill site or can be recognised in the radargram at that site. Their ages are estimated by interpolation, assuming that the relation between height of the layer above the bedrock (*h*) and age (*t*) is given by:

$$\frac{\langle h \rangle}{H} = C \exp^{-k t}, \tag{4}$$

with *H* the local thickness of the ice sheet, and C and *k* two constants derived by fitting to the nearest dated layers above and below the layer of unknown age. As layer thickness are relatively constant down to layers ca. 8 kyrs in age, this interpolation is close to linear. Note that mean depths for each fold were used for the interpolation. All ages are reported as before the year 2000 CE.

6.3 Procrustes analysis

To determine common trends, we use principles of shape analysis as used in biology or anthropology. These disciplines often face the problem of comparing shapes, for example to assign or distinguish fossil remains of modern humans versus Neanderthals[52]. Here the issue is to find commonalities and difference between the shapes of the various amplitude (*A*) versus depth (*z*) graphs (*Az*-graphs). We therefore employ a similar normalisation procedure, known as Procrustes analyis[53,54], to remove scale and absolute amplitude of the *Az*-graphs. Furthermore, to be able to group folds, we need comparable data points, known as "landmarks" in geometric morphometrics. For this we first determine the amplitude *A(t,i)* of each fold limb (*i*) for a fixed series of ages (*t*), here every 100 years, by linear interpolation of the raw amplitude-age data. This was done for the period from 7500 yr BP to the present, to ensure that data for this period are available for all fold limbs. Each *Az*-graph is thus defined by 76 such landmarks.

The first step of the Procrustes normalisation is shifting all landmarks to a common reference, here the mean amplitude (<*A(i)*>): *A'(t,i)= A(t,i)* - <*A(i)*>. The next step is the normalisation for scale, defined by the mean absolute shifted amplitude <|*A'(i)*|>: *A''(t,i)= A'(t,i)*/< |*A'(i)*|>.

Fold limbs were then divided into two groups: (i) folds in or near the shear margins, and (ii) folds inside NEGIS (only measured in the downstream section) and folds well outside of the shear margin on the southeastern side of NEGIS. Due to the very strong distortion in the southern shear margin, no folds were analysed directly inside this margin. Depths of layers are measured from the surface of the ice sheet, which means that amplitudes at the surface are zero, by definition. For plotting, the normalised *A''* data are therefore shifted so that *A''*(i)=0 m. Data are plotted (Fig. 3) with 1σ error bars.

6.4 Strain from rotation of fold hinges and the reduction of fold wavelength

Outside NEGIS fold hinges are oriented at an angle α relative to the shear margin (Fig. 4d). Inside the shear margin the hinges are rotated to an angle α', depending on the amount of shear strain (γ). The shear strain is given, assuming perfect simple shear, by:

$$\gamma = 2\left\{ \frac{\left(1-\cos\left(2\alpha\right)\right)}{\tan\left(\alpha-\alpha'\right)} - \sin\left(2\alpha\right) \right\}^{-1} \tag{5}$$

Shear in the margins does not only rotate the fold axes, but also reduces the wavelength. Folds in the shear margins are therefore much narrower than outside the margins. We use the ratio w/w', where w is the wavelength outside the shear margin and w' the wavelength inside the shear margin, measured in the direction perpendicular to the shear margin (Fig. 4d). Assuming simple shear we obtain:

$$\frac{w}{w'} = \sqrt{1+\gamma^2}\cos\left(\arctan\left(\gamma\right)-\alpha\right) \tag{6}$$

Unfortunately, there is no simple analytical solution to this equation, but the iterative solution for γ is trivial.

Three fold traces (shown in black in Fig. 5a) were traced. They enter the shear margin to the east of EGRIP. Their spacing w was determined where the fold-hinge trend α, relative to the shear margin, ranges from 54° to 75° and w from 15.9 to 16.6 km. In the marginal shear zone, the fold train narrows to approximately one km, giving w/w' ranging from 15.9 to 16.6, depending on the value of α that varies within the fold train. Within the shear margin α' is about 3°. Table 1 provides the shear strain estimates, resulting in an estimated shear strain of $\gamma \approx 18$.

Table 1. Shear strain estimates, assuming perfect simple shear and a final angle of '=3° for three traced fold axes, treated as passive marker lines.

fold	α (°)	w_0 (km)	γ(wavelength)	γ(rotation)
1	54.1	16.2	19.3	18.4
2	62.1	15.9	17.5	18.6
3	74.8	16.6	16.9	18.8
mean			17.9	18.6

6.5 Shear zone softening

The full-field ELLE+VPFFT[32,55–57] simulation code was used to estimate the amount of weakening due to simple shearing along a vertical plane in ice with a strong crystallographic preferred orientation (CPO) in which the basal planes are initially aligned along the horizontal plane. In the semi-2D model, the material is described by 256x256 elements or crystallites, each with their own crystallographic orientation. C-axes were initially randomly oriented within ±5° perpendicular to the model plane. The code uses a spectral solver[39] to determine the stress and strain-rate field compatible with the imposed boundary conditions. An average dextral simple-shear velocity field and zero strain rate in the 3rd dimension was used as boundary conditions.

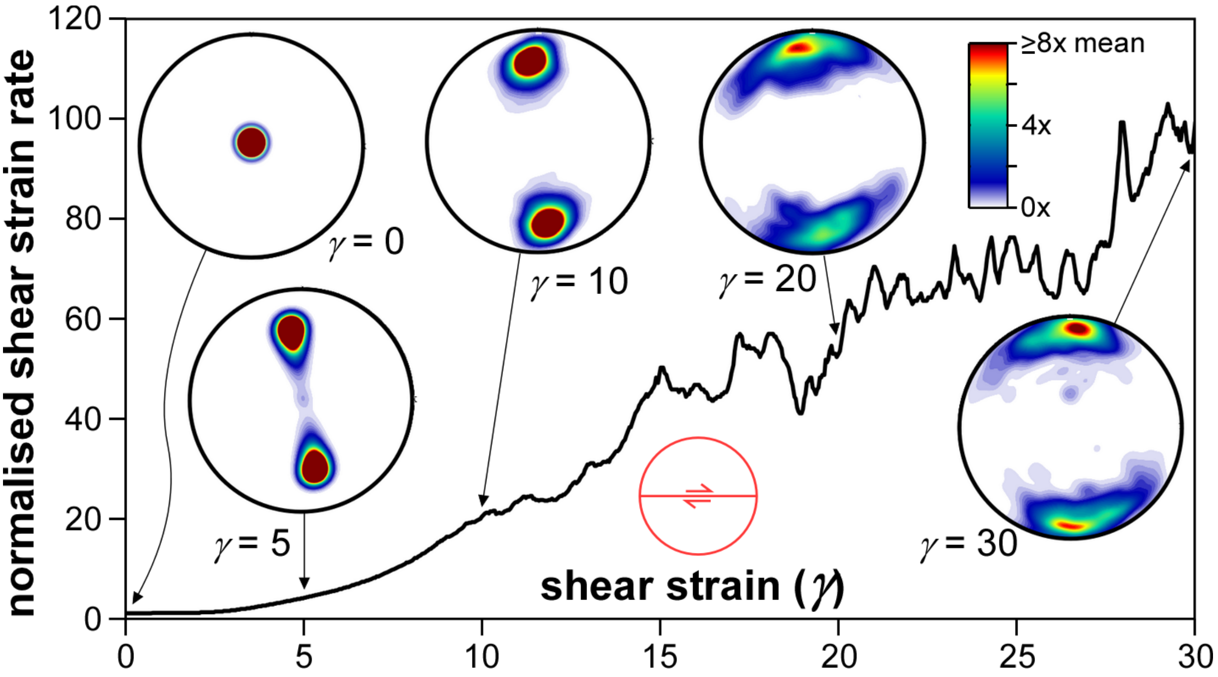

Figure7: Modelling shear zone softening. ELLE+VPFFT[32,33,55] results of simple shearing of ice 1h, starting with a strong vertical point maximum of the c-axis orientations (+-5°), a 16x weaker basal plane, and a stress exponent of 4. The simulation illustrates the evolution and reorientation of the CPO from the ice sheet into the shear margin. The modelled plane is horizontal (bedrock parallel) and is then subjected to simple shear with a vertical shear plane. The graph shows the normalized shear strain rate (at a constant stress) vs. shear strain as well as pole figures (lower hemisphere; classical glaciologic projection looking down a drill core into the ice) until a shear strain of $\gamma = 30$. The single point maximum orientation of c-axes first divides into two point maxima until a shear strain of $\gamma = 10$. Between $\gamma = 10$ and $\gamma = 20$ a transition occurs, when the two point maxima rotate towards a broad new single maximum perpendicular to the shear plane. The total softening is about a hundred at a shear strain of $\gamma = 30$, and already 20 at a shear strain of $\gamma = 10$.

The code assumes that deformation is achieved by power-law slip along the basal, prismatic and pyramidal crystallographic planes of ice 1h, using a stress exponent[58] of 4. The strong anisotropy of ice 1h is incorporated by setting the friction parameter or critical resolved shear stress 16x lower for the basal plane than for any other slip planes. Ice deforming by basal slip only is thus 16x weaker than ice deforming by slip along the other planes at a given strain rate. Von Mises stress and strain-rates are used to describe the bulk strength of the material as a function of strain (Fig. 7). Each step, the velocity field is used to calculate and update the lattice rotation in each element. The CPO is visualised (Fig. 7) by plotting the c-axes' ODF (orientation density function) which represents the volume fraction of crystallites with a certain orientation in a lower hemisphere stereographic projection (using the texture analysis software MTEX[59]).

6.6 Folding of anisotropic ice.

In another ELLE+VPFFT simulation, similar to that to model the shear softening, we investigated the folding of passive lines parallel to the shortening direction in pure-shear shortening. Modelling code and all settings were identical to those described for modelling shear softening (see above), except for the boundary conditions. The initially square model was deformed under plane-strain, pure-shear velocity boundary conditions with horizontal shortening and vertical extension in steps of 2% shortening. C-axes (normal to the easy-glide basal plane) where initially aligned parallel (±5° standard deviation) to the vertical extension direction. The deformation of initially horizontal passive marker lines was traced, using the calculated velocity field for each step, to reveal folding induced by deformation of the anisotropic material. Figure 8a shows that folds form and that the CPO evolves from an initial point maximum to a girdle with two maxima, and finally towards a point maximum parallel to the shortening direction. Fold amplitudes were determined by taking the distance between the highest and lowest point along one folded marker line. Figure 8b shows that active fold amplification ceases from about 25% shortening.

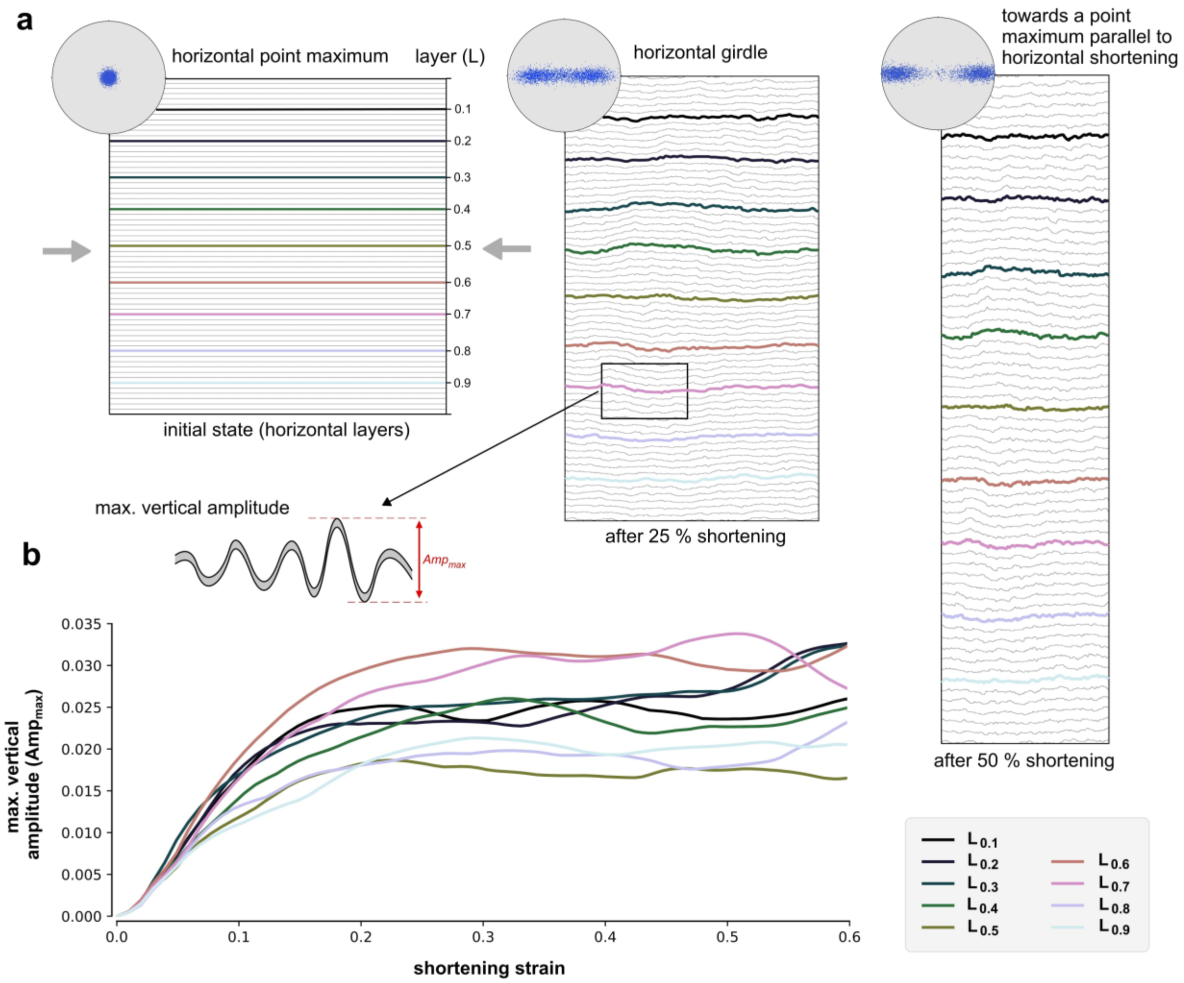

Figure 8: Result of numerical modelling of folding in anisotropic ice (Elle+VPFFT). (**a**) Whole model at three stages of plane-strain horizontal shortening (0, 25 and 50%) with passive marker lines that illustrate the folding of originally horizontal, mechanically passive layers (L). Insets show the distribution of c-axes that are perpendicular to the easy glide basal planes of ice. Projection is looking down from the top of the model, parallel the vertical extension direction. C-axes are thus initially aligned parallel to the extension direction with a standard deviation of ±5°. Folding of the aligned basal planes leads to the formation of a girdle distribution with two point maxima that move to the shortening direction with increasing strain. (**b**) Graph of the maximum vertical amplitude of nine equally spaced, initially horizontal passive marker lines, highlighted in colour in (**a**). The maximum vertical amplitude is the difference between the highest and lowest point along a marker line (inset). Fold amplification ceases at about 25% shortening when the initial strong alignment of c-axes is converted to a partial girdle.

Data Availability

The ice thickness data of the EGRIP-NOR-2018 survey and refined bed topography[11] is available at: https://doi.pangaea.de/10.1594/PANGAEA.907918

The complete radar data set will be made available as part of a data collection for Northern Greenland. The GICC05-EGRIP-1 timescale for the EGRIP ice core[21] can be obtained here: https://doi.org/10.1594/PANGAEA.922139. Amplitudes, depths and age of the picked isochrones for the dating of the folds are available as Extended Data Material.

Acknowledgements

We thank the Ken Borek crew of the research aircraft Polar 6 and system engineer Lukas Kandora. Logistical support in the field was provided by the East Greenland Ice-Core Project (EGRIP). EGRIP is directed and organised by the Center of Ice and Climate at the Niels Bohr Institute. It is supported by funding agencies and institutions in Denmark (A. P. Møller Foundation, University of Copenhagen), USA (US National Science Foundation, Office of Polar Programs), Germany (Alfred Wegener Institute, Helmholtz Centre for Polar and Marine Research), Japan (National Institute of Polar Research and Arctic Challenge for Sustainability), Norway (University of Bergen and Bergen Research Foundation), Switzerland (Swiss National Science Foundation), France (French Polar Institute Paul-Emile Victor, Institute for Geosciences and Environmental research) and China (Chinese Academy of Sciences and Beijing Normal University). We acknowledge the use of the CReSIS toolbox from CReSIS generated with support from the University of Kansas, NASA Operation IceBridge grant NNX16AH54G, and NSF grants ACI-1443054, OPP-1739003, and IIS-1838230. Steven Franke was funded by the AWI Strategy fund and the DFG Walter Benjamin Programme (project number: 563506043073), Daniela Jansen was funded by the AWI Strategy funds and the Helmholtz Young investigator group HGF YIG VH-NG-802, Yu Zhang by the China Scholarship Council (grant no. 202006010063), Yuanbang Hu by the China Scholarship Council (grant no. 202008510177), Maria-Gema Llorens by the Spanish Ministry of Science, Innovation and Universities through a Juan de la Cierva-Incorporación fellowship (grant no. IJC2018-036826-I). Catherine Bauer was funded by the DFG grant DFG BA643/1-1

Author contributions

DJ, SF and PDB were the lead authors

DJ conceived the idea of folds dragged into the ice stream, while PDB conceived the method to date folding events

TB, DJ, and OE designed the grid of airborne radar flights with input from PDB

TB, DJ, and JP collected the radar data

SF, JP and DJ processed the radar data

SF and DJ constructed the 3D model and stratigraphic surface

TdR and G-ML determined the weakening as a result of CPO change

YH carried out ELLE+VPFFT folding simulations

YZ, CCB and PDB collected the amplitude-depth data

PDB carried out the strain analyses for the shear margins

IW, JE, JK, and NS measured ice fabric data and processed the results

NN provided the data for calculating the strain rate field

All authors participated in writing and discussing the final results.

References

1. Choi, Y., Morlighem, M., Rignot, E. & Wood, M. Ice dynamics will remain a primary driver of Greenland ice sheet mass loss over the next century. *Commun Earth Environ* 2, 26 (2021).

2. Khan, S. A. *et al.* Sustained mass loss of the northeast Greenland ice sheet triggered by regional warming. *Nat Clim Change* 4, 292–299 (2014).

3. Christianson, K. *et al.* Dilatant till facilitates ice-stream flow in northeast Greenland. *Earth Planet Sc Lett* 401, 57–69 (2014).

4. Keisling, B. A. *et al.* Basal conditions and ice dynamics inferred from radar-derived internal stratigraphy of the northeast Greenland ice stream. *Ann Glaciol* 55, 127–137 (2014).

5. Karlsson, N. B. & Dahl-Jensen, D. Response of the large-scale subglacial drainage system of Northeast Greenland to surface elevation changes. *Cryosphere* 9, 1465–1479 (2015).

6. Schoof, C. & Mantelli, E. The role of sliding in ice stream formation. *Proc Royal Soc* 477, 20200870 (2021).

7. Krieger, L., Floricioiu, D. & Neckel, N. Drainage basin delineation for outlet glaciers of Northeast Greenland based on Sentinel-1 ice velocities and TanDEM-X elevations. *Remote Sens Environ* 237, 111483 (2020).

8. Joughin, I., Smith, B. E. & Howat, I. M. A complete map of Greenland ice velocity derived from satellite data collected over 20 years. *J Glaciol* 64, 1–11 (2018).

9. Morlighem, M. *et al.* BedMachine v3: Complete Bed Topography and Ocean Bathymetry Mapping of Greenland From Multibeam Echo Sounding Combined With Mass Conservation. *Geophys Res Lett* 44, 11,051-11,061 (2017).

10. Fahnestock, M., Abdalati, W., Joughin, I., Brozena, J. & Gogineni, P. High Geothermal Heat Flow, Basal Melt, and the Origin of Rapid Ice Flow in Central Greenland. *Science* 294, 2338–2342 (2001).

11. Franke, S. *et al.* Bed topography and subglacial landforms in the onset region of the Northeast Greenland Ice Stream. *Ann Glaciol* 61, 143–153 (2020).

12. Franke, S. *et al.* Complex Basal Conditions and Their Influence on Ice Flow at the Onset of the Northeast Greenland Ice Stream. *J Geophys Res Earth Surf* 126, (2021).

13. Hvidberg, C. S. *et al.* Surface velocity of the Northeast Greenland Ice Stream (NEGIS): assessment of interior velocities derived from satellite data by GPS. *Cryosphere* 14, 3487–3502 (2020).

14. Grinsted, A. *et al.* Accelerating ice flow at the onset of the Northeast Greenland Ice Stream. *Nat Commun* 13, 5589 (2022).

15. Bons, P. D. *et al.* Comment on “Exceptionally high heat flux needed to sustain the Northeast Greenland Ice Stream” by Smith-Johnsen et al. (2020). *Cryosphere* 15, 2251–2254 (2021).

16. Franke, S. *et al.* Holocene ice-stream shutdown and drainage basin reconfiguration in northeast Greenland. *Nat Geosci* 15, 995–1001 (2022).

17. Smith-Johnsen, S., Fleurian, B. de, Schlegel, N., Seroussi, H. & Nisancioglu, K. Exceptionally high heat flux needed to sustain the Northeast Greenland Ice Stream. *Cryosphere* 14, 841–854 (2020).

18. Franke, S. *et al.* Airborne ultra-wideband radar sounding over the shear margins and along flow lines at the onset region of the Northeast Greenland Ice Stream. *Earth Syst Sci Data* 14, 763–779 (2022).

19. Rodriguez-Morales, F. *et al.* Advanced Multifrequency Radar Instrumentation for Polar Research. *Ieee T Geosci Remote* 52, 2824–2842 (2013).

20. Alfred Wegener Institut, Helmholtz-Zentrum für Polar und Meeresforschung. Polar aircraft Polar5 and Polar6 operated by the Alfred Wegener Institute. *J Large-scale Res Facil Jlsrf* 2, 87 (2016).

21. Mojtabavi, S. *et al.* A first chronology for the East Greenland Ice-core Project (EGRIP) over the Holocene and last glacial termination. *Clim Past* 16, 2359–2380 (2020).

22. Winter, K. *et al.* Airborne radar evidence for tributary flow switching in Institute Ice Stream, West Antarctica: Implications for ice sheet configuration and dynamics. *J Geophys Res Earth Surf* 120, 1611–1625 (2015).

23. Siegert, M. J. *et al.* Ice Flow Direction Change in Interior West Antarctica. *Science* 305, 1948–1951 (2004).

24. Catania, G. A., Scambos, T. A., Conway, H. & Raymond, C. F. Sequential stagnation of Kamb Ice Stream, West Antarctica. *Geophys Res Lett* 33, (2006).

25. Schroeder, D. M. *et al.* Five decades of radioglaciology. *Ann Glaciol* 61, 1–13 (2020).

26. Ross, N., Corr, H. & Siegert, M. Large-scale englacial folding and deep-ice stratigraphy within the West Antarctic Ice Sheet. *Cryosphere* 14, 2103–2114 (2020).

27. Vieli, G. J.-M. C. L., Martín, C., Hindmarsh, R. C. A. & Lüthi, M. P. Basal freeze-on generates complex ice-sheet stratigraphy. *Nat Commun* 9, 4669 (2018).

28. MacGregor, J. A. *et al.* Radiostratigraphy and age structure of the Greenland Ice Sheet. *J Geophys Res Earth Surf* 120, 212–241 (2015).

29. Bell, R. E. *et al.* Deformation, warming and softening of Greenland’s ice by refreezing meltwater. *Nat Geosci* 7, 497–502 (2014).

30. Wolovick, M. J., Creyts, T. T., Buck, W. R. & Bell, R. E. Traveling slippery patches produce thickness-scale folds in ice sheets. *Geophys Res Lett* 41, 8895–8901 (2014).

31. Bons, P. D. *et al.* Converging flow and anisotropy cause large-scale folding in Greenland’s ice sheet. *Nat Commun* 7, 11427 (2016).

32. de Riese, T. de *et al.* Shear localisation in anisotropic, non-linear viscous materials that develop a CPO: A numerical study. *J Struct Geol* 124, 81–90 (2019).

33. Llorens, M.-G. *et al.* Full-field predictions of ice dynamic recrystallisation under simple shear conditions. *Earth Planet Sc Lett* 450, 233–242 (2016).

34. Young, T. J. *et al.* Inferring Ice Fabric From Birefringence Loss in Airborne Radargrams: Application to the Eastern Shear Margin of Thwaites Glacier, West Antarctica. *J Geophys Res Earth Surf* 126, (2021).

35. Gerber, T. *et al.* Crystal fabric anisotropy causes directional hardening of the Northeast Greenland Ice Stream. (2022) doi:10.21203/rs.3.rs-1812870/v1.

36. Carreras, J., Cosgrove, J. W. & Druguet, E. Strain partitioning in banded and/or anisotropic rocks: Implications for inferring tectonic regimes. *J Struct Geol* 50, 7–21 (2013).

37. Ramsay, J. G. Shear zone geometry: A review. *J Struct Geol* 2, 83–99 (1980).

38. Lebensohn, R. A. N-site modeling of a 3D viscoplastic polycrystal using Fast Fourier Transform. *Acta Mater* 49, 2723–2737 (2001).

39. Lebensohn, R. A. & Rollett, A. D. Spectral methods for full-field micromechanical modelling of polycrystalline materials. *Comp Mater Sci* 173, 109336 (2020).

40. Griera, A. *et al.* Numerical modelling of porphyroclast and porphyroblast rotation in anisotropic rocks. *Tectonophysics* 587, 4–29 (2013).

41. Ran, H. *et al.* Time for anisotropy: The significance of mechanical anisotropy for the development of deformation structures. *J Struct Geol* 125, 41–47 (2019).

42. Larsen, N. K. *et al.* Instability of the Northeast Greenland Ice Stream over the last 45,000 years. *Nat Commun* 9, 1872 (2018).

43. Miller, G. H. *et al.* Temperature and precipitation history of the Arctic. *Quaternary Sci Rev* 29, 1679–1715 (2010).

44. Axford, Y., Vernal, A. de & Osterberg, E. C. Past Warmth and Its Impacts During the Holocene Thermal Maximum in Greenland. *Annu Rev Earth Pl Sc* 49, 1–29 (2020).

45. Bennike, O. & Weidick, A. Late Quaternary history around Nioghalvfjerdsfjorden and Jøkelbugten, North-East Greenland. *Boreas* 30, 205–227 (2001).

46. Stokes, C. R., Margold, M., Clark, C. D. & Tarasov, L. Ice stream activity scaled to ice sheet volume during Laurentide Ice Sheet deglaciation. *Nature* 530, 322–326 (2016).

47. Passchier, C. W. & Platt, J. P. Shear zone junctions: Of zippers and freeways. *J Struct Geol* 95, 188–202 (2017).

48. Fox-Kemper, B. *et al.* Ocean, Cryosphere and Sea Level Change. in *Climate Change 2021: The Physical Science Basis. Contribution of Working Group I to the Sixth Assessment Report of the Intergovernmental Panel on Climate Change* (eds. ["Masson-Delmotte et al.) 1211–1362 (Cambridge University Press). doi:10.1017/9781009157896.011.

49. Dansgaard, W. & Johnsen, S. J. A Flow Model and a Time Scale for the Ice Core from Camp Century, Greenland. *J Glaciol* 8, 215–223 (1969).

50. Nye, J. F. The distribution of stress and velocity in glaciers and ice-sheets. *Proc Royal Soc Lond Ser Math Phys Sci* 239, 113–133 (1957).

51. Raymond, M. J. & Gudmundsson, G. H. On the relationship between surface and basal properties on glaciers, ice sheets, and ice streams. *J Geophys Res Solid Earth* 110, (2005).

52. Benazzi, S. *et al.* Early dispersal of modern humans in Europe and implications for Neanderthal behaviour. *Nature* 479, 525–528 (2011).

53. Rohlf, F. J. & Marcus, L. F. A revolution morphometrics. *Trends Ecol Evol* 8, 129–132 (1993).

54. O'Higgins, P. The study of morphological variation in the hominid fossil record: biology, landmarks and geometry. *J Anat* 197, 103–120 (2000).

55. Steinbach, F. *et al.* Strain localization and dynamic recrystallization in the ice–air aggregate: a numerical study. *Cryosphere* 10, 3071–3089 (2016).

56. Llorens, M.-G. *et al.* Dynamic recrystallization during deformation of polycrystalline ice: insights from numerical simulations. *Philosophical Transactions Royal Soc Math Phys Eng Sci* 375, 20150346 (2017).

57. Piazolo, S. *et al.* A review of numerical modelling of the dynamics of microstructural development in rocks and ice: Past, present and future. *J Struct Geol* 125, 111–123 (2019).

58. Bons, P. D. *et al.* Greenland Ice Sheet: Higher Nonlinearity of Ice Flow Significantly Reduces Estimated Basal Motion. *Geophys Res Lett* 45, 6542–6548 (2018).

59. Mainprice, D., Bachmann, F., Hielscher, R. & Schaeben, H. Descriptive tools for the analysis of texture projects with large datasets using MTEX: strength, symmetry and components. *Geological Soc Lond Special Publ* 409, 251–271 (2015).

61. de Riese, T. et al. Shear localisation in anisotropic, non-linear viscous materials that develop a CPO: A numerical study. *J. Struct. Geol*. **124**, 81-90 (2019).

62.Llorens, G.-M. et al. Dynamic recrystallisation of ice aggregates during co-axial viscoplastic deformation: a numerical approach. *Journal of Glaciology* **62**, 359-377 (2016).

63. Steinbach, F. et al. Strain localisation and dynamic recrystallisation in the ice-air aggregate: A numerical study. *The Cryosphere*, **10**, 3071-3089 (2016).

Appendix

A1 VPFFT + Elle setup

A1.1 Structure of initial Elle file

The initial elle file is consists of several sections.

First is the ‘OPTIONS’ section (Fig. A1), contains some basic setting of environmental parameters. The ‘SwitchDistance’ here related to the *unode* distance, means the minimum and maximum distance between each *unode*. When the distance greater than maximum distance, the system would add one more *unode*, while the distance less than minimum distance, the system would remove one *unode*. The total number of *unode*s remain same. The maximum distance value always 2 - 2.2 times the minimum (Fig. A1). The ‘SpeedUp’ means incremental number of each step. The ‘CellBoundingBox’ means the current box size, related to the initial setting and boundary conditions the system experienced. Here in this example the box setting is 2.0 width, 0.5 height (Fig. A1). ‘Timestep’ is the assumed time per step, no influence on the simulated results.

Second, the ‘FLYNNS’ section (Fig. A1). In this section, the system defines the shapes of grains by connected the sequence number of *bnode*s within the system. Here in this example, the first grain (*flynn*) is made by the *bnode* numbers: 0, 580, 0, 2, 12, 13 …, all sequence numbers displayed here as one line in text, here is line 21 (Fig. A1). The total amount of lines related to the total grains (*flynn*s) numbers.

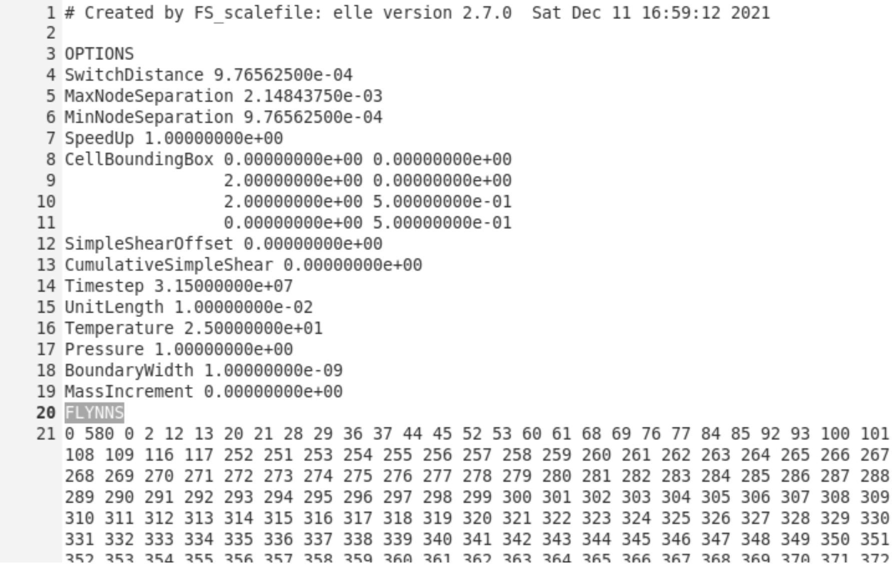

```
 1 # Created by FS_scalefile: elle version 2.7.0  Sat Dec 11 16:59:12 2021
 2
 3 OPTIONS
 4 SwitchDistance 9.76562500e-04
 5 MaxNodeSeparation 2.14843750e-03
 6 MinNodeSeparation 9.76562500e-04
 7 SpeedUp 1.00000000e+00
 8 CellBoundingBox 0.00000000e+00 0.00000000e+00
 9                 2.00000000e+00 0.00000000e+00
10                 2.00000000e+00 5.00000000e-01
11                 0.00000000e+00 5.00000000e-01
12 SimpleShearOffset 0.00000000e+00
13 CumulativeSimpleShear 0.00000000e+00
14 Timestep 3.15000000e+07
15 UnitLength 1.00000000e-02
16 Temperature 2.50000000e+01
17 Pressure 1.00000000e+00
18 BoundaryWidth 1.00000000e-09
19 MassIncrement 0.00000000e+00
20 FLYNNS
21 0 580 0 2 12 13 20 21 28 29 36 37 44 45 52 53 60 61 68 69 76 77 84 85 92 93 100 101
   108 109 116 117 252 251 253 254 255 256 257 258 259 260 261 262 263 264 265 266 267
   268 269 270 271 272 273 274 275 276 277 278 279 280 281 282 283 284 285 286 287 288
   289 290 291 292 293 294 295 296 297 298 299 300 301 302 303 304 305 306 307 308 309
   310 311 312 313 314 315 316 317 318 319 320 321 322 323 324 325 326 327 328 329 330
   331 332 333 334 335 336 337 338 339 340 341 342 343 344 345 346 347 348 349 350 351
   352 353 354 355 356 357 358 359 360 361 362 363 364 365 366 367 368 369 370 371 372
```

Fig. A1: Example of the ‘OPTIONS’ section and part of ‘FLYNNS’ section.

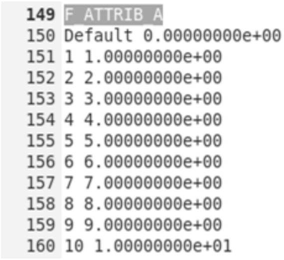

```
F_ATTRIB_A
Default 0.00000000e+00
1 1.00000000e+00
2 2.00000000e+00
3 3.00000000e+00
4 4.00000000e+00
5 5.00000000e+00
6 6.00000000e+00
7 7.00000000e+00
8 8.00000000e+00
9 9.00000000e+00
10 1.00000000e+01
```

Fig. A2: Example of the ‘F_ATTRIB_A’ section

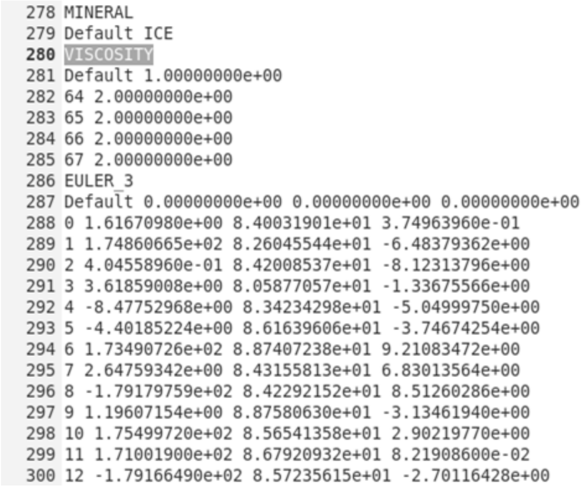

```
MINERAL
Default ICE
VISCOSITY
Default 1.00000000e+00
64 2.00000000e+00
65 2.00000000e+00
66 2.00000000e+00
67 2.00000000e+00
EULER_3
Default 0.00000000e+00 0.00000000e+00 0.00000000e+00
0 1.61670980e+00 8.40031901e+01 3.74963960e-01
1 1.74860665e+02 8.26045544e+01 -6.48379362e+00
2 4.04558960e-01 8.42008537e+01 -8.12313796e+00
3 3.61859008e+00 8.05877057e+01 -1.33675566e+00
4 -8.47752968e+00 8.34234298e+01 -5.04999750e+00
5 -4.40185224e+00 8.61639606e+01 -3.74674254e+00
6 1.73490726e+02 8.87407238e+01 9.21083472e+00
7 2.64759342e+00 8.43155813e+01 6.83013564e+00
8 -1.79179759e+02 8.42292152e+01 8.51260286e+00
9 1.19607154e+00 8.87580630e+01 -3.13461940e+00
10 1.75499720e+02 8.56541358e+01 2.90219770e+00
11 1.71001900e+02 8.67920932e+01 8.21908600e-02
12 -1.79166490e+02 8.57235615e+01 -2.70116428e+00
```

Fig. A3: Example of the ‘MINERAL’ section, ‘VISCOSITY’ section and ‘EULER_3’ section

The third section is ‘F_ATTRIB_A’. Stores the numbers of *flynns*. Not in use now.

Then the following three sections are ‘MINERAL’ section, ‘VISCOSITY’ section and ‘EULER_3’ section. ‘MINERAL’ section stored the mineral information of grain (*flynn*), here is not in use, because the information of mineral(s) is differed by ‘VISCOSITY’ section.

‘VISCOSITY’ section stores the information of phases within the grain (*flynn*) of the system. If the simulation is modelled with one single mineral, so all the grains (*flynns*) are the same, so the ‘VISCOSITY’ here can be default 1, otherwise the setting of grain (*flynn*) which is setup with the second phase, the ‘VISCOSITY’ can be 2, the third can be 3…, etc. Here in Fig. A3, the grains (*flynns*) number of 64, 65, 66, 67 are setting with ‘VISCOSITY’ = 2, and all rest grains (*flynns*) are setting with default = 1.

‘EULER_3’ section contains the information of grains (*flynns*) in the system. All angles are described by three Euler angles α, β, and γ.

The seventh section is ‘LOCATION’. The location of *bnodes* which are used to define the shape of *flynns*.

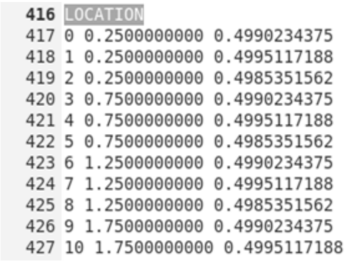

```
LOCATION
0 0.2500000000 0.4990234375
1 0.2500000000 0.4995117188
2 0.2500000000 0.4985351562
3 0.7500000000 0.4990234375
4 0.7500000000 0.4995117188
5 0.7500000000 0.4985351562
6 1.2500000000 0.4990234375
7 1.2500000000 0.4995117188
8 1.2500000000 0.4985351562
9 1.7500000000 0.4990234375
10 1.7500000000 0.4995117188
```

Fig. A4: Example of the ‘LOCATION’ section

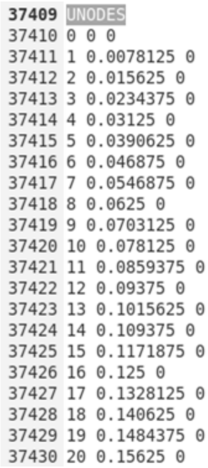

```
UNODES
0 0 0
1 0.0078125 0
2 0.015625 0
3 0.0234375 0
4 0.03125 0
5 0.0390625 0
6 0.046875 0
7 0.0546875 0
8 0.0625 0
9 0.0703125 0
10 0.078125 0
11 0.0859375 0
12 0.09375 0
13 0.1015625 0
14 0.109375 0
15 0.1171875 0
16 0.125 0
17 0.1328125 0
18 0.140625 0
19 0.1484375 0
20 0.15625 0
```

Fig. A5: Example of the ‘UNODES’ section

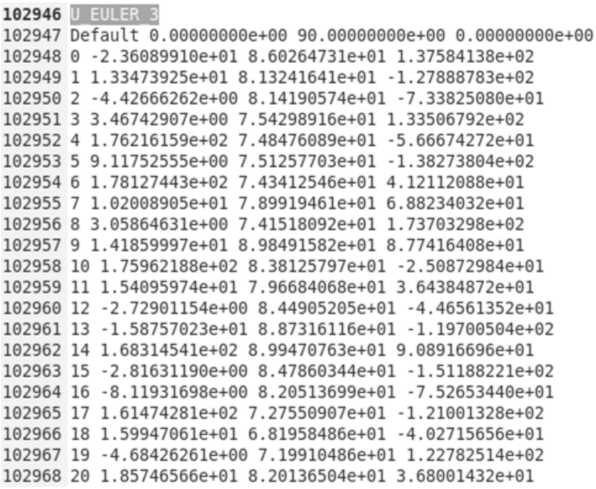

```
U_EULER_3
Default 0.00000000e+00 90.00000000e+00 0.00000000e+00
0 -2.36089910e+01 8.60264731e+01 1.37584138e+02
1 1.33473925e+01 8.13241641e+01 -1.27888783e+02
2 -4.42666262e+00 8.14190574e+01 -7.33825080e+01
3 3.46742907e+00 7.54298916e+01 1.33506792e+02
4 1.76216159e+02 7.48476089e+01 -5.66674272e+01
5 9.11752555e+00 7.51257703e+01 -1.38273804e+02
6 1.78127443e+02 7.43412546e+01 4.12112088e+01
7 1.02008905e+01 7.89919461e+01 6.88234032e+01
8 3.05864631e+00 7.41518092e+01 1.73703298e+02
9 1.41859997e+01 8.98491582e+01 8.77416408e+01
10 1.75962188e+02 8.38125797e+01 -2.50872984e+01
11 1.54095974e+01 7.96684068e+01 3.64384872e+01
12 -2.72901154e+00 8.44905205e+01 -4.46561352e+01
13 -1.58757023e+01 8.87316116e+01 -1.19700504e+02
14 1.68314541e+02 8.99470763e+01 9.08916696e+01
15 -2.81631190e+00 8.47860344e+01 -1.51188221e+02
16 -8.11931698e+00 8.20513699e+01 -7.52653440e+01
17 1.61474281e+02 7.27550907e+01 -1.21001328e+02
18 1.59947061e+01 6.81958486e+01 -4.02715656e+01
19 -4.68426261e+00 7.19910486e+01 1.22782514e+02
20 1.85746566e+01 8.20136504e+01 3.68001432e+01
```

Fig. A6: Example of the ‘U_EULER_3’ section

‘UNODES’ section stored the absolute location related to the ‘CellBoundingBox’. Due to the Elle platform models only 2d processes, so only x-axis and y-axis is stored. The total numbers of *unode* in the example (Fig. A5) is 65536 by 256 x 256 pixels. Each *unode* represent a lattice or a mineral.

Last ‘U_EULER_3’ section contains the information of angles of *unodes* in the system. All angles are also described by three Euler angles α, β, and γ. Due to the total numbers of *unode* in the example (Fig. A5) is 65536, so the setting of ‘U_EULER_3’ contains 65536 euler angles of *unodes* (Fig. A6). The initial CPO used in this thesis are stored in ‘U_EULER_3’ section of each elle file.

A1.2 Initial package of simulation setting

The VPFFT + Elle package is assembled by several files displayed in Fig. A7. This package contains boot file (*.*sh*), elle file (*.*elle*), phase file (*.*sx*) and boundary condition file (*ppc.in*).

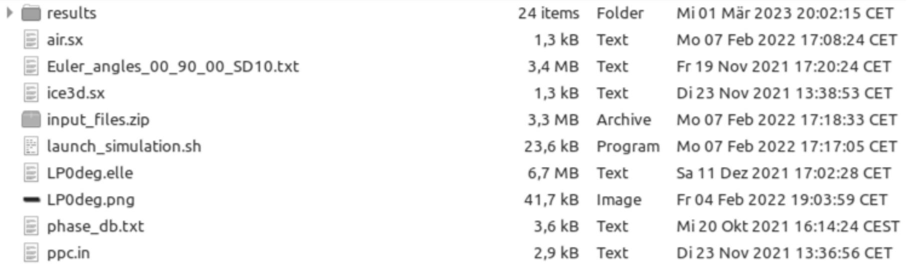

results	24 items	Folder	Mi 01 Mär 2023 20:02:15 CET
air.sx	1,3 kB	Text	Mo 07 Feb 2022 17:08:24 CET
Euler_angles_00_90_00_SD10.txt	3,4 MB	Text	Fr 19 Nov 2021 17:20:24 CET
ice3d.sx	1,3 kB	Text	Di 23 Nov 2021 13:38:53 CET
input_files.zip	3,3 MB	Archive	Mo 07 Feb 2022 17:18:33 CET
launch_simulation.sh	23,6 kB	Program	Mo 07 Feb 2022 17:17:05 CET
LP0deg.elle	6,7 MB	Text	Sa 11 Dez 2021 17:02:28 CET
LP0deg.png	41,7 kB	Image	Fr 04 Feb 2022 19:03:59 CET
phase_db.txt	3,6 kB	Text	Mi 20 Okt 2021 16:14:24 CEST
ppc.in	2,9 kB	Text	Di 23 Nov 2021 13:36:56 CET

Fig. A7: General assemble of VPFFT + Elle package.

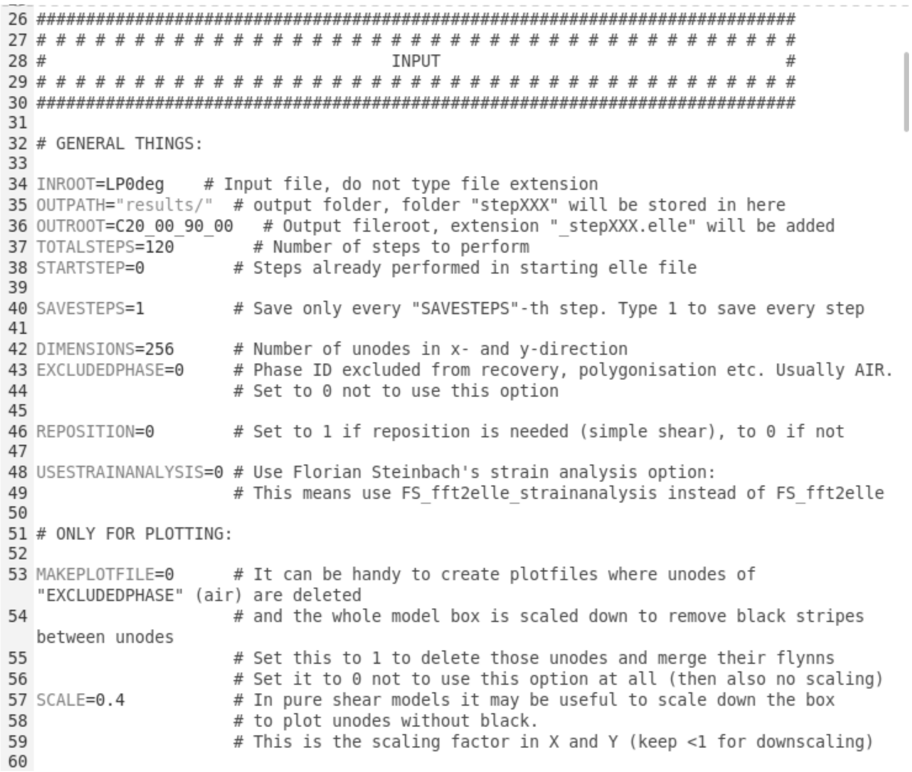

```
#############################################################################
# # # # # # # # # # # # # # # # # # # # # # # # # # # # # # # # # # # # # # #
#                                   INPUT                                   #
# # # # # # # # # # # # # # # # # # # # # # # # # # # # # # # # # # # # # # #
#############################################################################

# GENERAL THINGS:

INROOT=LP0deg    # Input file, do not type file extension
OUTPATH="results/"  # output folder, folder "stepXXX" will be stored in here
OUTROOT=C20_00_90_00   # Output fileroot, extension "_stepXXX.elle" will be added
TOTALSTEPS=120        # Number of steps to perform
STARTSTEP=0         # Steps already performed in starting elle file

SAVESTEPS=1         # Save only every "SAVESTEPS"-th step. Type 1 to save every step

DIMENSIONS=256      # Number of unodes in x- and y-direction
EXCLUDEDPHASE=0     # Phase ID excluded from recovery, polygonisation etc. Usually AIR.
                    # Set to 0 not to use this option

REPOSITION=0        # Set to 1 if reposition is needed (simple shear), to 0 if not

USESTRAINANALYSIS=0 # Use Florian Steinbach's strain analysis option:
                    # This means use FS_fft2elle_strainanalysis instead of FS_fft2elle

# ONLY FOR PLOTTING:

MAKEPLOTFILE=0      # It can be handy to create plotfiles where unodes of
"EXCLUDEDPHASE" (air) are deleted
                    # and the whole model box is scaled down to remove black stripes
between unodes
                    # Set this to 1 to delete those unodes and merge their flynns
                    # Set it to 0 not to use this option at all (then also no scaling)
SCALE=0.4           # In pure shear models it may be useful to scale down the box
                    # to plot unodes without black.
                    # This is the scaling factor in X and Y (keep <1 for downscaling)

```

Fig. A8: Input setting of the boot file (*.*sh*).

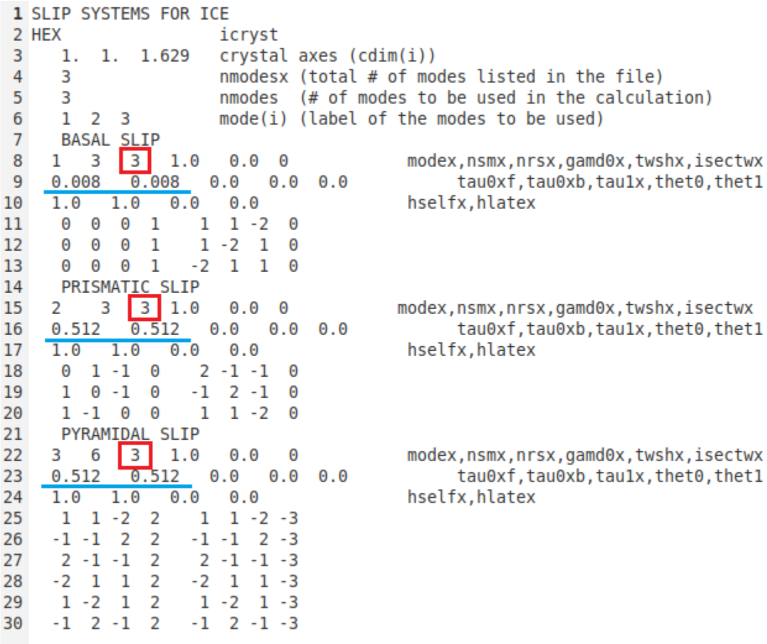

```
SLIP SYSTEMS FOR ICE
HEX                icryst
   1.  1.  1.629   crystal axes (cdim(i))
   3               nmodesx (total # of modes listed in the file)
   3               nmodes  (# of modes to be used in the calculation)
   1  2  3         mode(i) (label of the modes to be used)
   BASAL SLIP
  1   3   3   1.0   0.0  0            modex,nsmx,nrsx,gamd0x,twshx,isectwx
  0.008   0.008   0.0   0.0  0.0           tau0xf,tau0xb,tau1x,thet0,thet1
  1.0   1.0   0.0   0.0               hselfx,hlatex
   0  0  0  1    1  1 -2  0
   0  0  0  1    1 -2  1  0
   0  0  0  1   -2  1  1  0
   PRISMATIC SLIP
  2    3   3  1.0   0.0  0           modex,nsmx,nrsx,gamd0x,twshx,isectwx
  0.512   0.512   0.0   0.0  0.0           tau0xf,tau0xb,tau1x,thet0,thet1
  1.0   1.0   0.0   0.0               hselfx,hlatex
   0  1 -1  0    2 -1 -1  0
   1  0 -1  0   -1  2 -1  0
   1 -1  0  0    1  1 -2  0
   PYRAMIDAL SLIP
  3   6   3   1.0   0.0   0           modex,nsmx,nrsx,gamd0x,twshx,isectwx
  0.512   0.512   0.0   0.0  0.0           tau0xf,tau0xb,tau1x,thet0,thet1
  1.0   1.0   0.0   0.0               hselfx,hlatex
   1  1 -2  2    1  1 -2 -3
  -1 -1  2  2   -1 -1  2 -3
   2 -1 -1  2    2 -1 -1 -3
  -2  1  1  2   -2  1  1 -3
   1 -2  1  2    1 -2  1 -3
  -1  2 -1  2   -1  2 -1 -3
```

Fig. A9: Phase file (*.*sx*) setting.

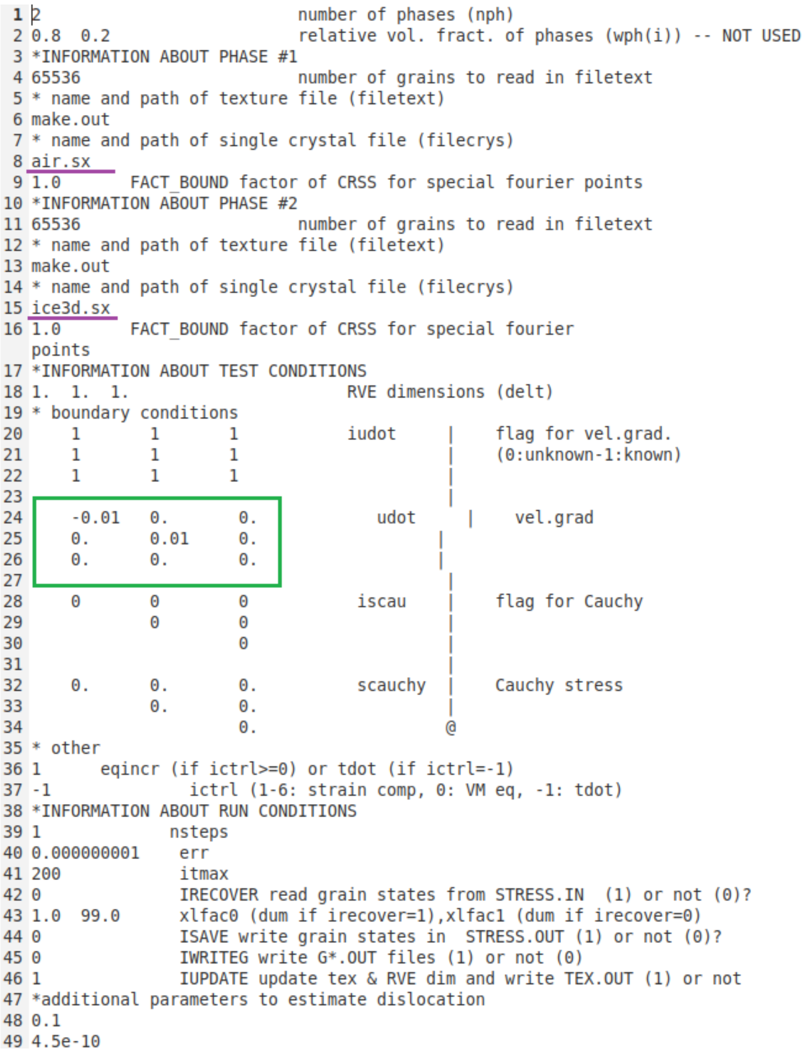

```
2                          number of phases (nph)
0.8  0.2                   relative vol. fract. of phases (wph(i)) -- NOT USED
*INFORMATION ABOUT PHASE #1
65536                      number of grains to read in filetext
* name and path of texture file (filetext)
make.out
* name and path of single crystal file (filecrys)
air.sx
1.0       FACT_BOUND factor of CRSS for special fourier points
*INFORMATION ABOUT PHASE #2
65536                      number of grains to read in filetext
* name and path of texture file (filetext)
make.out
* name and path of single crystal file (filecrys)
ice3d.sx
1.0       FACT_BOUND factor of CRSS for special fourier points
*INFORMATION ABOUT TEST CONDITIONS
1.  1.  1.                      RVE dimensions (delt)
* boundary conditions
    1       1       1           iudot      |    flag for vel.grad.
    1       1       1                      |    (0:unknown-1:known)
    1       1       1                      |
                                           |
    -0.01   0.       0.            udot      |    vel.grad
    0.      0.01     0.                   |
    0.      0.       0.                   |
                                           |
    0       0        0           iscau     |    flag for Cauchy
            0        0                     |
                     0                     |
                                           |
    0.      0.       0.          scauchy   |    Cauchy stress
            0.       0.                    |
                     0.                    @
* other
1      eqincr (if ictrl>=0) or tdot (if ictrl=-1)
-1              ictrl (1-6: strain comp, 0: VM eq, -1: tdot)
*INFORMATION ABOUT RUN CONDITIONS
1             nsteps
0.000000001    err
200            itmax
0              IRECOVER read grain states from STRESS.IN  (1) or not (0)?
1.0  99.0      xlfac0 (dum if irecover=1),xlfac1 (dum if irecover=0)
0              ISAVE write grain states in  STRESS.OUT (1) or not (0)?
0              IWRITEG write G*.OUT files (1) or not (0)
1              IUPDATE update tex & RVE dim and write TEX.OUT (1) or not
*additional parameters to estimate dislocation
0.1
4.5e-10
```

Fig. A10: Boundary condition file (*ppc.in*) setting.

The boot file (*.sh*, shell file) is the guidance to progress the simulation steps. The main loop (details in Steinbach, 2017), which includes all processes that operate in an VPFFT + Elle simulation are included in boot file. The simplest numerical procedure as a loop here contains (1) data from Elle to VPFFT, (2) calculation with VPFFT-code, includes polycrystal deformation by dislocation glide, strain-rate and stress fields, CPO re-orientation and dislocation density, (3) data from VPFFT to Elle, (4) Import VPFFT data to ellefile, (5) Elle process with several topology checks, (6) Subloop steps in Elle, include Recovery, Nucleation and Polygonisation and Grain Boundary Migration (only polyphase), (7) attribute the data from *flynns* to *unodes*, about viscosity, CPO information, (8) create and store new .elle file.

Fig. A8 displays the main controlling parameters and interpretation in running the simulation. Including: (1) the name of input elle file, (2) the name of outroot, (3) total steps, how many steps (loops) the simulation will run, (4) dimensions, how many *unodes* in x- or y- direction, generally the two directions have same amount of *unodes*, (5) reposition (if simulation run under the boundary condition of simple shear).

The phase file (**.sx*, Fig. A9) contains the shape of lattice, the slip system information that define the shear resistances (critical resolved shear stress, CRSS) of each gliding plane, and the viscous property of object mineral or material. In this thesis, the *ice3d.sx* usually used as competent material while *air.sx* as incompetent material. The stress exponent (n) of each material is defined as the value in red cubes (Fig. A9) also in phase file. $n = 1$ is used to simulate linear viscous material that deform as Newtonian flow, while $n \neq 1$ is used to simulate power-law viscous material that deform as a non-Newtonian flow. The numbers have blue underlines define the shear resistances (CRSS) of each slip plane. Intensity of mechanical anisotropy is defined by shear resistance difference of basal and non-basal planes, in this example displayed in Fig.A9 the intensity of anisotropy is 64.

The boundary condition file (*ppc.in*, Fig. A10) includes the phases that involve into the simulation system, the name of phase files (**.sx*) have purple underlines show in this initial setting there are two phases of materials are involved. The matrix with the green cube defines the boundary condition of this initial setting and the simulation the system will experience. The value defines the incremental strain in different x- or y- directions. An iterative solver based on Fast Fourier Transformation is implemented as iteration number of corrections of the calculations.

A2 Visualisation of progressive deformation with elle files

The program ‘showelle’ (Bons et al., 2008) within the Elle platform could display the many different information that included in the elle files, e.g., In *flynn*, viscosity (here the viscosity is the different minerals or materials) of *flynn*, Euler angles of *flynn*, and e.g., in *unodes*, Euler angles of each *unode*, strain-rate field, etc.

As the requirement of display the layers, includes passive marker layer or *foliation* (the mechanical anisotropy) evolving, a C script compiled to achieve the purpose (Fig. A11).

```c
/*
 ============================================================================
 Name        : elle_uGRID_pure shear
 Author      : bons
 Version     :
 Copyright   : Your copyright notice
 Description : Hello World in C, Ansi-style
 rotine to draw a deformed grid from an arbitrary initial orientation from a set of elle files
 ============================================================================
 */

#include <stdio.h>
#include <math.h>
#include <stdlib.h>
#include <stddef.h>
#include <string.h>

#define NR_END 1
#define PI 3.141592653589793238462643383279502884
#define X 0
#define Y 1


char FilenameBase[256];
double  **UnodeXY1,**UnodeXY2,DefaultPhase;
int     **colourmap,shiftx,shifty;
double  boundingbox[4][2]; // coordinates of bounding box corners from bottom left (0,0) and then anti-clockwise
long int    Nnodes; //number of nodes, like 256x256
double  shearstrain;
FILE    *colourmovie;
double  **lineXY0,**lineXY1; // original and final positions of map nodes
double  size=256.0; //size in unodes x unodes
long int **nbUnodes; //stores the 3 neighbouring Unodes for the interpolation and in zeroth position the next map node to connect to
long int    **UnodeNeighbours, NphaseUnodes,*UnodePhase; // list with all 8 neighbours of a unode that is not default phase and the number of such nodes and which they are UnodePhase
long int Nlinenodes;
double  Hdim,Vdim; // dimensions of the model, which changes in pure shear
double  scale; // stretching factor to project model on image of size imagesize
int     Nsteps,Nslices;

long int    intsize=256; // size of model, e.g. 256x256
int     firststep=0,laststep=120;
int     stepsize=1; // normally one, but larger if skipping elle steps
double  layerangle=0; //-26.56505118; // angle with the x-axis of layers in degrees
int     imagesize=1200;
double nodespacing=0.0025; // spacing between nodes along the grid lines
double  Hdimstart=2.0,Vdimstart=0.5; //dimension of the model at the start of the run at stage 000

void ReadFirstElleFile_UnodeXY_check(int step, double **xy);

int main(void) {
    int step;

    strcpy(FilenameBase,"C20_00_90_00_step"); // later change to enter file name base

```

Fig. A11 Example of part of C script use to Visualisation of progressive deformation

As displayed in Fig. A11, several parameters are related to modification for different purposes. Firstly, the C script wants to know the number of *unodes* in x- or y- direction within the series of elle files. And also, the initial size.

Next, inputting the sequence number of the first step and last step that one wants to. If the first step is 0, the last step is 120, the output file would have 121 steps that contain the initial state.

An important modification is about the layer angles. If the layer angle is set parallel to the mechanical anisotropy (CPO), then the lines or curvatures in output file could represent the CPO evolution and deformation. If the layer angle is set unparallel to the mechanical anisotropy (CPO), the lines or curvatures could be treated as passive marker layer that show different geometries.

Then, the setting of image size leads the output file different length of its side. One can also change the node spacing or line spacing to better visualise.

Finally, letting the C script knows the sequences of elle files, so modify the name from the outroot like displayed in Fig. A11, but remove the sequence number.

A3 Numerical setup

Table A1: List of simulations in this PhD projection

	description	elle	layer number		air	A_inc	ice3D	A_c	steps	boundary condition	Euler_aplha
test6	C										
C10	single layer horizontal	layer_horizental	16		2.00E-04	64	1	1	200	vertical compretion	
C12	single layer horizontal	layer_horizental	16		2.00E-03	64	1	1	200	vertical compretion	
C9	single layer horizontal	layer_horizental	16		2.00E-04	64	1	1	120		00/45/90
C11	single layer horizontal	layer_horizental	16		2.00E-03	64	1	1	120		00/45/90
C13	single layer horizontal	layer_horizental	16		8.00E-03	16	1	1	120		00/11/22/33/45/66/77/90
C14	single layer horizontal	layer_horizental	16		3.00E-02	16	1	1	120		00/11/22/33/45/66/77/90
C15	single layer horizontal	LP0deg	32		4.00E-03	16	1	1	120		00/11/22/33/45/56/67/78/90
											-11/-33/-45/-56/-78/-90
C15	single layer horizontal	LP0deg	32		8.00E-03	16	1	1	120		00/33/45/90
C16	ABAB	LP0deg	32		8.00E-03	16	1	1	100		00/33/45/90
C17	single layer horizontal*512	LP0deg512	32		4.00E-03	16	1	1	100		00/33/45/56/90
C18	two layer horizontal 5 gaps	LP0deg	32		4.00E-03	16	1	1	120		00/33/45/56/90
											-11/-33/-45/-56/-78/-90
C19	single layer horizontal	LP0deg	32		3.00E-02	16	1	1	120	horizontal compretion	00/22/33/45/56/78/90
											-11/-33/-45/-56/-78
C20	single layer horizontal	LP0deg	32		8.00E-03	64	1	1	140	horizontal compretion	00/22/33/45/56/78/90
											-11/-33/-45/-56/-78
C21	single layer horizontal	LP0deg	32		4.00E-03	64	1	1	120	horizontal compretion	00/22/33/45/56/78/90
											-11/-33/-45/-56/-78
C22	single layer horizontal	LP0deg	32		1.00E-02	64	1	1	120	horizontal compretion	00/22/33/45/56/78/90
											-11/-33/-45/-56/-78
C23	single layer horizontal	LP0deg	32		1.50E-02	64	1	1	140	horizontal compretion	00/11/22/33/45/56/67/78/90
C24	single layer horizontal	LP0deg	32		2.00E-02	64	1	1	120	horizontal compretion	00/11/22/33/45/56/67/78/90
C25	single layer horizontal	LP0deg	32		3.00E-02	64	1	1	140	horizontal compretion	00/11/22/33/45/56/67/78/90
C26	single layer horizontal	LP0deg	32		2.50E-02	64	1	1	120	horizontal compretion	00/11/22/33/45/56/67/78/90
C27	single layer horizontal	LP0deg	32		1.60E-02	64	1	1	120	horizontal compretion	00/11/22/33/45/56/67/78/90
C28	single layer horizontal	LP0deg	32		1.20E-02	64	1	1	140	horizontal compretion	00/11/22/33/45/56/67/78/90
C29	single layer horizontal	LP0deg	32		1.40E-02	64	1	1	140	horizontal compretion	00/11/22/33/45/56/67/78/90
C30	single layer horizontal	LP0deg	32		6.00E-03	64	1	1	140	horizontal compretion	00/11/22/33/45/56/67/78/90
C31	single layer horizontal	LP0deg	32		1.80E-02	64	1	1	140	horizontal compretion	00/11/22/33/45/56/67/78/90
C32	single layer horizontal	LP0deg	32		3.50E-02	64	1	1	140	horizontal compretion	00/11/22/33/45/56/67/78/90
C33	single layer horizontal	LP0deg	32		4.00E-02	64	1	1	140	horizontal compretion	00/11/22/33/45/56/67/78/90
C34	single layer horizontal	LP0deg	32		5.00E-02	64	1	1	140	horizontal compretion	00/11/22/33/45/56/67/78/90
C51	single layer horizontal	LP0deg	32		8.00E-03	16	1	1	140	horizontal compretion	00/11/22/33/45/56/67/78/90
C52	single layer horizontal	LP0deg	32		1.00E-02	16	1	1	140	horizontal compretion	00/11/22/33/45/56/67/78/90
C53	single layer horizontal	LP0deg	32		1.50E-02	16	1	1	140	horizontal compretion	00/11/22/33/45/56/67/78/90
C54	single layer horizontal	LP0deg	32		2.00E-02	16	1	1	140	horizontal compretion	00/11/22/33/45/56/67/78/90
C55	single layer horizontal	LP0deg	32		2.50E-02	16	1	1	140	horizontal compretion	00/11/22/33/45/56/67/78/90
C19/C56	single layer horizontal	LP0deg	32		3.00E-02	16	1	1	140	horizontal compretion	00/11/22/33/45/56/67/78/90
C57	single layer horizontal	LP0deg	32		3.50E-02	16	1	1	140	horizontal compretion	00/11/22/33/45/56/67/78/90
C58	single layer horizontal	LP0deg	32		4.00E-02	16	1	1	140	horizontal compretion	00/11/22/33/45/56/67/78/90
C59	single layer horizontal	LP0deg	32		4.50E-02	16	1	1	140	horizontal compretion	00/11/22/33/45/56/67/78/90
C60	single layer horizontal	LP0deg	32		5.00E-02	16	1	1	140	horizontal compretion	00/11/22/33/45/56/67/78/90
C61	single layer horizontal	LP0deg	32		6.00E-02	16	1	1	140	horizontal compretion	00/11/22/33/45/56/67/78/90
C62	single layer horizontal	LP0deg	32		7.00E-02	16	1	1	140	horizontal compretion	00/11/22/33/45/56/67/78/90
C63	single layer horizontal	LP0deg	32		8.00E-02	16	1	1	140	horizontal compretion	00/11/22/33/45/56/67/78/90
C64	single layer horizontal	LP0deg	32		9.00E-02	16	1	1	140	horizontal compretion	00/11/22/33/45/56/67/78/90
C65	single layer horizontal	LP0deg	32		1.00E-01	16	1	1	140	horizontal compretion	00/11/22/33/45/56/67/78/90

	description	elle	layer number		air	A_inc	ice3D	A_c	steps	boundary condition	Euler_aplha
test9	n=3										
0LSS	test about angle45 in diff angleLayer										
re6-1	0L SS layer horizontal	LP0deg	32		8.00E-03	64	1	1	200	dextral SS	00/22/45/67/90/-22/-45/-67
L16D0-1	0L SS layer horizontal	LP0deg	16		8.00E-03	64	1	1	200	dextral SS	00/11/22/33/45/56/67/78/90
											-11/-22/-33/-45/-56/-67/-78

	description	elle	layer number		air	A_inc	ice3D	A_c	steps	boundary condition	Euler_aplha
test13	both air and ice are anisotropic										
CI1	single layer horizontal	LP0deg	32		8.00E-03	64	1	16	140	horizontal compretion	00/11/22/33/45/56/67/78/90
CI2	single layer horizontal	LP0deg	32		1.60E-02	64	1	16	140	horizontal compretion	00/11/22/33/45/56/67/78/90
CI3	single layer horizontal	LP0deg	32		1.50E-02	64	1	16	140	horizontal compretion	00/11/22/33/45/56/67/78/90
CI4	single layer horizontal	LP0deg	32		2.00E-02	64	1	16	140	horizontal compretion	00/11/22/33/45/56/67/78/90
CI5	single layer horizontal	LP0deg	32		2.50E-02	64	1	16	140	horizontal compretion	00/11/22/33/45/56/67/78/90
CI6	single layer horizontal	LP0deg	32		3.00E-02	64	1	16	140	horizontal compretion	00/11/22/33/45/56/67/78/90
CI7	single layer horizontal	LP0deg	32		3.50E-02	64	1	16	140	horizontal compretion	00/11/22/33/45/56/67/78/90
CI8	single layer horizontal	LP0deg	32		4.00E-02	64	1	16	140	horizontal compretion	00/11/22/33/45/56/67/78/90
CI9	single layer horizontal	LP0deg	32		5.00E-02	64	1	16	140	horizontal compretion	00/11/22/33/45/56/67/78/90
CI10	single layer horizontal	LP0deg	32		6.00E-02	64	1	16	140	horizontal compretion	00/11/22/33/45/56/67/78/90
CI11	single layer horizontal	LP0deg	32		7.00E-02	64	1	16	140	horizontal compretion	00/11/22/33/45/56/67/78/90
CI12	single layer horizontal	LP0deg	32		1.00E-01	64	1	16	140	horizontal compretion	00/11/22/33/45/56/67/78/90
CI51	single layer horizontal	LP0deg	32		8.00E-03	16	1	16	140	horizontal compretion	00/11/22/33/45/56/67/78/90
CI53	single layer horizontal	LP0deg	32		1.50E-02	16	1	16	140	horizontal compretion	00/11/22/33/45/56/67/78/90
CI54	single layer horizontal	LP0deg	32		2.00E-02	16	1	16	140	horizontal compretion	00/11/22/33/45/56/67/78/90
CI56	single layer horizontal	LP0deg	32		3.00E-02	16	1	16	140	horizontal compretion	00/11/22/33/45/56/67/78/90
test14	air exponent=4										
CE4	single layer horizontal	LP0deg	32		3.20E-02	16	1	1	140	horizontal compretion	00/11/22/33/45/56/67/78/90
CE4-2	single layer horizontal	LP0deg	32		5.00E-02	25	1	1	140	horizontal compretion	00/11/22/33/45/56/67/78/90
E4-1	single layer horizontal	LP0deg	32		8.00E-03	16	1	1	140	horizontal compretion	00/11/22/33/45/56/67/78/90
E4-3	single layer horizontal	LP0deg	32		1.50E-02	16	1	1	140	horizontal compretion	00/11/22/33/45/56/67/78/90
E4-4	single layer horizontal	LP0deg	32		2.00E-02	16	1	1	140	horizontal compretion	00/11/22/33/45/56/67/78/90
test15	exponent=1										
CE1	single layer horizontal	LP0deg	32		8.00E-03	64	1	1	140	horizontal compretion	00/11/22/33/45/56/67/78/90

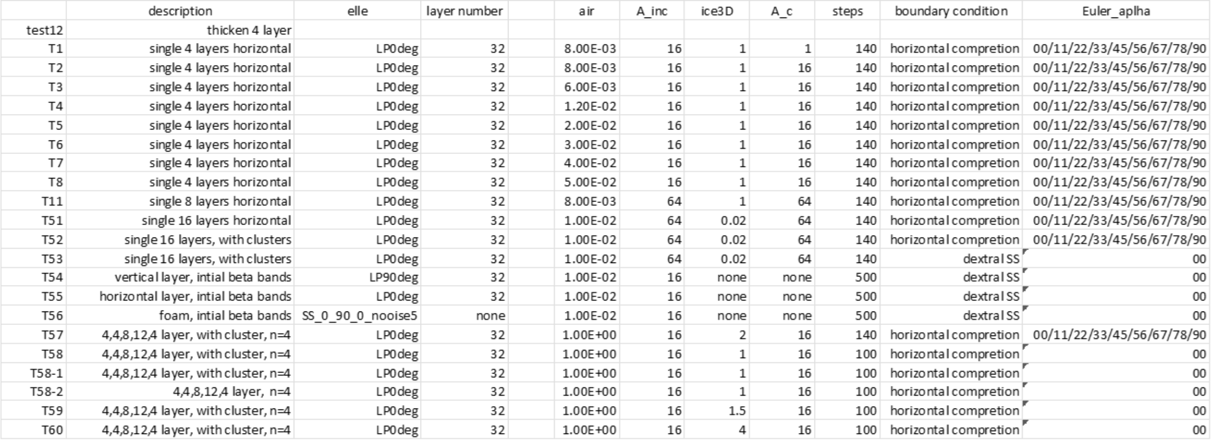

	description	elle	layer number		air	A_inc	ice3D	A_c	steps	boundary condition	Euler_aplha
test12	thicken 4 layer										
T1	single 4 layers horizontal	LP0deg	32		8.00E-03	16	1	1	140	horizontal compretion	00/11/22/33/45/56/67/78/90
T2	single 4 layers horizontal	LP0deg	32		8.00E-03	16	1	16	140	horizontal compretion	00/11/22/33/45/56/67/78/90
T3	single 4 layers horizontal	LP0deg	32		6.00E-03	16	1	16	140	horizontal compretion	00/11/22/33/45/56/67/78/90
T4	single 4 layers horizontal	LP0deg	32		1.20E-02	16	1	16	140	horizontal compretion	00/11/22/33/45/56/67/78/90
T5	single 4 layers horizontal	LP0deg	32		2.00E-02	16	1	16	140	horizontal compretion	00/11/22/33/45/56/67/78/90
T6	single 4 layers horizontal	LP0deg	32		3.00E-02	16	1	16	140	horizontal compretion	00/11/22/33/45/56/67/78/90
T7	single 4 layers horizontal	LP0deg	32		4.00E-02	16	1	16	140	horizontal compretion	00/11/22/33/45/56/67/78/90
T8	single 4 layers horizontal	LP0deg	32		5.00E-02	16	1	16	140	horizontal compretion	00/11/22/33/45/56/67/78/90
T11	single 8 layers horizontal	LP0deg	32		8.00E-03	64	1	64	140	horizontal compretion	00/11/22/33/45/56/67/78/90
T51	single 16 layers horizontal	LP0deg	32		1.00E-02	64	0.02	64	140	horizontal compretion	00/11/22/33/45/56/67/78/90
T52	single 16 layers, with clusters	LP0deg	32		1.00E-02	64	0.02	64	140	horizontal compretion	00/11/22/33/45/56/67/78/90
T53	single 16 layers, with clusters	LP0deg	32		1.00E-02	64	0.02	64	140	dextral SS	00
T54	vertical layer, intial beta bands	LP90deg	32		1.00E-02	16	none	none	500	dextral SS	00
T55	horizontal layer, intial beta bands	LP0deg	32		1.00E-02	16	none	none	500	dextral SS	00
T56	foam, intial beta bands	SS_0_90_0_nooise5	none		1.00E-02	16	none	none	500	dextral SS	00
T57	4,4,8,12,4 layer, with cluster, n=4	LP0deg	32		1.00E+00	16	2	16	140	horizontal compretion	00/11/22/33/45/56/67/78/90
T58	4,4,8,12,4 layer, with cluster, n=4	LP0deg	32		1.00E+00	16	1	16	100	horizontal compretion	00
T58-1	4,4,8,12,4 layer, with cluster, n=4	LP0deg	32		1.00E+00	16	1	16	100	horizontal compretion	00
T58-2	4,4,8,12,4 layer, n=4	LP0deg	32		1.00E+00	16	1	16	100	horizontal compretion	00
T59	4,4,8,12,4 layer, with cluster, n=4	LP0deg	32		1.00E+00	16	1.5	16	100	horizontal compretion	00
T60	4,4,8,12,4 layer, with cluster, n=4	LP0deg	32		1.00E+00	16	4	16	100	horizontal compretion	00

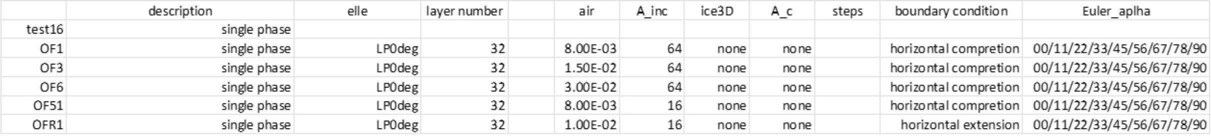

	description	elle	layer number		air	A_inc	ice3D	A_c	steps	boundary condition	Euler_aplha
test16	single phase										
OF1	single phase	LP0deg	32		8.00E-03	64	none	none		horizontal compretion	00/11/22/33/45/56/67/78/90
OF3	single phase	LP0deg	32		1.50E-02	64	none	none		horizontal compretion	00/11/22/33/45/56/67/78/90
OF6	single phase	LP0deg	32		3.00E-02	64	none	none		horizontal compretion	00/11/22/33/45/56/67/78/90
OF51	single phase	LP0deg	32		8.00E-03	16	none	none		horizontal compretion	00/11/22/33/45/56/67/78/90
OFR1	single phase	LP0deg	32		1.00E-02	16	none	none		horizontal extension	00/11/22/33/45/56/67/78/90

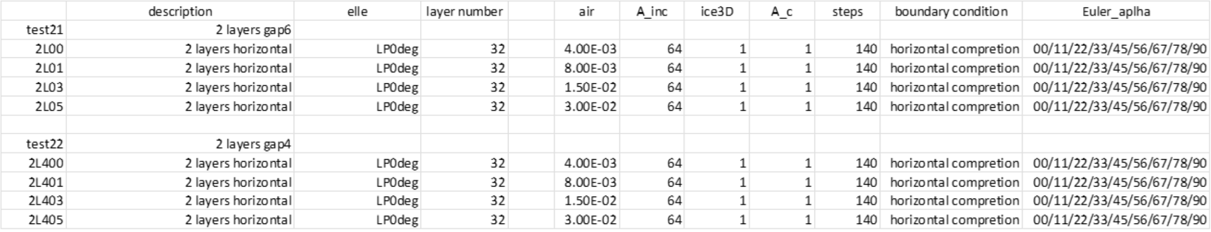

	description	elle	layer number		air	A_inc	ice3D	A_c	steps	boundary condition	Euler_aplha
test21	2 layers gap6										
2L00	2 layers horizontal	LP0deg	32		4.00E-03	64	1	1	140	horizontal compretion	00/11/22/33/45/56/67/78/90
2L01	2 layers horizontal	LP0deg	32		8.00E-03	64	1	1	140	horizontal compretion	00/11/22/33/45/56/67/78/90
2L03	2 layers horizontal	LP0deg	32		1.50E-02	64	1	1	140	horizontal compretion	00/11/22/33/45/56/67/78/90
2L05	2 layers horizontal	LP0deg	32		3.00E-02	64	1	1	140	horizontal compretion	00/11/22/33/45/56/67/78/90
test22	2 layers gap4										
2L400	2 layers horizontal	LP0deg	32		4.00E-03	64	1	1	140	horizontal compretion	00/11/22/33/45/56/67/78/90
2L401	2 layers horizontal	LP0deg	32		8.00E-03	64	1	1	140	horizontal compretion	00/11/22/33/45/56/67/78/90
2L403	2 layers horizontal	LP0deg	32		1.50E-02	64	1	1	140	horizontal compretion	00/11/22/33/45/56/67/78/90
2L405	2 layers horizontal	LP0deg	32		3.00E-02	64	1	1	140	horizontal compretion	00/11/22/33/45/56/67/78/90

Reference

Bons, P.D., Koehn, D, Jessell, M.W., (Eds) (2008). Microdynamic Simulation. Lecture Notes in Earth Sciences 106, Springer, Berlin. 405 pp. ISBN 978-3-540-44793-1.

Steinbach, F., (2017). Numerical modelling of deformation and recrystallisation mechanics in ice and ice-air aggregates. Eberhard Karls University Tübingen, Doktorat Dissertation